



Thermodynamic modelling of ultra-long-term durability
of cementitious binders for waste immobilisation

By

Dale Prentice

Academic Supervisors:

John L. Provis and Susan A. Bernal

Industrial supervisors:

Mark Bankhead and Martin Hayes

A thesis submitted in fulfilment of the requirements for the degree of

Doctor of Philosophy

Department of Materials Science and Engineering

The University of Sheffield

September 2018

Abstract

Treatment of intermediate-level waste (ILW) generated as a by-product from nuclear power in the UK requires a long-term strategy to safely dispose of the waste. Encapsulation of ILW in a cement matrix is the current UK methodology, followed by storing the waste for potentially thousands of years in geological disposal facilities (GDFs). Understanding of the cement phase assemblage is key to predicting how these cements will behave in the long term. Thermodynamic modelling of cement hydrate phases is a powerful tool which can be used to predict the effects of cement hydration. This thesis investigates the quality of thermodynamic modelling to predict stable phase assemblages of blast furnace slag-Portland cement (BFS-PC) cements, representing UK nuclear industry practice, under conditions that are expected during the storage of encapsulated ILW.

Three BFS-PC ratios (1:1, 3:1 and 9:1) were tested at different curing ages to determine the degree of hydration of the precursor materials to use as input parameters for thermodynamic modelling. Characterisation of the phase assemblages were compared to the thermodynamic modelling results to assess the robustness of the modelling approach. A solid solution model for C(-A)-S-H was used to explicitly incorporate aluminium into the C-S-H phase to more accurately portray the chemical structure in the BFS-PC system. Thermodynamic modelling was capable of accurately simulating the change in phase assemblage as curing time increased. Variation of precursor materials was effectively modelled.

Temperature fluctuations are expected to occur within the GDF once the waste is stored within it. BFS-PC samples were cured for one year at 35 °C followed by periods of curing at 50 °C, 60 °C and 80 °C. Major phase changes were not observed until the curing temperature reached 60 °C, whereby hem碳酸盐 and ettringite destabilised. At a curing temperature of 80 °C, the sulphate and carbonate AFm and AFt phases were not observed in cement phase assemblages, however siliceous hydrogarnet was present. Two thermodynamic modelling approaches were used to simulate the effects of temperature change. It was determined that the thermodynamic simulation should not contain siliceous hydrogarnet when simulating BFS-PC hydration up to 60 °C but should contain siliceous hydrogarnet for higher temperatures.

The Pitzer model used as a means to produce activity coefficients, was compared with the generalised dominant electrolyte activity model, Truesdell-Jones, to assess whether modelling of cement phases may be improved. A large ion-interaction parameter database was required to use the Pitzer model for simulating cement hydration. Solubility studies of cement phases and cement pore solution data were used as a means to compare the activity coefficient models. The more complex nature of the Pitzer model caused the simulations to require runtimes up to 18 times more than the Truesdell-Jones method. The pore solution of the BFS-PC systems was compared with the predictions from the activity coefficient models, which determined that the Pitzer model provided minimal improvement over the Truesdell-Jones method. However, the Pitzer model proved more effective for simulating higher concentration systems, therefore, the Pitzer model may be required in future modelling projects when simulating concentrated groundwater interactions with the cement wastefoms.

Acknowledgements

Before I began working on this thesis I knew relatively nothing of cement or its importance and versatility in this world. There are some people whom I need to thank for opening my eyes to the wonderful world of cementitious materials. First and foremost, I must express my gratitude to my academic supervisors, Professor John L. Provis and Dr. Susan A. Bernal. Without their tutelage and never-ending vigour for the subject matter, I would never have been able to complete this work. The years spent on this work flew by due to their optimism and amazing support they shared with me. For that I will always be grateful.

Thanks must be given to my industrial sponsor, The National Nuclear Laboratory, for co-funding this project and specific thanks to my industrial supervisors Dr. Mark Bankhead and Dr. Martin Hayes. With help from Mark and Martin, I was always able to keep focused on the bigger picture of the project and how my work may be used for practical means. A special thanks to Mark for providing a wonderful work environment during my placement at NNL and helping me become a part of his team for a short period of time.

I owe a great deal of gratitude to all of those who helped train me and provide a fantastic experience over the years working in the Immobilisation Science Laboratory. Thanks to Dr. Oday Hussein for training me on every piece of equipment and he's unending patience with the 'Pore press saga'. A great deal of thanks to Dr. Samuel A. Walling, Dr. Laura J. Gardner and Dr. Brant Walkley for helping me analyse so many different pieces of data and teaching me how to streamline my efforts. Also, a grounding thanks to Dr. Daniel J. Bailey for always reminding me that cements are lame, and ceramics are amazing.

Of course, I must thank all of the other students who I shared countless experiences with from the office over the years and helped me see the fun side of academic work, along with the scientific. I would inevitably forget to mention someone, so instead, I express my gratitude to everyone who shared the office with me.

Finally, I would never have had the courage to pursue my goals without the support of my family and to them I offer my greatest thanks.

Contents

Abstract.....	I
Acknowledgements.....	III
List of Figures	VII
List of Tables	XV
1 Synopsis.....	1
2 Introduction and Literature Review.....	3
2.1 Nuclear Waste Management	3
2.1.1 Geological disposal facility.....	5
2.1.2 Temperature profile of cemented wasteforms in the GDF	8
2.2 Portland cement and blended cement	9
2.2.1 Portland cement	9
2.2.2 Cement and supplementary materials.....	10
2.2.3 Blast Furnace Slag (BFS)	11
2.2.4 Phase assemblage of BFS-PC cements	11
2.2.5 Pore solution	19
2.3 Thermodynamic modelling for cementitious systems.....	21
2.3.1 Law of mass action (LMA) and Gibbs energy minimisation (GEM) methods.....	22
2.3.2 Activity coefficient models.....	26
2.4 Cement thermodynamic database	29
2.5 Conclusion.....	31
3 Materials and Methods.....	33
3.1 Materials	33
3.2 Mix design	34
3.3 Analytical techniques.....	34
3.3.1 Selective dissolution – EDTA dissolution.....	34
3.3.2 X-ray diffraction (XRD)	36
3.3.3 ²⁷ Al and ²⁹ Si magic angle spinning (MAS) nuclear magnetic resonance (NMR).....	37
3.3.4 Scanning electron microscopy	42
3.3.5 Pore solution extraction and ICP-OES.....	42
3.4 Thermodynamic modelling	42
4 Phase evolution of slag-rich cementitious grouts for immobilisation of nuclear wastes: an experimental and modelling approach.....	45
4.1 Introduction	45

4.2	Experimental methodology.....	47
4.2.1	Mix Design.....	47
4.2.2	Analytical techniques.....	47
4.2.3	²⁷ Al and ²⁹ Si MAS NMR.....	48
4.2.4	Thermodynamic modelling.....	48
4.3	Experimental results and discussion.....	49
4.3.1	X-ray diffraction.....	49
4.3.2	²⁷ Al MAS NMR.....	51
4.3.3	²⁹ Si MAS NMR.....	54
4.3.4	Determination of degree of hydration using ²⁹ Si MAS NMR and selective dissolution.....	58
4.4	Thermodynamic modelling.....	61
4.4.1	Calculating the hydrate phase assemblage.....	61
4.4.2	Comparison of C-A-S-H gel structural characteristics between model and experiment.....	63
4.4.3	Modelling of aged BFS:PC cements.....	64
4.5	Conclusions.....	66
5	Thermodynamic modelling of BFS-PC cements under temperature conditions relevant to the geological disposal of nuclear wastes.....	67
5.1	Introduction.....	67
5.2	Effect of temperature on the mineralogy of cements.....	68
5.3	Experimental methodology.....	70
5.3.1	Mix Design.....	70
5.3.2	Analytical techniques.....	71
5.4	Experimental Results and Discussion.....	73
5.4.1	Degree of hydration of BFS.....	73
5.4.2	X-ray diffraction and qualitative analysis.....	74
5.4.3	Determination of chemical composition of the C(-A)-S-H phase by SEM.....	81
5.4.4	Chemical composition of hydrotalcite-like phase using SEM-EDS.....	87
5.5	Evaluation of the efficacy of thermodynamic modelling.....	90
5.5.1	Selection of potential phase assemblage constituents.....	90
5.6	Phase assemblage as a function of temperature.....	91
5.6.1	Chemical composition of C-A-S-H phase using thermodynamic modelling as a function of temperature.....	95
5.6.2	Chemical composition of the hydrotalcite-like phase (MA-OH-LDH – solid solution model) using thermodynamic modelling as a function of temperature.....	98
5.7	Conclusions.....	99
6	Using Pitzer parameters in GEMS for predicting blended cements.....	101

6.1	Introduction	101
6.2	Modelling approach	102
6.2.1	Activity coefficient models.....	102
6.2.2	Incorporating Pitzer equations into GEMS	106
6.2.3	Estimating Pitzer parameters.....	107
6.2.4	Testing applicability of the Pitzer model and simulation setup.....	108
6.2.5	Assessing the quality of the calculated data.....	109
6.3	Pore solution extraction from hydrated samples	110
6.4	Modelling results comparing the Pitzer model with the Truesdell-Jones equation.....	111
6.4.1	Portlandite	112
6.4.2	Ca-Al-OH.....	116
6.4.3	Ca-Al-SO ₄ -OH.....	120
6.4.4	Ca-Al-CO ₃ -OH	126
6.4.5	Mg-Al-OH	127
6.4.6	Ca-Si-Al-OH.....	133
6.5	Pore solution of blended cements.....	150
6.5.1	Experimental results	150
6.5.2	Thermodynamic modelling of pore solutions	154
6.5.3	Influence of the different modelling methods.....	158
6.5.4	Computing time	161
6.6	Conclusions	161
7	Conclusions and future work	163
7.1	Conclusions	163
7.2	Future work.....	165
8	Appendix	167
8.1	Analysis of siliceous hydrogarnet phase	167
8.2	Summary of SEM-EDS results.....	169
8.3	Thermodynamic data for phases used in simulations	170
8.4	Pitzer parameter database	180
	References	186
	Publications from thesis.....	210
	Journal Publications	210
	Conference Publications	210
	Other conference presentations.....	210

List of Figures

Figure 2.1: Volume proportion of total packaged waste comprising of HLW, ILW and LLW (VLLW included in the LLW) as of 2016 [4]. 4

Figure 2.2: Schematic of the multiple barrier approach for intermediate level waste and high level waste [23]. 6

Figure 2.3: Schematic of a generic GDF proposed for in the UK (SF: spent fuel; UILW: unshielded ILW; SILW: shielded ILW)[28]. 7

Figure 2.4: Approximate temperature profile of an ILW waste package due to GDF emplacement and backfilling [8,10,30,31]. 8

Figure 2.5: Ternary phase diagram showing the CaO, Al₂O₃ and SiO₂ composition of Portland cement and SCMs, based on phase diagram produced by Lothenbach et al. [37]. 10

Figure 2.6: The C-S-H/C-A-S-H structure depicted using dreierketten units. The green triangles represent paired silicate dimers, blue triangles are bridging silicon tetrahedra, the red triangles represent silicon replacement with aluminium, the purple, orange and pink circles represent Ca²⁺, K⁺ and Na⁺ ions respectively. 14

Figure 2.7: The Ca/Si of C-S-H as a function of a) calcium concentration and b) silicon concentration. The dotted and solid line indicates the Ca/Si when silica and portlandite forms, respectively. Optimal solubility data collated by Walker et al. [65] from the following sources: [53,54,65,69–83]. 15

Figure 2.8: Impact of molar ratios of SO₃/Al₂O₃ versus CO₂/Al₂O₃ on the possible phase assemblage of AFm/Aft phases in the presence of excess portlandite [97]. 18

Figure 2.9: Potassium and sodium concentrations in the pore solution of BFS-PC cements of variable water to binder ratios (w/b) at different levels of slag replacement. The central black lines indicate the 95% interval within CEM I data collated by Vollpracht et al. [104]. 20

Figure 2.10: The difference in Gibbs energy between portlandite and reactants until the point of precipitation, thereafter portlandite precipitates out of solution as more Ca(OH)₂ is added to the system. 25

Figure 2.11: Thermodynamic modelling of the activity coefficients for Ca^{2+} and OH^- ions in the $\text{Ca}(\text{OH})_2$ system, with varying concentration of $\text{Ca}(\text{OH})_2$ added to solution.	25
Figure 2.12: Thermodynamic modelling of brucite and magnesium-oxychloride (MgOxyCl) in the Mg-Cl-OH system using the Pitzer model (P) and Truesdell-Jones (T) equation. The Pitzer parameters and solubility data used are from Harvie et al. [100].	28
Figure 2.13: No miscibility gaps in the calcium to silicon molar ratios (C/S or Ca/Si) are observed when predicting the mole fractions of the end-members in the a) CSHQ and b) CNASH_ss models. Modified from Kulik [64] and Myers et al. [146], respectively.....	31
Figure 3.1: X-ray diffractograms of anhydrous a) PC and b) BFS.	37
Figure 3.2. Fitting of the ^{29}Si MAS NMR spectrum of anhydrous PC: a) experimental data, b) fitted deconvolution, c) alite spectrum, and d) belite spectrum.....	40
Figure 3.3. Fitting of the ^{29}Si MAS NMR spectrum of anhydrous slag: a) experimental data and b) fitted deconvolution.	40
Figure 4.1: X-ray diffractograms of hydrated BFS:PC, a) 1:1, b) 3:1 and c) 9:1 ratios, up to a curing time of 360 days.	50
Figure 4.2: ^{27}Al MAS NMR spectra for a) 1:1, b) 3:1 and c) 9:1 BFS:PC grouts.	53
Figure 4.3: Example deconvolutions of ^{29}Si MAS NMR spectra for a) 1:1, c) 3:1 and e) 9:1 grouts after 360 days, and ^{29}Si MAS NMR spectra for b) 1:1, d) 3:1 and f) 9:1 grouts from 28 days to 360 days of curing.	55
Figure 4.4: Degree of reaction of BFS within the different blend ratios, based on ^{29}Si NMR MAS deconvolutions (NMR) and on selective dissolution (EDTA).	60
Figure 4.5: Degree of reaction of calcium silicate clinker phases (alite and belite) within the different blend ratios, based on ^{29}Si MAS NMR spectral deconvolutions.	60
Figure 4.6: Hydrate phase assemblages predicted using thermodynamic modelling, for a) 1:1, b) 3:1 and c) 9:1 grouts reacting at 35°C , based on the experimentally determined (NMR) degree of hydration data up to 360 days.....	62

Figure 4.7: Calculated phase assemblage of BFS:PC cements using the degree of hydration and precursor materials reported by Taylor et al. [45]. 64

Figure 5.1: Degree of hydration (DoH) of BFS determined from EDTA selective dissolution, within BFS-PC blended cements of ratio 1:1, 3:1 and 9:1, for the temperature profiles 360A, 28B, 28C and 28D. 74

Figure 5.2: XRD patterns of a) 1:1, b) 3:1 and c) 9:1 BFS-PC samples cured at 35 °C for 1 year (360A) and then at either 60 °C (tC) or 80 °C (tD) for a further 28 days. Phases identified are: C – C-A-S-H, P – portlandite, E – ettringite, M – monosulphate, H – hemicarbonate, Mc – monocarbonate, Ht – hydrotalcite, B – belite, and Si – siliceous hydrogarnet..... 76

Figure 5.3: Highlighted low-angle regions of the XRD patterns of a) 1:1, b) 3:1 and c) 9:1 BFS-PC samples cured at 35 °C for 1 year and then at either 60 °C (C) or 80 °C (D) for up to 28 days. Phases identified are: E – ettringite, M – monosulphate, H – hemicarbonate, Mc – monocarbonate, and Ht – hydrotalcite 79

Figure 5.4: XRD patterns for 1:1 BFS:PC cements after curing at 35 °C for one year and being transferred to 80 °C for up to 360 days (temperature profile D). The $C_3AS_{0.41}H_{5.18}$ and $C_3AS_{0.84}H_{4.30}$ chemical formulae depict the siliceous hydrogarnet phases available in the CEMDATA14 database. 80

Figure 5.5: Unit cell size plot as a function of Si-hydrogarnet: PDF data used include card numbers 24–0217 ($a = 12.57$ for C_3AH_6); 32–0151 ($a = 12.29$ for C_3ASH_4); 31–0250 ($a = 12.00$ for $C_3AS_2H_2$) and 33–0260 ($a = 11.846$ for C_3AS_3). References include: [149,210,211,217] and t.s. = this study. 81

Figure 5.6: Histograms of the molar ratios of spot analyses of the 1:1 BFS-PC cement cured at 35 °C for 360 days, showing a) Si/Ca and b) Al/Ca molar ratios determined from calibrated SEM-EDS analysis. 83

Figure 5.7: Al/Ca versus Si/Ca graph of the a) 1:1 b) 3:1 and c) 9:1 BFS-PC cement cured at 35 °C for 360 days. The dashed oval highlights the region where a C-A-S-H phase with $Ca/Si \sim 1.0 - 1.6$ and $Al/Si \sim 0.1 - 0.2$ would appear. The tie lines leading from the centre of the circle lead to the other prominent cement hydrates which may intermix with C-A-S-H (AFt – ettringite, AFm – monosulphate, CH – portlandite). The red square denotes the statistically determined Ca/Si and Al/Si ratio for the individual formulations..... 84

Figure 5.8: Al/Ca versus Si/Ca graphs for the 3:1 BFS-PC cement cured at 35 °C for 360 days and then exposed to (a) 35 °C, (b) 50 °C, (c) 60 °C and (d) 80 °C for a further 28 days. The dashed oval highlights

the region where a C-A-S-H phase with Ca/Si 1.0 – 1.6 and Al/Si 0.1 – 0.2 would appear. The tie lines leading from the centre of the circle lead to the other prominent cement hydrates which may intermix with C-A-S-H (AFt – ettringite, AFm – monosulphate and CH – portlandite). The red square denotes the statistically determined Ca/Si and Al/Si ratio for the individual formulations..... 85

Figure 5.9: BSE-SEM images of 3:1 BFS-PC cement cured at a) 35 °C for 360 days and then exposed to b) 50 °C, c) 60 °C, and d) 80 °C for a further 28 days. 86

Figure 5.10: Mg/Si versus Al/Si atom ratios from EDS analysis for the a) 1:1 b) 3:1 and c) 9:1 28B BFS:PC. Data manipulation was conducted using Mg/Al minimum of 1.0, Mg/Al maximum of 2.5, and Al/Si maximum of 0.5. The red line highlights the line of best fit through the data points and the Mg/Al value is taken from the gradient. The green and blue tie-lines are example lines of gradient 2, which is generally indicative of the lower Mg/Al examples of a hydrotalcite-group LDH. 88

Figure 5.11: Phase assemblages of a) 1:1, b) 3:1 and c) 9:1 BFS-PC cements determined using the thermodynamic modelling software GEMS [132]. The prediction of phase formation was determined as a function of temperature while the remnant precursor content was kept constant. Siliceous hydrogarnet was only allowed to form above 60 °C, and each graphic shows a break at this point to reflect the change in model assumptions. The phase notations correspond to: BFS – Blast furnace slag, PC – Portland cement, C – C-A-S-H, P – portlandite, E – ettringite, M – monosulphate, H – hemicarbonate, Mc – monocarbonate, Ht – hydrotalcite and Si – siliceous hydrogarnet..... 92

Figure 5.12: XRD patterns of a) 1:1, b) 3:1 and c) 9:1 BFS-PC cements exposed to different temperature regimes. Phases identified are: C – C-A-S-H, P – portlandite, E – ettringite, M – monosulphate, H – hemicarbonate, Mc – monocarbonate, Ht – hydrotalcite, B – belite and Si – siliceous hydrogarnet.. 94

Figure 5.13: Molar ratios of a) Ca/Si and b) Al/Si within C-A-S-H as a function of temperature using the two different modelling approaches (*SH* above, and *NS* below, a cutoff temperature of 60 °C in each case) as a function of the BFS:PC ratios. The symbols correspond to SEM-EDS results, while the lines represent the modelling results. The solid line represents the *NS* method and the dotted line represents the *SH* method..... 97

Figure 5.14: Molar ratio of Mg/Al within the magnesium hydrotalcite-like LDH phase of 1:1, 3:1 and 9:1 BFS-PC, using the MA-OH-LDH model developed by Myers et al [123]. 98

Figure 6.1: Programme structure for Pitzer parameter database lookup. 107

Figure 6.2: Pore press used for acquisition of pore fluid from cured BFS-PC cement samples. The dimensions of the press are represented: a) before the sample has been compressed, and b) at the expected maximum level of compression of a cement sample. 111

Figure 6.3: The application of different parameterisations of the Pitzer aqueous solution model to the prediction of portlandite solubility in NaCl solutions: a) highlighting the importance of selection and parameterisation of the aqueous species; P(CaOH⁺) denotes the Pitzer model including CaOH⁺ in the calculations, P denotes a fully parameterised Pitzer model without CaOH⁺, and S denotes the Pitzer model using only the parameters generated from the Simoes estimation equations; b) showing the detrimental effect that the Pitzer model with all parameters set to zero (PF – equation 6.17) has on the predictions in comparison with the Truesdell-Jones (T) equation. Both plots show experimental data from Duchesne and Reardon [66]...... 114

Figure 6.4: Portlandite solubility in a) NaOH and b) KOH, with different aqueous modelling approaches, Pitzer parameter sets, and aqueous species used for calculations. P denotes a fully parameterised Pitzer model, T denotes the Truesdell-Jones equation, and S denotes the Pitzer model including parameters generated only from the Simoes Pitzer estimation equations. Experimental data are from Duchesne and Reardon [66] (D&R-Exp)...... 115

Figure 6.5: Modelling the aqueous solution within the Ca-Al-OH system based on the solubility data of Lothenbach et al. [233]. The Pitzer aqueous solution model using parameters from the literature, P, was compared with parameters obtained from estimating interaction parameters using the equations created by Simoes et al. [225], S; with the literature data being supplemented by estimated parameters, SP; and with the Truesdell-Jones aqueous solution model, T. The variables affected were a) OH⁻ concentration, b) Ca concentration, c) Al concentration and d) pH. 117

Figure 6.6: Invariant points using the Pitzer model for the a) Ca-Al-OH, b) Ca-Al-K-OH and c) Ca-Al-Na-OH systems. The coloured lines represent the phases present in the modelling at given concentrations. The square represents the invariant point of Al(OH)₃ + C₃AH₆ [150] and the circle represents invariant point of C₃AH₆ + CH (a) - [150], b) – [234] and c) - [235]. 118

Figure 6.7: Simulated portlandite and gypsum precipitation using the P and T methods. The coloured lines denote when portlandite (CH) or gypsum (Gp) were predicted to precipitate from solution using the different activity coefficient models. Data obtained from Duchesne and Reardon [66]. 121

Figure 6.8: Phase diagram of the Mg-Al-OH system constructed through thermodynamic modelling. The MA-OH-LDH phase consists of an solid-solution model fitted by Myers et al. [146]. 129

Figure 6.9: Aqueous solution properties in the Mg-Cl-Na-Al-OH system ($MgOH_2 = 0.125$ mol/L, $Al(OH)_3 = 0.0625$ mol/L, and $0 < NaCl < 2.5$ mol/L), considering the effect of increasing concentration of NaCl on: a) pH, b) magnesium solubility, c) aluminium solubility, d) γ_{OH^-} , e) $\gamma_{AlO_2^-}$ and f) $\gamma_{Mg^{2+}}$, using different aqueous solution methods. P denotes a fully parameterised Pitzer model, T denotes the Truesdell-Jones equation, S denotes the Pitzer model including parameters generated only from the Simoes Pitzer estimation equations and SP denotes the Pitzer parameters supplemented with Simoes parameters. Solubility data were taken from Gao and Li [242]. 132

Figure 6.10: The C-S-H/C-A-S-H structure using a) dreierketten units and b) in high Na^+ and K^+ concentrations. The green triangles represent paired silicate dimers, blue triangles are bridging silicon tetrahedra, the red triangles represent silicon replacement with aluminium, the purple, orange and pink circles represent Ca^{2+} , K^+ and Na^+ ions respectively. 133

Figure 6.11: Considering the aqueous speciation of a) calcium and b) silicon in the Ca-Si-OH system, and c) how removing different aqueous species impacts the solubility of calcium and silicon using the Truesdell-Jones equation. Experimental data collected from the literature: [53,54,65,69–83]. 135

Figure 6.12: Comparison of a) pH, b) calcium vs. silicon concentration, c) calcium concentration vs. Ca/Si of the C-S-H, and d) silicon concentration vs. Ca/Si of the C-S-H, in the Ca-Si-OH system. Literature data are from [53,54,65,69–83], compared to predictions from different aqueous solution models, with the $CaOH^+$ and $SiO_2(aq)$ species removed from the Pitzer models. The Pitzer aqueous solution model using parameters from the literature is denoted P; with parameters obtained from estimating interaction parameters using method of Simoes et al. [225] is shown as S; the literature data supplemented by estimated parameters is SP; and the Truesdell-Jones aqueous solution model, T. 138

Figure 6.13: Modelling the impact of K_2O concentration on the a) calcium concentration and b) pH, and the impact of Na_2O concentration on the c) calcium concentration and d) pH. The concentrations of K_2O and Na_2O modelled were 1, 50 and 300 mmol/L, for models P, S, SP, and T. Solubility data taken from Hong and Glasser (filled circles) [59]. 139

Figure 6.14: Comparison of the measured values (from L'Hopital et al. [63]) for a) Ca/Si, b) Al/Si and c) pH versus the values calculated using the C-A-S-H end-member model. The Pitzer model (P) was used to compare the datasets in the above graphs. The different colours represent the Ca/Si ratios in the bulk solution, ranging from 0.6 to 1.6, and the different shapes represent a range of Al/Si ratios from 0.03 to 0.33. The dotted lines indicate the estimated experimental error for the data acquisition, represented as difference from the solid line $y = x$ 143

Figure 6.15: Comparison of the calculated and measured concentration of aqueous species a) aluminium, b) OH⁻, c) silicon and d) calcium, using the C-A-S-H end-member model to compare to solubility data from L'Hopital et al. [63]. The different colours represent the Ca/Si ratios in the bulk solution, ranging from 0.6 to 1.6, and the different shapes represent a range of Al/Si ratios from 0.03 to 0.33. The dotted lines indicate a ± 1 order of magnitude difference from the solid line $y = x$. The red dotted line in a) denotes the experimental detection limit. 144

Figure 6.16: Comparison of the calculated and measured values for a) Ca/Si, b) Al/Si and c) pH, using data collected by L'Hopital et al. [63]. The Pitzer model (P) was used in all model calculations shown. The different colours represent a range of Ca/Si in the bulk solution from 0.6 to 1.6 and the different shapes represent a range of KOH concentration from 0.01 to 0.5 mol/L. The dotted lines indicate the maximum possibility of error for the data acquisition from the experimental study, as difference from the solid line $y = x$. The black triangle represents Ca/Si = 1.0, Al/Si = 0.1 and a KOH concentration of 0.5 mol/L. 146

Figure 6.17: Comparison of the calculated and measured concentration of aqueous species a) aluminium, b) OH⁻, c) silicon and d) calcium, using solubility data from L'Hopital et al. [63]. The different colours represent a range of Ca/Si ratios in the bulk solution from 0.6 to 1.6, and the different shapes represent a range of KOH concentration from 0.01 to 0.5 mol/L. The dotted lines indicate a ± 1 order of magnitude difference from the solid line $y = x$. The black triangle represents Ca/Si = 1.0, Al/Si = 0.1 and a potassium hydroxide concentration of 0.5 mol/L. The red dotted line in a) denotes the experimental detection limit. 148

Figure 6.18: Comparison of the Pitzer model (P) and Truesdell-Jones (T) equation for prediction of gibbsite precipitation in the presence NaOH across a range of ionic strengths (IS). The experimental data was taken from Wesolowski [111]. 149

Figure 6.19: Pore solution compositions of the a) 1:1, b) 3:1 and c) 9:1 BFS-PC cements at different curing ages. 152

Figure 6.20: Simulation of the pore solution of BFS-PC with varying ratios, a) and b) 1:1, c) and d) 3:1 and e) and f) 9:1. The different aqueous solution models used were Pitzer – a), c) and e), and Truesdell-Jones equation – b), d) and f). Colours indicate the different aqueous elements, and the different curing ages are shown as different shapes. 155

Figure A8.1: XRD patterns for cements with BFS:PC ratios a) 1:1, b) 3:1 and c) 9:1 after curing at 35 °C for one year and being transferred to 80 °C for up to 360 days (temperature profile D). The $C_3AS_{0.41}H_{5.18}$

and $C_3AS_{0.84}H_{4.30}$ chemical formulae depict the siliceous hydrogarnet phases available in the CEMDATA14 database. 168

Figure A8.2: XRD patterns of cements with BFS:PC ratios 1:1, 3:1 and 9:1 after curing at 35 °C for 360 days and being transferred to 80 °C for 360 days (temperature profile D). Silicon content of the siliceous hydrogarnet determined from unit cell analysis, Figure 5.5 from section 5.4.3 Figure 5.5 of the main article. 169

List of Tables

Table 3.1: Major constituents of raw materials, as determined by X-ray fluorescence (XRF) and represented as oxides.	33
Table 3.2: Blaine fineness and particle size distribution (PSD) analysis of raw materials.	34
Table 3.3. Clinker phases present in anhydrous PC, as quantified by ^{29}Si MAS NMR and by the Taylor-Bogue method.....	39
Table 3.4: Chemical shift ranges in which the different silicon Q^x species are located using ^{29}Si NMR.	41
Table 3.5: Chemical shift ranges that the different silicon Q^x species are located using ^{27}Al NMR.	41
Table 3.6: Thermodynamic data for the end-members in the solid-solution model for C-A-S-H. Standard thermodynamic properties at 25 °C and 1 bar.....	43
Table 4.1: Site allocations for silicon environments in ^{29}Si MAS NMR spectra.....	54
Table 4.2: Results of deconvolution of the ^{29}Si MAS NMR spectra as a function of time and cement composition.	57
Table 4.3: Summary of structural characteristics of the C-A-S-H gel forming in BFS:PC cements based on the ^{29}Si MAS NMR results	58
Table 4.4: Summary of structural characteristics of the C-A-S-H gel derived from thermodynamic modelling.	64
Table 4.5: Portlandite content, as weight percentage of the hydrates formed at varying degrees of slag replacement. Results from 20 year sample are from Taylor et al. [45].....	65
Table 4.6: Structural characteristics of the C-A-S-H gel of the 20 year old sample (20 y) analysed by Taylor et al. [45] and thermodynamic modelling (GEMS) for these systems.	66
Table 5.1: Approximate temperature profile of an ILW waste package due to GDF emplacement and backfilling [8,10,30,31].....	68
Table 5.2: Sample reference IDs for the different curing profiles; t is time in days.	70

Table 5.3: Comparison of the molar ratios of the BFS, obtained from XRF and SEM-EDS data, and the corrected values obtained by calibration of the EDS data using information from XRF.	72
Table 5.4: Elemental correction factors used to correct the SEM-EDS analysis.	72
Table 5.5: Molar ratios of common cement phases (precursors and hydrates) which may affect the chemical composition measurements.	82
Table 5.6: SEM-EDS analysis of the Mg/Al ratio of the hydrotalcite-like phase for different BFS-PC ratios and temperatures of curing. Samples were cured at 35 °C for 1 year (360A) and then at either 60 °C (tC) or 80 °C (tD) for a further 28 days. Samples were cured at 35 °C for 1 year, followed by 80 °C for 1 year and finally cured for 28 days at 50 °C (tE). Samples cured at 35 °C for 2 years (720A).	90
Table 5.7: Clinker degree of hydration values used in thermodynamic modelling. Taylor-Bogue analysis determined the clinker phase ratios in the initial PC: C ₃ S = 71.9 wt.%, C ₂ S = 6.8 wt.%, C ₃ A = 8.0 wt.%, C ₄ AF = 7.7 wt.% [122].	91
Table 6.1: Concentration limits and step sizes for the concentration arrays used to model the Ca-Al-SO ₄ -OH and Ca-Al-CO ₃ -OH systems.	109
Table 6.2: Invariant points determined using the <i>P</i> , <i>T</i> , <i>S</i> and <i>SP</i> methods in the Ca-Al-OH system. The term nm denotes a value that was not measured.	119
Table 6.3: Invariant points determined using the <i>P</i> , <i>T</i> , and <i>S</i> methods in the Ca-SO ₄ -OH system.	122
Table 6.4: Invariant points determined using the <i>P</i> , <i>T</i> , <i>S</i> and <i>SP</i> methods in the Ca-Al-SO ₄ -OH system.	123
Table 6.5: Invariant points determined using the <i>P</i> , <i>T</i> , <i>S</i> and <i>SP</i> methods in the Ca-Al-SO ₄ -OH systems with the inclusion of KOH or NaOH.	125
Table 6.6: Invariant points determined using the <i>P</i> , <i>T</i> , <i>S</i> and <i>SP</i> methods in the Ca-Al-CO ₃ -OH systems.	127
Table 6.7: Invariant points within the Mg-Al-OH system determined from XRD analysis of the crystal structure compared to the invariant points determined from the MA-OH-LDH solid solution model [146].	128

Table 6.8: The sum of squared errors (SSE) for the pH, OH⁻, Mg and Al concentrations in solution, comparing the thermodynamic modelling results in GEMS to the experimental data for the Mg-Al-Na-Cl-OH system. The four aqueous solution model methods compared were the Pitzer model with literature parameters (P), Pitzer model using estimated Simoes parameters (S), Pitzer parameters from the literature supplemented by Simoes parameters (SP) and the Truesdell-Jones equation (T). 130

Table 6.9: Concentration of calcium required in the Ca-Si-OH system for portlandite to precipitate. 137

Table 6.10: The logarithm of the sum of square errors (SSE) for calcium and pH concentration calculated across the 1, 5, 15, 50, 100 and 300 mmol/L concentrations of Na₂O or K₂O, using the different modelling methods. Solubility data taken from Hong and Glasser [59]. The Pitzer aqueous solution model, P, was compared with parameters obtained from estimating interaction parameters using the equations created by Simoes et al. [225], S; with the literature data being supplemented by estimated parameters, SP; and with the Truesdell-Jones aqueous solution model, T. 140

Table 6.11: Thermodynamic properties of C-S-H and C-A-S-H end-members in the model used for simulation of C-A-S-H formation. Standard thermodynamic properties at 25 °C and 1 bar 141

Table 6.12: Log SSE values, comparing the calculated results using the C-A-S-H end-member model with measured solubilities in the Ca-Al-Si-OH system [63]. 142

Table 6.13: The log SSE values highlighting the difference of the modelled results compared to the calculated results using the C-A-S-H end-member model, compared to the solubility study of the Ca-Al-Si-OH system in NaOH or KOH [108]. 149

Table 6.14: Pore solution chemistry determined for the 1:1, 3:1 and 9:1 BFS-PC cements at curing ages ranging from 14 to 360 days. nm denotes a value which was not measured. Curing ages for the samples were different due to malfunctions of the pore press at different dates of pore solution acquisition. 151

Table 6.15: Log SSE values of the various aqueous species simulated in the pore solution of the 1:1, 3:1 and 9:1 BFS-PC using the different aqueous solution models, with HS⁻ Pitzer parameters [247]. 159

Table 6.16: Log SSE values of the various aqueous species simulated in the pore solution of the 1:1, 3:1 and 9:1 BFS-PC using the different aqueous solution models, without HS⁻ Pitzer parameters. ... 160

Table 6.17: Time taken to run the simulations for the 1:1, 3:1 and 9:1 BFS-PC systems to simulate one year of hydration using the Pitzer model and the Truesdell-Jones equation.....	161
Table A8.1: Silicon hydrogarnet phases silicon content linked to the lattice parameter a	167
Table A8.2: Results of calibrated SEM-EDS analysis of the Ca/Si and Al/Si ratios of the C-A-S-H phase, for different BFS-PC ratios and temperature regimes.	170
Table A8.3: Thermodynamic properties of the solid phases forming in each of the modelling approaches. The 'x' marked in the 'Presence in simulation' column, denotes whether the phase was allowed to form in the two different modelling options. Standard thermodynamic properties at 25 °C and 1 bar.	171
Table A8.4: Aqueous species used during the modelling. Standard thermodynamic properties at 25 °C and 1 bar.	175
Table A8.5: Gaseous species used for thermodynamic modelling. Standard thermodynamic properties at 25 °C and 1 bar.....	179
Table A8.6: Binary species Pitzer parameters.....	180
Table A8.7: Mixed electrolyte Pitzer parameters.	182

1 Synopsis

Intermediate level waste (ILW) is defined as waste that has a higher than acceptable radioactivity for waste to be categorised as low-level waste, but does not generate significant heat, generated during the operational phase of the nuclear fuel cycle. This waste is currently encapsulated by blended cement composed of blast furnace slag (BFS) and Portland cement (PC), in the UK. The current long-term objective is to store this waste in a geological disposal facility (GDF). Thermodynamic modelling may be an option to predict how the blended cements will react over an extended period of time.

The purpose of this thesis was to assess the effectiveness and potential improvement of thermodynamic modelling for predicting the phase assemblage and pore solution of BFS-PC. Experimental studies are conducted to validate the thermodynamic modelling and assessment of a more complex aqueous solution modelling approach is tested to improve the modelling approach.

Chapter 2 outlines the current UK policy and waste management approach for ILW and how cements have been used in the past to treat this wasteform. The expected conditions of these wasteforms are detailed, to highlight how the changing conditions may impact the chemistry of the BFS-PC used to encapsulate the waste. Specific consideration is given to the effect of changing temperatures on phase evolution of cements. In addition, an overview is provided of how thermodynamic modelling has been used to effectively model cement systems, specifically blended cements.

Chapter 3 summarises the materials and experimental procedures used to validate the thermodynamic modelling. This includes an overview of how thermodynamic modelling simulates phase precipitation from aqueous solution, and the difference between the aqueous solution models available.

Chapter 4 assesses the effectiveness of thermodynamic modelling for simulating BFS-PC hydration over 360 days of curing. Throughout the thesis, three formulations of BFS-PC are tested (1:1, 3:1 and 9:1) to assess the robustness of the modelling approach. The variation in BFS content was performed

to simulate how changing the chemistry of the cement effected the simulated phase assemblage. Degree of hydration data are collected using EDTA selective dissolution and ^{29}Si solid state magic angle spinning nuclear magnetic resonance (MAS-NMR) to provide input data to simulate the BFS-PC hydration. Characterisation techniques such as X-ray diffraction (XRD), ^{29}Si and ^{27}Al MAS-NMR are used to determine the phases formed at various ages of curing, to compare to the simulated results.

Chapter 5 considers the impact of curing cement samples at 35 °C for 360 days and then exposing them to temperatures of 50, 60 and 80 °C up to 360 days, to simulate the temperature changes that may occur for the cements in the underground repository. Characterisation of the phases is performed using XRD and analysis of the chemical structure of the calcium aluminosilicate hydrate phase (C-A-S-H). The phase assemblage and chemical structure of C-A-S-H are compared to the thermodynamic modelling results considering the effects of the change of temperature on the three different formulations.

An extensive investigation of a more complex aqueous solution model known as the Pitzer ion-interaction model is conducted in chapter 6, to simulate cement phase hydration. Cement phase solubility data and pore solution of the 1:1, 3:1 and 9:1 BFS-PC cements are used as the basis to compare the Truesdell-Jones aqueous solution model with the Pitzer model. Assessment of the computing time and ease of use are conducted to form a final recommendation of which aqueous model to use.

Chapter 7 summarises the work performed throughout this thesis and concludes with recommendations of how best to continue improving thermodynamic modelling of blended cements.

2 Introduction and Literature Review

2.1 Nuclear Waste Management

The first nuclear reactors in the UK were built in 1947/48 at Harwell, Oxfordshire and in 1950/51 at Windscale, Cumbria, for the procurement of plutonium to use in the UK military nuclear weapons programme and to further the understanding of nuclear reactors [1]. The first power generating reactors were commissioned in 1956 at Calder Hall where four Magnox reactors producing 60 MWe each provided power while producing plutonium [2]. Over the next 60 years, further nuclear power plants were constructed and added to the power generation of the UK electricity grid. As of 2017 the UK produced 21% of the national energy supply from nuclear power [3].

A by-product of nuclear power is the production of radioactive waste. Approximately 188 000 m³ of radioactive waste has been produced in the UK as of 2016 [4]. Management of radioactive material involves the containment and isolation of material that contains or is contaminated with radionuclides at concentrations which exceed standardised safety levels. Waste produced from the production of nuclear power can be placed into three main categories [5]:

- High level waste (HLW) – exceeds clearance levels of radioactivity and produces high levels of heat output. Higher heat output is considered when designing the treatment for this waste.
- Intermediate level waste (ILW) – material exceeding the radioactivity levels of LLW. Specialty handling is required which includes; shielding in handling and storage but does not have to include heat input when designing the treatment process. Storage of this waste may be at ground level.
- Low level waste (LLW) – contains radioactive material below clearance levels. Material containing activity below this level can be disposed with standard waste, otherwise it must be sent to specialty disposal facilities. This does not require shielding in handling or storage.

The main criteria for treating these radioactive materials includes volume reduction, removal of radionuclides and the change of physical state and chemical composition [5]. To satisfy these criteria, management methods of these wastes vary in design.

HLW is derived from reprocessing of fuel and contains the vast majority of the radioactivity produced from the nuclear fuel cycle, consisting of 95.4% of total radioactivity [6]. Currently in the UK, HLW is treated using a vitrification process that incorporates the waste into a glass matrix and stored in stainless steel canisters. This method immobilises the radionuclides and turns the waste form into a glass and greatly reduces the waste volume [5,7]. Packaged, this waste contributes less than 1% of the total volume of nuclear waste (Figure 2.1) [4].

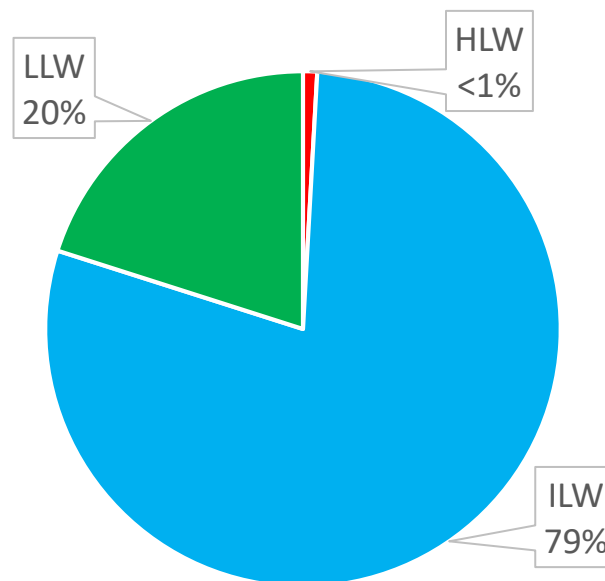


Figure 2.1: Volume proportion of total packaged waste comprising of HLW, ILW and LLW (VLLW included in the LLW) as of 2016 [4].

The main constituents that form ILW are a Magnox alloy, aluminium cladding, plutonium contaminated material, sludges, ion exchange resins and other low radioactive wastes [7,8]. A method to encapsulate ILW involves mixing the waste with blended cements and pouring the mixture into stainless steel drums of varying sizes [9,10]. Encapsulation of ILW in cementitious matrices is the preferred method for its management in the UK. Combinations of supplementary cementitious materials (SCM) and Portland cement (PC) contribute to the grouts used in this process [11]. The high pH of the blended cements, normally 12 or higher [12], is intended to cause the radionuclides to be insoluble, and the cementitious environment creates hydration products that promote the sorption and ion substitution of key radionuclides [13,14]. Restricting the movement of the radioactive material is the main objective of encapsulation [15].

A highly durable cement wasteform provides a safer method to store and transport potentially hazardous material [5]. Blast furnace slag (BFS) blended with PC is used extensively for this purpose, at varying degrees of replacement (75 to 90% replacement). High replacement levels are used because of the slower reactivity of BFS with water, which decreases the heat released by hydration of grout constituents during the early stages of curing [16–18]. Blended cements are also widely available and relatively inexpensive for the purpose of encapsulating a wide range of wastes.

Due to the large volumes of waste still awaiting treatment, as well as the need to monitor and maintain the cemented products now in interim storage awaiting final disposal, further understanding of potential interactions between the cementitious grouts and the encapsulated wastes is necessary. Despite the large volumes of waste being produced, supply of the precursor materials has been a constant issue over the years [19], therefore a method to be able to predict how the old and new cementitious constituents react to form different phase assemblages is required.

LLW is treated in a similar way to ILW through mixing it with cement, however the waste packages contain greater volumes of waste due to the lower levels of activity [20]. These waste packages are currently being stored at different sites around the UK depending on the severity of their activity. For instance, LLW is stored at a dedicated repository site at Drigg [21].

2.1.1 Geological disposal facility

As in many countries, the current policy to manage current and future nuclear waste in England and Wales would involve storage within a geological disposal facility (GDF) [22]. This facility would be the heart of a multi-barrier defence system to ensure that nuclear waste is stored safely and away from the biosphere (Figure 2.2). The multi-barrier method consists of treating the waste into a durable wasteform (e.g. cemented ILW), encasing the wasteform, designed barriers that act as buffers if the waste package was to be damaged or release of radionuclides occurs and a stable geological environment that the facility is hosted within [23].

An Example Multi-barrier System for Intermediate Level Waste

An Example Multi-barrier System for High Level Waste

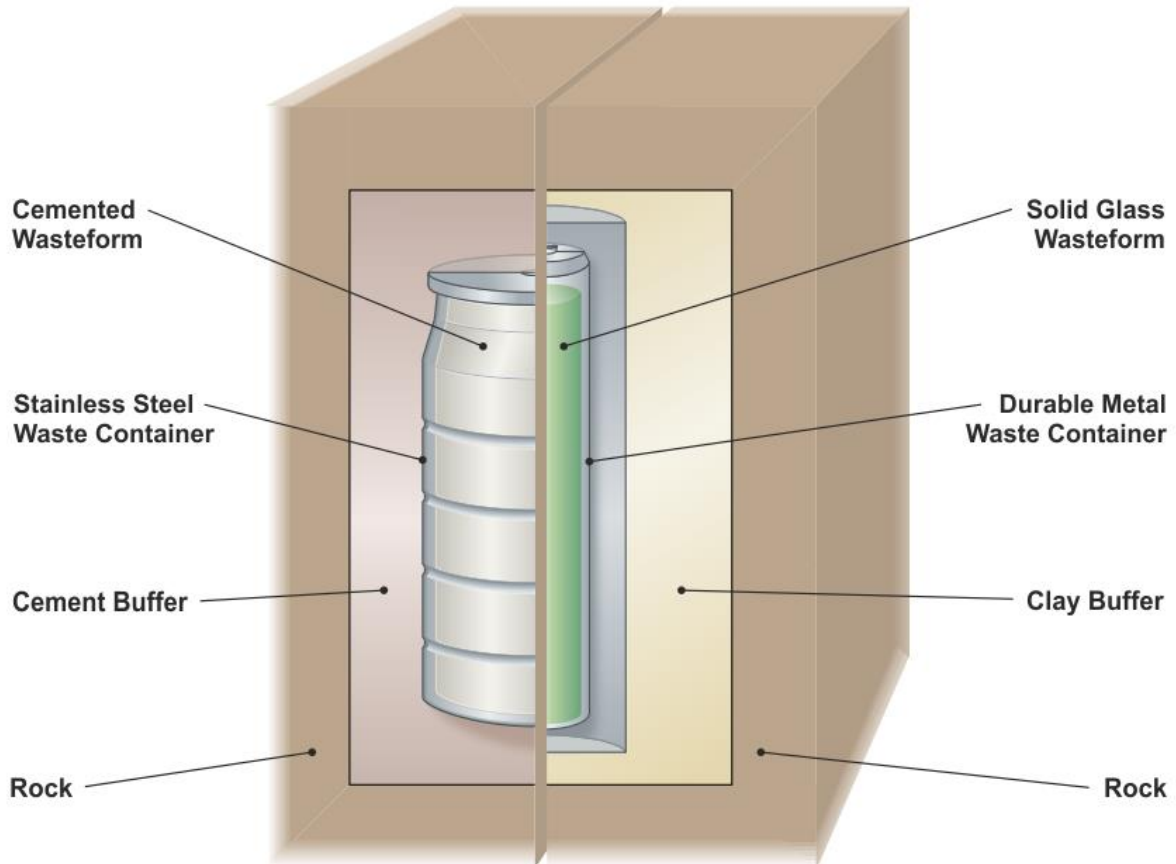


Figure 2.2: Schematic of the multiple barrier approach for intermediate level waste and high level waste [23].

The GDF will be a subterranean facility, up to 1 km below the ground, with vaults to store ILW and HLW, as shown in Figure 2.3. When these vaults are filled to capacity they will be sealed by Nirex Reference Vault Backfill (NRVB) [24,25], a cementitious high-pH engineered material, to further reduce any transport of radionuclides from the vaults. The UK design is an adaptation of the KBS-3V design concept developed for Sweden and Finland. In the KBS-3V design, Bentonite is the key backfill component [26].

The purpose of the GDF is for long-term storage of the wasteforms in an understood geological environment which may be considered as stable for millions of years [27]. This concept has been considered the preferred means of storage, as opposed to near-surface storage, as the rock formation to be chosen would isolate and contain the movement of radionuclides, thus limiting movement to

the environment [23]. Further consideration must be given to the location and rock formations chosen as to prevent future issues arising from seismic activity and glaciation in the distant future [27].

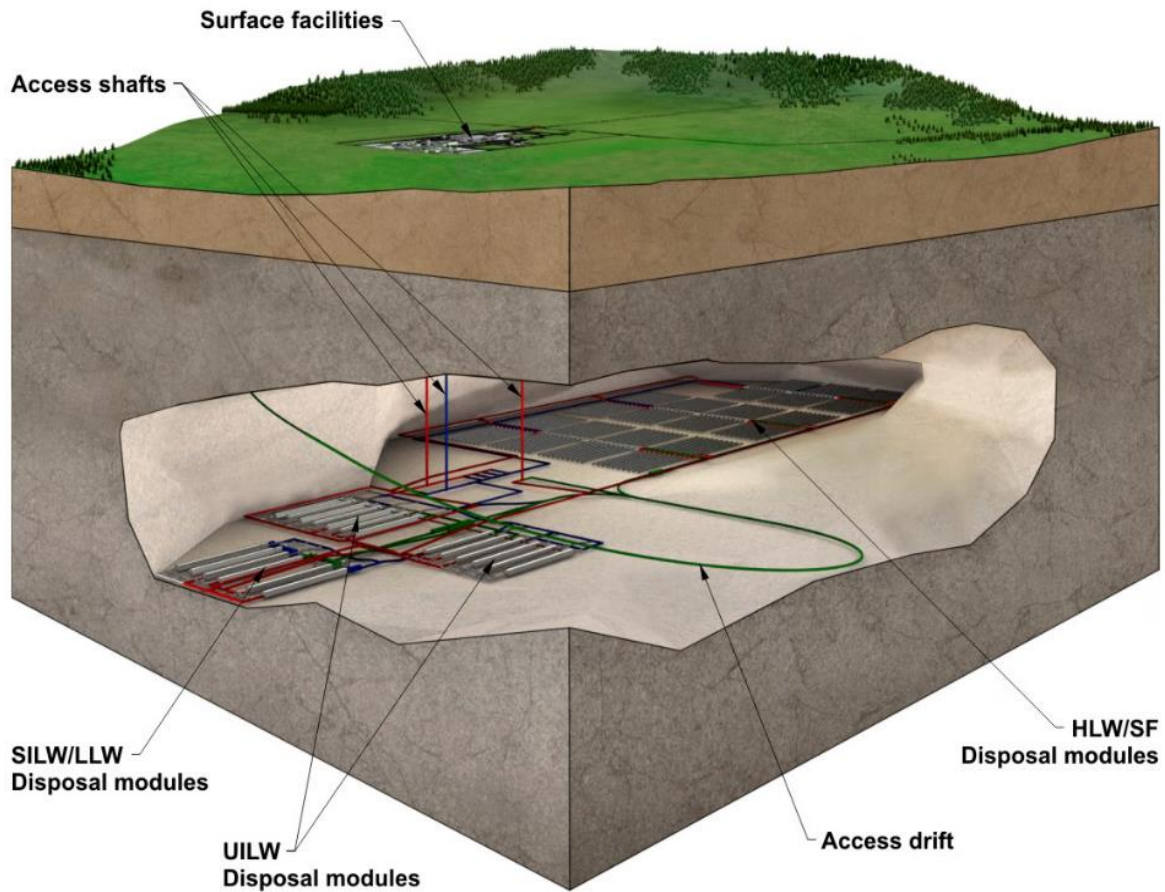


Figure 2.3: Schematic of a generic GDF proposed for in the UK (SF: spent fuel; UILW: unshielded ILW; SILW: shielded ILW)[28].

The safety and security of the GDF is of the greatest concern, as it will not be built unless high safety, security and environmental protection standards are met which are required by the UK Environment Agency and Office for Nuclear Regulation. The latest update considering the framework for implementing a GDF, highlights the importance of community involvement for choosing a site for the GDF [29]. Community involvement is imperative as the basis of the framework states that the community can withdraw from the process up to a specific point - the Test of Public Support (a mechanism to determine whether the inhabitants of the host community agree to the siting of the GDF). Therefore, within the framework, constant communication and cooperation with the potential host community is key.

It is expected to take 15 to 20 years to identify and select a site that may be suitable for GDF and a further 10 years to construct the repository. As of the 2018 ‘Implementing Geological Disposal’ report, no communities or sites have been chosen [29].

2.1.2 Temperature profile of cemented wastefoms in the GDF

The required lifespan of a UK GDF remains to be defined, and a location has not yet been selected. However, an approximate temperature profile has been created to enable scientific work to support a safety case, considering the possible extremes in the conditions to which the cement wastefoms may be exposed Figure 2.4 [8,10,30,31].

UK ILW waste packages are currently stored above ground at locations across the UK. An average expected temperature of 20 °C has been assumed for this period based on the storage locations [8,10,30,31]. Thermal modelling conducted by the Nuclear Decommissioning Authority (NDA) created an extreme case scenario based on the possible heat output of ILW waste packages stored in underground vaults) [10,31]. In this study, a heat output of 6 Wm⁻³ was used to model the most extreme scenario (average heat output from low heat generating waste – 1.1 Wm⁻³ until 2040 and declining to 0.5 Wm⁻³ by 2090; heat generation from non-radiogenic mechanisms – 3 Wm⁻³ due to corrosion of waste; microbial degradation of materials – 2 Wm⁻³ [10]).

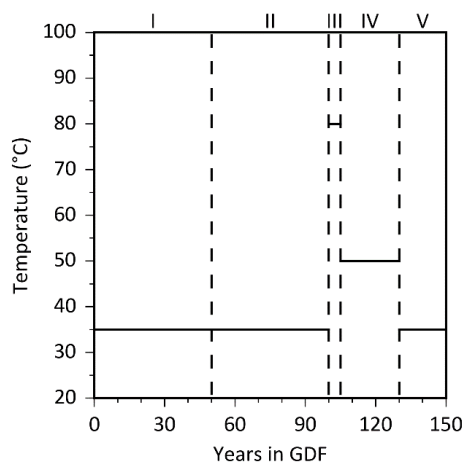


Figure 2.4: Approximate temperature profile of an ILW waste package due to GDF emplacement and backfilling [8,10,30,31].

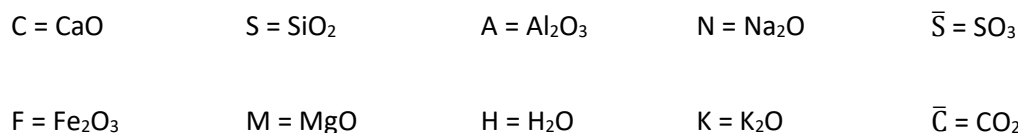
During the periods of transporting and storing the waste packages within excavated GDF vaults, taking an expected 50 years, the general air temperature was predicted to be 35 °C (period I in Figure 2.4). A further period of 50 years for care and maintenance is also expected to produce an average air temperature of 35 °C (period II). After the GDF has been filled with waste packages, the vaults will be backfilled with NRVB. The expected heat output from the hydration of the NRVB in an enclosed space, coupled with reduced ventilation within the vault, is expected to raise the temperature of the GDF to a maximum of 80 °C, for a period of 5 years (period III). After this point, the vaults are expected to cool to 50 °C for 25 years (period IV), then eventually return to temperatures of 35 – 45 °C (period V). A clear understanding of how the cement may react based on the changing temperatures is an imperative for predicting the suitability of using blended cement for long-term storage.

2.2 Portland cement and blended cement

2.2.1 Portland cement

Portland cement is a hydraulic binder primarily created from thermal treatment of limestone and clay [32]. When mixed with water, the hydraulic phases within the cement react exothermically to produce a hardened paste [33]. The main operational feature of cement formation is the heating of the limestone and clay in kilns to temperatures over 1400 °C [32], where they form nodules which are called clinker. With the clinker, oxides are formed which differ from those that were present in the minerals before heating. The cement once formed is ground into a fine powder and combined with gypsum ($\text{CaSO}_4 \cdot 2\text{H}_2\text{O}$) or other calcium sulphate compounds to control the rate of setting and strength development [33].

The four main phases produced within the cement clinker are alite (C_3S), belite (C_2S), aluminate (C_3A) and ferrite (C_4AF). It is common practice in cement chemistry to abbreviate the oxide containing components as seen below:



Portland cement contains 50-70% C_3S , 15-30% C_2S , 5-0% C_3A and 5-15% C_4AF [33]. Of these phases C_3S and C_3A are the most rapidly hydrating phases. These provide early strength formation, however C_3A reacts much more rapidly and must be controlled by the addition of the calcium sulphates to slow

down the rate of hydration to achieve longer, and more desirable setting times [32]. Slower hydrating phases such as C_2S and C_4AF contribute to later strength development [34]. Each of the clinker phases has a variety of polymorphs and can change in composition due to ionic substitutions, altering the kinetics of hydration [33].

2.2.2 Cement and supplementary materials

Supplementary cementitious materials (SCMs) are widely used in concrete by either being added to the cement during the grinding phase or separately in the concrete mixer [35]. Material considered as SCMs such as blast furnace slag, fly ash from coal combustion and other pozzolanic materials are used to replace fractions of cement [35]. Pozzolanic materials are natural or synthetic compounds that react with calcium hydroxide and water to form a hardened substance [36]. The main advantage of using these materials is that they are considered by-products from other processes and thus are considered to contribute no CO_2 to the use of cement or concrete [37]. They are generally different from cement as can be seen in Figure 2.5. In terms of treatment with radioactive material, the reduced heat of hydration exhibited by PC-SCM hydration, yet retaining a high pH ($pH > 12$), makes these materials ideal for treating ILW.

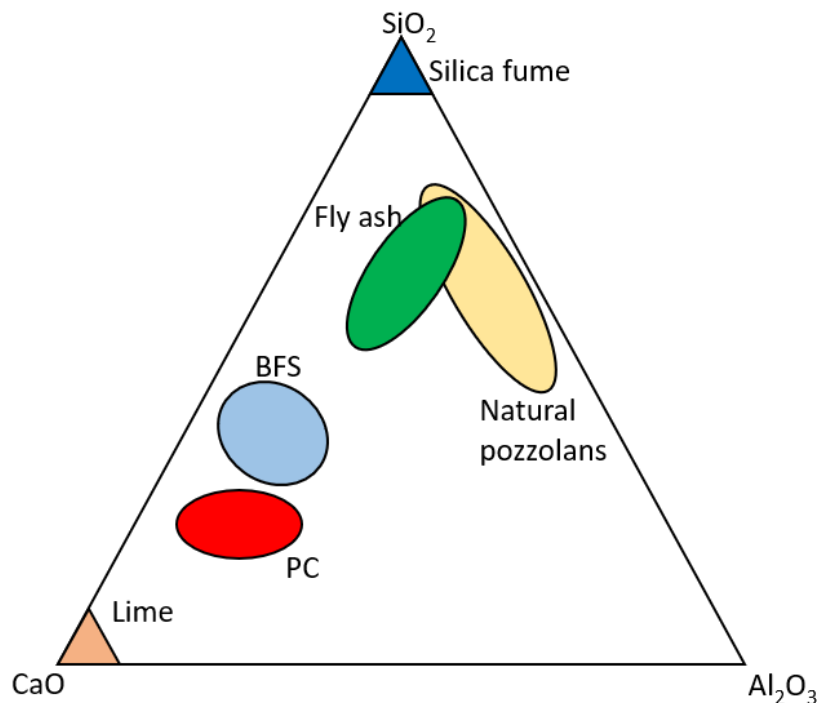


Figure 2.5: Ternary phase diagram showing the CaO , Al_2O_3 and SiO_2 composition of Portland cement and SCMs, based on phase diagram produced by Lothenbach et al. [37].

2.2.3 Blast Furnace Slag (BFS)

Similarly to Portland cement production, BFS is the result of reactions at high temperatures. It is formed as a liquid between 1350 and 1550 °C during the extraction of iron [38]. Silica and alumina react with the limestone present in the ore during the extraction process [12]. If left to cool slowly, the BFS forms a stable crystalline phase with no cementitious properties; however, when cooled rapidly to temperatures below 800 °C, it forms a glass with hydraulic capabilities [39]. Of the solid formed from this process 50 – 90% of this is a hydraulic glassy compound where the rate of cooling influences the amount of glass formed. In general, the higher percentage of vitreous material formed, the greater the reactivity of the slag [40].

The chemical composition of BFS from any single steel plant remains relatively stable in the short term, however, even from the same plant over the last 30 years the composition may change [19,38]. This is most likely down to the varying composition of the ore extracted from the ground. The general composition of BFS contains MgO, 4-10%; Al₂O₃, 10-20%; SiO₂, 30-40% and CaO, 35-45%, as well as a small amount of sulphur [38].

Along with composition, the specific surface area affects reactivity. The glassy structure is ground up into fine particles similar in surface area to Portland cement (PC), known as ground granulated blast furnace slag (GGBFS). The average specific surface area of PC is approximately 330 m²/kg [32] while GGBFS can range from 230 – 350 m²/kg [19]. In the nuclear waste industry a coarser BFS of average specific surface area 340 m²/g is used to reduce the level of reactivity to reduce the level of heat output during hydration [19]. The densities of granulated or pelletized blast furnace slags are typically 2880-2960 kg/m³ [33].

2.2.4 Phase assemblage of BFS-PC cements

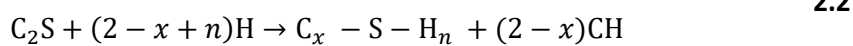
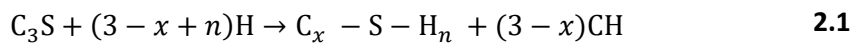
Reactivity of BFS has been shown to be significantly slower than that of PC in the presence of water, whereby in BFS-PC cements the degree of reaction of the BFS decreases as the level of replacement increases [40–42]. Increasing the pH through the addition of greater levels of PC or alkali activators, leads to an increased degree of reaction of the slag [33,40]. In the case of PC, it has been reported that the clinker phases have a much higher solubility than that of the hydrate phases that are formed [37,43]. The higher solubility of the precursor material leads to the dissolution of these phases quite

readily. In the presence of PC, the Ca(OH)_2 produced from the hydration of the clinker phases has been identified as activating the vitreous BFS structure. Studies have highlighted the reduced level of Ca(OH)_2 as the BFS replacement increases, indicating its consumption to aid in the formation of hydrate phases [14,40,44]. After long-term hydration of a completely BFS containing system hydrated by water, the degree of hydration reached 22% after 20 years and contained no Ca(OH)_2 , highlighting the importance of an activating material [45].

The main hydrate phases observed in BFS-PC are calcium aluminosilicate hydrate (C-A-S-H), portlandite (Ca(OH)_2 or CH), ettringite ($\text{Ca}_3\text{Al}_2\text{O}_6 \cdot 3\text{CaSO}_4 \cdot 32\text{H}_2\text{O}$), calcium monosulfoaluminate hydrate ($\text{Ca}_3\text{Al}_2\text{O}_6 \cdot \text{CaSO}_4 \cdot 12\text{H}_2\text{O}$ - monosulfate), calcium monocarboaluminate hydrate ($\text{Ca}_3\text{Al}_2\text{O}_6 \cdot \text{CaCO}_3 \cdot 11\text{H}_2\text{O}$ - monocarbonate), calcium hemicarboaluminate hydrate ($\text{Ca}_3\text{Al}_2\text{O}_6 \cdot \text{CaCO}_3 \cdot 12\text{H}_2\text{O}$ - hemicarbonate) and magnesium aluminium hydrotalcite-like hydrate (M-A-H – hydrotalcite-like) [37,46]. The variation of oxide content in precursor material of the BFS-PC cement leads to alteration of the cement phases formed.

2.2.4.1 Ca-Al-Si-OH

The main hydration phases of Portland cement are formed through the hydration reaction of the silicon containing clinker phases:



Whereby tricalcium silicate (C_3S) and dicalcium silicate (C_2S) dissolve to form the precipitates C-S-H and portlandite as shown in equation 2.1 and 2.2, respectively [47]. The main hydrate phase in PC, calcium silicate hydrate (C-S-H), consists of a disordered layered silicate gel with variable calcium, silicon and water content. Ordinarily in PC the molar ratio of Ca/Si of the C-S-H is greater than 1.5 and may be described as a disordered jennite-like phase - $(\text{CaO})_{1.5-1.9}\text{SiO}_2 \cdot (\text{H}_2\text{O})_x$ or C-S-H(II). Replacement of the PC with BFS reduces the overall Ca/Si within the system thus altering the C-S-H structure to form a lower Ca/Si phase similar to a tobermorite-like structure - $(\text{CaO})_{0.83}\text{SiO}_2 \cdot (\text{H}_2\text{O})_{1.5}$ or C-S-H(I). In cement systems a combination of the two phases is generally observed [33,48,49].

Silicate tetrahedra bond together through oxygen bridges (Si-O-Si) to produce a chain structure (Figure 2.6). The different structural forms of silica are denoted as Q^0 , Q^1 , Q^2 , Q^3 and Q^4 , whereby each superscript corresponds to the number of silicon species which are linked with the silicon tetrahedra [50–52]. Paired tetrahedra (which can form dimers, denoted as Q^1) are joined to calcium oxide layers. Two silicate tetrahedra may join onto a third which does not come in contact with the calcium oxide layer. This combination of three silicate tetrahedra forms a dreierketten unit. The third silicon tetrahedron acts as a bridge between other paired silicate sites to create the silicate chain (Figure 2.6). The chains encompass a calcium oxide layer which may connect two parallel silicate chains. Low calcium cement systems produce longer mean chain lengths (MCLs) through the incorporation of additional silicon into the chain structure. In low pH ($\text{pH} < 10.5$) and low Ca/Si ($\text{Ca/Si} < 0.85$) conditions, the bridging tetrahedra may form a cross-link (denoted as Q^3) to link two silicate chains to form a phase similar to naturally occurring tobermorite [49,53,54]. The ratio of calcium to silicon in solution impacts the chain length and overall silicate structure of C-S-H, whereby this Ca/Si ratio becomes a defining feature [55–58].

The linear chains have an interlayer space between them which allows the presence of water to interact with the silicate chains. On bridging sites or at the end of silicate chains, cationic species act as charge balancers ($-\text{Si-O-X}^+$) which give rise to different chemical environments for the silicon species [59–61]. At higher pH levels the chemical environment becomes saturated in OH^- ions which reduces the connectivity of the silicate chains ($-\text{Si-OH}$) and reduces the inclusion of charge balancing ions [59,62,63].

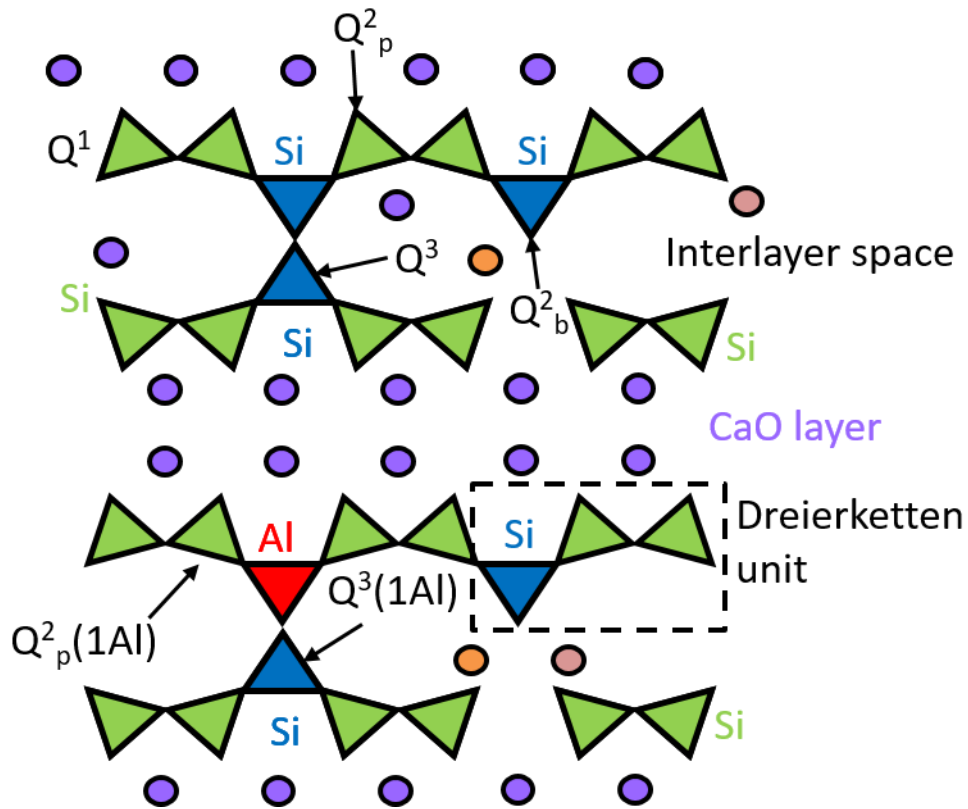


Figure 2.6: The C-S-H/C-A-S-H structure depicted using dreierketten units. The green triangles represent paired silicate dimers, blue triangles are bridging silicon tetrahedra, the red triangles represent silicon replacement with aluminium, the purple, orange and pink circles represent Ca^{2+} , K^+ and Na^+ ions respectively.

Synthesis of the C-S-H phase indicates the importance of the bulk chemistry of the environment on the chemical composition formed. Reviews performed by Kulik [64] and Walker et al. [65] highlight the shifting Ca/Si based on the concentrations of calcium and silicon in solution as shown in Figure 2.7. From the data summarised by Walker et al. [65], it is easy to observe the clear dependence of the Ca/Si on the calcium and silicon concentrations, as calcium levels increase, the Ca/Si increases and the opposite occurs when the silicon concentration increases. Formation of secondary phases cause a limit of the concentration of calcium and silicon in solution. Portlandite formation occurs at $[\text{Ca}] > 18$ mmol/L which leads to a maximum calcium concentration in the C-S-H system (Figure 2.7a) [66]. Amorphous silica precipitates at $[\text{Si}]$ of approximately 2-5 mmol/L [67,68].

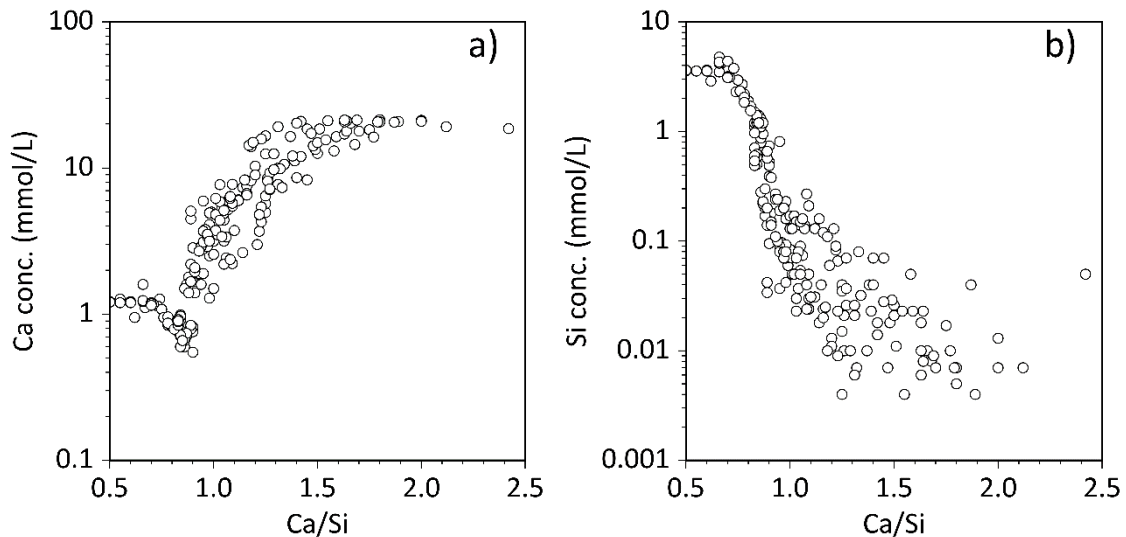


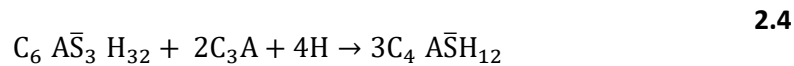
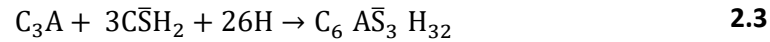
Figure 2.7: The Ca/Si of C-S-H as a function of a) calcium concentration and b) silicon concentration. The dotted and solid line indicates the Ca/Si when silica and portlandite forms, respectively. Optimal solubility data collated by Walker et al. [65] from the following sources: [53,54,65,69–83].

Increasing replacement of PC with BFS causes a decrease in the Ca/Si within the C-S-H as the bulk Ca/Si of the system decreases [37,45,84]. An increasing presence of aluminium within the system leads to the replacement of silicon with aluminium. Bridging silicon tetrahedra may also be replaced by aluminium, to form a C-A-S-H gel (Figure 2.6). Variation of the aluminium concentration in solution causes corresponding aluminium substitution into the aluminosilicate chains, whereby the Al/Si and Ca/Al values now define the phase [57,58,63,85]. The Al[IV] species may replace the Q^2_b or Q^3 sites in the silicate chain by maintaining the dreierketten unit [50,86]. Based on *ab initio* calculation, it is understood that aluminium can predominantly only replace the bridging sites in the aluminosilicate chain as aluminium inclusion in paired sites is very thermodynamically disfavoured [87]. Aluminium cannot form a bridge with another aluminium ion (Al-O-Al) due to Loewenstein's principle [88] which limits the level of replacement in the aluminosilicate chain. Substitution of these sites may provide an Al/Si of up to 0.33 within the dreierketten unit. In BFS-PC cements, due to the compositional changes of the system, the Ca/Si often decreases as the Al/Si increases [37,45,84,89,90].

2.2.4.2 Ca-Al-SO₄-CO₃-OH

Calcium sulphoaluminate phases are the result of hydration of C₃A and sulphur containing species within the cement. The hydration phases are much more likely to form in standard cement systems

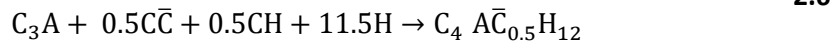
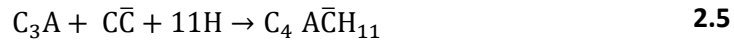
due to the presence of sulphur than, other calcium aluminate hydrates such as; C_2AH_8 , C_4AH_{19} and C_3AH_6 . The C-A-H phases are avoided in Portland cement mixtures as they increase porosity and disrupt the paste microstructure which has negative effects for the cement durability [91]. It is issues such as these, and problems of flash setting (rapid AFm formation), that require sulphate phases such as gypsum to be introduced so that reactions as shown below occur instead [33]:



The initial hydration product formed is ettringite (equation 2.3), provided there are enough sulphate ions available from the dissolution of gypsum (or an equivalent) [34]. Once the concentration of sulphate ions becomes lower than 0.01 mmol/L, ettringite becomes unstable and breaks down with the aid of further hydration into monosulphate (equation 2.4) [92].

If any C_3A remains before all of the monosulphate has been converted, then a solid solution between $C_4\bar{A}\bar{S}H_{12}$ and C_4AH_{13} will form [91]. This solid solution persists due to an interstitial layer between sheets of $Ca_2Al(OH)_6^+$ where SO_4^{2-} ions and water molecules reside [33,91]. Due to this interstitial layer, other anions such as CO_3^{2-} can occupy interlayer positions. Along with substitution in the interstitial layer, Fe^{3+} can replace Al^{3+} in the sheet layers, creating possible variation in composition of these phases [93]. The solid solution formula for these AFm phases is $[Ca_2(Al, Fe)(OH)_6 \cdot 12H_2O] \cdot X \cdot xH_2O$, where X can be any anion which balances the positive charges of the cation sheets and $x \leq 2$ [33]. The ettringite phase is also exposed to these possible substitutions and so belongs to a group of compounds known as AFt phases with the general formula $[Ca_3(Al, Fe)(OH)_6 \cdot 12H_2O]_2 \cdot X_3 \cdot xH_2O$, where X is a double charged anion or two single charged anions, and $x \leq 2$ [33].

Limestone or calcite ($CaCO_3$), a precursor to cement production may be used as a filler or another SCM to reduce the cost of cement production and contribute to the cement phase assemblage [94–96]. Introduction of this phase creates competition for the aluminium available in the system and the presence of CO_3^{2-} acts as a charge balancer in the AFm structure to form monocarbonate or once the CO_3^{2-} concentration falls below 3×10^{-4} mmol/L, further hydration to hemiacarbonate occurs:



Higher levels of PC in the system which are higher in calcium and generally sulphate and carbonate levels, causes the portlandite, ettringite and monocarbonate phases to form in greater quantities. When BFS replacement increases, these phases decrease in concentration and lower calcium containing phases become more abundant.

Despite the higher aluminium content available in the slag for formation of sulphate and carbonate Aft or AFm phases, with increasing slag content less of these are expected to form, due to less gypsum and calcite being available from the PC. Less oxidised sulphur will be available as there is only S^{2-} found in slag [39]. Ettringite and monosulphate formation relies on the availability of SO_4^{2-} ions in solution, therefore with only highly reduced sulphur available, the possibility of these phases forming is greatly reduced [12]. However, the ettringite which does form, acts as a sink for Al^{3+} and Ca^{2+} ions from the dissolution of the anhydrous slag which accelerates further dissolution of Al from BFS [12,33]. Reduction of $CaCO_3$ in the system with the reduction of PC content will reduce the CO_3^{2-} available, which will impact the possible phase assemblage. Matschei et al. [97] was able to identify the impact of the molar ratios of SO_3 , CO_2 and Al_2O_3 (Figure 2.8), and how the combination of the elements, impact the AFm or Aft phases formed. The lower solubility of CO_2 -containing phases, as shown through various solubility studies [92,98–100], causes the carbonate-containing AFm phases to precipitate out of solution more readily and require lower CO_2/Al_2O_3 than SO_3/Al_2O_3 to form.

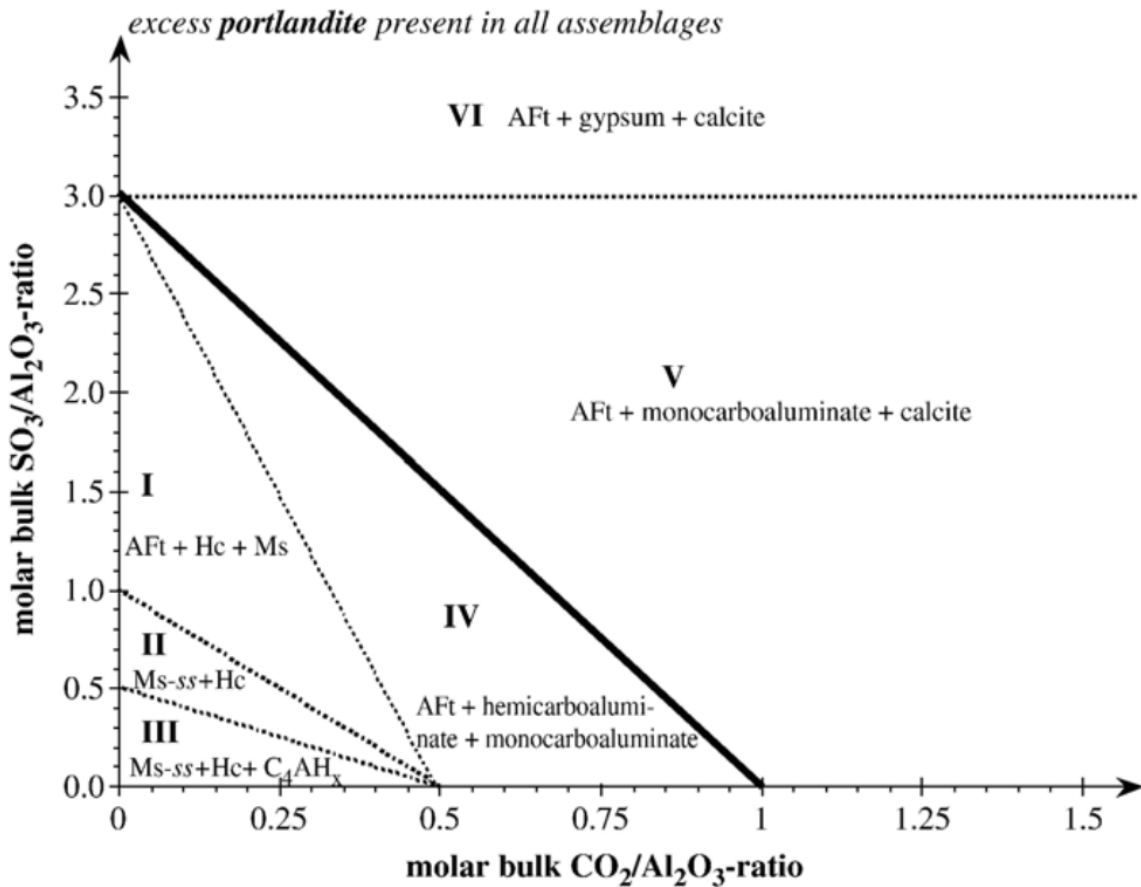


Figure 2.8: Impact of molar ratios of $\text{SO}_3/\text{Al}_2\text{O}_3$ versus $\text{CO}_2/\text{Al}_2\text{O}_3$ on the possible phase assemblage of AFm/Aft phases in the presence of excess portlandite [97].

2.2.4.3 Mg-Al-OH

Higher levels of MgO and Al_2O_3 have a large influence on the hydration phases. With larger amounts of these compounds, hydrotalcite-like solid solution levels are expected to increase [60,101,102]. For this phase, the magnesium to aluminium ratio (M/A) is key. A hydrotalcite-like solid solution ($\text{Mg}_{1-x}\text{Al}_x(\text{OH})_{2+x} \cdot m\text{H}_2\text{O}$) [103], which has a layered double hydroxide form, incorporates the MgO from the BFS-PC aqueous solution [101].

This hydration phase has been proposed to have an inhibitory effect on C-A-S-H formation as the MgO content increases, because the aluminium is less likely to be taken up by the C-A-S-H phase and is used to form the hydrotalcite-like phase instead [102]. Bernal et al. [60] on the other hand, argue that hydrotalcite formation benefits the formation of the C-S-H phase, because the hydrotalcite acts as an aluminium sink. With less aluminium available to substitute with the silicon, longer chain lengths are observed due to less bridging site substitution. It can be argued that the lower level of substitution

adds to the strength and stability of the gel-like phase [60]. Therefore, although the magnesium inhibits the C-A-S-H formation, it promotes the development of C-S-H [60].

2.2.5 Pore solution

The pore solution of cement systems is key to forming cement hydrate phases. Once the solid precursors dissolve, it is the void areas or the pores of the cement structure that become saturated and leads to the precipitation of solid phases [47]. As the curing age increases, the concentration of ions in solution alters based on the rate of reaction of the precursor materials. In general, the concentrations of elements in solution are higher at early ages (0 – 10 days) and plateau after 28 days [104].

High solubility of sodium and potassium released from sulphate phases (Na_2SO_4 or K_2SO_4) or incorporated in the clinker phases, leads to a sharp increase of alkalinity in PC systems at young ages (< 10 days) [33]. The weight percentages of Na_2O and K_2O in the initial precursor materials impact the maximum concentration of sodium and potassium in solution. At higher BFS replacement, the weight percentage of Na_2O and K_2O in the precursors are much lower than PC systems, resulting in a lower concentration of Na^+ and K^+ . The potassium and sodium concentrations individually may exceed 800 mmol/L depending on the precursor compositions, whereas BFS-PC may have concentrations as low as 50 mmol/L [104,105], as shown in Figure 2.9.

The Na^+ and K^+ species act as charge balancing ions for many of the cement phases, specifically the C-S-H or C-A-S-H phases and become withdrawn from solution. For PC systems, the high Ca/Si of the C-S-H phase has a reduced alkali distribution ratio (R_d) which causes the Na^+ and K^+ concentrations to increase as the clinker phases continue to hydrate [59,62]. In BFS-PC cements, the reduction of the Ca/Si ratio causes the R_d to increase as the slag hydrates which reduces the Ca/Si ratio of the C-A-S-H phase. The lengthening of the MCL requires greater levels of charge balancing in the aluminosilicate chain, thus the uptake of Na^+ and K^+ ions increases as the MCL increases [61,85,104,106–108].

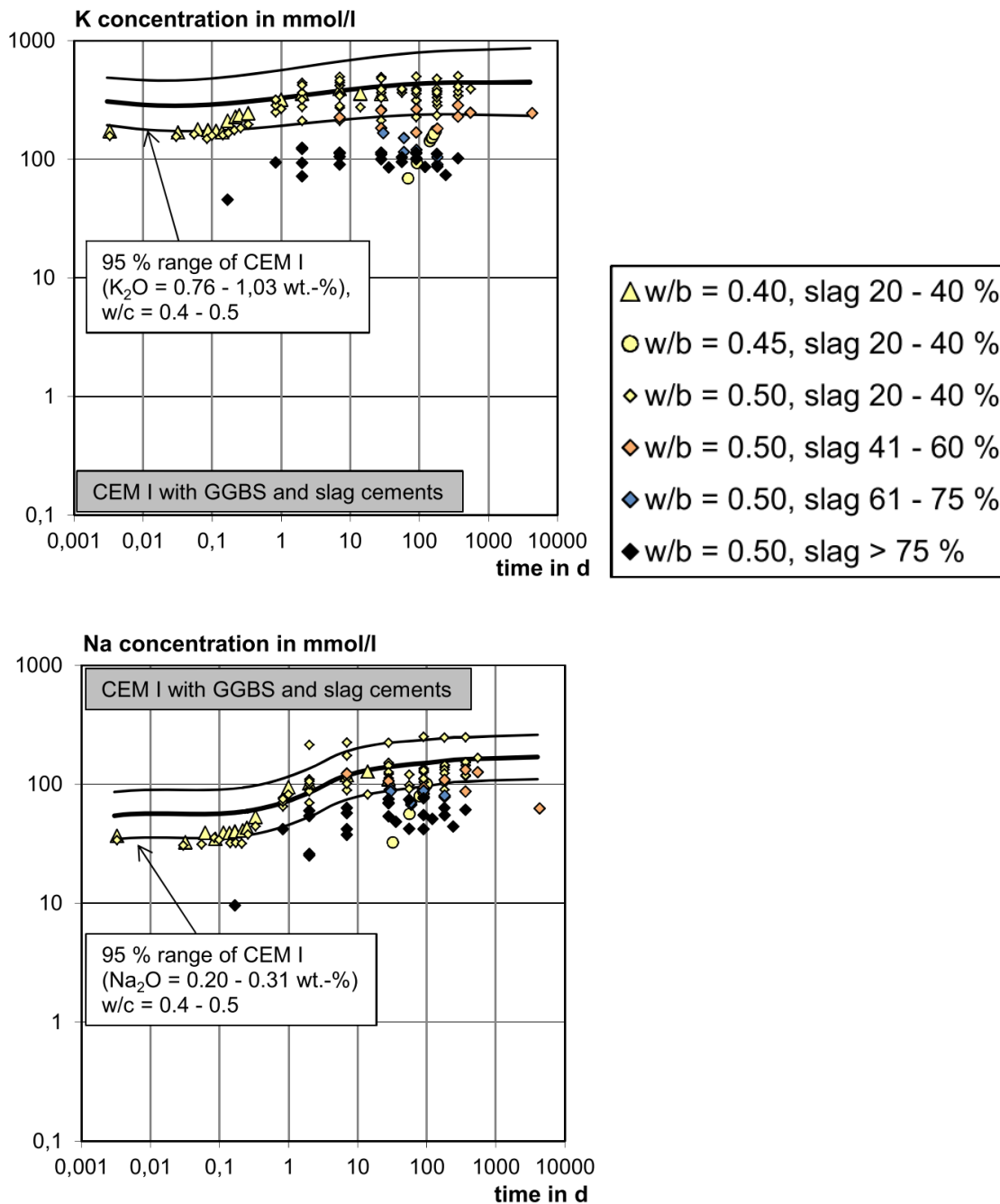


Figure 2.9: Potassium and sodium concentrations in the pore solution of BFS-PC cements of variable water to binder ratios (w/b) at different levels of slag replacement. The central black lines indicate the 95% interval within CEM I data collated by Vollpracht et al. [104].

Greater levels of Na^+ and K^+ ions in solution cause the concentration of OH^- ions to increase, thus raising the pH of the system, due to the charge balancing nature of the pore solution. The water to solids ratio (w/s) of the cement formulation impacts the concentration of OH^- , Na^+ and K^+ in the pore

solution, at lower w/s the concentrations of these ions increase [104]. The resulting pH of cements are between 12 and 14 [37].

Calcium solubility is highly dependent on pH, and this precipitates out of solution more readily in the presence of OH⁻ ions to form portlandite [66]. Due to the high pH and readily available abundance of OH⁻ ions in PC and BFS-PC cements, there is minimal difference in the concentrations recorded in the different systems, where calcium concentrations are commonly less than 10 mmol/L [37,104]. At pH greater than 12 in the presence of calcium, silicon concentrations are less than 1 mmol/L, due to the low solubility of the C-S-H and C-A-S-H phases [48,64,65].

Solubility of aluminium and magnesium phases are significantly low (often below instrumental detectable limits) which results in very low concentrations in both PC and BFS-PC systems which causes minimal difference of the recorded concentrations in the literature [109–111].

Sulphate concentrations are recorded between 1 and 80 mmol/L for BFS-PC cements at later age, which is lower than that observed in the PC systems [104]. The increase of pH in the Ca-SO₃-Al₂O₃-OH system causes the solubility of ettringite and monosulphate to increase due to the solubility of portlandite decreasing, which reduces the concentration of calcium available to form sulphur-containing phases [112,113]. Therefore a higher concentration of sulphate is required in solution to force the equilibrium to allow both phases to form [98,113]. However, the main sulphur species in BFS is S²⁻ which does not form hydrate phases readily. The review conducted by Vollpracht et al. [104], investigated the total sulphur concentrations in BFS-PC cements. However, due to the increasing sulphide concentration with increased BFS replacement, the total sulphur concentration may increase with time as is the case with alkali activated slag (AAS) [114].

2.3 Thermodynamic modelling for cementitious systems

Development of different cementitious systems to constantly improve carbon efficiency, to take advantage of new resources or for waste treatment purposes, requires further understanding of the hydration phases forming. This can be performed using many geochemical modelling software packages such as PHREEQC [115], Geochemist's Workbench (GWB) [116] and GEM-Selektor (GEMS) [117]. Using software packages such as GEMS it is possible to predict the phase assemblage of cement

systems by using degree of hydration (DoH) or degree of reaction (DoR) data as input parameters. Utilising thermodynamic databases of cement phases, for instance CEMDATA14 within GEMS, it is possible to assess what phases may form. This is important for assessing how altering the precursor material will affect the final phase assemblage. Implementing this modelling approach has been used for PC systems [118–121], SCM cements [37,122–126] and alternative cements such as calcium sulphoaluminate cements [127]. There are two main approaches that are used in the modelling packages, the law of mass action (LMA) algorithm or Gibbs energy minimisation (GEM) technique. Both are described extensively in geochemical textbooks [116,117,128].

2.3.1 Law of mass action (LMA) and Gibbs energy minimisation (GEM) methods

Equilibrium constants are imperative to LMA methods for determining stable phase assemblages within aqueous solutions [117]. The LMA technique utilises $\log K$ values for the aqueous complexes at a given temperature and pressure [129]. In LMA coding these are used to produce saturation indexes (SIs) along with other values to mass and charge balance, bulk composition. It is completed using Newton-Raphson iterations. This method uses linear approximations to find the correct root of a problem. It involves estimating the likely answer and iterates using the linear (tangent line) approximation. If used correctly this iterative method can be very useful and produce results to a high degree of accuracy [130]. However, this method is based on ‘local’ information, therefore if the initial approximation is not close enough to the root, then an incorrect root is determined, or the iteration does not converge. For thermodynamic modelling it is a logical process to use since the Newton-Raphson iterations attempt to find the lowest possible value, which in thermodynamics indicates the most stable phase [131].

The solubility product (K_{SO}) can be used to determine the saturation index (SI) of a compound in aqueous solution. The purpose of determining the SIs of a compound ($[AB]$) is to calculate the likelihood that they will precipitate or dissolve in aqueous solutions [129]. They take into account the activities of the components at equilibrium ($K_{SO} = \{A\}_{eq}^a \{B\}_{eq}^b$) and activities while interacting within water ($IAP = \{A\}_{actual}^a \{B\}_{actual}^b$) in the system that is being modelled. When $SI = 0$, the solution is at equilibrium between the mineral and solution, $SI < 0$ the product is at subsaturation and $SI > 0$ the product is supersaturated [121]. This is one method of determining the likelihood of a solid phase forming from an aqueous solution and is a main underlying step in the LMA procedure.

$$SI = \log\left(\frac{IAP}{K_{SO}}\right) \quad 2.7$$

Another approach to determine stable phase assemblages is the Gibbs Energy Minimisation (GEM) technique. In this method, the stable phase assemblage is determined by finding the minimum Gibbs free energy which indicates the system is at equilibrium whereby no more spontaneous reactions are likely to occur [132]. Gibbs free energy of a system is defined as $G = \sum_i n_i \mu_i$, where n_i is the moles of the i component and μ_i is the partial molal Gibbs free energy [133]. The GEM approach works on a mass and charge balance basis of the entire system. Composition at equilibrium is defined from the stoichiometrically possible phases based on the bulk composition [121]. The Gibbs free energy of reaction can be linked to the solubility product [129] and provide the solid phase using Gibbs free energy of formation data at standard conditions (2.8):

$$\Delta_r G^\circ = \sum_i v_i \Delta_f G^\circ = -RT \ln K_{SO} \quad 2.8$$

In the equation, v_i corresponds to the stoichiometric coefficients of the reactants, $R = 8.31451 \text{ J/mol/K}$ is the universal gas constant and T , is the temperature in Kelvin. From this approach, the solubility product is determined from thermodynamic data in addition to mass and molar balance information alone [120]. GEMS converts the standard chemical potential of species (μ_i^0) into the actual chemical potential (μ_i), by applying corrections based on the system:

$$\mu_i = \mu_i^0 + RT \ln \gamma_i c_i \quad 2.9$$

Where μ_i is the calculated chemical potential, R is the universal gas constant, T is temperature (K), activity coefficients of aqueous species (γ_i) and c_i is the molal concentration of species i . The activity coefficients of aqueous species consider the aqueous environment of each aqueous species in solution and define how readily these species react. The combination $\gamma_i c_i$ may be referred to as the activity (a_i). An example of an activity coefficient model is the Truesdell-Jones equation, which is an extension of the Debye-Hückel equation [134]:

$$\log_{10}\gamma_i = \frac{-A_\gamma z_i^2 \sqrt{I}}{1 + \hat{a} B_\gamma \sqrt{I}} + b_\gamma I + \log_{10} \frac{X_{jw}}{X_w} \quad \mathbf{2.10}$$

Here, γ_i and z_i are the activity coefficient and charge of the i^{th} aqueous species respectively, A_γ and B_γ are temperature and pressure dependent coefficients, I is the molal ionic strength ($I = 0.5 \sum_{i=1}^n c_i z_i^2$), X_{jw} is the molar quantity of water, and X_w is the total molar amount of the aqueous phase. A common ion size parameter, \hat{a} and short-range interaction parameter, b_γ , are used [104,134]. The activity coefficient is applied to the standard chemical potential, μ_i^0 , of each aqueous species to provide a better representation of how it would realistically behave in solution.

Use of this modelling approach may be highlighted by considering the portlandite system. The corrections applied to the standard chemical potentials that form portlandite (Ca^{2+} and OH^-) are displayed in equation 2.11 and 2.12. Incrementally increasing the $\text{Ca}(\text{OH})_2$ concentration from 0 to 18.8 mmol/L in solution, causes no portlandite to form as shown in Figure 2.10 as the difference between the Gibbs energy of formation of the reactants and the hydrate phase was not less than zero (2.13 and 2.14). Saturating the solution with the reactants combined with applying the activity coefficient, causes portlandite to precipitate out of solution at $\text{Ca}(\text{OH})_2$ concentrations greater than 18.8 mmol/L.

$$\mu_{\text{Ca}^{2+}} = \mu_{\text{Ca}^{2+}}^0 + RT \ln \gamma_{\text{Ca}^{2+}} c_{\text{Ca}^{2+}} \quad \mathbf{2.11}$$

$$\mu_{\text{OH}^-} = \mu_{\text{OH}^-}^0 + RT \ln \gamma_{\text{OH}^-} c_{\text{OH}^-} \quad \mathbf{2.12}$$

$$\Delta G = G_{CH}^0 - (\mu_{\text{Ca}^{2+}} + 2\mu_{\text{OH}^-}) \quad \mathbf{2.13}$$

$$\Delta G = \text{negative} \quad \text{- Portlandite precipitates} \quad \mathbf{2.14}$$

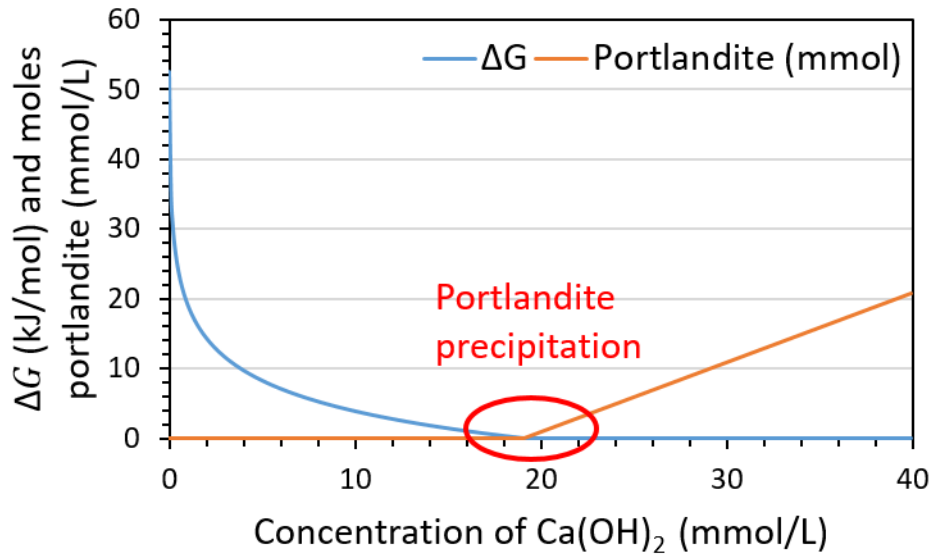


Figure 2.10: The difference in Gibbs energy between portlandite and reactants until the point of precipitation, thereafter portlandite precipitates out of solution as more Ca(OH)_2 is added to the system.

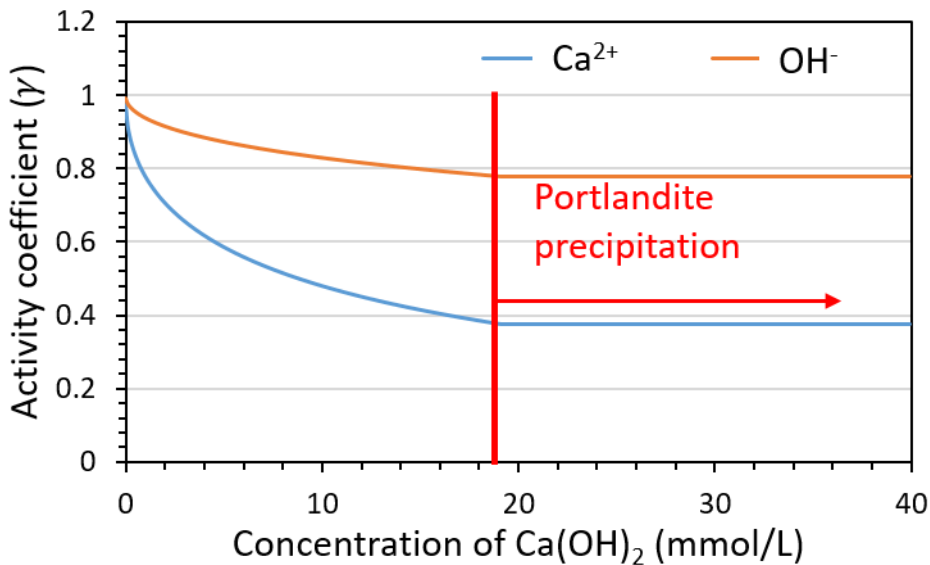


Figure 2.11: Thermodynamic modelling of the activity coefficients for Ca^{2+} and OH^- ions in the Ca(OH)_2 system, with varying concentration of Ca(OH)_2 added to solution.

Once the saturation point of 18.8 mmol/L of Ca(OH)_2 is reached in solution, any further Ca(OH)_2 added to the system precipitates out of solution, hence the linear increase of portlandite formation after 18.8 mmol/L. The constant concentration of Ca(OH)_2 remaining in solution results in a constant activity coefficient of Ca^{2+} and OH^- ions in solution as the concentration of the solution does not change thereafter (Figure 2.11).

2.3.2 Activity coefficient models

Activity coefficients are introduced to apply more realistic representations of the short and long range interactions of ions within the aqueous phases [117]. They are applied to both LMA and GEMS methods. Some activity coefficient models consider the aqueous solution in a broad sense, thus have constants relating to the level of ionic activity (ionic strength), within the solution and constants specific to the main ionic components within the electrolyte [135]. This overall electrolyte approach results in the activity coefficient models as shown in Equation 2.15 - 2.17:

$$\log_{10}\gamma_i = -Az_i^2 \left(\frac{\sqrt{I}}{1 + \sqrt{I}} + 0.3I \right) \quad I < 0.1 - 0.7 \quad \mathbf{2.15}$$

‘Davies’

$$\log_{10}\gamma_i = \frac{-Az_i^2\sqrt{I}}{1 + aB\sqrt{I}} + bI \quad I < 0.5 - 2.0 \quad \mathbf{2.16}$$

‘Extended Debye-Hückel’

$$\log_{10}\gamma_i = \frac{-A_\gamma z_i^2 \sqrt{I}}{1 + \dot{a}B_\gamma \sqrt{I}} + b_\gamma I + \log_{10} \frac{X_{jw}}{X_w} \quad I < 0.5 - 2.0 \quad \mathbf{2.17}$$

‘Truesdell-Jones’

The notation is similar to the Truesdell-Jones equation previously discussed for Equation 2.10. The A and B parameters are temperature and pressure dependent coefficients and vary for each equation. The common ion size parameter, \dot{a} or a , and short-range interaction parameter, b_γ or b may use the same parameters [104,134]

The increased level of complexity of each model, leads to an increasing ionic range that the model may be used within. For instance the Davies equation is capable of predicting activity coefficients for monovalent species for ionic strength values up to 0.7 mol/L when compared with experimental data [129,136], but because it does not contain ion specific parameters (a or b), it can only provide a general activity coefficient of species i , based on the charge of the ion. Including additional terms to describe the main electrolyte in solution, as is the case for the Extended Debye Hückel equation (2.16), which dictates the effects of short and long range interactions to best represent the average interaction of coulombic forces in solution, increases the effectiveness at higher ionic strength [137]. Further additions such as the X_{jw}/X_w term in the Truesdell-Jones equation, introduce the impact of the availability of water in solution, which is important at higher ionic strengths where water

molecules are less available to form hydrating spheres [136]. Development of the equations 2.15 to 2.17 provide general descriptions of the aqueous solution and provide activity coefficients based on the charge of the ions, however are not ion specific, which is not the case with the Pitzer model:

$$\begin{aligned}
 \ln \gamma_M = z_M^2 F + \sum_a m_a (2B_{Ma} + ZC_{Ma}) & \quad I < 0.5 - 6.0 \text{ [135]} \quad \mathbf{2.18} \\
 + \sum_c m_c (2\Phi_{Mc} + \sum_a m_a \psi_{Mca}) & \quad \text{'Pitzer model'} \\
 + \sum_{a < a'} \sum_{a'} m_a m_{a'} \psi_{aa'M} & \\
 + |z_M| \sum_c \sum_a m_c m_a C_{ca} &
 \end{aligned}$$

The Pitzer model (Equation 2.18 – expanded in Chapter 6) determines the activity coefficients of individual aqueous species through parameterising interactions of individual aqueous species in solution, through virial expansion [135]. The model contains an initial Debye-Hückel term (F) which describes the solution as a whole, followed by second (B_{Ma}, C_{Ma}) and third (Φ_{Mc}, ψ_{Mca}) virial expansions. The second virial expansion considers the interactions of a binary aqueous solution containing species of different charges. Inclusion of a third aqueous species may incorporate electrolyte mixing terms if the parameter values exist. The mixing terms describe the interaction of like-signed species (Φ_{Mc}), or like-signed species in contact with a third species of a different sign (ψ_{Mca}). At higher ionic strengths ($IS > 2$ mol/L) the higher density of ions in solution forces the interactions of like-signed ions and ternary species [136]. The use of ion specific interaction parameters therefore improve this modelling approach by providing specific ion values. Through the use of fitting tools, it is possible to determine the interaction parameters of multicomponent systems.

The Pitzer model was originally developed to improve existing aqueous solution modelling to improve the accuracy at ionic strengths of greater than 0.1 [138–141]. The Pitzer model has been remarked to have ‘unparalleled precision’ for determining thermodynamic properties of strong electrolyte systems, however reduces in quality when parameters for aqueous species are missing in multicomponent solutions [142]. A key disadvantage to the Pitzer model is the large dependence on

large amounts of solubility data required to maintain a thorough parameter database [100,110,143–145]. A clear advantage of the Pitzer model over the Truesdell-Jones equation can be seen in Figure 2.12 when considering precipitation of magnesium oxychloride in the presence of brucite. The Pitzer model, due to the high level of parameterisation, was capable of modelling the transition of brucite to magnesium oxychloride in high concentrations of MgCl_2 . However, the Truesdell-Jones equation became less effective at modelling the system at MgCl_2 concentrations greater than 1 mol/L. This may be important for predicting how magnesium-containing wastes interacts with nearby groundwater [110].

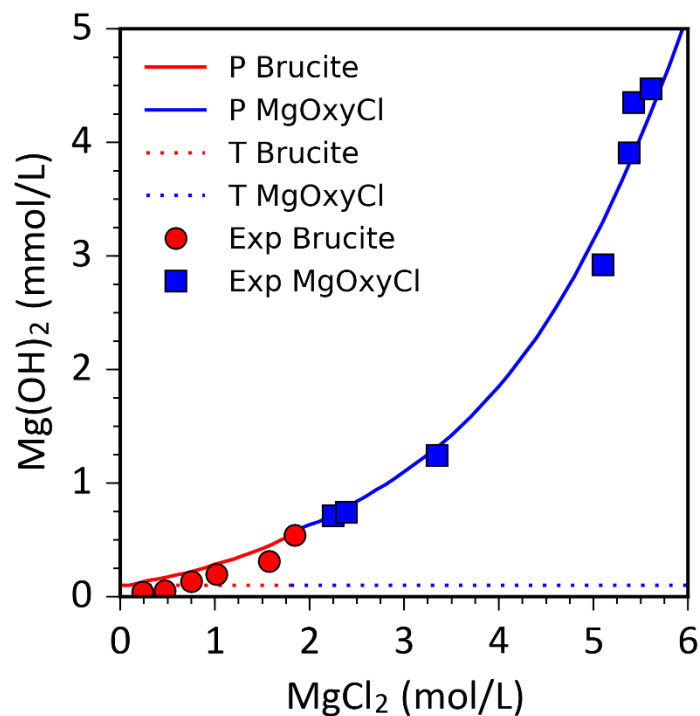


Figure 2.12: Thermodynamic modelling of brucite and magnesium-oxychloride (MgOxyCl) in the Mg-Cl-OH system using the Pitzer model (P) and Truesdell-Jones (T) equation. The Pitzer parameters and solubility data used are from Harvie et al. [100].

The extended Debye-Hückel and Truesdell-Jones equations have been used extensively for modelling cement systems [37,118–127] as the IS of cement is generally between 0.5 and 3.0 which is within effective range of these models [104,146,147]. Use of the more complicated and parameter database intensive Pitzer model is rarely used when considering cement phases and has not been used to simulate cement hydration, but only specific cement phases [66,98,99,148]. The high quality of the results and ease of use when using the simpler equations, reduces the requirement for using the Pitzer

parameters. However, as shown in Figure 2.12, the Pitzer model has a greater quality of modelling more complex systems, which may arise when cement systems are in contact with waste.

2.4 Cement thermodynamic database

The thermodynamic database used throughout this work was the CEMDATA14 which has been developed to include iron containing phases [119,149], AFm and AFt phases in the Ca-Al-SO₄-CO₃-OH system [97,150], a magnesium hydrotalcite-like solid-solution model [123,146], a C-S-H solid solution model [64] and other minor phases observed in cement phases [118,123,151,152].

The use of solid-solution models was incorporated into the database to accurately portray how variable composition phases such as the magnesium hydrotalcite-like [123], ettringite, monosulphate [150], C-S-H [64] and C-(A)-S-H [122] phases form. Solid solution models may determine the chemical composition of the solid-solution based on the chemical environment and may react to any changes, without any extra coding when setting up modelling projects. For instance the Ca/Si of the C-S-H model may be altered based on the available [Ca] and [Si] which results in greater accuracy of the aqueous solution [64,114,146].

The solid-solutions are comprised of end-members (*i*) that have individual thermodynamic properties. In the case of the C-S-H end-member model developed by Kulik [64], four end-members were chosen based on known chemical structures of tobermorite-like and jennite-like structures. The total Gibbs free energy of a solid solution (ΔG_{ss}) may be determined through the following equations:

$$\Delta G_{ss} = \sum_i X_i \Delta_f G_i^o + G_M \quad \mathbf{2.19}$$

$$G_M = \Delta G_{id} + \Delta G_M^{ex} \quad \mathbf{2.20}$$

$$\Delta G_{id} = RT \sum_i X_i \ln X_i \quad \mathbf{2.21}$$

$$\Delta G_M^{ex} = RT \sum_i X_i \ln \gamma_i \quad \mathbf{2.22}$$

Where, X_i is the mole fraction of end-member *i*, $\Delta_f G_i^o$ is the standard Gibbs energy of formation of the end-member, G_M is the Gibbs energy of a mechanical mixture end-members, ΔG_{id} is the Gibbs

energy of mixing of an ideal solid solution, ΔG_M^{ex} is the excess Gibbs energy of mixing of a solid solution and γ_i is the activity coefficient of end member, i . The initial equation (2.19) is in a similar form to that of equation 2.9 whereby the chemical potential of the phase (μ_i^0) is the sum of all of the end-members that form the solid solution and the mole fraction of each end-member has an impact on the total Gibbs energy of the solid solution. The G_M term represents the correction of the standard chemical potential (a_i) by considering the aqueous environment in the system.

An ideal solid solution has an excess Gibbs energy of mixing (ΔG_M^{ex}) equal to zero due to the solid solution being capable of mixing in all proportions within the solid-solution model range. For instance, the C-S-H and later the C(-N)-A-S-H model were developed as ideal models, as the Ca/Si range in C-S-H that the models were designed for (0.67 – 1.63 and 0.67 – 1.3, respectively), were capable of achieving any Ca/Si value within the specified range based on solubility data. At either end of the Ca/Si ranges, secondary phases formed (amorphous silica formed at Ca/Si < 0.67 and portlandite formed at Ca/Si > 1.63 or 1.3) which was therefore outside the compositional range of the models as highlighted in Figure 2.13. The limitations of the CNASH_ss models for use in high calcium content systems is the maximum Ca/Si of 1.3 and the CSHQ model does not have aluminium inclusion. Neither model accurately portrays the chemical composition of C(-A)-S-H in BFS-PC cements, as the Ca/Si ratio in BFS-PC cement commonly exceeds 1.3 and includes silicon substitution with aluminium [44,45]. However, a combination of the two models may provide a useful insight into the formation of C-A-S-H [122,125].

The solid solution models developed by Matschei et al. [92,150] required the inclusion of ΔG_M^{ex} mixing terms to correctly model the AFm and AFt phases due to the miscibility gaps in the solid solution models. For instance the monosulphate solid solution, $C_4 \bar{A}S_x H_{13-x}$, contains a miscibility gap between $0.03 \leq x \leq 0.5$.

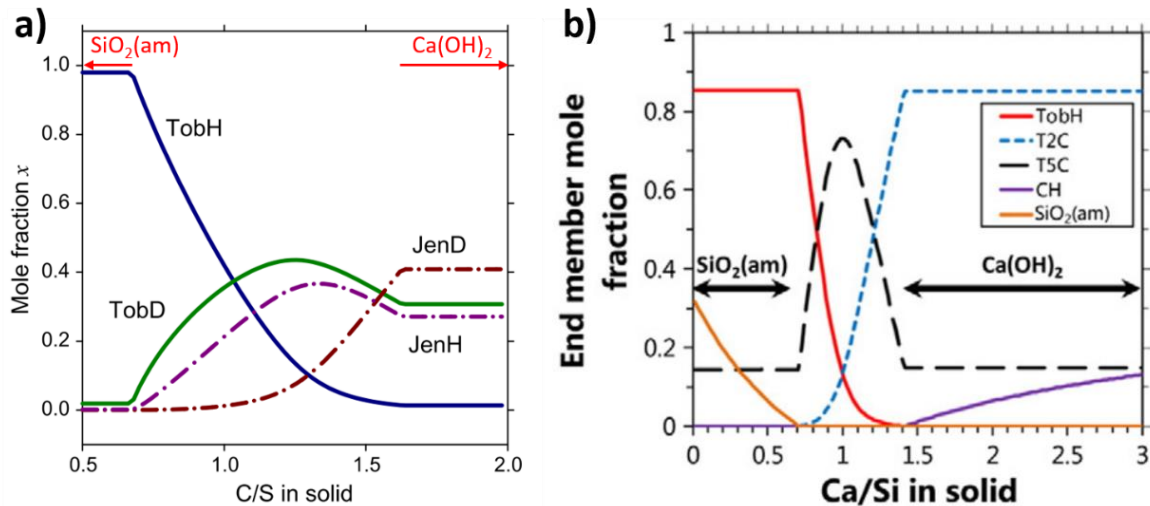


Figure 2.13: No miscibility gaps in the calcium to silicon molar ratios (C/S or Ca/Si) are observed when predicting the mole fractions of the end-members in the a) CSHQ and b) CNASH_{ss} models. Modified from Kulik [64] and Myers et al. [146], respectively.

2.5 Conclusion

Blended cements are a viable waste management option for the encapsulation of ILW material for large scale disposal due to the adsorption properties of the hydrate phases, low heat of hydration and long-term durability. Based on the long-term goals for storing the waste using blended cements, it is imperative that modelling approaches are assessed for the applicability of predicting how these cements may develop over different curing ages and temperatures. Assessment of the modelling approach requires degree of hydration data for the precursor materials as input parameters, recorded chemical composition of variable composition phases (such as C(-A)-S-H and magnesium hydroxalcalite-like phase), characterised hydrate phase assemblages at various curing ages and pore solution data.

Curing BFS-PC samples with different BFS-PC ratios will provide a good basis for assessing the robustness of the modelling approach for evaluating cement systems with variable precursor compositions. Use of thermodynamic modelling therefore could provide the possibility of future proofing changing cement supplies or alterations in the precursor composition.

Inclusion of a more ion specific activity coefficient modelling approach, the Pitzer model, may further improve predictive capabilities for thermodynamic modelling. The greater capability of using a multi parameter aqueous solution model may produce greater accuracy for predicting the precipitation of

solid phases out of solution, therefore improving the accuracy for predicting the pore solution chemistry of blended cement systems. However, a large aqueous species interaction database is required to utilise the Pitzer model.

3 Materials and Methods

3.1 Materials

The precursor materials used were Ribblesdale CEM I 52.5N PC and Port Talbot ground granulated BFS (BS EN 15167-1 GGBS), supplied by the National Nuclear Laboratory. The oxide compositions of the precursors used are displayed in Table 3.1 as determined by X-ray fluorescence (XRF). The powders presented were used throughout the study as they are representative of the materials used currently by the UK national nuclear industry for waste immobilisation [3]. The Blaine fineness, and a summary of the particle size distribution (PSD) obtained using laser diffraction, of the PC and BFS are reported in Table 3.2.

Table 3.1: Major constituents of raw materials, as determined by X-ray fluorescence (XRF) and represented as oxides.

Oxide (wt.%)	PC	BFS
CaO	63.7	39.2
SiO ₂	20.8	35.1
Al ₂ O ₂	5.1	13.4
Fe ₂ O ₃	2.6	0.2
MgO	2.3	9.9
SO ₃	3.7	1.0
Na ₂ O	0.6	0.2
K ₂ O	0.8	0.6
TiO ₂	0.2	0.8
MnO ₂	0.1	0.2
P ₂ O ₅	0.2	-

Table 3.2: Blaine fineness and particle size distribution (PSD) analysis of raw materials.

Particle parameter	PC	BFS
Blaine fineness (cm ² /g)	4241	4870
PSD D ₁₀ /μm	2.18	2.16
PSD D ₅₀ /μm	14.3	15.3
PSD D ₉₀ /μm	46.9	53.1

3.2 Mix design

Cementitious grouts composed of 1:1, 3:1 and 9:1 BFS:PC were produced with a water/solids (w/s) mass ratio of 0.35, cured at 35 °C . These mix ratios and curing temperature conditions were chosen to resemble the current interim storage conditions of ILW waste packages. A variation of the curing regime is introduced in Chapter 5 to replicate the possible temperature changes that may occur in a GDF site and are discussed further in that chapter [8,10,30,31].

3.3 Analytical techniques

A variety of analytical techniques were applied to assess the degree of hydration of the precursor materials and to characterise the hydration phases formed. Selective dissolution using EDTA was performed to determine the degree of hydration of the slag and these results were compared with ²⁹Si magic angle spinning (MAS) nuclear magnetic resonance (NMR) experiments to confirm the quality of the results. X-ray diffraction (XRD) alongside ²⁷Al and ²⁹Si MAS NMR were performed to identify the solid phases forming at different curing ages. The use of ²⁹Si MAS NMR and scanning electron microscopy (SEM) were used to determine the chemical composition of the C-A-S-H phase.

3.3.1 Selective dissolution – EDTA dissolution

The crystal structures observed in PC hydration allow the use of crystallographic techniques to determine the extent of reaction of the original clinker phases, however the amorphous nature of BFS creates difficulty in assessing the degree of hydration when using techniques common to PC calculations, such as Rietveld refinement [46,96,153]. Selective dissolution is a widely used technique to assess the degree of hydration of BFS in blended cement systems [41,154].

Kocaba et al. [89,155] determined that the selective dissolution technique was ineffective at calculating the degree of hydration of BFS, however Tan [105] argued that the selective dissolution used in the Kocaba studies was not considered the most effective selective dissolution technique. A round-robin study conducted by Durdzinski et al. [156] highlighted the issues with different degree of hydration testing methods and resolved that each technique had flaws which required addressing. The main benefits of selective dissolution are that it is a simpler, less analytically intensive and a well-documented technique within the literature which provides reasonably reliable results [40,41,154,157].

Selective dissolution [41,105,154] was performed to provide a quantitative determination of the degree of hydration of the BFS by dissolving PC and hydration products while leaving slag grains intact. Selective dissolution of the hydrated cement phases was performed and discussed in Chapters 4 and 5.

The selective dissolution method developed by Luke and Glasser was used in this study [154]. Initially, 93.0 g of disodium EDTA·2H₂O was dissolved in a mixture of 250 mL of triethanolamine and 500 mL of water. The solution was transferred to a volumetric flask. 173 mL of diethylamine was added into the solution, then the mixture was made up to 1000 mL with water. For each extraction test, 50 mL of the above solution was pipetted into a beaker and diluted to 800 mL with distilled water. After the diluted solution was brought to a temperature of 20 ± 2 °C, 0.5 g of dried and ground sample (particles size smaller than 63 μm) was weighed to the nearest 1 mg, then sprinkled over the surface of solution. The solution was stirred using a magnetic mixer for 120 ± 5 min maintaining a constant temperature, then filtered under vacuum through a 90 mm diameter Whatman GF/C filter which had been previously washed with 100 mL of distilled water, dried at 105 °C, and weighed. The residue was washed 5 times with 10 mL of distilled water per washing, dried at 105 °C for 1 hour, and weighed to the nearest 1 mg.

Anhydrous PC and BFS were dissolved by EDTA solution using the same method as used for the hydrated samples, to determine the proportion of PC and BFS dissolved, 2.0% and 86.9%, respectively. Corrections were applied to the data for the hydrated samples, to account for the minor amounts of PC remaining after selective dissolution, the few percent of anhydrous slag that was dissolved, and the hydrotalcite-group minerals that are not dissolved, in the residue [154,158]. It was assumed that

the MgO content of the slag would react to form $\text{Mg}_4\text{Al}_2(\text{OH})_{12}\text{CO}_3 \cdot 4\text{H}_2\text{O}$, which is insoluble in EDTA. Equations 3.1 to 3.4 summarise the methodology for the hydrotalcite corrections:

$$\text{HT}_m = \frac{m_{\text{MgO}}}{m_{\text{MgO/HT}}/100} \quad \mathbf{3.1}$$

$$\text{HT}_s = R \times \text{HT}_m \quad \mathbf{3.2}$$

$$D = \frac{R(100 + m_{\text{MgO/HT}})}{100} \quad \mathbf{3.3}$$

$$I = D - \text{HT}_s \quad \mathbf{3.4}$$

Where HT_m is the maximum quantity of this hydrotalcite-group phase (mineralogically resembling quintinite as a phase with a 4:2 Mg:Al ratio) formed by 100% hydration of slag (29.93 g), m_{MgO} is the mass of MgO within the BFS, $m_{\text{MgO/HT}}$ is the mass percentage of MgO within $\text{Mg}_4\text{Al}_2(\text{OH})_{12}\text{CO}_3 \cdot 4\text{H}_2\text{O}$ (33.08 wt.%), HT_s is the mass of $\text{Mg}_4\text{Al}_2(\text{OH})_{12}\text{CO}_3 \cdot 4\text{H}_2\text{O}$ created based on the percentage of slag reacted, R is the residue after dissolution including PC and BFS corrections, D is the corrected degree of hydration, and I is the calculated initial residue.

These calculations assume that all of the available MgO is used to form $\text{Mg}_4\text{Al}_2(\text{OH})_{12}\text{CO}_3 \cdot 4\text{H}_2\text{O}$. Equation 3.2 to 3.4 are solved iteratively, replacing R with D each time. The sum of squared errors (SSE) between the iterated initial residue and the calculated initial residue was minimised to obtain the actual degree of hydration of the slag.

3.3.2 X-ray diffraction (XRD)

The use of XRD is widely used when analysing the crystal and amorphous phases formed as a result of cement hydration and when analysing the anhydrous precursor materials (Figure 3.1) [46,155,159]. Distinct peaks observed in XRD scans highlight the crystal phases as can be seen in Figure 3.1a, which displays the crystalline clinker phases and additional precursor material calcite and gypsum. The amorphous hump between 17.5 and 37.5° 2θ shown in Figure 3.1b represents the disordered amorphous BFS precursor.

Upon reaching the specified testing exposure time, hardened specimens were crushed and ground using acetone as a lubricant, to a particle size below 63 μm . The powders were then submerged in acetone for 15 minutes and vacuum filtered, to ensure that hydration had ceased [160]. Analysis of mineralogy was performed using powder X-ray diffraction (XRD) on a Bruker D2 Phaser instrument with Cu $K\alpha$ radiation (1.54 \AA) and a nickel filter. Scans were conducted with a step size of 0.020° , for 2 seconds per step, with front-loading sample holders. The Inorganic Crystal Structure Database (ICSD) and the Powder Diffraction File (PDF) were used in phase identification. Characterisation of the hydrated cement phases using XRD analysis was performed in Chapters 4 and 5.

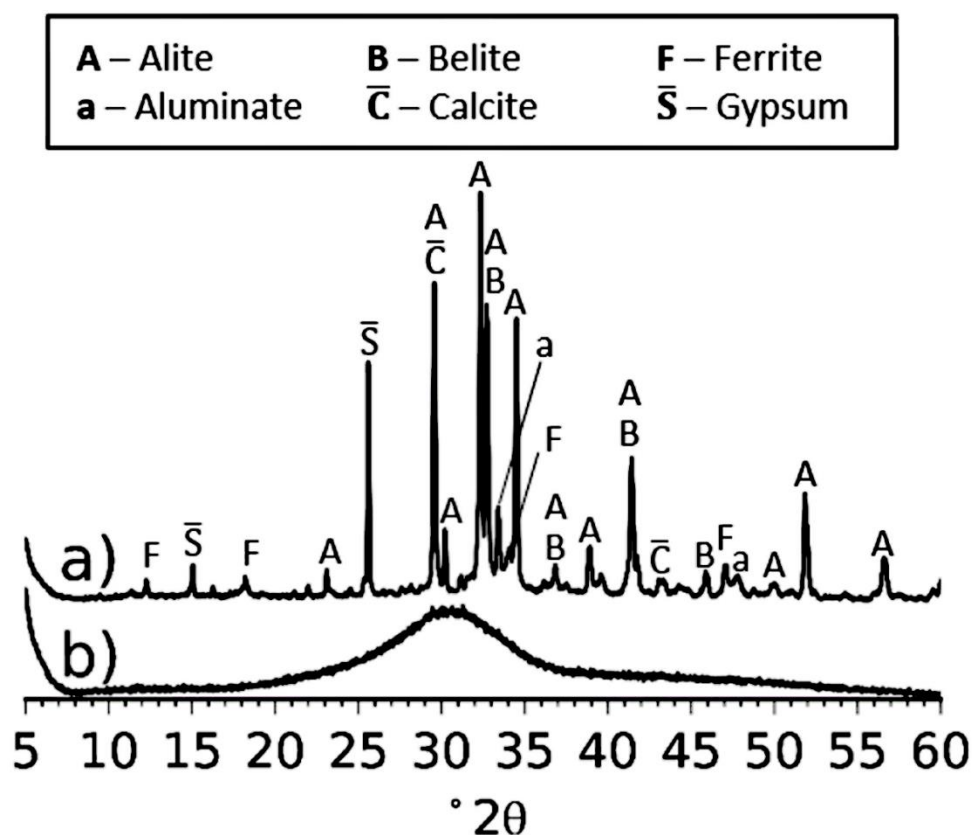


Figure 3.1: X-ray diffractograms of anhydrous a) PC and b) BFS.

3.3.3 ^{27}Al and ^{29}Si magic angle spinning (MAS) nuclear magnetic resonance (NMR)

Magic angle spinning (MAS) nuclear magnetic resonance (NMR) spectroscopy can be used to provide structural information of poorly crystalline phases [161,162]. This technique can provide useful information regarding the chemical environment which surrounds the nucleus of interest by measuring the natural magnetic moment to measure the interactions of the nucleus with other

surrounding nuclei [163]. Using information from this technique, it is possible to measure the average chemical composition of amorphous material such as C(-A)-S-H [45,58,60,164,165]. In this study ^{29}Si MAS NMR was used to determine the degree of hydration of the silicon-containing clinker phases and BFS, determine the chemical composition and mean chain length of C(-A)-S-H. ^{27}Al MAS NMR was used to confirm the presence of aluminium within the C-S-H structure.

Solid-state ^{27}Al and ^{29}Si magic angle spinning nuclear magnetic resonance (MAS NMR) spectra were collected on a Varian VNMRS 400 (9.4 T) spectrometer with either a 4 mm zirconia (for ^{27}Al) or 6 mm zirconia (for ^{29}Si) rotor. The ^{27}Al MAS NMR single pulse experiments were collected at 104.198 MHz using the following parameters: 14 kHz spinning speed, minimum of 5700 scans, pulse width of 1 μs (25°) and a 0.2 s relaxation delay. The ^{29}Si MAS NMR single-pulse experiments were recorded at 79.435 MHz using the following parameters: 6.8 kHz spinning speed, minimum of 7000 scans, pulse width of 4.7 μs (90°) and a relaxation delay of 5 s. Poulsen et al. [162] showed that a 5 s relaxation delay may result in an under-quantification of belite as there may not be enough time for the nuclei to fully relax prior to the next pulse, depending on the iron content of the cement tested, and its incorporation into different clinker phases. Edwards et al. [166] also showed a difference between the intensity ratio of alite to belite as a function of relaxation delay, however for delays between 3 and 70 s, the difference was minimal. It is also not clear whether differences in relaxation behaviour between different Si environments in the hydrate products will have a significant influence on quantification under the experimental conditions used here. Therefore, no correction of the silicon intensities for this effect was performed here, and the error in the quantification of resonances due to the differences in relaxation behaviour between different silicon sites is estimated to be $\pm 5\%$. ^{29}Si , and ^{27}Al chemical shifts are referenced to external samples of tetramethylsilane (TMS), and a 1.0 M aqueous solution of $\text{Al}(\text{NO}_3)_3$, respectively.

Deconvolutions were performed using non-linear minimisation of the sum of squared errors using Gaussian curves to obtain the best fit for comparing the deconvolution with the experimental data [60,123,167,168]. Constraints were placed on the linewidths and peak positions dependent on the peak being analysed, as detailed below.

Quantification and deconvolution of the anhydrous PC was performed using 9 overlapping peaks with varying linewidths for alite (-64.5 to -76.5 ppm) and a single peak for belite (-71.3 ppm) with an

observed linewidth (FWHM) of 0.33 ppm [162] (Figure 3.2). A relative belite to alite intensity of 0.13 was determined. This relative intensity was used in conjunction with the CaO and SiO₂ contents determined by XRF (Table 3.1) to determine the quantity of alite and belite available in the PC [162]. This calculation is in good agreement with the quantity of alite and belite determined using the modified Taylor-Bogue method [169] as seen in Table 3.3. These clinker compositions were used to define the thermodynamic modelling precursor values. Fitting of the anhydrous BFS showed a large broad resonance from -65 to -90 ppm (Figure 3.3). It was assumed that all hydration of the anhydrous material was congruent.

Table 3.3. Clinker phases present in anhydrous PC, as quantified by ²⁹Si MAS NMR and by the Taylor-Bogue method.

	²⁹ Si MAS NMR	Taylor-Bogue
Alite	72.6	71.9
Belite	7.6	6.8
Aluminate	-	8.0
Ferrite	-	7.7

Potential ranges of chemical shifts indicating the chemical environments observed in the C(-A)-S-H phase are summarised in Table 3.4. The chemical shifts determined from literature sources were used as a guideline for determining the chemical shifts used in Chapter 4.

The ²⁷Al spectra in addition to the ²⁹Si spectra may provide confirmation of the aluminium substitution in the C-S-H phase. The ²⁷Al spectra is divided into three main regions to signify the different coordination numbers of aluminium: Al[IV], Al[V] and Al[VI]. The aluminium species incorporated into cement phases are summarised in Table 3.5.

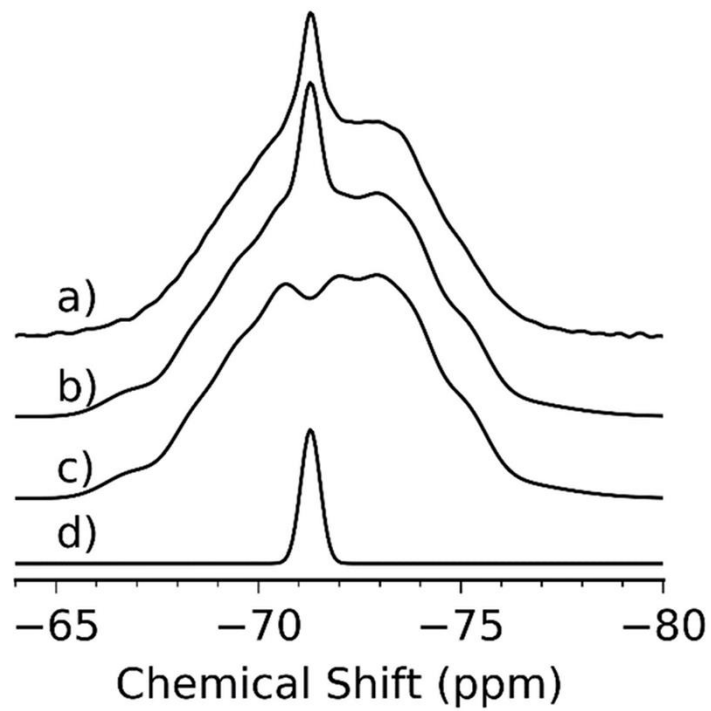


Figure 3.2. Fitting of the ^{29}Si MAS NMR spectrum of anhydrous PC: a) experimental data, b) fitted deconvolution, c) alite spectrum, and d) belite spectrum.

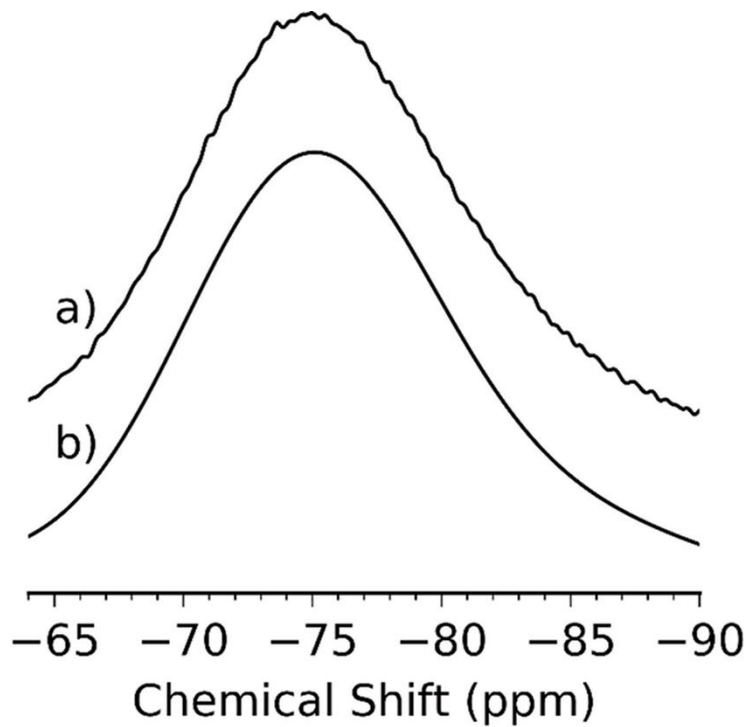


Figure 3.3. Fitting of the ^{29}Si MAS NMR spectrum of anhydrous slag: a) experimental data and b) fitted deconvolution.

Table 3.4: Chemical shift ranges in which the different silicon Q^x species are located using ²⁹Si NMR.

Silicon environment	Configuration	Chemical shift (ppm)	Ref.
Q ⁰	$\begin{array}{c} \text{O}^- \\ \\ \text{O}^- - \text{Si} - \text{O}^- \\ \\ \text{O} \end{array}$	-74.0	[60,168,170]
Q ¹	$\begin{array}{c} \text{O}^- \\ \\ \text{O}^- - \text{Si} - \text{O} - \text{Si} \\ \\ \text{O} \end{array}$	-77.8 to -79.85	[50,51,60,63,158,170-172]
Q ² (1Al)	$\begin{array}{c} \text{O}^- \\ \\ \text{Si} - \text{O} - \text{Si} - \text{O} - \text{Al} \\ \\ \text{O} \end{array}$	-80 to -83	[50,51,60,63,158,170-172]
Q ²	$\begin{array}{c} \text{O}^- \\ \\ \text{O}^- - \text{Si} - \text{O} - \text{Si} \\ \\ \text{O}^- \end{array}$	-84.5 to -86.0	[50,51,60,63,158,170-172]
Q ³ (1Al)	$\begin{array}{c} \text{O}^- \\ \\ \text{Si} - \text{O} - \text{Si} - \text{O} - \text{Si} \\ \\ \text{O} \\ \\ \text{Al} \end{array}$	-89.0 to -92.5	[50,60]
Q ³	$\begin{array}{c} \text{O}^- \\ \\ \text{Si} - \text{O} - \text{Si} - \text{O} - \text{Si} \\ \\ \text{O} \end{array}$	-93.0 to -96.0	[50,60,63]

Table 3.5: Chemical shift ranges that the different silicon Q^x species are located using ²⁷Al NMR.

Aluminium co-ordination	Phases present	Chemical shift range (ppm)	Ref.
Al[IV]	C-A-S-H, C ₃ A, BFS	> 50	[50,51,173-176]
Al[V]	Interlayer charge balancing aluminium (IT)	20-50	[50]
Al[VI]	Ettringite, monosulphate, magnesium hydrotalcite-like, third aluminate hydrate (TAH)	< 20	[33,51,173]

3.3.4 Scanning electron microscopy

Scanning electron microscopy (SEM) was performed using a Hitachi TM 3030 instrument with a 20 kV accelerating voltage, a working distance of 8 mm and a backscatter detector. Samples were cut and polished using non-aqueous lubricants immediately prior to analysis. An evenly distributed selection of points across a representative 400 μm \times 400 μm section of the sample was analysed using a Bruker Quantax 70 X-ray energy dispersive spectroscopy (EDS) detector to determine chemical compositions. Further explanation of the methods used to determine chemical composition of the C(-A)-S-H and hydrotalcite-like phase are in Chapter 5.

3.3.5 Pore solution extraction and ICP-OES

Pore solution of the blended cements were obtained using the steel-die method [118,177–179] to compare activity coefficient models in Chapter 6. Further explanation of the methodology may be found in Chapter 6, section 6.3 (Pore solution extraction from hydrated samples).

3.4 Thermodynamic modelling

Thermodynamic modelling was performed using GEM-Selektor v3 [132,180] using the CEMDATA14 database which is an updated version of CEMDATA07 [151]. GEMS utilises a Gibbs energy minimisation algorithm which determines the most stable phase assemblage. Included within this study is a solid-solution model for C-A-S-H adapted from the work of Myers et al. [146] and Kulik [64], in Table 3.6. This adaptation was used to provide a greater Ca/Si ratio within the modelled C-A-S-H gel to describe BFS:PC cements, as opposed to the alkali-activated slags for which the CNASH_ss model was originally developed [146]. A similar approach was also adopted by Elakneswaran et al. [125] using PHREEQC [115,129]. A hydrotalcite-like solid solution model (MA-OH-LDH [146]) replaced the OH-Hydrotalcite phase found within CEMDATA14 to better represent the magnesium aluminate hydrate (M-A-H) phase. The solid, aqueous and gaseous phases utilized throughout this study are shown in Table A8.3 to A8.5 found in the Appendix.

Table 3.6: Thermodynamic data for the end-members in the solid-solution model for C-A-S-H. Standard thermodynamic properties at 25 °C and 1 bar.

End-member	Composition	$\Delta_f H$ (kJ/mol)	$\Delta_f G$ (kJ/mol)	Ref.
5CA	$(\text{CaO})_{1.25}(\text{Al}_2\text{O}_3)_{0.125}(\text{SiO}_2)_1(\text{H}_2\text{O})_{1.625}$	-2491	-2293	[146]
INFCA	$(\text{CaO})_1(\text{Al}_2\text{O}_3)_{0.15625}(\text{SiO}_2)_{1.1875}(\text{H}_2\text{O})_{1.65625}$	-2551	-2343	[146]
T2C	$(\text{CaO})_{1.5}(\text{SiO}_2)_1(\text{H}_2\text{O})_{2.5}$	-2721	-2300*	[146]
T5C	$(\text{CaO})_{1.25}(\text{SiO}_2)_{1.25}(\text{H}_2\text{O})_{2.5}$	-2780	-2517	[146]
TobH	$(\text{CaO})_{1.25}(\text{SiO}_2)_{1.5}(\text{H}_2\text{O})_{2.5}$	-2831	-2560	[146]
JenD	$(\text{CaO})_{1.5}(\text{SiO}_2)_{0.67}(\text{H}_2\text{O})_{2.5}$	-2400	-2170	[64]

*Altered to incorporate the higher Ca/Si ratio end-member of JenD from Kulik (2011)

In Chapters 4, 5 and 6 the activity coefficients of aqueous species (γ_i) were determined using the Truesdell-Jones equation which is an extension of the Debye-Hückel equation (Eq. 5) [134].

$$\log_{10}\gamma_i = \frac{-A_\gamma z_i^2 \sqrt{I}}{1 + aB_\gamma \sqrt{I}} + b_\gamma I + \log_{10} \frac{X_{jw}}{X_w} \quad 3.5$$

The common ion size parameter, \hat{a} and short-range interaction parameter, b_γ , 3.67 Å and 0.123 kg/mol, respectively, were used, treating KOH as the background electrolyte [134]. The KOH values were chosen as it is often the most prominent aqueous species found in BFS-PC pore solution [104,108]. The Pitzer model was used in Chapter 6 to compare the modelling results of common cement hydrates with the Truesdell-Jones equation. A further explanation of that method may be found in Chapter 6. The Pitzer parameters used are shown in Table A8.6 found in the Appendix.

The degree of hydration data obtained through selective dissolution and ^{29}Si NMR deconvolutions was used as the input parameters for the thermodynamic modelling work simulating degree of hydration.

Alkali distribution ratios (R_d) to simulate alkali uptake in the C-A-S-H phase were used for sodium and potassium. The distribution ratios calculate the uptake of alkalis from solution based on the mass of C-A-S-H formed and the concentration of alkalis in solution:

$$R_d = \frac{c_s w}{c_d s} \quad \mathbf{3.6}$$

Where, c_s is the concentration of the alkali in the solid phase (mol/mL), c_d is the concentration of the alkali in solution (mol/mL) and w/s is the water to solid ratio (mL/g). Alkali distribution ratios for Na_2O and K_2O of 2 and 1.2, respectively, were used for the C-A-S-H phase, following the method of Lothenbach et al. [151]. These values were chosen as they are similar to the values determined by Hong and Glasser [59,85] for C-S-H and C-A-S-H phases with Ca/Si values between 1.2 and 1.6.

4 Phase evolution of slag-rich cementitious grouts for immobilisation of nuclear wastes: an experimental and modelling approach

Note: This chapter is based primarily on the paper “*Phase evolution of slag-rich cementitious grouts for immobilisation of nuclear wastes*” by D. P. Prentice, S. A. Bernal, M. Bankhead, M. Hayes and J. L. Provis. Published in *Advances in Cement Research*. 2017, 30(8), pp. 345-360.

4.1 Introduction

Encapsulation of intermediate level radioactive waste (ILW) in cementitious matrices is the preferred method for its disposal in the UK. Combinations of supplementary cementitious materials (SCM) and Portland cement (PC) contribute to the grouts used in this process [11]. The high pH of the blended cements, normally 12 or higher [12], is intended to cause the radionuclides to be insoluble, and the cementitious environment creates hydration products that promote the sorption and ion substitution of key radionuclides [13,14]. Restricting the movement of the radioactive material is the main objective of encapsulation [15].

A highly durable cement wasteform provides a safer method to store and transport potentially hazardous material [5]. Blast furnace slag (BFS) blended with PC is used extensively for this purpose, at varying degrees of replacement (75 to 90% replacement). High replacement levels are used because of the slower reactivity of BFS with water, which decreases the heat released by hydration of grout constituents during the early stages of curing [16–18]. Blended cements are also widely available and relatively inexpensive for the purpose of encapsulating a wide range of wastes.

In the UK, 108,000 m³ of ILW had already been generated by April 2016, of which 41,400 m³ had been converted into cemented wasteforms awaiting long term storage, leaving large quantities still awaiting treatment [4]. Therefore, due to the large volumes of waste still awaiting treatment, as well as the need to monitor and maintain the cemented products now in interim storage awaiting final disposal, further understanding of potential interactions between the cementitious grouts and the encapsulated wastes is necessary. Despite the large volumes of waste being produced, supply of the

precursor materials has been a constant issue over the years [19], therefore a method to be able to predict how the old and new cementitious constituents react to form different phase assemblages is required.

Investigations of cement for immobilisation of radioisotopes have primarily focused on the incorporation of ions within the cement hydrate phases such as calcium silicate hydrates (C-S-H), ettringite, and calcium monosulphoaluminate hydrate (“monosulphate”), due to the variety of cationic and anionic substitutions that may take place within these stable phases. The silicate chain-based, layered structure of C-S-H offers a variety of sites to host substituents, whether within the silicate chain, such as the replacement of silicon by aluminium to form C-A-S-H type products [86,165,167,181], or as charge balancing ions within the interlayer region [108,146,170]. The high surface area of the C-A-S-H gel provides a surface for ionic sorption or substitution for interlayer sites [182]. Ettringite ($\text{Ca}_3\text{Al}_2\text{O}_6 \cdot 3\text{CaSO}_4 \cdot 32\text{H}_2\text{O}$) hosts numerous SO_4^{2-} ions located within the channels of columns of calcium and aluminium polyhedra which provides the possibility for anionic replacement. At lower sulphate concentrations, monosulphate ($\text{Ca}_3\text{Al}_2\text{O}_6 \cdot \text{CaSO}_4 \cdot 12\text{H}_2\text{O}$) is more dominant [45,89,183] and forms a lamellar hexagonal structure. Both ettringite and monosulphate require charge balancing of a cationic structure by exchangeable anions, which can be replaced by anionic radionuclides [182,184,185]. Another main phase associated with BFS-rich cements is a Mg-Al-hydroxalite-like phase, and although this is well known to act as a good receptor for Cl^- and CO_3^{2-} binding [186,187], its role in uptake of important radionuclides still requires further investigation.

The nature and amount of hydration products forming in BFS-PC blended cements are highly dependent on temperature, curing time, PC and slag content, and slag composition [45,89,151,183,188–191]. Although BFS:PC grouts have been extensively studied over recent decades, evaluation has mostly focused on assessment of young specimens and a small portfolio of samples which have been analysed at regular intervals since the 1990s [44,45,86,90], and therefore there remain open questions around the chemical, mineralogical and microstructural changes these materials will undergo over the potentially millions of years for nuclear waste cementation [27].

Thermodynamic modelling is a very useful tool that can be used to predict how the changes in blend ratios of a cement system will affect the aqueous and solid hydration products in the longer term [118,120,121]. This can be performed using geochemical modelling software packages such as GEM-

Selektor (GEMS) [132,180], and utilises solid-solution models in conjunction with thermodynamic databases for defined phases to predict the formation of cement hydrates. The key limitation of this method at present is the difficulty in accurately parameterising an end-member model for the complex multi-component hydrates present in cements, based on limited and often conflicting experimental results [64,65,146]. Therefore, the purpose of this study is to assess the effectiveness of a geochemical model for C(-A)-S-H in predicting phase assemblages of the slag cement systems used in the UK nuclear industry. Using this technique, predictions based on the precursor materials used for nuclear waste encapsulation may be performed to quickly and accurately assess whether new supplies of BFS and PC are capable of providing the necessary performance characteristics in the long term.

4.2 Experimental methodology

4.2.1 Mix Design

Cementitious grouts composed of 1:1, 3:1 and 9:1 BFS:PC (compositions in Table 3.1) were produced with a water/solids (w/s) mass ratio of 0.35, cured at 35 °C. These mix ratios and curing temperature conditions were chosen to resemble the current interim storage conditions of ILW waste packages. A summary of the materials were provided in Chapter 3, Section 3.1.

4.2.2 Analytical techniques

Upon reaching the specified curing age, hardened specimens were crushed and ground using acetone as a lubricant, to a particle size below 63 µm. They were then vacuum washed with acetone to ensure hydration had ceased [160].

Analysis of the crystalline phases was performed using powder X-ray diffraction (XRD) on a Bruker D2 Phaser instrument with Cu K α radiation and a nickel filter. Scans were conducted with a step size of 0.020°, for 2 seconds per step. Samples were front loaded by pouring the sample into a sample holder, then smoothed over with a glass tile.

Selective dissolution of the hydrated samples was conducted to determine the degree of hydration of the BFS in each sample. The EDTA method was used [41,105,154]. The technique used was explained in Chapter 3, Section 3.3.1.

4.2.3 ²⁷Al and ²⁹Si MAS NMR

Data collected from these scans were used to: (1) determine the degree of hydration for direct comparison with the results obtained through selective dissolution, (2) obtain the degree of hydration of clinker phases, and (3) identify poorly crystalline reaction products which are difficult to observe by XRD.

Solid-state ²⁷Al and ²⁹Si magic angle spinning nuclear magnetic resonance (MAS NMR) spectra were collected on a Varian VNMRS 400 (9.4 T) spectrometer with either a 4 mm zirconia (for ²⁷Al) or 6 mm zirconia (for ²⁹Si) rotor. ²⁹Si, and ²⁷Al chemical shifts are referenced to external samples of tetramethylsilane (TMS), and a 1.0 M aqueous solution of Al(NO₃)₃, respectively. Further explanation can be found in Chapter 3, Section 3.3.3.

4.2.4 Thermodynamic modelling

Thermodynamic modelling was performed using GEM-Selektor v3 [132,180] using the CEMDATA14 database which is an updated version of CEMDATA07 [151]. A summary of the solid, aqueous and gaseous phases used are summarized in Table A8.3 to A8.5, found in the Appendix.

The activity coefficients of aqueous species (γ_i) were determined using the Truesdell-Jones equation which is an extension of the Debye-Hückel equation (Equation 4.1) [134].

$$\log_{10}\gamma_i = \frac{-A_\gamma z_i^2 \sqrt{I}}{1 + aB_\gamma \sqrt{I}} + b_\gamma I + \log_{10} \frac{X_{jw}}{X_w} \quad \mathbf{4.1}$$

Here, γ_i and z_i are the activity coefficient and charge of the i^{th} aqueous species respectively, A_γ and B_γ are temperature and pressure dependent coefficients, I is the molal ionic strength, X_{jw} is the molar

quantity of water, and X_w is the total molar amount of the aqueous phase. A common ion size parameter, \hat{a} (3.67 Å) and short-range interaction parameter, b_γ (0.123 kg/mol), were used, treating KOH as the background electrolyte [134].

Alkali distribution ratios for Na₂O and K₂O of 2 and 1.2 [59,85,118], respectively, were used for the C-A-S-H phase, as explained in Chapter 3, Section 3.4.

4.3 Experimental results and discussion

4.3.1 X-ray diffraction.

X-ray diffractograms highlighting the impact of the varying levels of slag in the hydration products of the blended cements assessed are depicted in Figure 4.1. Phases present for each curing time and blend ratio are portlandite (ICSD #15471), calcium hemicarboaluminate-AFm (hemihydrate, PDF #00-036-0129), calcium monocarboaluminate-AFm (monohydrate, PDF #00-036-0377), calcium monosulphoaluminate-AFm (monosulphate, ICSD #100138), a hydrotalcite-like phase (PDF #00-014-0525), ettringite (ICSD #16045), and C-A-S-H (PDF 34-0002).

In the 1:1 BFS:PC grout, evidence of the formation of ettringite (with a distinctive peak at 9.08° 2θ) can be seen at each age tested, however between 28 days and 56 days the intensity of this peak drops just as a slight increase in monosulphate (9.93° 2θ) emerges. The ettringite transforms into monosulphate when the ratio of SO₄²⁻ to Al³⁺ decreases [192], as it is the case as more slag reacts. The 3:1 BFS:PC system exhibits a very small ettringite peak intensity after 28 days and none at later curing ages, while the 9:1 blend exhibits no ettringite and has a much more distinct monosulphate peak.

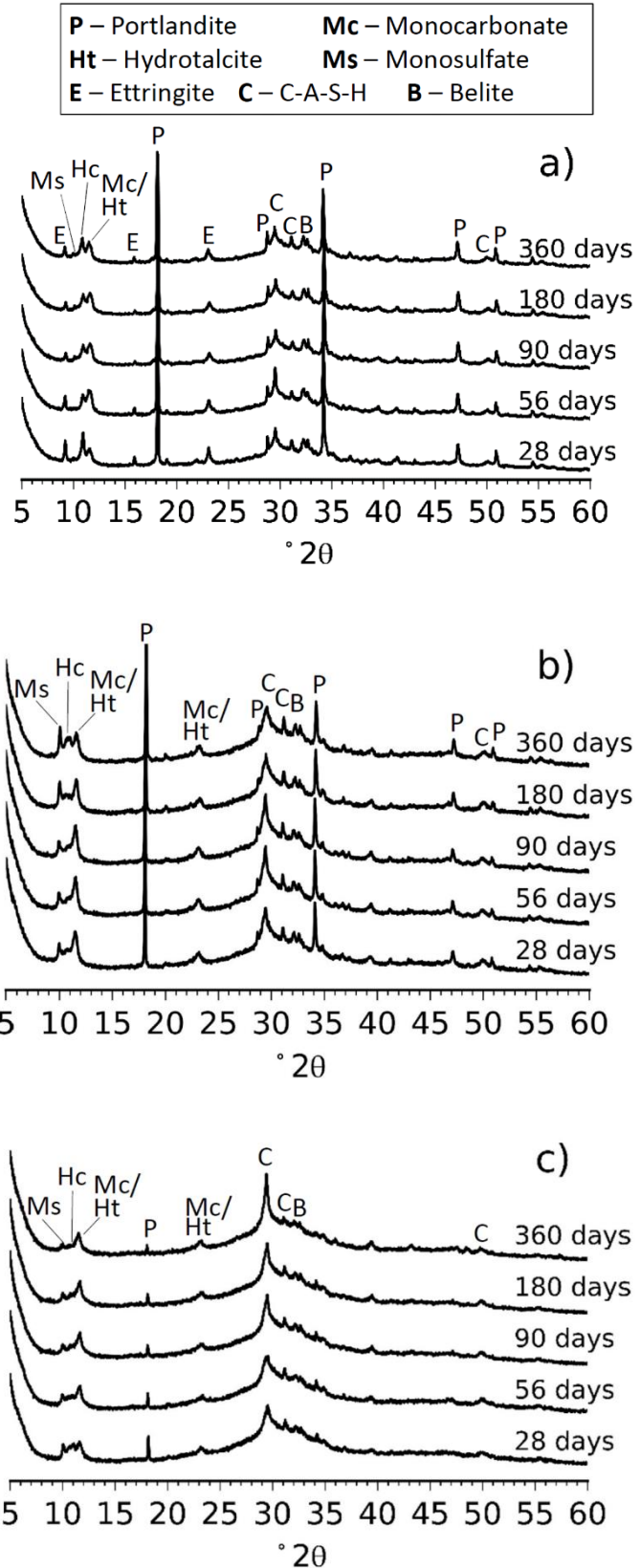


Figure 4.1: X-ray diffractograms of hydrated BFS:PC, a) 1:1, b) 3:1 and c) 9:1 ratios, up to a curing time of 360 days.

Other AFm phases such as hemicarboaluminate and monocarboaluminate are detected (10.75° and $11.5^\circ 2\theta$) as a result of reaction of the small amount of calcite in the cement (as identified by XRD, Figure 4.4) during hydration, and potentially some superficial carbonation contamination of the samples. The availability of calcite restricts the formation of monosulphate [193], leading to a weak reflection assigned to this phase within the 1:1 grout. Within the 3:1 and 9:1 grouts the monosulphate peak is more pronounced compared with grouts with lower BFS content, as the sulphate levels are not high enough to form ettringite at the elevated curing temperature used here (35°C), except perhaps in the very early stages of hydration, and instead AFm phases were formed.

The hydrotalcite-like phase is formed as a solid solution with a varying Mg:Al ratio which impacts its crystal structure [194,195], therefore the position of its basal reflection peak may vary between 11.2° and $11.6^\circ 2\theta$ [186,187,196]. All three grouts assessed have distinct peaks at $11.6^\circ 2\theta$; within the 1:1 grout this can also be attributed to monocarbonate, however for the 3:1 and 9:1 grouts it is likely that this peak is instead due to a hydrotalcite-like phase. The MgO content of the slag used in this study is 9.9 wt.%, Table 3.1, which is sufficient for hydrotalcite-group minerals to form in slag-dominated binders [197]. There is also less calcite available to form carboaluminate phases when the PC content is low, which further supports this line of reasoning. The peaks corresponding to the hydrotalcite-like phase have a much greater intensity in the 3:1 grout than the others, which is attributed to the greater degree of hydration of slag in this cement.

Portlandite and C-A-S-H gel were the hydration products with the highest peak intensities for the 1:1 and 3:1 grouts. The peak intensity of portlandite decreased with the increasing of BFS content, and in the case of the 9:1 grout, at longer curing times. The consumption of portlandite with time in the 9:1 grout leads to the formation of more C-A-S-H, as more silicon becomes available from the dissolution of slag, as the hydration progresses.

4.3.2 ^{27}Al MAS NMR

Figure 4.2 includes the ^{27}Al MAS NMR spectra of the anhydrous PC and BFS, along with those of the hydrated samples. The spectrum of the anhydrous BFS displays a very broad resonance between 50 and 80 ppm, centred around 67 ppm. This is consistent with a tetrahedral aluminium coordination state. Anhydrous cement contains two aluminium-containing phases; tricalcium aluminate (aluminate) and tetracalcium aluminoferrite (ferrite). From the broad peak around 81 ppm [51,173]

and the sharp peak at 9.4 ppm it is assumed that only aluminate can be identified here by NMR, due to the suppression of the signal from the ferrite phase due to the close proximity of iron to the aluminium nuclei in that phase [198].

Samples cured for 28 days or more, across all blend ratios, do not display any evidence of the C_3A peak at 81 ppm, indicating that essentially all of the aluminate in the PC has reacted. Within the Al(IV) region, a shoulder emerges to the left of the slag peak at 71 ppm for all samples. A resonance at this chemical shift is indicative of aluminium substitution within the C-S-H silicate chains [50,51,174–176]. There is clearly a greater influence in the Al(IV) region with increasing slag content in the grouts. In the 1:1 grouts there is only a slight shoulder on the underlying broad feature, however in the 3:1 and particularly the 9:1 grout the peak at 71 ppm becomes more defined. The increasing definition of the 71 ppm peak indicates more incorporation of aluminium within the C-S-H gel, which takes place mainly at the Q^2 bridging sites within the dreierketten silicate chain structure (Richardson 2014; L'Hôpital et al. 2016).

The Al(V) species exhibited at 36 ppm was identified in all formulations as interlayer charge balancing aluminium (denoted IT) [50].

Noticeable changes occur within the Al(VI) region of the spectra between 0 and 20 ppm as a function of curing time and slag content. Within this region it is evident that ettringite is only observed, at around 13 ppm [51,173], in the 1:1 grout from 28 to 360 days. The sharp ettringite peak appears to become less defined at longer curing times. This peak is not evident at all in the 3:1 and 9:1 grouts, consistent with the XRD data (Figure 4.2b, 4c). There are clearly not enough sulphate ions within the solution to stabilise the ettringite in the lower PC containing grouts and for later age 1:1 grouts.

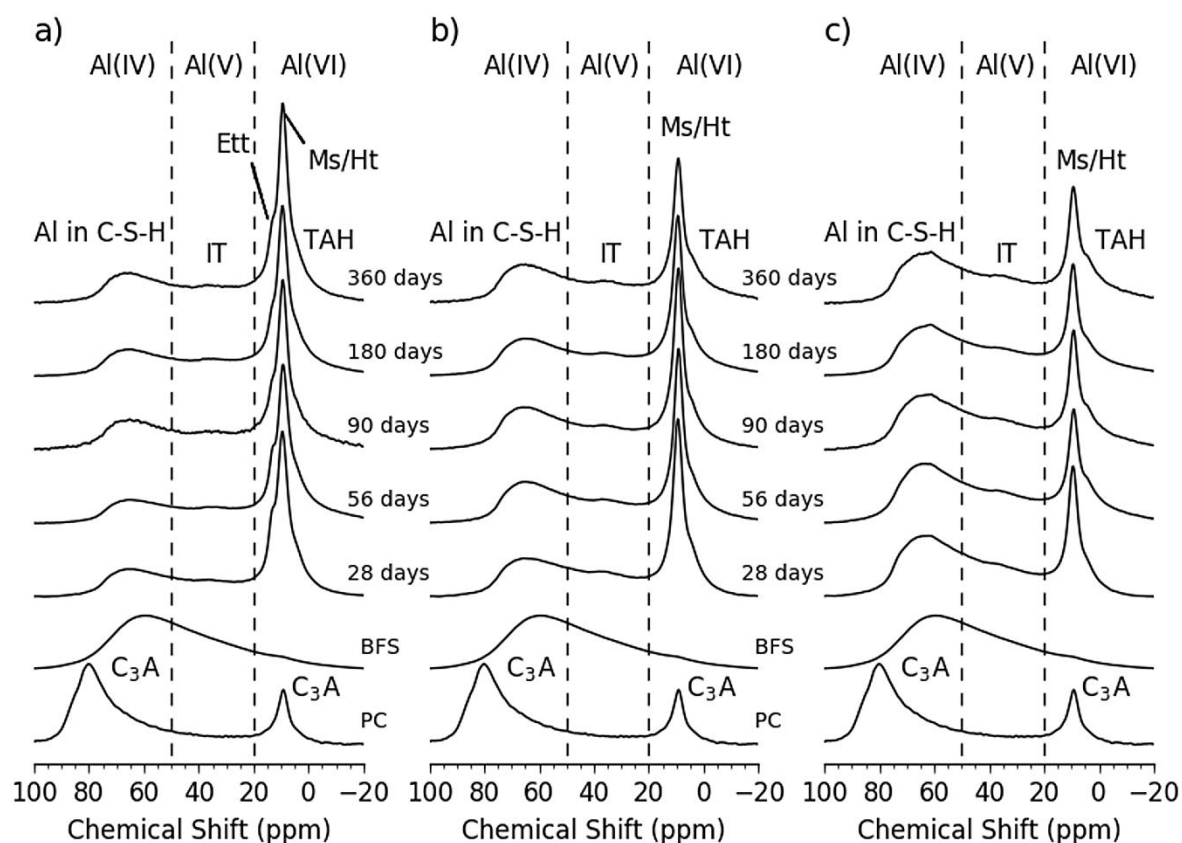


Figure 4.2: ^{27}Al MAS NMR spectra for a) 1:1, b) 3:1 and c) 9:1 BFS:PC grouts.

Clear evidence of AFm phase formation can be seen at 9.8 ppm; this can be attributed to monosulphate, hemicarboxylate and/or monocarbonate due to the interchangeability of the charged ion within AFm phases, $[\text{Ca}_2(\text{Al}(\text{OH})_6) \cdot \text{X} \cdot x\text{H}_2\text{O}]$ where X is one unit of a single charged ion or half a unit of a doubly charged ion [33]. This peak may also indicate the presence of octahedral aluminium in hydrotalcite (expected at 9.7 ppm, so strongly overlapping the AFm resonance). All of these phases were identified in these grouts by XRD (Figure 4.2) and contribute to the peak intensity in this region. A stronger resonance at this chemical shift was observed in the 1:1 grout as a result of the presence of larger amounts of cement supplying calcite and gypsum. At 3.9 ppm, the third aluminate hydrate (TAH) was identified in all grouts and curing times. The lack of sulphate ions and an increase in aluminium present in the cements with the higher BFS contents leads to a more distinct resonance assigned to the TAH phase [173].

4.3.3 ^{29}Si MAS NMR

Figure 4.3 shows the ^{29}Si MAS NMR spectra of each sample analysed; Figure 4.3a, c and e show examples of the deconvoluted ^{29}Si MAS NMR of the 1:1, 3:1 and 9:1 grouts, respectively, after 360 days of curing, while Figure 4.3b, d and f show the full sets of spectra as a function of curing time. In conducting the deconvolutions, peaks associated with the C-A-S-H gel were limited to a linewidth of 3.5 ppm (FWHM) and the peak positions were allowed to vary within ± 0.1 ppm of the values provided in Table 4.1, to account for the variation of the local environments of silicon within this disordered phase.

Table 4.1: Site allocations for silicon environments in ^{29}Si MAS NMR spectra.

Silicon site	Chemical shift (ppm)
Q^0	-74.0
Q^1 (I)	-77.8
Q^1 (II)	-79.8
Q^2 (1Al)	-81.6
Q^2	-84.7
Q^3 (1Al)	-88.0
Q^3	-93.0

The broad glassy slag peaks overlaps the signals from unreacted alite and belite, alongside the Q^0 , Q^1 (I), Q^1 (II) and Q^2 (1Al) sites of C-A-S-H gel, where the two Q^1 environments are distinguished by the nature of the charge-balancing cations (monovalent and divalent), whose differing field strengths lead to the observation of separate resonances [146,168]. The slag peak overlaps the monomeric and dimeric silicate species (Q^0 , Q^1 (I) and Q^1 (II)) to a significant extent, which may impact the quantification of the Ca/Si ratio within the C-A-S-H gel. The site located at -74.0 ppm, represents a hydrated silicon monomer, Q^0 , however the precise structure in which this site is located is still unknown. Previous studies have highlighted that this silicon environment is linked with greater slag content within the BFS:PC system [60,86,168], and this was the case for the 3:1 grout as seen in Table 4.2, where raising the slag content and increasing the hydration of the slag results in a greater Q^0 intensity than was observed for the 1:1 grout. This was not the case for the 9:1 ratio; it is possible that the lower degree of slag hydration in the 9:1 system resulted in a lower intensity for this peak.

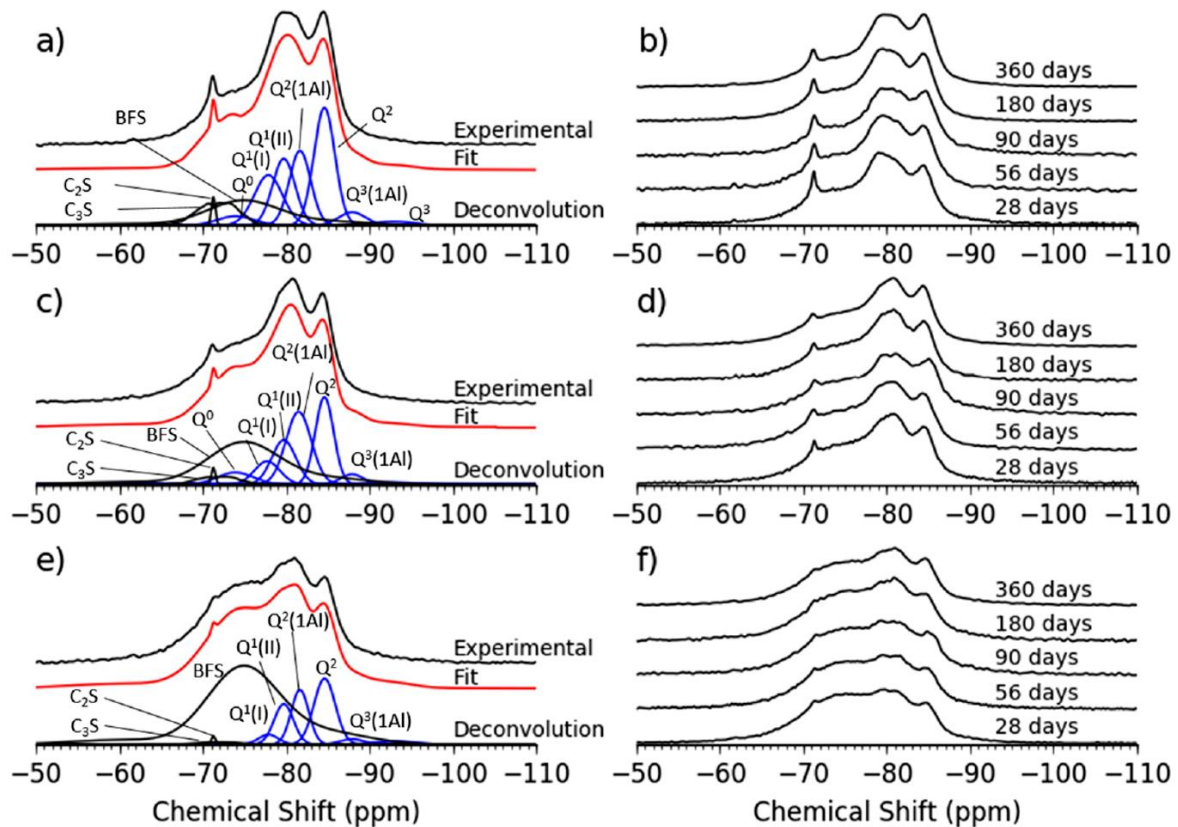


Figure 4.3: Example deconvolutions of ^{29}Si MAS NMR spectra for a) 1:1, c) 3:1 and e) 9:1 grouts after 360 days, and ^{29}Si MAS NMR spectra for b) 1:1, d) 3:1 and f) 9:1 grouts from 28 days to 360 days of curing.

Increased PC content resulted in the presence of more Q^1 sites due to the higher level of calcium supplied by PC. Correspondingly, the Q^1 prevalence decreased, and $\text{Q}^2(1\text{Al})$ and Q^2 increased, over time as more slag hydrated, thus increasing the amount of silicon available to extend the silicon chains within the C-A-S-H gel. The chemical shift values used in the deconvolutions for the silicon linked to the aluminium substituted sites ($\text{Q}^2(1\text{Al})$) and the paired silicon sites (Q^2) were more similar to those used in the literature for white PC and BFS:PC [50,158,171,172] than those found in alkali activated slag [168], as the chemical environments of these peaks are influenced by the alkali concentration. Each specimen exhibited signs of aluminium substitution within a cross-linking site in the C-A-S-H gel ($\text{Q}^3(1\text{Al})$) at -88 ppm, and small signs of cross-linking silicon (Q^3) at -93 ppm. These peak intensities are much smaller than the other peaks, and are observed at similar levels across each time and blend ratio. Cross-linking is most dominant within the 1:1 and 9:1 systems, where aluminium substitution is most prevalent.

Table 4.3 summarises the structural characteristics of the C-A-S-H gel in each sample, calculated from the deconvoluted NMR spectra [58]. The mean chain length (MCL) (Equation 4.2) was seen to increase with BFS content and curing duration, as a result of the increased aluminium and silicon levels within the C-A-S-H; Ca/Si ratios calculated from Equation 16 of the paper of Richardson [58] decreased with increased curing duration, while Al/Si (Equation 4.3) remained constant, consistent with the discussion presented above. Despite evidence of less cross-linking within the 3:1 system than the others, it still achieved a greater MCL because of the higher proportion of bridging sites when compared with the 1:1 system.

$$\text{MCL} = \frac{2}{\left(\frac{Q^1}{Q^1 + Q^2(0Al) + \frac{3}{2}Q^2(1Al) + Q^3(0Al) + Q^3(1Al)} \right)} \quad 4.2$$

$$\frac{\text{Al}}{\text{Si}} = \frac{\frac{1}{2}Q^2(1Al)}{Q^1 + Q^2(0Al) + Q^2(1Al) + Q^3(0Al) + Q^3(1Al)} \quad 4.3$$

The Ca/Si ratio of each grout calculated from this method was significantly lower than what has been observed in the literature for comparable cements [44]. Rarely has the Ca/Si ratio been published when derived from ²⁹Si MAS NMR data of hydrated cementitious materials, however the Al/Si and MCL are often provided using this methodology [50,51,171,172]. Generally, TEM-EDX or SEM-EDX data are considered to provide more accurate results when considering the Ca/Si values of C-A-S-H gels in hydrated cementitious systems.

Table 4.2: Results of deconvolution of the ^{29}Si MAS NMR spectra as a function of time and cement composition.

Sample BFS: PC ratio	Curing time (days)	Q ⁰	Q ¹ (I)	Q ¹ (II)	Q ¹	Q ² (1Al)	Q ²	Q ³ (1Al)	Q ³
1:1	28	0.17	17.9	21.8	39.6	24.1	31.7	3.2	1.2
	56	1.7	16.1	21.9	37.9	22.2	33.4	3.7	1.1
	90	0.7	14.4	21.8	36.2	23.2	32.6	4.7	2.8
	180	2.2	14.4	21.8	36.2	23.2	32.6	4.7	2.8
	360	2.4	14.8	20.4	35.2	21.7	35.8	3.8	1.1
3:1	28	0.0	10.6	21.8	32.4	30.9	34.6	1.5	0.7
	56	0.6	9.6	23.7	33.3	28.7	35.0	2.4	0.0
	90	0.9	9.4	22.6	32.0	27.7	37.0	2.3	0.0
	180	4.6	11.0	21.2	32.2	28.2	32.0	3.0	0.0
	360	4.6	9.6	20.8	30.4	27.6	33.3	3.6	0.7
9:1	28	0.0	6.4	24.5	30.9	31.2	36.6	1.2	0.2
	56	0.0	6.0	24.0	30.0	31.0	35.8	2.2	1.2
	90	0.0	6.8	22.1	28.9	29.9	35.5	3.4	2.3
	180	2.8	7.8	20.1	27.9	30.6	32.6	4.5	1.6
	360	0.3	5.6	22.3	27.8	30.8	36.2	3.1	1.8

The nature of the process of deconvoluting NMR spectra based on the local environment of silicon contains many issues because of the wide variety of potential interaction ions that impact the chemical shift of each silicon species, specifically the dimer species (Q¹), which would have the greatest impact on the Ca/Si values. As a result of the high level of variation and overlapping signal of anhydrous material, a fully detailed structural model considering the Ca/Si based on the site concentration values determined from NMR has yet been created to convert this information into Ca/Si values similar to those determined by more direct methods. Richardson [58] provided an in-depth overview of how

using different structural models influenced the Ca/Si ratio determined using NMR data, and highlighted the variation in the possible results based on which model was used. It was concluded that the use of NMR data consistently yielded lower Ca/Si values when compared to SEM or TEM results. Analysis using the CSTM method [164] provides good agreement for NMR data of alkali activated slag (AAS) systems, but its application here also tended to produce low Ca/Si values. Despite these issues, NMR data can still supply useful information about the trend in Ca/Si values based on the blend ratio and time of curing of the cement systems of interest in this study; the actual values should be treated as semi-quantitative rather than absolute.

Table 4.3: Summary of structural characteristics of the C-A-S-H gel forming in BFS:PC cements based on the ²⁹Si MAS NMR results

Time (days)	Al/Si			Ca/Si			Mean Chain Length (MCL)		
	1:1	3:1	9:1	1:1	3:1	9:1	1:1	3:1	9:1
28	0.12	0.15	0.16	1.13	1.07	1.05	5.64	7.13	7.49
56	0.11	0.14	0.15	1.11	1.07	1.05	5.77	6.83	7.71
90	0.12	0.14	0.15	1.11	1.05	1.04	6.14	7.06	7.95
180	0.12	0.15	0.16	1.11	1.08	1.05	6.14	6.80	8.07
360	0.11	0.14	0.15	1.08	1.06	1.03	6.16	7.19	8.27

4.3.4 Determination of degree of hydration using ²⁹Si MAS NMR and selective dissolution

As described in section 4.2.3, the fitted ²⁹Si MAS NMR spectra of the anhydrous materials were scaled and used as components in the deconvolution of the spectra of the reaction products, to determine the degree of hydration of each constituent within the hydrated samples. Comparison of the degree of hydration between the (independent) ²⁹Si MAS NMR and selective dissolution techniques for BFS, Figure 4.4, displays good agreement between the two techniques. The BFS in the 1:1 and 3:1 blends was slower to react when compared to some reports of other BFS:PC blended cements of the same proportions [41,96], but does align better with various other reports in the literature [40,46,156]. This may be attributed to the rather lower w/s ratio used here, which is based on the UK nuclear industry's specification for acceptable mixes [17,19]. Determination of the extent of reaction by NMR spectral deconvolution has an error margin of approximately 5% as previously discussed based on the

relaxation delay [52,162], whilst the selective dissolution technique used here has reported errors of up to 10% [199], so these possible variations must also be considered when comparing the results reported here to those available in the literature. Higher slag inclusion would be expected to result in a lower degree of hydration of the slag, as there is less portlandite produced by PC hydration that would activate the latent hydraulic character of the slag, and this trend was borne out in the current results. After 360 days the 9:1 system had approximately half the degree of reaction of the 3:1, whereas the difference between 3:1 and 1:1 was less marked; both of these systems contained significant residual portlandite according to the XRD data in Figure 4.1, so this was evidently less of a limitation at slag contents of up to 75%.

Across all blend ratios, the degree of alite hydration as determined by deconvolution of ^{29}Si MAS NMR spectra reached at least 79.0% after 28 days, but from this time up to 360 days there was only a small further increase (Figure 4.5). Higher BFS content led to a higher degree of hydration of the alite, possibly due to the higher water to alite ratio in the higher-BFS systems, where the slower reaction of the slag means that more water and space are available for PC hydration in the early stages of the reaction process, in a form of the filler effect commonly seen in blended cements, but taken to an extreme case where the cement is only 10-25% PC. A moderate degree of reaction of belite can be seen in all blends assessed, but not exceeding 65% even at 360 days in any of the cements evaluated; the belite in the 9:1 grout showed very little reaction beyond 90 days. This may be because belite is more prone to react at higher pH [42], and the pore solution pH of BFS:PC cements is reduced when they contain very high fractions of BFS [104].

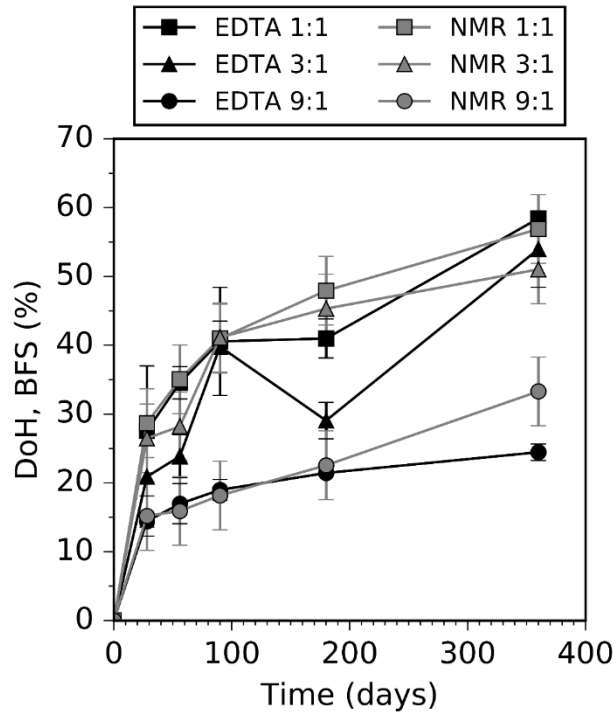


Figure 4.4: Degree of reaction of BFS within the different blend ratios, based on ²⁹Si NMR MAS deconvolutions (NMR) and on selective dissolution (EDTA).

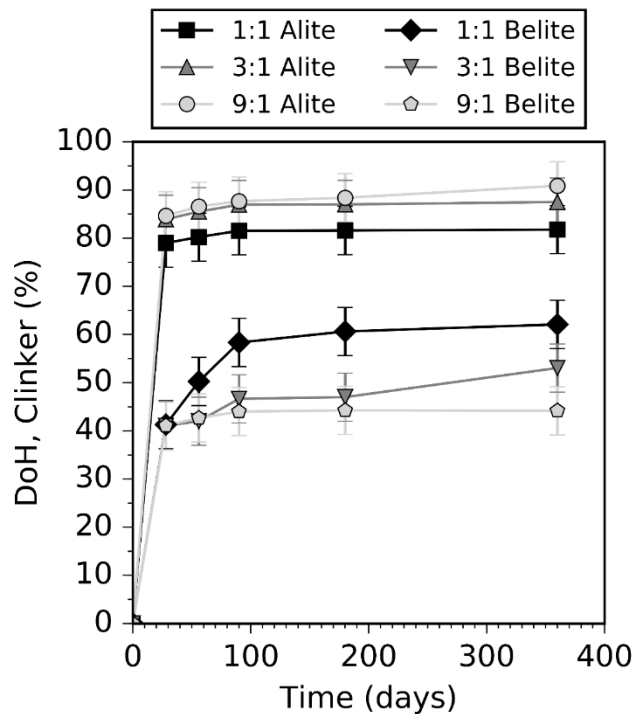


Figure 4.5: Degree of reaction of calcium silicate clinker phases (alite and belite) within the different blend ratios, based on ²⁹Si MAS NMR spectral deconvolutions.

4.4 Thermodynamic modelling

4.4.1 Calculating the hydrate phase assemblage

Using the degree of hydration data presented above, prediction of the phase assemblages via thermodynamic modelling (Figure 4.6) gave results which corresponded well with the phases identified experimentally.

As expected, the C-A-S-H gel was dominant in all grouts, and was predicted to entirely consume portlandite by 28 days in the 9:1 system. The fact that this was not observed experimentally (i.e. a small quantity of portlandite persisted at all ages in Figure 4.1) may indicate spatial heterogeneity of the blended cement leading to deviations from the assumed equilibrium behaviour, as has been discussed recently by Skocek et al. [200] for other low-clinker cements. Portlandite formation was much higher in the 1:1 cement (14 wt.% after 360 days) than the 3:1 cement (10 wt.% after 360 days), which corresponds well with the XRD data.

Ettringite appears in the model phase assemblages at early age for all blends assessed, however in the 3:1 and 9:1 cements it was predicted to be replaced by monosulphate, after 60 days and 6 days, respectively. From the experimental data presented above, only a small amount of ettringite was observed in the 3:1 system at 28 days, and none from 56 days onwards, while no ettringite was observed in the 9:1 system. Ettringite was still predicted in the 1:1 system after 360 days, along with increasing monosulphate as curing time and the degree of hydration of the BFS increased. It is possible that experimental factors not fully captured in the thermodynamic model – particularly the influence of sulphide provided by the slag, which can be incorporated into AFm phases [201] and/or oxidised to sulphate – will lead to under-prediction of the stability of ettringite in the model applied here. However, the predicted increase in monosulphate content in higher-BFS cements did align well with the experimental data. It should also be noted that the TAH phase identified by NMR was not included within the thermodynamic database used in this work.

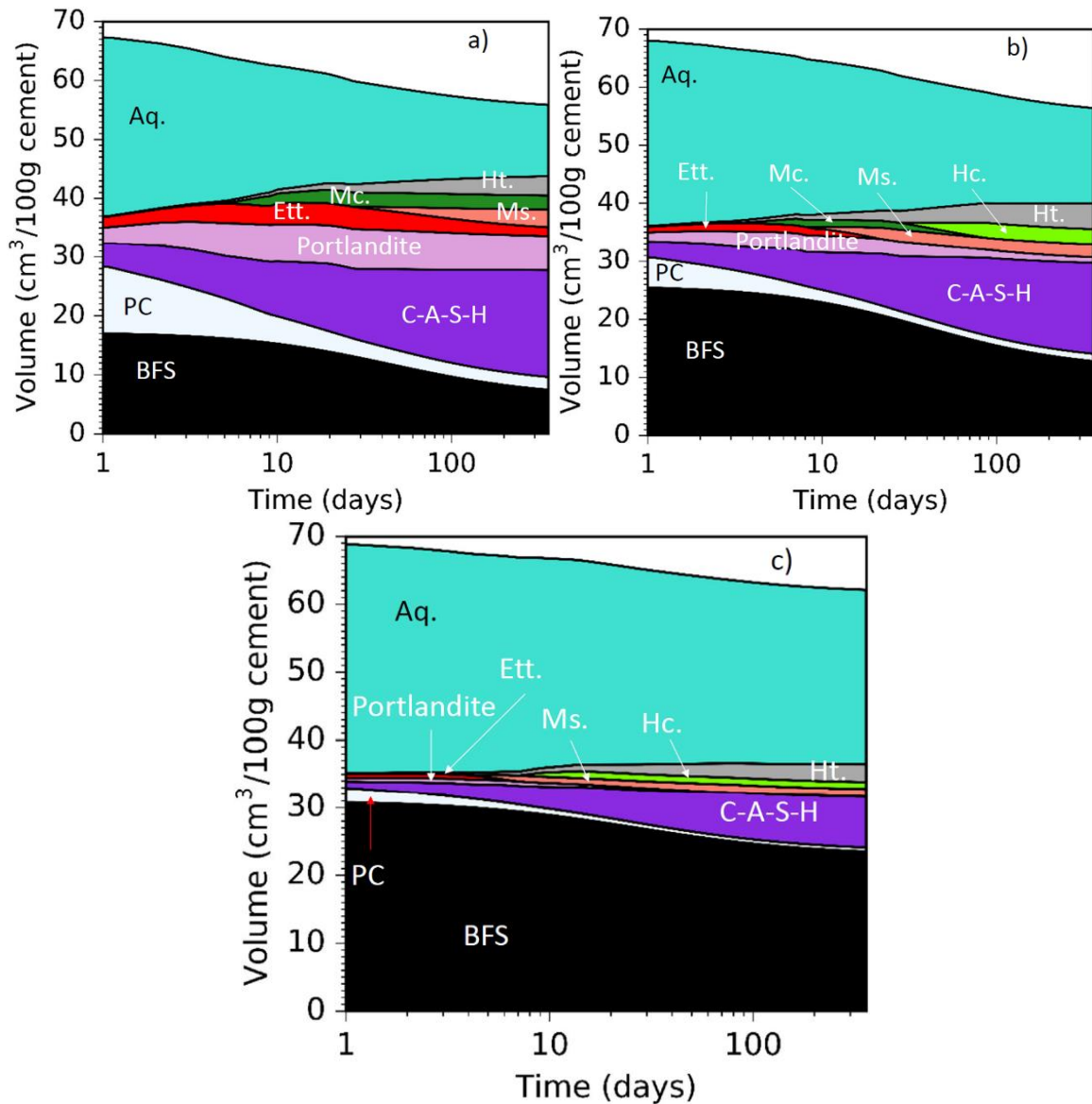


Figure 4.6: Hydrate phase assemblages predicted using thermodynamic modelling, for a) 1:1, b) 3:1 and c) 9:1 grouts reacting at 35°C, based on the experimentally determined (NMR) degree of hydration data up to 360 days.

Hydroxalcalite-group phase formation was predicted to increase with BFS content and degree of hydration of the slag; after 360 days hydroxalcalite comprised as much as 12.6 wt.% of the solid binder constituents in the 9:1 system, respectively. Thus, we identify the peak at $11.6^\circ 2\theta$ in Figure 4.1 as mainly attributed to hydroxalcalite formation. Figure 4.6 displays the reducing amount of monocarbonate forming when lower levels of PC are available in the system to provide calcite. In the 3:1 and 9:1 system, hemicarbonate becomes the dominant carbonate hydrate phase at later ages, rather than monocarbonate, as can be seen in the XRD results. Matschei et al. [95,97] demonstrated

that the lower amount of CO_3^{2-} ions present in the pore solution causes this phase transition from monocarbonate to hemicarbonates.

4.4.2 Comparison of C-A-S-H gel structural characteristics between model and experiment

The use of the high-Ca/Si end-members in the model may be the cause of the under-prediction of portlandite formation in the 9:1 system. The Ca/Si ratio of C-A-S-H in the modelled 9:1 system after 360 days was 1.373 (Table 4.4), which is higher than the 1.03 determined from the NMR spectra here (Table 4.3), but more similar to the value published by Richardson & Groves for a 9:1 cement also based on UK nuclear industry-specification materials, which was 1.29 [44]. There was a better agreement for the 3:1 system as it was closer to the value expected from literature data, Ca/Si between 1.34 – 1.40 [44]. In the 3:1 and 9:1 systems, the Ca/Si ratio decreases as Al/Si increases. As expected, the Ca/Si ratio in the C-A-S-H is highest in the 1:1 formulation but using this model, it was only marginally higher than the 3:1 after 360 days.

Only the 1:1 system shows no alteration of the calculated C-A-S-H molar ratios with time, consistent with the NMR results (Table 4.3 which showed minimal variation). Under-prediction of the Ca/Si in the 1:1 system corresponds to the over-prediction of Al/Si within the C-A-S-H gel. Another limitation is that once the Ca/Si ratio of the C-A-S-H gel reaches 1.4 to 1.5, portlandite formation is more favourable than incorporating more calcium within the C-S-H gel, which limits the Ca/Si ratio to this range.

As a result of the minimum Ca/Si of C-A-S-H formation required before portlandite can be formed, no portlandite was observed in the simulated 9:1 system, despite the fact that portlandite was observed in the X-ray diffractograms up to 360 days. This issue was highlighted in the creation of the CSHQ model whereby once the C-S-H reached a Ca/Si of 1.5, portlandite would begin to form alongside the C-S-H [64].

However, a promising trend in the model results is that with higher levels of slag hydration, the Ca/Si value decreases and the Al/Si value increases, as was seen in the NMR results. Overprediction of the mean chain length (MCL) within the 1:1 grout occurs due to the poor agreement of the Ca/Si and Al/Si values, however the 3:1 and 9:1 systems display better agreement despite the differences between predicted and experimental Ca/Si ratios.

Table 4.4: Summary of structural characteristics of the C-A-S-H gel derived from thermodynamic modelling.

Time (days)	Al/Si			Ca/Si			MCL		
	1:1	3:1	9:1	1:1	3:1	9:1	1:1	3:1	9:1
28	0.137	0.135	0.156	1.424	1.427	1.408	7.234	7.204	7.494
56	0.137	0.136	0.161	1.424	1.430	1.404	7.234	7.206	7.496
90	0.137	0.140	0.161	1.424	1.424	1.403	7.232	7.260	7.576
180	0.137	0.144	0.162	1.424	1.420	1.384	7.232	7.320	7.754
360	0.137	0.144	0.163	1.424	1.419	1.373	7.232	7.320	7.860

4.4.3 Modelling of aged BFS:PC cements

Applicability of this method to samples cured for extended durations than those evaluated in this study is of critical importance when applying this method to long-term storage or disposal of wastes. Here it is the thermodynamic modelling approach described in Section 2.4 is applied for modelling 20 year old BFS:PC samples, whose detailed characterisation was carried out by Taylor et al. [45]. The phase assemblage predictions show good agreement with the identified hydration products forming in the aged cements (Figure 4.7). The dominant phases at later age are hydroxalite and C-A-S-H gel, and the good agreement regarding portlandite content is particularly notable (Table 4.5).

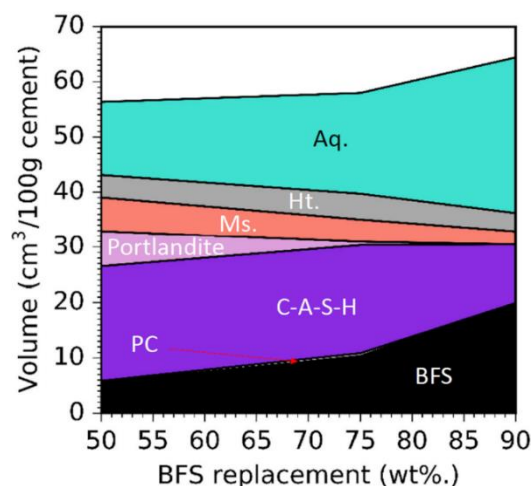


Figure 4.7: Calculated phase assemblage of BFS:PC cements using the degree of hydration and precursor materials reported by Taylor et al. [45].

At advanced curing ages the end-member model used in this study for blended cements was struggling with the same issues as the earlier age samples in section 4.4.2, whereby the C-A-S-H gel required a certain Ca/Si ratio before portlandite could form. This has led to an over-prediction of the Ca/Si ratio of the C-A-S-H gel (Table 4.6) and no predicted portlandite formation in the 9:1 system. There was a greater variation of the Ca/Si ratio in the 9:1 system when compared to the 1:1 and 3:1 systems, due to the much lower amount of calcium available for reaction.

Table 4.5: Portlandite content, as weight percentage of the hydrates formed at varying degrees of slag replacement. Results from 20 year sample are from Taylor et al. [45].

BFS:PC blend ratios	% portlandite in phase assemblage	
	20 year sample	GEMS
1:1	10	14
3:1	3	2
9:1	1	0

Under-prediction of the Al/Si ratio was not as severe as the over-prediction of the Ca/Si ratio. There was a small increase in Al/Si as BFS replacement increased. Based on the geochemical equilibrium calculations that govern the software, the bulk Ca/Si and Al/Si ratios govern the performance of the C-A-S-H end-member model. As similar levels of bulk Al/Si were observed in each system (approx. Al/Si = 0.35), there was little variation in the Al/Si ratio of the C-A-S-H (which is limited in the model by the allowable degree of incorporation of Al into Si sites in the tobermorite structure), however, the Ca/Si ratio was much lower within the 9:1 system which caused the greater variation as a function of age. Following the experimental results, the later age samples had a larger MCL than the earlier age samples modelled. Values from the modelling work were significantly lower than those observed experimentally, however the clear increase of MCL in all grouts when compared to the earlier age samples does indicate reasonable applicability of the model to later age cements.

Table 4.6: Structural characteristics of the C-A-S-H gel of the 20 year old sample (20 y) analysed by Taylor et al. [45] and thermodynamic modelling (GEMS) for these systems.

BFS:PC blend ratios	Al/Si		Ca/Si		MCL	
	20 y	GEMS	20 y	GEMS	20 y	GEMS
1:1	0.14	0.14	1.32	1.43	13.8	8.2
3:1	0.16	0.14	1.31	1.43	16.1	8.2
9:1	0.18	0.15	1.18	1.30	14.3	9.5

4.5 Conclusions

Prediction of cement hydrate phase assemblages using thermodynamic modelling is fundamentally dependent on the availability of a complete and accurate database for all phases present, and this work has demonstrated that this still poses some challenges in the description of BFS-PC blends at high BFS content. Qualitatively, good agreement of the predicted phase assemblage can be observed for the one year cured cement systems between the NMR and XRD results. All the main phases observed experimentally were present in the simulated phase assemblages, and in comparable proportions at each age of curing. This agreement highlights the potential use of using ²⁹Si MAS NMR with careful spectral deconvolution for determination of the degree of hydration for silicon-containing cement constituents.

The calculation of structural characteristics of the C-A-S-H gel using a thermodynamic modelling approach still has limitations, however it is promising that the trend of Ca/Si, Al/Si and MCL follows what is observed from experimental results. The end-member compositions and energetics of the C-A-S-H gel still require refinement, possibly including introduction of alkali containing end-members and/or the incorporation of aluminium into interlayer sites. Improvement of the aqueous solution modelling approach may also be a method of improving the structural accuracy of the solid solution phases within blended cements. Methods such as the specific ion interaction theory (SIT) or Pitzer models may lead to an improved ability to predict the phase assemblages of these complex systems. Introducing these methods will also allow a greater level of accuracy when combining this method for predicting interactions of cements with wastes.

5 Thermodynamic modelling of BFS-PC cements under temperature conditions relevant to the geological disposal of nuclear wastes

5.1 Introduction

Nuclear power has been used as an energy source across Europe for approximately 70 years, and in the United Kingdom alone, approximately 146 520 m³ of radioactive waste has been produced as of 2016 [4]. Of this, 110 000 m³ will require processing and storing in a secure facility. As in many countries, the current policy to manage current and future nuclear waste in England and Wales is to store it within a geological disposal facility (GDF) [22]. This facility would be the heart of a multi-barrier defence system to ensure that nuclear waste is stored safely and away from the biosphere. The GDF will be a subterranean facility, up to 1 km below the ground, with vaults to store intermediate level waste (ILW) and high level waste (HLW). When these vaults are filled to capacity they will be sealed by Nirex Reference Vault Backfill (NRVB) [24,25], a cementitious high-pH engineered material, to further reduce any transport of radionuclides from the vaults.

To date, UK ILW has been encapsulated in blended cements, primarily Portland Cement (PC) blended with blast furnace slag (BFS). BFS-PC cements have desirable properties for treating nuclear fuel cycle wastes [5,11–15,17]:

- The blended cement creates a highly durable, affordable wasteform to store and transport the waste [5];
- High pH of the pore solution (≥ 12) reduces radionuclide solubility [13–15];
- Cementitious hydration products create high surface area and binding sites for the sorption and/or ionic substitution of radionuclides [13,14];
- Blending PC with high volumes of BFS gives a lower heat of hydration at early age, to avoid excessive temperature rises that may be detrimental to stability [17];
- Stability at varying temperature ranges ensures good durability in a changing temperature environment [17].

The required lifespan of a UK GDF remains to be defined, and a location has not yet been selected. However, an approximate temperature profile has been created to enable scientific work to support

a safety case, considering the possible extremes in the conditions to which the cement wasteforms may be exposed (Table 5.1) [8,10,30,31].

Table 5.1: Approximate temperature profile of an ILW waste package due to GDF emplacement and backfilling [8,10,30,31].

	Phase of completion	Timescale (years)	Temperature (maximum - °C)
I	Emplacement	50	30 – 40
II	Care and maintenance	50	30 – 40
III	Short-term backfill	5	80
IV	Long-term backfill	25	50
V	Post-closure of GDF	-	35 – 45

5.2 Effect of temperature on the mineralogy of cements

Changing the temperature of Portland cement alters the mineralogy of the hydrate phases formed [151], including changing the solubility relationships that determine the concentrations of key ions in the pore solution, which define the stability of cement hydrates [150,202,203].

The solubility relationships that drive formation of calcium silicate hydrate, C-S-H, the dominant binding phase in hydrated PC, are not particularly sensitive to changes in temperature within the range of interest here [151,202]. Martinez-Ramirez and Frías [204], and Bahafid et al. [205], showed that the Ca/Si ratio of C-S-H in hydrated Portland cements decreased with increasing temperature, which resulted in a longer mean chain length (MCL) of the C-S-H, and densification. Similar trends are also observed in Al rich C-S-H (C-A-S-H), forming in Portland cements blended with supplementary cementitious materials (SCMs), presenting an increased silicon content driven by an increased extent of the pozzolanic reaction at higher temperatures [188,191,206]. At higher temperatures, increased incorporation of aluminium from solution into bridging sites of the C-A-S-H phase also increases the MCL [167,202], as well as the Al/Si ratio [189,207].

Portlandite formation in hydrated PC is only marginally affected by an increase in temperature [151,202,208]. Escalante-Garcia [40,190] showed that during hydration of BFS-PC blends at elevated temperatures, BFS exhibits a greater acceleration in its reaction kinetics than alite. This increasing slag

hydration reaction results in increased consumption of portlandite and leads to a further reduction in portlandite content in the system [191,206].

It has been well documented that ettringite ($\text{Ca}_3\text{Al}_2\text{O}_6 \cdot 3\text{CaSO}_4 \cdot 32\text{H}_2\text{O}$) becomes unstable above 48 °C in hydrated PC and blended cement systems [120,150,151,203]; above 48 °C, AFm-structured calcium monosulphoaluminate ('monosulphate' - $\text{Ca}_3\text{Al}_2\text{O}_6 \cdot \text{CaSO}_4 \cdot 12\text{H}_2\text{O}$) becomes the dominant sulphoaluminate phase [192,209] up to ~80 °C. Carbonate AFm phases ('monocarbonate' - $\text{Ca}_3\text{Al}_2\text{O}_7 \cdot \text{CaCO}_3 \cdot 11\text{H}_2\text{O}$ and 'hemicarbonates' - $\text{Ca}_3\text{Al}_2\text{O}_6 \cdot 0.5\text{CaCO}_3 \cdot 12\text{H}_2\text{O}$) are also stable up to 40-90 °C [150].

Silica-free hydrogarnet (katoite - $\text{Ca}_3\text{Al}_2(\text{OH})_{12}$) is stable at temperatures above 8 °C, however SO_4^{2-} and CO_3^{2-} tend to destabilise katoite in favour of sulphate or carbonate AFm phases up to 55 °C [120,149,150,210]. Siliceous hydrogarnet ($\text{Ca}_3\text{Al}_2(\text{SiO}_4)_y(\text{OH})_{4(3-y)}$; $0 < y < 3$) has been synthesised at temperatures up to 350 °C [211], and at higher temperatures, more $[\text{SiO}_4]^{4-}$ ions replace the OH^- ions. At lower temperatures (25 – 55 °C), the higher pH in hydrated PC drives the solid solution towards a higher OH^- content, thus reducing the silicon uptake in this phase. When the temperature increases, the pH drops and siliceous hydrogarnet is more stable than katoite or AFm phases [210].

Hydrotalcite-group layered double hydroxide (LDH) type phases ($\text{Mg}_{(1-x)}\text{Al}_x(\text{OH})_{(2+x)} \cdot m\text{H}_2\text{O}$, $0.2 \leq x \leq 0.33$) [103] are prominent in blended or alkali-activated cements due to the high levels of magnesium and aluminium in the precursor materials [37,67,123]; these remain stable throughout the temperature range of interest here (30 – 80 °C).

It is essential to understand how temperature changes in the context of a GDF will affect the hydrate phases in blended cements that encapsulate ILW, to enable reliable prediction of how the waste packages will evolve over the millennia that they will be stored. Therefore, this study considers the influence of temperature changes on cured BFS-PC cements with varying BFS:PC ratios and temperature profiles, to simulate anticipated GDF conditions. It should be noted that no interaction with the backfill material or groundwater is described in this work; the scope of this study relates solely to the performance of the wastefirms themselves. Thermodynamic modelling has been shown to accurately and reliably predict the stability of cement hydrate phases under different conditions

[123,150,151]. Therefore, thermodynamic modelling can predict phase assemblage, and hence enabling to infer how cementitious wasteforms may perform under GDF conditions.

5.3 Experimental methodology

5.3.1 Mix Design

Cementitious grouts with ratios of 1:1, 3:1 and 9:1 BFS:PC (compositions in Table 3.1) were produced with a water to solids (w/s) mass ratio of 0.35, to span the formulation envelope for UK ILW grouts. The precursor materials used were Ribblesdale CEM I 52.5N PC and Port Talbot ground granulated BFS, (BS EN 15167-1 GGBS), supplied by the National Nuclear Laboratory. The oxide compositions of the precursors used are displayed in Table 3.1. Samples were mixed in batches then poured into 50 mL tubes, sealed, and cured in an oven according to the specified temperature regime (see below) until testing.

Table 5.2: Sample reference IDs for the different curing profiles; t is time in days.

Sample name	Curing temperature profile
tA	Samples cured at 35 °C for time, t.
tB	Samples cured at 35 °C for 1 year, then cured at 50 °C for time, t.
tC	Samples cured at 35 °C for 1 year, then cured at 60 °C for time, t.
tD	Samples cured at 35 °C for 1 year, then cured at 80 °C for time, t.
tE	Samples cured at 35 °C for 1 year, then cured at 80 °C for 1 year, and finally cured for 28 days at 50 °C.

After 360 days of curing at 35 °C, the samples were transferred to ovens at either 50 °C, 60 °C or 80 °C. Samples were analysed 1, 3, 7 and 28 days after being transferred to the higher temperature ovens, and also 360 days after being transferred to an oven at 80 °C. Additional samples that had been cured at 35 °C for one year and exposed to 80 °C for another year were then transferred to an oven at 50 °C for 28 days. Samples were also cured at 35 °C for up to 720 days as a reference point. The notation used throughout the manuscript for each temperature profile is summarised in Table 5.2. While the timeframes used in this study do differ from those shown in Table 5.1 for reasons of practicality, this

was deemed the most suitable approach to testing the applicability of thermodynamic modelling to these systems. It was chosen that one year was an acceptable timeframe to represent 50 years because the phases formed show little variation between 1 and 20 years as was shown by Richardson and Groves [44] and Taylor et. al [45]. Therefore, it was assumed that minimal phase changes would occur between 1 and 50 years.

5.3.2 Analytical techniques

Upon reaching the specified testing exposure time, hardened specimens were crushed and ground using acetone as a lubricant, to a particle size below 63 μm . The powders were then submerged in acetone for 15 minutes and vacuum filtered, to ensure that hydration had ceased [160].

Analysis of mineralogy was performed using powder X-ray diffraction (XRD) on a Bruker D2 Phaser instrument with Cu K α radiation (1.54 \AA) and a nickel filter. Scans were conducted with a step size of 0.020°, for 2 seconds per step, with front-loading sample holders. The Inorganic Crystal Structure Database (ICSD) and the Powder Diffraction File (PDF) were used in phase identification.

Scanning electron microscopy (SEM) was performed using a Hitachi TM 3030 instrument with a 20 kV accelerating voltage, a working distance of 8 mm and a backscatter detector. Samples were cut and polished using non-aqueous lubricants immediately prior to analysis. An evenly distributed selection of points across a representative 400 μm \times 400 μm section of the sample was analysed using a Bruker Quantax 70 X-ray energy dispersive spectroscopy (EDS) detector to determine chemical compositions.

Comparison of the EDS data with the XRF results for the BFS was performed to provide an external calibration for the EDS results on the basis of molar elemental ratios (Table 5.3). The EDS data analysis was conducted using 20 points from each of 5 identifiable slag grains that were embedded in the grout matrix of the 9:1 system that had been hydrated for 360 days at 35 °C; the points selected were for areas which had clearly not undergone any hydration.

A slight difference between some of the molar ratios was observed when comparing the EDS and XRF results, particularly the ratios containing calcium and magnesium. As the EDS was conducted on a benchtop SEM instrument, its precision is expected to be challenged by the differences in interaction

volume in elemental analysis for lower vs. higher atomic number elements [212], and the difficulty in mapping of oxygen [183,213]. Using a linear regression solver, correction factors for the measured EDS intensities of silicon, aluminium, calcium and magnesium were created to best match the EDS molar ratios to the XRF results, Table 5.4. These correction factors were applied to calibrate the point analysis data obtained for the hydrated samples.

Table 5.3: Comparison of the molar ratios of the BFS, obtained from XRF and SEM-EDS data, and the corrected values obtained by calibration of the EDS data using information from XRF.

	Ca/Si	Si/Ca	Al/Si	Al/Ca	Ca/Al	Mg/Si	Mg/Al	Mg/Ca
XRF	1.20	0.85	0.45	0.38	2.63	0.42	0.94	0.36
Original EDS ($\mu\pm\sigma$)	1.32(0.13)	0.76(0.10)	0.45(0.05)	0.34(0.06)	2.90(0.46)	0.40(0.04)	0.90(0.10)	0.31(0.05)
Post-corrections	1.20	0.84	0.44	0.38	2.66	0.41	0.93	0.35

Table 5.4: Elemental correction factors used to correct the SEM-EDS analysis.

Silicon	Aluminium	Calcium	Magnesium	Sulphur
0.97	0.96	0.88	1.00	1.00

Degree of hydration values for the Portland clinker and BFS in each blend after 360 days at 35 °C were taken from Chapter 4. For samples that were cured for longer durations, the degree of hydration of slag was determined using the same selective dissolution technique as described in [122].

Thermodynamic modelling was performed using GEM-Selektor v3 (GEMS) [132,180] using the CEMDATA14 database which is an updated version of CEMDATA07 [151]. Activity coefficients for aqueous species were determined using the Truesdell-Jones extension to the Debye-Hückel equation [134]:

$$\log_{10}\gamma_i = \frac{-A_\gamma z_i^2 \sqrt{I}}{1 + aB_\gamma \sqrt{I}} + b_\gamma I + \log_{10} \frac{X_{jw}}{X_w} \quad 5.1$$

Here, γ_i and z_i are the activity coefficient and charge of the i^{th} aqueous species respectively, A_γ and B_γ are temperature and pressure dependent coefficients, I is the molal ionic strength, X_{jw} is the molar quantity of water, and X_w is the total molar amount of the aqueous phase. A common ion size

parameter, \dot{a} (3.67 Å) and short-range interaction parameter, b_γ (0.123 kg/mol), were used, treating KOH as the background electrolyte [104,134].

Alkali distribution ratios for Na₂O and K₂O of 2 and 1.2 [59,85,118], respectively, were used for C-A-S-H phase for both modelling approaches, as was performed in Chapter 4.

Mineral phases within CEMDATA14 are recorded at standard conditions (298 K and 1 atm), therefore temperature corrections for the Gibbs energy of formation, ΔG_T , of these minerals are required to extrapolate to the temperatures of interest, T . Integration of the heat capacity function (Eq. 5.2) is used in GEMS [120,151,203]:

$$\begin{aligned} \Delta_a G_{T_0}^0 &= \Delta_f G_{T_0}^0 - S_{T_0}^0 (T - T_0) - \int_{T_0}^T \int_{T_0}^T \frac{C_p^0}{T} dT dT & \text{5.2} \\ &= \Delta_f G_{T_0}^0 - S_{T_0}^0 (T - T_0) - a_0 \left(T \ln \frac{T}{T_0} - T + T_0 \right) - a_1 (T - T_0)^2 \\ &\quad - a_2 \frac{(T - T_0)}{2T \cdot T_0^2} - a_3 \frac{(\sqrt{T} - \sqrt{T_0})^2}{\sqrt{T_0}} \end{aligned}$$

Where $\Delta_f G_{T_0}^0$ is the standard Gibbs energy of formation, $S_{T_0}^0$ is the standard absolute entropy at $T_0 = 298$ K, and C_p^0 is the standard heat capacity. where a_0 , a_1 , a_2 , and a_3 are the empirical coefficients of the heat capacity equation $C_p^0 = a_0 + a_1 T + a_2 T^{-2} + a_3 T^{-0.5}$. The apparent Gibbs free energy of formation, $\Delta_a G_{T_0}^0$, refers to the free energies of the elements.

5.4 Experimental Results and Discussion

5.4.1 Degree of hydration of BFS

In all blends, BFS hydration increased slightly when transferring a sample that had been cured at 35 °C for a year to a higher curing temperature for an additional 28 days (Figure 5.1), consistent with previously reported data showing that BFS hydration in BFS-PC cements increases at higher temperature [40,214]. However, the maximum increase in hydration degree was 2.2%, as the majority of the anhydrous material had already reacted during the first year of curing at 35°C, and variations of the calculated values lie within the experimental errors. A lack of pore space due to the initially low

w/s used for producing the assessed cements (w/s 0.35) may also have restricted the further hydration after one year of curing. For curing regimes 360D and 28E, each blend showed an increase of no more than 2% in BFS hydration degree beyond the degree reached for a given condition (i.e. the 80 °C point in Figure 5.1).

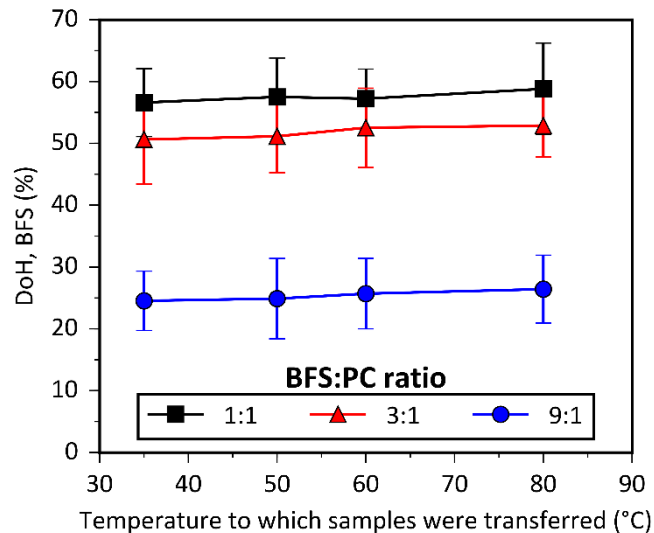
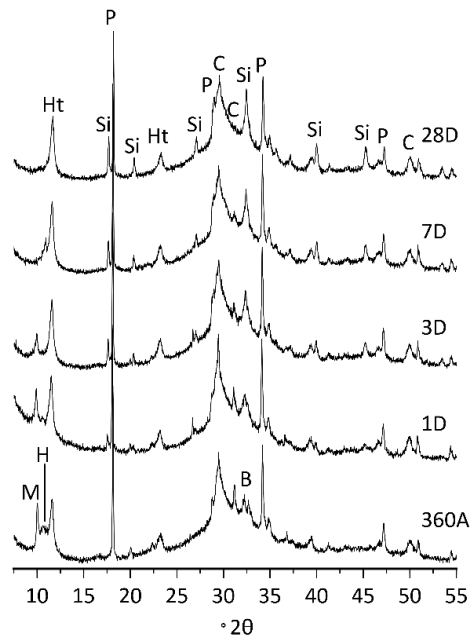
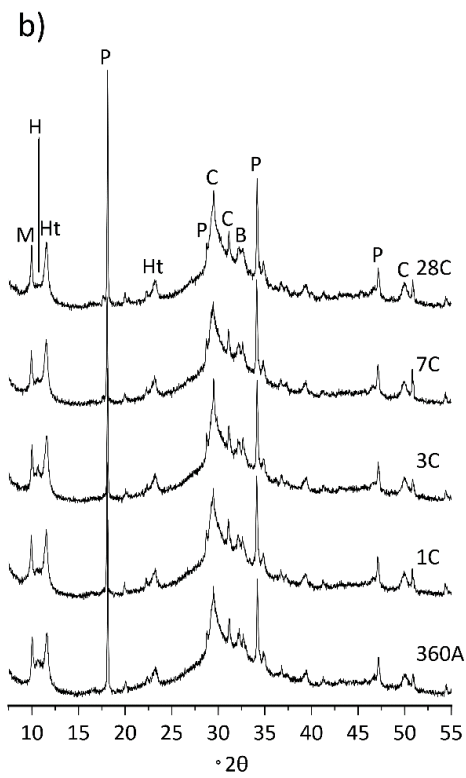
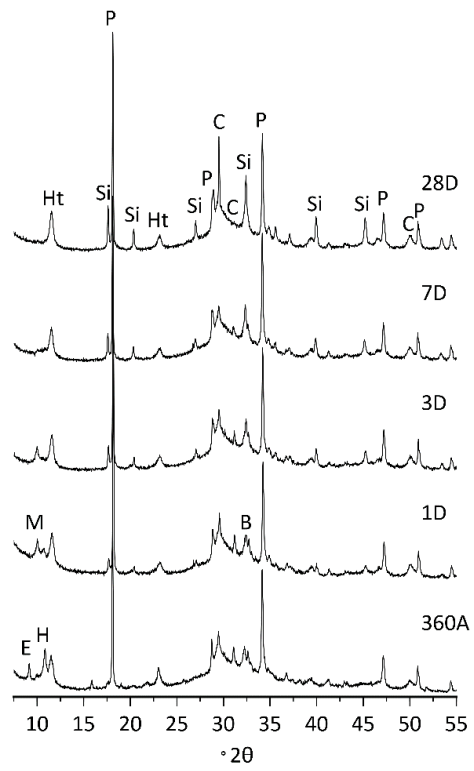
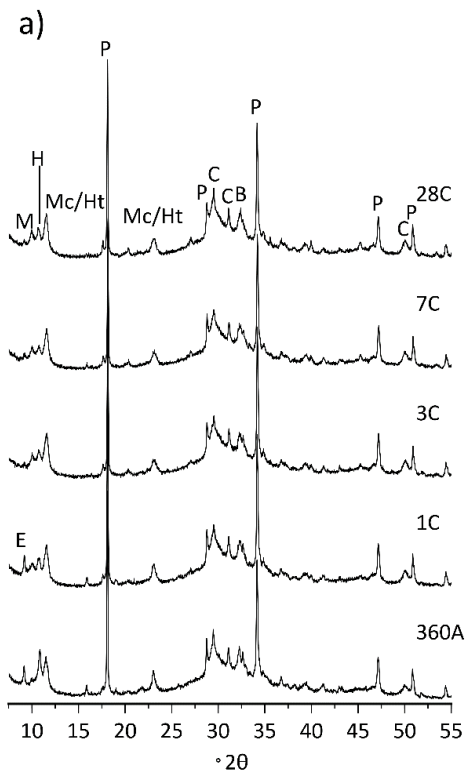


Figure 5.1: Degree of hydration (DoH) of BFS determined from EDTA selective dissolution, within BFS-PC blended cements of ratio 1:1, 3:1 and 9:1, for the temperature profiles 360A, 28B, 28C and 28D.

5.4.2 X-ray diffraction and qualitative analysis

5.4.2.1 Effect of curing temperatures at 60 and 80 °C

The powder diffraction patterns for the cement pastes cured with temperature profiles 1 to 28C and 1 to 28D (i.e. pastes transferred to 60 or 80 °C after a year at 35 °C), with 360A as a reference point, are presented in Figure 5.2. All pastes show some residual belite peaks; there are also minor contributions from alite and ferrite clinker components (see section 4.1), although these are too small to mark on Figure 5.2.



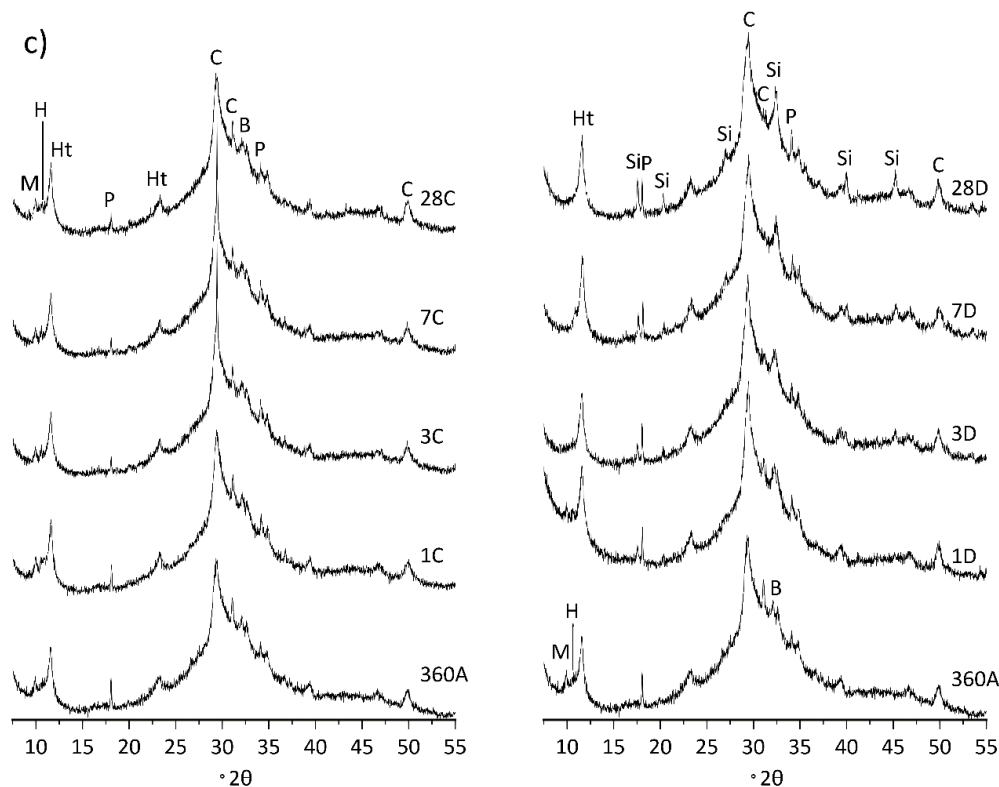


Figure 5.2: XRD patterns of a) 1:1, b) 3:1 and c) 9:1 BFS-PC samples cured at 35 °C for 1 year (360A) and then at either 60 °C (tC) or 80 °C (tD) for a further 28 days. Phases identified are: C – C-A-S-H, P – portlandite, E – ettringite, M – monosulphate, H – hemicarbonate, Mc – monocarbonate, Ht – hydrotalcite, B – belite, and Si – siliceous hydrogarnet.

The three formulations showed minimal loss or alteration of portlandite (ICSD #15471), or C-A-S-H formation, when exposed to higher temperatures for 28 days after initial curing at 35°C for one year. In the 3:1 and 9:1 cements after 1 and 3 days at both 60 and 80 °C, the peak at 29.4° 2θ attributed to a C-A-S-H type phase resembling Al-substituted tobermorite (PDF #34-0002) becomes sharper as the sudden elevation in temperature causes a spike in crystallinity of the C-A-S-H phase. After 28 days of curing at high temperature the reflection broaden and the sharpness become less prominent, which is attributed to lengthening of the aluminosilicate chains with silicate polymerization at elevated temperature [215,216], inducing some structural disorder.

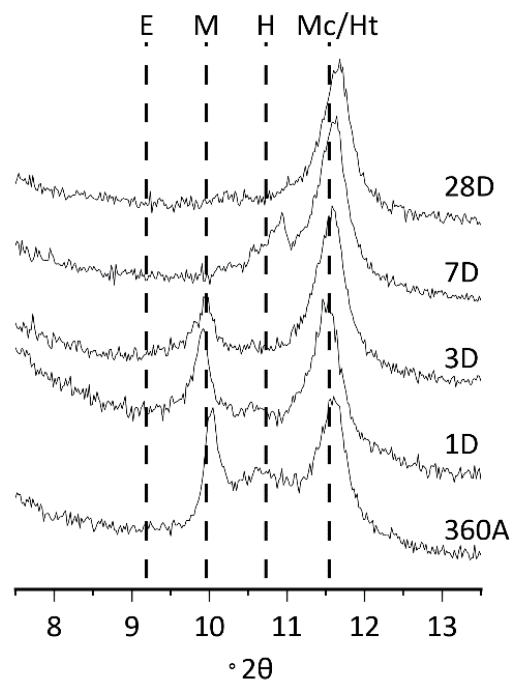
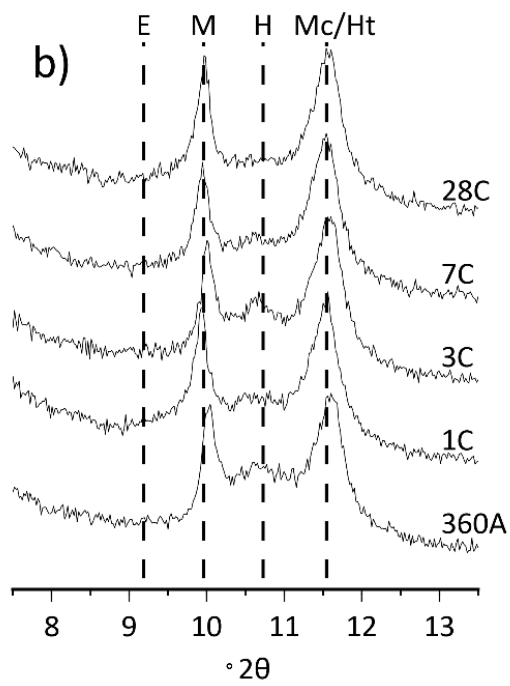
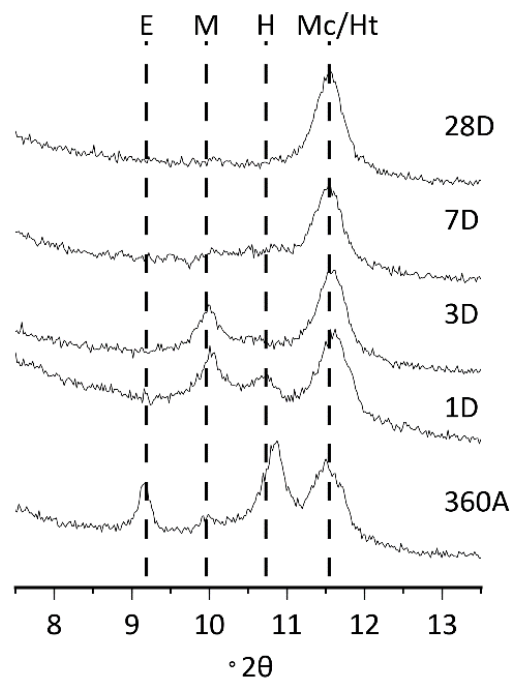
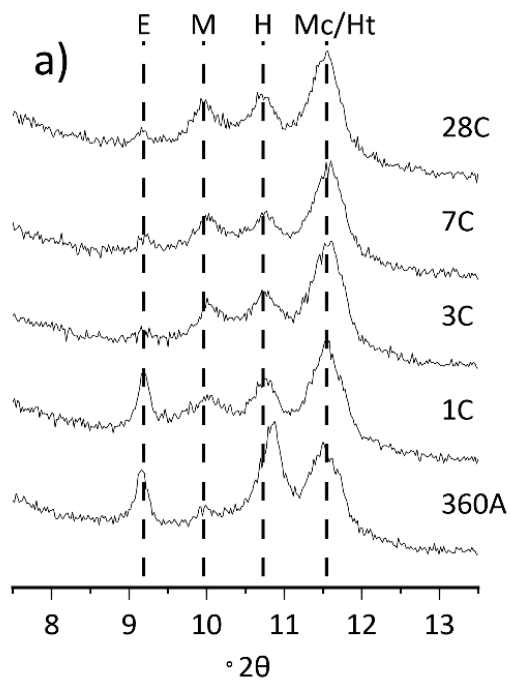
The impact of temperature on the sulphate and carbonate AFm and AFt type phases can be observed in Figure 5.3. Ettringite (ICSD #16045) was only observed in the 1:1 cement after 360 days at 35 °C. After 3 days at 60 °C, the majority of the ettringite reflection peak was depleted, indicating that

ettringite had been destabilised at higher temperature. This depletion was completed within 1 day at 80 °C. At both of these temperatures, the resulting release of sulphate into the pore solution led to the formation of monosulphate (ICSD #100138).

The monosulphate peak intensity increased continuously with time in the samples transferred to 60 °C because of the decomposition of ettringite; this also occurs in the 80 °C samples up until 3 days. However, after 7 days at 80 °C, monosulphate can no longer be observed in the 1:1, 3:1 or 9:1 cements, although it persists at a curing temperature of 60 °C in the 1:1, 3:1 and 9:1 cements after 28 days.

Depletion of the hemicarboxylate (PDF #00-036-0129) reflection intensity at 60 °C was observed in the 1:1 and 3:1 systems after 28 days at elevated temperature. This is attributed to depletion of OH⁻ ions corresponding to the known phenomenon of a pH drop at increased temperature [203]. There is some overlap of the main reflection peaks assigned to monocarbonate (approx. 11.7° 2θ, PDF #00-036-0377) and the broader peak attributed to hydrotalcite-like LDH phase (11.2 – 11.6° 2θ, PDF #00-014-0525), making it difficult to differentiate between these two phases [187]. Similarly to the sulphate-containing AFm phases, after 28 days at 80 °C, hemicarboxylate peaks were no longer observable, and the remaining peak at 11.6° 2θ was most likely to represent hydrotalcite-like LDH. The significantly lower solubility of magnesium and aluminium [109] from the hydrotalcite-like LDH caused this phase to persist at higher temperatures. The peak at 11.6° 2θ may be attributed to monocarbonate, however due to the low content of carbonate in the system, this phase was unlikely to persist at this temperature.

In general, hydrates containing higher contents of water became destabilised by the increase of temperature more rapidly than those with lower water content. This is evident through the persistence of the portlandite (2 moles of water per formula unit), C-A-S-H phase (2 – 4 moles of water), and the formation of siliceous hydrogarnet (3 – 6 moles of water) at 80 °C. The exception to this trend was hydrotalcite-like LDH (10 - 14 moles of water), as this phase is more stable against dissolution as mentioned above, and there are not obvious less-hydrated magnesium aluminates to which it could be converted in this temperature range.



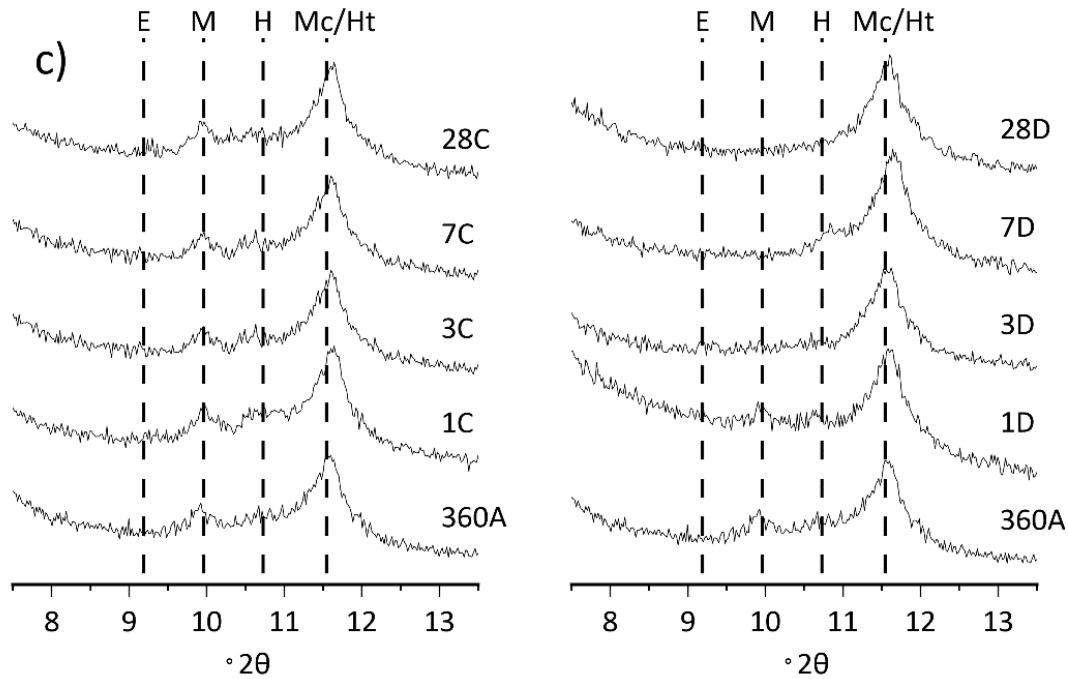


Figure 5.3: Highlighted low-angle regions of the XRD patterns of a) 1:1, b) 3:1 and c) 9:1 BFS-PC samples cured at 35 °C for 1 year and then at either 60 °C (C) or 80 °C (D) for up to 28 days. Phases identified are: E – ettringite, M – monosulphate, H – hemihydrate, Mc – monocarbonate, and Ht – hydroxycarbonate

5.4.2.2 Siliceous hydrogarnet ($\text{Ca}_3\text{Al}_2(\text{SiO}_4)_{3-y}(\text{OH})_{4y}$) formation at 80 °C

Within the CEMDATA14 database used in GEMS, there are two forms of siliceous hydrogarnet: $\text{C}_3\text{AS}_{0.41}\text{H}_{5.18}$ and $\text{C}_3\text{AS}_{0.84}\text{H}_{4.30}$. Understanding which phase to use in this instance was based upon the method of Dilnesa et al. [149], and Okoronkwo and Glasser [210]. The silicon content of the cubic siliceous hydrogarnet structure was determined using the lattice parameter a , obtained from XRD analysis and interpolating between grossular (C_3AS_3) and katoite (C_3AH_6) on a linear scale; Kyritsis et al. [211] and Rivas et al. [217] have shown experimentally that this method is effective, and highlighted the miscibility gap between $\text{C}_3\text{AS}_{0.41}\text{H}_{5.18}$ and $\text{C}_3\text{AS}_{0.84}\text{H}_{4.30}$. The lattice parameter values for $\text{C}_3\text{AS}_{0.41}\text{H}_{5.18}$ and $\text{C}_3\text{AS}_{0.84}\text{H}_{4.30}$ are 12.480 and 12.376 Å, respectively, and these were used to determine which form of siliceous hydrogarnet was most similar to the phase formed at 80 °C in the cements used in this study.

From Figure 5.4 it is evident that the higher-Si siliceous hydrogarnet phase ($\text{C}_3\text{AS}_{0.84}\text{H}_{4.30}$) was more representative of the phase observed in the XRD data obtained for the BFS-PC cements assessed in

this study. The lattice parameter a of siliceous hydrogarnet determined using the samples cured at 35 °C for 360 days then at 80 °C for a further 360 days (360D) was 12.355 Å for the 1:1 blend, and 12.324 Å for the 3:1 and 9:1 blends as displayed in Figure 5.5. These values equated to a silicon content of 0.92 mol in the 1:1, and 1.05 mol in the 3:1 and 9:1 cements, Figure 5.5. The bulk Ca/Si ratio in the 1:1 cement was higher than in the 3:1 and 9:1 cements due to the lower slag replacement, which gave a lower level of silicon replacement within the siliceous hydrogarnet structure. Therefore, when utilising GEMS for the higher temperatures, the higher silicon content phase ($C_3AS_{0.84}H_{4.30}$) was used to represent siliceous hydrogarnet, as this was the phase within the database that gave the closest correspondence to the experimental results. The additional silicon content observed in the BFS-PC cements evaluated can be attributed to the high availability of silicon and the moderate pH of these cements, which favours incorporation of silicate over hydroxide in the hydrogarnet structure.

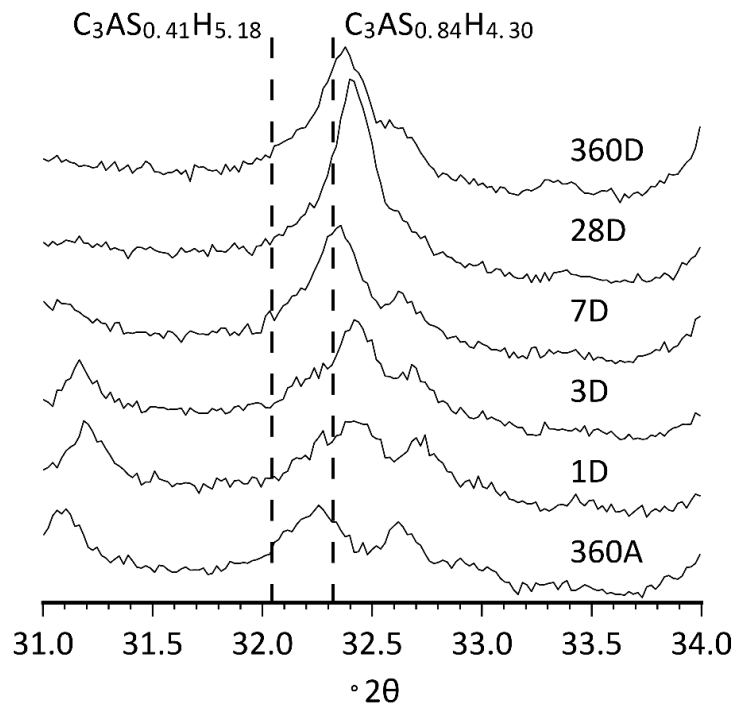


Figure 5.4: XRD patterns for 1:1 BFS:PC cements after curing at 35 °C for one year and being transferred to 80 °C for up to 360 days (temperature profile D). The $C_3AS_{0.41}H_{5.18}$ and $C_3AS_{0.84}H_{4.30}$ chemical formulae depict the siliceous hydrogarnet phases available in the CEMDATA14 database.

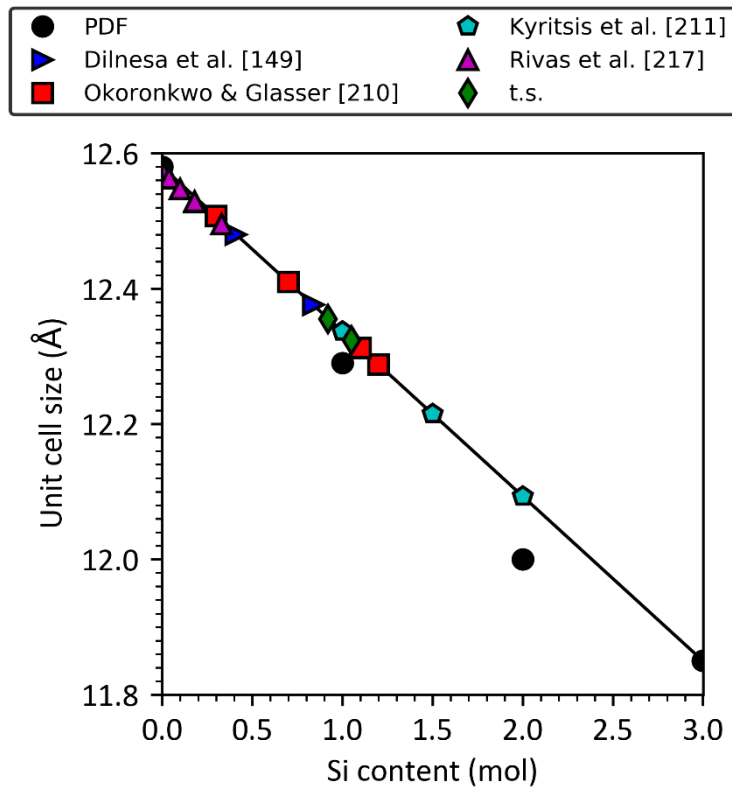


Figure 5.5: Unit cell size plot as a function of Si-hydrogarnet: PDF data used include card numbers 24–0217 ($a = 12.57$ for C_3AH_6); 32–0151 ($a = 12.29$ for C_3ASH_4); 31–0250 ($a = 12.00$ for $C_3AS_2H_2$) and 33–0260 ($a = 11.846$ for C_3AS_3). References include: [149,210,211,217] and t.s. = this study.

5.4.3 Determination of chemical composition of the C(A)-S-H phase by SEM

The composition of the C-A-S-H phase was determined by SEM-EDS point analysis, which was conducted manually by choosing 200 points focusing on C-A-S-H regions by selecting points on the darker rims around anhydrous grains and the light grey areas found in the cement matrix. Due to the nature of cement hydration, these areas are intermixed with other hydrate phases. Elemental ratio plots were used similarly to previous studies [183,188,213,218] to determine the least intermixed regions containing C-A-S-H phases, and quantification of the elemental ratios was calibrated as described in section 2.2 using the XRF and EDS data for anhydrous BFS grains. In a plot of Al/Ca vs. Si/Ca, the high Si/Ca (0.6 – 1.0) cluster of points represents the composition of the C-A-S-H phase, is summarised by the molar ratio comparisons in Table 5.5. Durdzinski et al. [183] and Rossen et al. [213] used a statistical approach to determine the area of least intermixing. A point two standard deviations above the mean ($\mu + 2\sigma$) of the distribution of Si/Ca values was deemed to best represent the point

of least intermixing; this is larger than 95% of values assuming a normal distribution and is therefore considered one of the highest Si/Ca values which can best describe pure C-A-S-H phases. The mean Al/Ca value is used to define the molar content of aluminium within C-A-S-H phases [183,213]. Dividing the Al/Ca by the Si/Ca value, it was possible to obtain the Al/Si value of the C-A-S-H phases.

Table 5.5: Molar ratios of common cement phases (precursors and hydrates) which may affect the chemical composition measurements.

Phase	Chemical formula	Al/Ca	Si/Ca	S/Ca	Mg/Al	Al/Si	Ca/Si
Alite	C ₃ S	-	0.33	-	-	-	3.00
Belite	C ₂ S	-	0.50	-	-	-	2.00
BFS	-	0.38	0.85	-	0.90	0.45	1.20
Siliceous-Hydrogarnet (Si molar ratio = 1.0)	C ₃ ASH ₄	0.67	0.33	-	-	2.00	3.00
Siliceous-Hydrogarnet (Si molar ratio = 0.84)	C ₃ AS _{0.84} H _{4.3}	0.67	0.28	-	-	2.38	3.57
Katoite	C ₃ AH ₆	0.67	0.00	-	-	-	-
C-A-S-H (Ca/Si = 1.2, Al/Si = 0.1)	C _{1.2} A _{0.1} SH	0.17	0.83	-	-	0.20	1.20
C-A-S-H (Ca/Si = 1.4, Al/Si = 0.075)	C _{1.4} A _{0.075} SH	0.11	0.71	-	-	0.15	1.40
C-A-S-H (Ca/Si = 1.6, Al/Si = 0.05)	C _{1.6} A _{0.05} SH	0.06	0.63	-	-	0.10	1.60
Ettringite (AFt)	C ₆ A ₃ H ₃₂	0.33	-	0.50	-	-	-
Monosulphate (AFm)	C ₄ A ₅ H ₁₂	0.50	-	0.25	-	-	-

An example of the analysis of the 1:1, 3:1 and 9:1 BFS:PC formulations after 360 days of curing at 35 °C can be seen in Figure 5.6 and Figure 5.7. The histogram plots shown in Figure 5.6 show the Si/Ca and Al/Ca values obtained from the EDS measurement of the 1:1 BFS-PC blend, which appear to be well described by a normal distribution. Most of the data points fall outside of the C-A-S-H phase region, shown in Figure 5.7; this is expected for these blended cement systems because of the intimate intermixing of hydrate species on a length scale finer than the EDS analysis spot size. However, there is clear evidence that the monosulphate and ettringite phases are heavily intermixed and varied within the sample, since not many of the points follow a distinct tie line to the other phases. Ettringite, monosulphate, hemicarbonate and monocarbonate may all shift the spread of data points to higher Al/Ca values, as summarised in Table 5.5.

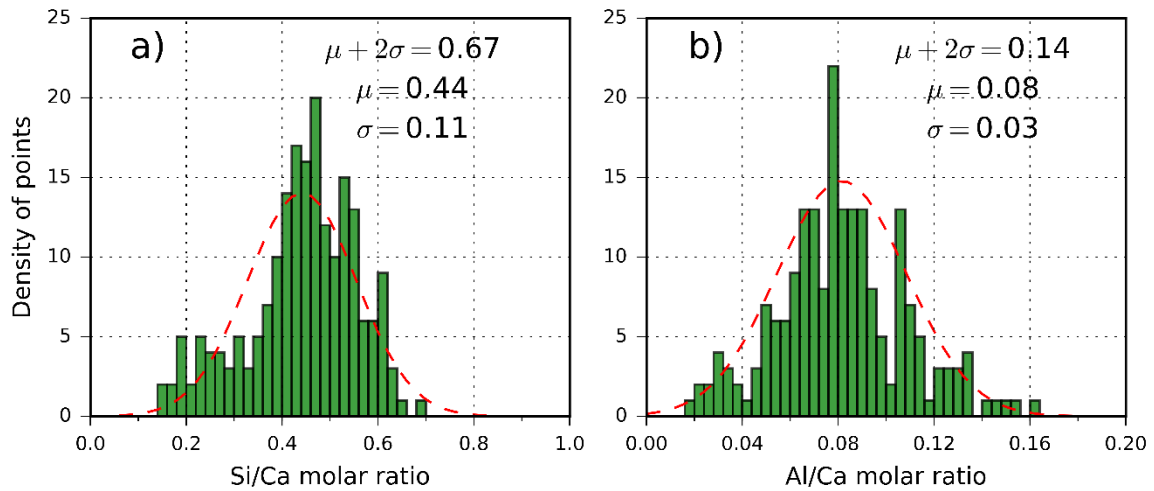


Figure 5.6: Histograms of the molar ratios of spot analyses of the 1:1 BFS-PC cement cured at 35 °C for 360 days, showing a) Si/Ca and b) Al/Ca molar ratios determined from calibrated SEM-EDS analysis.

This approach can also be applied to the 80 °C samples, although the siliceous hydrogarnet also contains silicon and will consequently influence the Si/Ca values observed. The maximum Si/Ca value the siliceous hydrogarnet may exhibit, based on the lattice parameter data, is 0.35. Figure 5.8 highlights the impact of siliceous hydrogarnet on the 3:1 cement at 35, 50, 60 and 80 °C. There was clear evidence of siliceous hydrogarnet EDS data points at 80 °C.

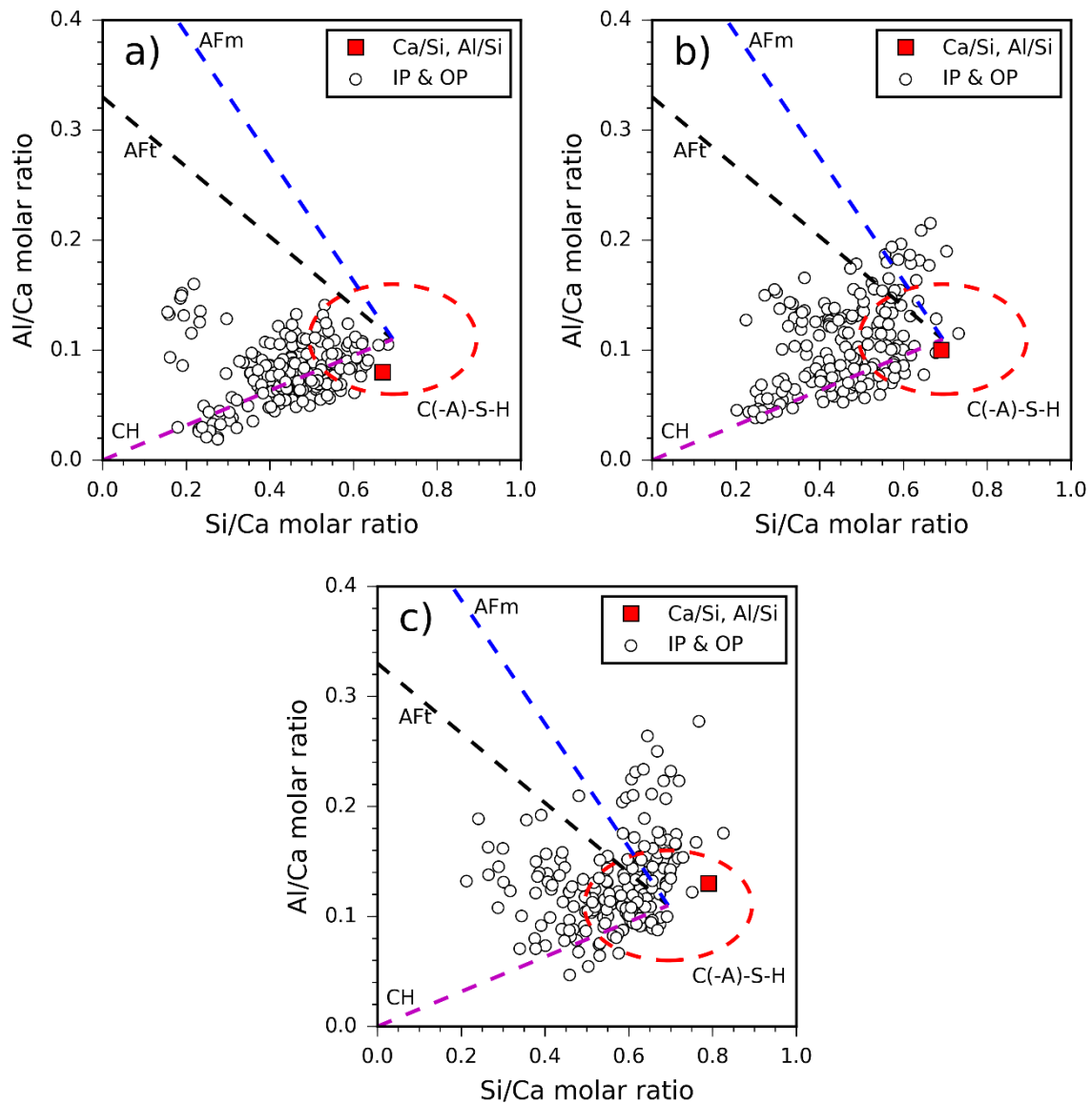


Figure 5.7: Al/Ca versus Si/Ca graph of the a) 1:1 b) 3:1 and c) 9:1 BFS-PC cement cured at 35 °C for 360 days. The dashed oval highlights the region where a C-A-S-H phase with Ca/Si \sim 1.0 – 1.6 and Al/Si \sim 0.1 – 0.2 would appear. The tie lines leading from the centre of the circle lead to the other prominent cement hydrates which may intermix with C-A-S-H (AFt – ettringite, AFm – monosulphate, CH – portlandite). The red square denotes the statistically determined Ca/Si and Al/Si ratio for the individual formulations.

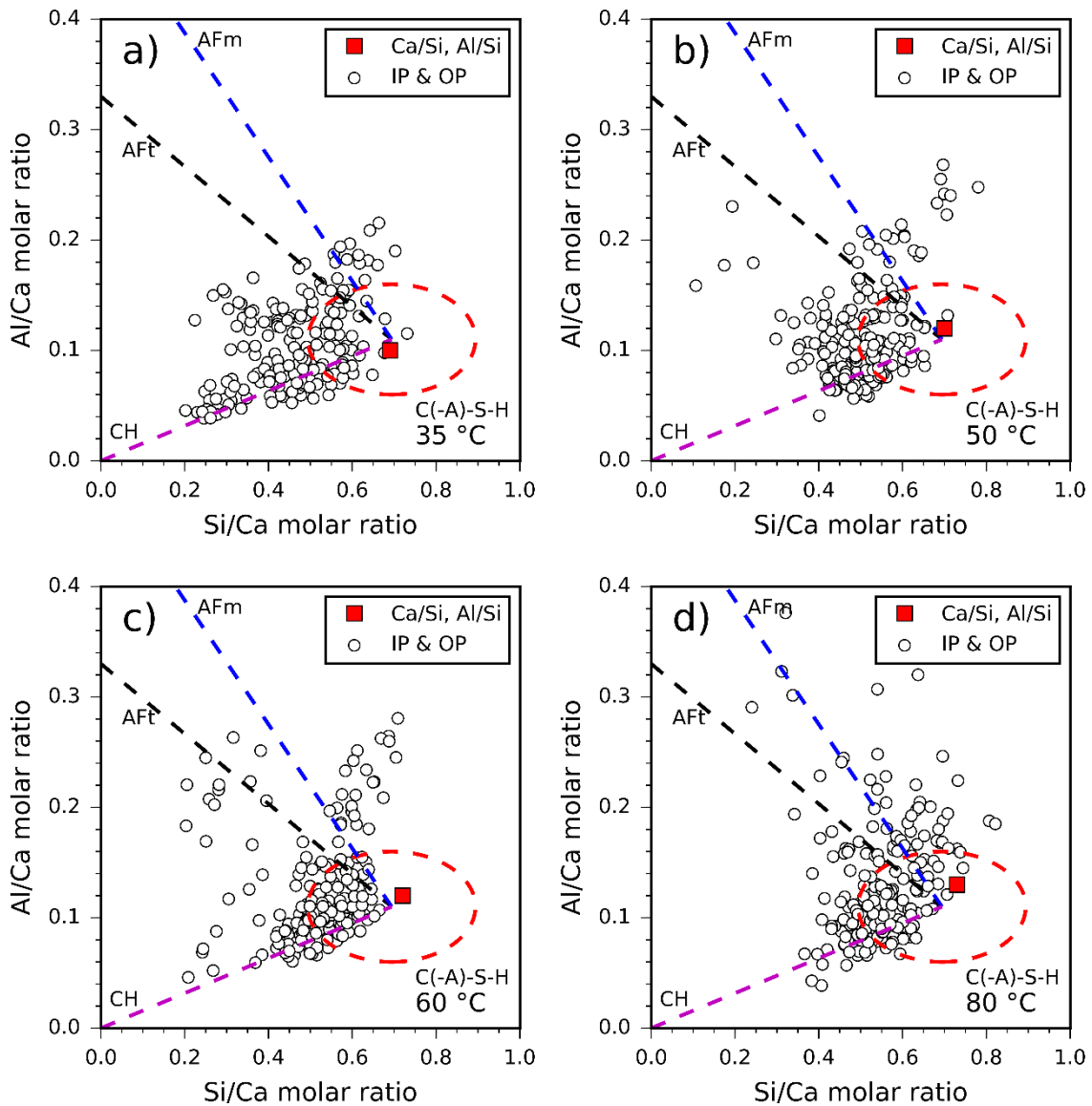


Figure 5.8: Al/Ca versus Si/Ca graphs for the 3:1 BFS-PC cement cured at 35 °C for 360 days and then exposed to (a) 35 °C, (b) 50 °C, (c) 60 °C and (d) 80 °C for a further 28 days. The dashed oval highlights the region where a C-A-S-H phase with Ca/Si 1.0 – 1.6 and Al/Si 0.1 – 0.2 would appear. The tie lines leading from the centre of the circle lead to the other prominent cement hydrates which may intermix with C-A-S-H (AFt – ettringite, AFm – monosulphate and CH – portlandite). The red square denotes the statistically determined Ca/Si and Al/Si ratio for the individual formulations.

The back scattered electron (BSE) images in Figure 5.9a-d highlight the variation of the morphology of the 3:1 BFS-PC cement cured at different temperatures. Region 1 in Figure 5.9a represents a fully hydrated BFS particle and the inner-product C-A-S-H phase (intermixed with hydroxalite-group LDH)

in close proximity to the slag grain. Region 2 in Figure 5.9b highlights the more porous structure of the outer-product C-A-S-H phase which forms within the initially fluid-filled space of the cement matrix. These regions appeared denser at higher temperatures, specifically highlighted in the 80 °C sample in region 3. Region 3 appears from its angular shape to have been a slag grain similar to region 1, but which has almost fully dissolved. Other hydrated and partially hydrated slag grains are observed in regions 4 and 5, respectively.

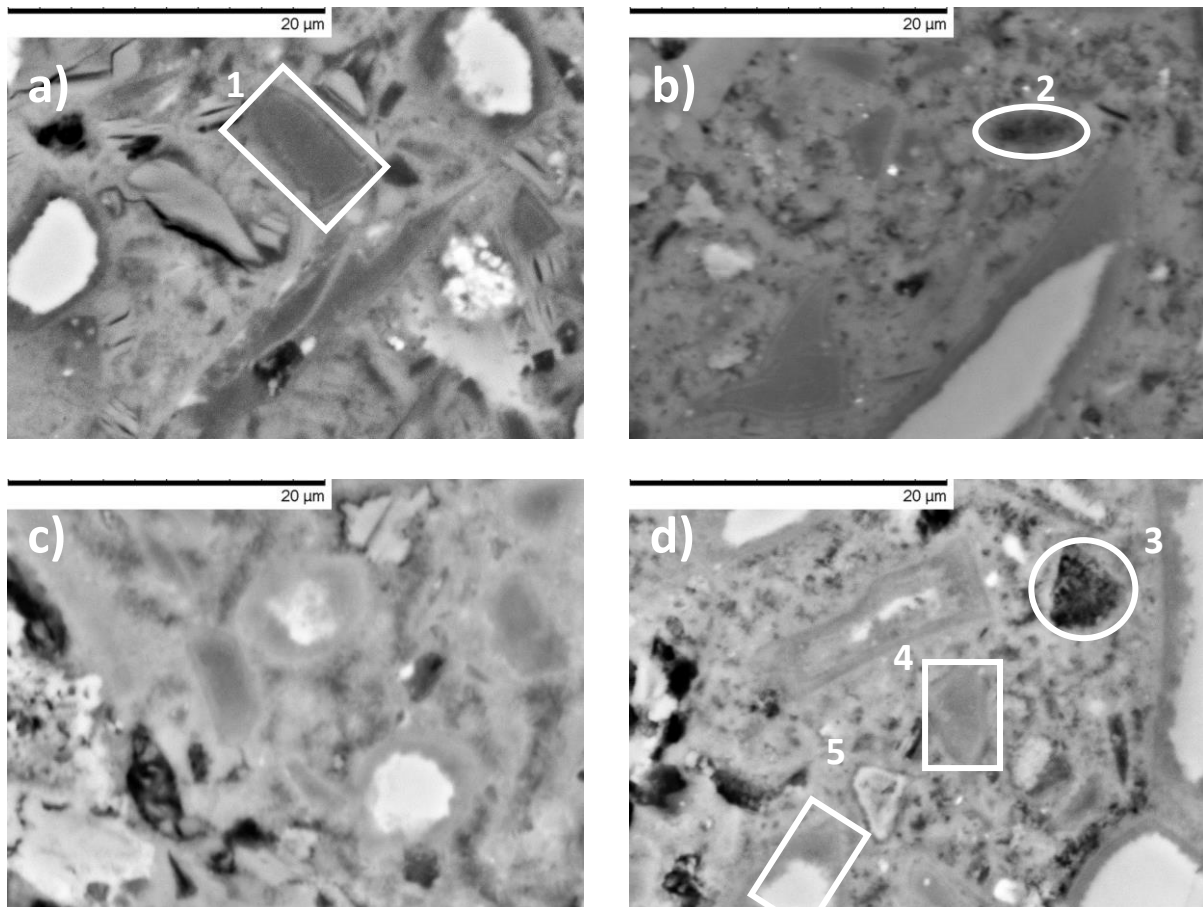


Figure 5.9: BSE-SEM images of 3:1 BFS-PC cement cured at a) 35 °C for 360 days and then exposed to b) 50 °C, c) 60 °C, and d) 80 °C for a further 28 days.

A decrease in Ca/Si and increase of Al/Si ratio (Table A8.2 in the Appendix) at higher temperature was observed across the three formulations. Condensation reactions of the monomeric and dimeric silicates may lead to an expulsion of calcium ions and water from the C-A-S-H phase, leading to higher polymerisation of the gel at increasing temperatures [216], consistent with this observation. The Ca/Si decrease was greatest in the 1:1 BFS-PC blend, with the ratio decreasing by as much as 0.1 units from 35 °C to 80 °C. The Ca/Si decrease may be more prominent in the 1:1 formulation because there was

more available Ca to be redistributed upon a change in temperature. This may be the cause of the greater variation in the Ca/Si observed in the work of Bahafid et al. [205] compared with the work of Burciaga-Diaz et al. [219]: Bahafid et al. considered a high Ca/Si class G cement and observed a drop in Ca/Si by 0.2 between 25 and 90 °C, whereas Burciaga-Diaz et al. studied alkali-activated slag cement systems (with much less Ca than class G cement) at 20 and 60 °C in which there was no clear overall change in the Ca/Si or Al/Si values.

An increasing abundance of silicate chain sites becoming available as a result of the condensation of calcium silicate species provided an opportunity for aqueous aluminium species to bridge gaps in the silicate chain. The additional opportunity for bridging in the aluminosilicate chains may be the cause for the increase of the Al/Si in all three formulations. The 1:1 formulation displayed the greatest rise in Al/Si ratio, increasing by 0.04 units. The 9:1 formulation exhibited the largest Al/Si values, at Al/Si reaching 0.19.

5.4.4 Chemical composition of hydrotalcite-like phase using SEM-EDS

The hydrotalcite-like phase was a major hydration product that persisted at the elevated temperatures. The hydrotalcite-like LDH formed, became intermixed with the other hydration products, specifically C-A-S-H because of the dependence on phase formation through slag dissolution [213,218]. Therefore, the points taken for the C-A-S-H analysis were also used in determining the Mg/Al molar ratio within hydrotalcite-like LDH.

In blended cement systems the structure of hydrotalcite-like LDH has been shown to be heavily reliant on the content of BFS and PC available. Richardson and others [44,45] observed higher Mg/Al values in hydrotalcite formed in blended cements with less BFS. The direct cause for this is the possibility for Al to react with other common AFm and AFt phases containing sulphate or carbonate. The Al which is not incorporated into these sulphate- and carbonate-containing hydrous calcium aluminate phases may then be split between the C-A-S-H and hydrotalcite-like LDH phases. There are no other phases in BFS-PC cements that contain Mg, therefore all of the available Mg forms hydrotalcite-like LDH, whereas Al may be distributed between other hydrates. A lower availability of sulphate and carbonate in the higher BFS systems causes an abundance of free Al ions, which in turn decreases the Mg/Al value in hydrotalcite-like LDH.

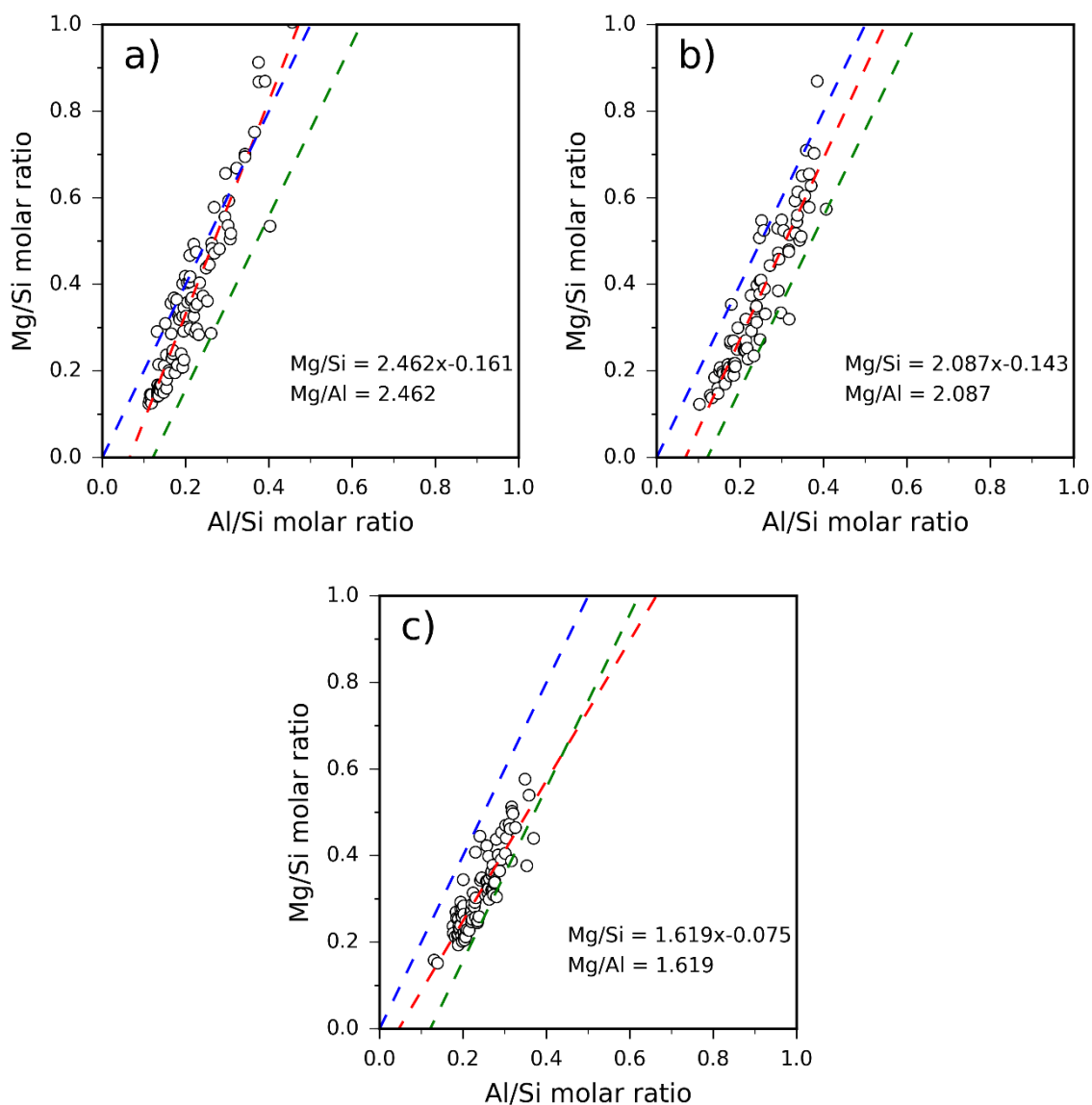


Figure 5.10: Mg/Si versus Al/Si atom ratios from EDS analysis for the a) 1:1 b) 3:1 and c) 9:1 28B BFS:PC. Data manipulation was conducted using Mg/Al minimum of 1.0, Mg/Al maximum of 2.5, and Al/Si maximum of 0.5. The red line highlights the line of best fit through the data points and the Mg/Al value is taken from the gradient. The green and blue tie-lines are example lines of gradient 2, which is generally indicative of the lower Mg/Al examples of a hydrotalcite-group LDH.

Taking the gradient of a line of best fit for the atom ratios Mg/Si versus Al/Si has been shown to provide the most reliable results for determining the Mg/Al of hydrotalcite-like LDH [218], as observed in the 1:1, 3:1 and 9:1 28B samples in Figure 5.10.

Directly plotting the line of best fit resulted in poor results which did not provide a good representation of the hydrotalcite-like LDH structure. A wide array of Mg/Si and Al/Si ratios has resulted in a poor description of the hydrotalcite-like LDH structure. A large amount of intermixing has occurred as a result of the finite EDS spot size, and the mineralogical complexity of these cements.

In previous studies, the Mg/Al line gradient was taken by assessing the 'left-most' data-points that were collected [186,218]. Emulating this approach, three limiting factors were applied to the data collected: 1) provide a maximum of the Al/Si of the dataset, 2) round the Al/Si to 3 decimal places and obtain the 'tail' value or lowest Mg/Al value associated with that Al/Si value (this was to determine 'left most value' at a given Al/Si), and 3) within the data array, create a minimum and maximum Mg/Al from the elemental atomic percentages. The settings that provided the Mg/Al line gradient most consistent with expected results were: maximum Al/Si = 0.5, minimum Mg/Al = 1.0, and maximum Mg/Al = 2.5. However, using this data manipulation method, no coherent or discernible pattern was obtained (Table 5.6). This method still relies heavily on the assumption that the intermixing Al containing species are restricted to C-A-S-H and hydrotalcite-like LDH. The sulphate and carbonate phases containing Al will also affect this method of analysis, reducing the effective Mg/Al ratio as these contribute Al but not Mg to the calculation. Therefore, an accurate representation of the effect of temperature and BFS-PC formulation on the hydrotalcite-like LDH structure cannot be definitively obtained from these data.

Table 5.6: SEM-EDS analysis of the Mg/Al ratio of the hydrotalcite-like phase for different BFS-PC ratios and temperatures of curing. Samples were cured at 35 °C for 1 year (360A) and then at either 60 °C (tC) or 80 °C (tD) for a further 28 days. Samples were cured at 35 °C for 1 year, followed by 80 °C for 1 year and finally cured for 28 days at 50 °C (tE). Samples cured at 35 °C for 2 years (720A).

Temperature regime	Formulation	Mg/Al
360A	1:1	1.378
360A	3:1	1.920
360A	9:1	1.917
720A	1:1	1.645
720A	3:1	1.660
720A	9:1	2.169
28B	1:1	2.462
28B	3:1	2.087
28B	9:1	1.619
28C	1:1	1.167
28C	3:1	2.336
28C	9:1	1.648
28D	1:1	2.077
28D	3:1	2.234
28D	9:1	1.687
360D	1:1	1.547
360D	3:1	1.404
360D	9:1	1.506
28E	1:1	2.283
28E	3:1	1.712
28E	9:1	1.742

5.5 Evaluation of the efficacy of thermodynamic modelling

5.5.1 Selection of potential phase assemblage constituents

Two modelling approaches were followed in this study, with calculations conducted with (“*SH approach*”) and without (“*NS approach*”) the presence of a siliceous hydrogarnet; the phases available for hydration are summarised in Table A8.3 found in the Appendix. A similar methodology was applied by Deschner et al. [188] and by Dilnesa et al. [119] for low pH cements and 3 year old cements, respectively. This approach was intended to ensure the correct phases form at the different temperatures, incorporating restrictions which may be kinetic rather than thermodynamic in foundation. Taylor and Richardson [45] showed that siliceous hydrogarnet does not form in blended cements up to 20 years of curing at 20 °C, therefore highlighting that its inclusion in potential phase assemblages at lower temperatures is unwarranted. Deschner et al. [188] used the SH approach for

temperatures above 50 °C, which causes the monosulphate, monocarbonate and hemicarbonate phases to become destabilised as siliceous hydrogarnet is a more stable alternative. In the current study, monosulphate, monocarbonate and hemicarbonate phases were observed up to 60 °C by XRD, and therefore the upper limit of the NS method and the lower limit of the SH method were changed to 60 °C.

A constant degree of reaction of the BFS and clinker phases was used for each system. The DoH of BFS at 60 °C was used for the *NS method* and the DoH of BFS at 80 °C was used for the *SH method* (Figure 5.1). The reaction of slag was assumed to be congruent. The DoH values of clinker phases were taken from Chapter 4, with an additional 5% reaction included to replicate the increase of temperature on the clinker phases. The 5% additional clinker reaction was estimated due to the higher degree of reaction of the clinker phases at the lower temperatures, therefore it was assumed this would occur at higher temperatures. A summary of the DoH values can be seen in Table 5.7. Calcite and gypsum were observed in the anhydrous PC XRD diffractograms and were quantified by Rietveld analysis (data not shown) to be 4.5 and 3.5 wt.%, respectively of the PC fraction of the systems.

Table 5.7: Clinker degree of hydration values used in thermodynamic modelling. Taylor-Bogue analysis determined the clinker phase ratios in the initial PC: C₃S = 71.9 wt.%, C₂S = 6.8 wt.%, C₃A = 8.0 wt.%, C₄AF = 7.7 wt.% [122].

Clinker phase	DoH (%)		
	1:1	3:1	9:1
C ₃ S	87	93	95
C ₂ S	68	55	47
C ₃ A	100	100	100
C ₄ AF	81	81	81

5.6 Phase assemblage as a function of temperature

The phases predicted by thermodynamic modelling to form in the 1:1 BFS:PC system exposed to temperatures below 60 °C were C-A-S-H, portlandite, ettringite, monosulphate, monocarbonate and hydrotalcite-like LDH (Figure 5.11a). The ettringite phase was no longer stable above 52 °C, consistent with the XRD results of this study where ettringite was still observed up to 50 °C as seen in Figure 5.12a and Figure 5.3a, and only after 28 days at 60 °C does it appear to have mostly converted into monosulphate.

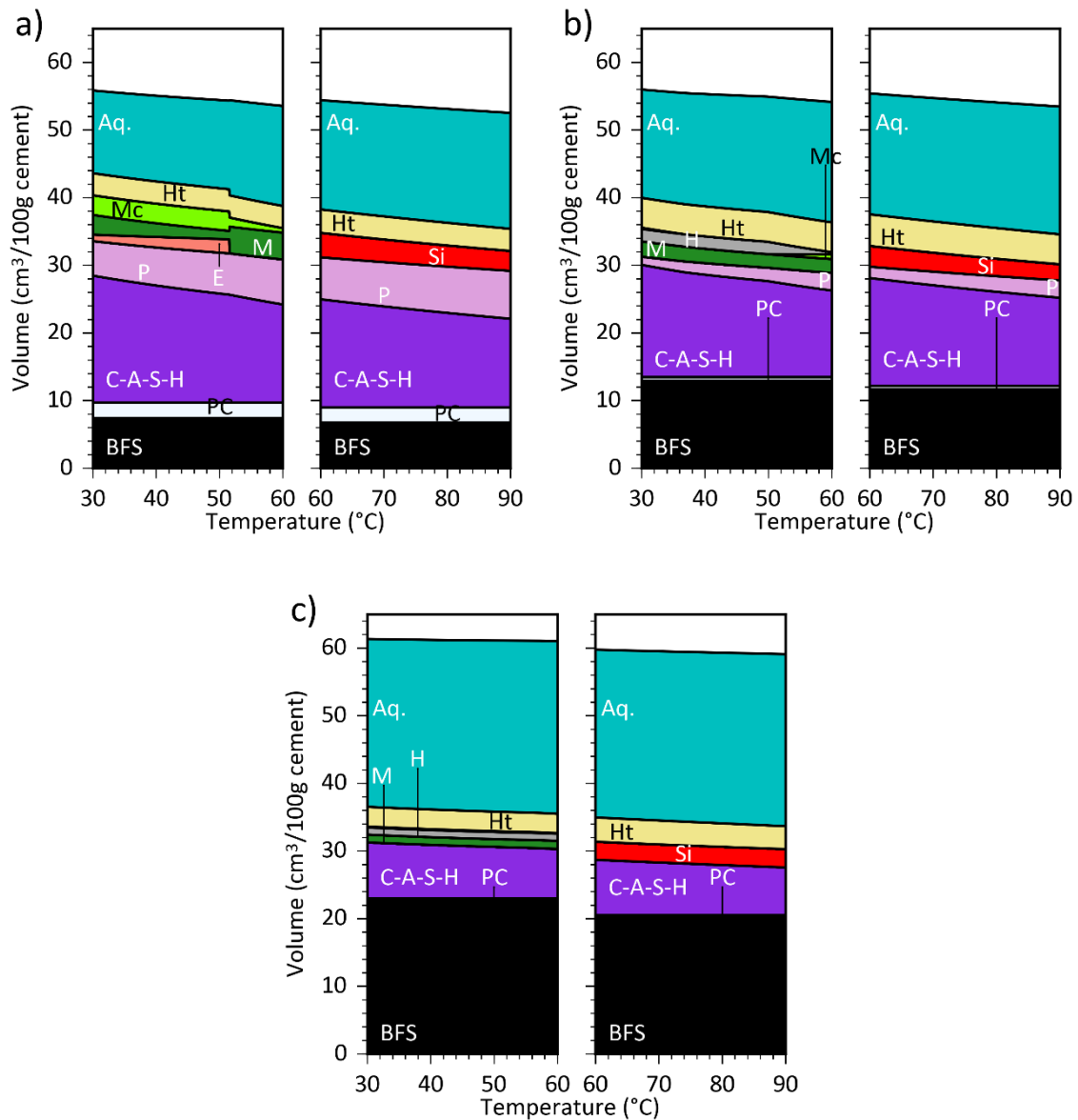


Figure 5.11: Phase assemblages of a) 1:1, b) 3:1 and c) 9:1 BFS-PC cements determined using the thermodynamic modelling software GEMS [132]. The prediction of phase formation was determined as a function of temperature while the remnant precursor content was kept constant. Siliceous hydrogarnet was only allowed to form above 60 °C, and each graphic shows a break at this point to reflect the change in model assumptions. The phase notations correspond to: BFS – Blast furnace slag, PC – Portland cement, C – C-A-S-H, P – portlandite, E – ettringite, M – monosulphate, H – hemicarbonate, Mc – monocarbonate, Ht – hydrotalcite and Si – siliceous hydrogarnet.

In the experimental results, hemicarbonate was observed at 50 and 60 °C (Figure 5.12), however due to the high $\text{CO}_3^{2-}/\text{AlO}_2^-$ ratio in the pore solution, monocarbonate was calculated to be thermodynamically more stable in the 1:1 BFS:PC system. Matschei et al. [97] highlighted the

importance of the $\text{SO}_3/\text{Al}_2\text{O}_3$ and $\text{CO}_2/\text{Al}_2\text{O}_3$ ratios within Portland cement systems, which determined which of the sulphate and carbonate AFm or Aft phases form in each specific instance, as there are small energetic differences between various members of these families. In the 1:1 cement the $\text{SO}_3/\text{Al}_2\text{O}_3$ and $\text{CO}_2/\text{Al}_2\text{O}_3$ ratios were 0.4 and 0.2, respectively. According to Matschei et al. [97], this pair of ratios should form monosulphate and hemicarboxate. However, due to the presence of the more thermodynamically stable C-A-S-H and hydrotalcite-like LDH phases, which withdraw the aluminium from solution, the effective sulphate and carbonate contents become much higher with respect to Al_2O_3 . This causes the thermodynamic model to predict the formation of higher SO_3 and CO_2 rich-phases. Within the 3:1 (Figure 5.11b) and 9:1 (Figure 5.11c) cements, monosulphate was consistently observed in the modelling and experimental results up to 60 °C. Hemicarboxate became destabilised at higher temperatures in the 3:1 cement, however as $\text{CO}_2/\text{Al}_2\text{O}_3$ increases with increasing temperature, formation of monocarbonate occurred. The $\text{CO}_2/\text{Al}_2\text{O}_3$ ratio was consistently lower in the 9:1 cement as this contained the lowest amount of calcite (supplied by the PC), therefore it was possible for hemicarboxate to persist.

A trend of decreasing volume of C-A-S-H and increasing portlandite was observed in the 1:1 and 3:1 blends as the temperature increased. The densification of the C-A-S-H phase at higher Al/Si and lower Ca/Si ratios (see the specific volumes of each end-member in the C-A-S-H model in Table A8.3 in the Appendix) led to a decreasing volume of the C-A-S-H phase as temperature increased. More calcium is available for formation of other phases as a result of the decreasing Ca/Si of the C-A-S-H, therefore the volume of portlandite increases.

Thermodynamic modelling appropriately describes the phases forming at the various temperatures investigated, however simulating the decrease of temperature from 80 °C to 50 °C using the *NS* and *SH* methodology may not be as effective. Figure 5.12 shows that the phases observed experimentally were the same as those predicted using the *SH method*, however the suggested protocol of determining the phase assemblage up to 60 °C disagrees with the recorded phase assemblage for the tE temperature profile, where the sample has been held at 80 °C for an extended period before returning to lower temperature. Therefore, it is recommended that once the cement has reached a temperature at which the siliceous-hydrogarnet phase may form, the *SH method* must be used to accommodate this change. This gives further indication that the limitation on formation of siliceous hydrogarnet at near-ambient temperature is kinetic rather than thermodynamic, as this phase persists after cooling once it has formed at higher temperature. Conversely, it is possible that a longer period

Volume expansion of the hydrates is not expected based on the results from Figure 5.11 which would be a cause of concern for potential cracking in the waste packages. The reduced possibility of cracking can be seen as a positive to reinforce the notion that cement encapsulation is a viable option for long-term storage of ILW. Small levels of shrinkage are expected as a result of the densification of the C-A-S-H phase.

5.6.1 Chemical composition of C-A-S-H phase using thermodynamic modelling as a function of temperature

The different phases allowed to form within a simulation of hydration of cements affect the predicted composition of the C-A-S-H phase (Figure 5.13). The *NS method* predicted a decline in Ca/Si and an increase in Al/Si for each cement up to 60 °C, coinciding with what was determined from SEM-EDS analysis. A notable decrease in the Ca/Si ratio (Figure 5.13a), with an increase in Al/Si (Figure 5.13b), was observed at 52 °C and 50 °C in the 1:1 and 3:1 cements, respectively, in the thermodynamic model outputs. This is caused by the decomposition of ettringite in the 1:1 BFS:PC system and the conversion of hemihydrate to monohydrate in the 3:1 cement. In each case, it is likely that an increase in aluminium concentration in the pore solution caused the sharp rise of Al/Si within the C-A-S-H phase.

A result of the dominance of the hydrogarnet phase in the *SH method*, a more consistent pattern in Ca/Si and Al/Si values was observed in those simulations. The highly stable siliceous hydrogarnet competes with the C-A-S-H phase for the calcium, aluminium and silicon in the system. Dilnesa et al. [149] highlighted the minimal effect of increasing temperature on the $C_3AS_{0.84}H_{4.3}$ hydrogarnet phase. Accordingly, the Ca/Si value of the 9:1 system described by the *SH model* did not vary a great deal (Figure 5.13a) because of the strong competition for the available silicon and calcium between the two phases: C-A-S-H and siliceous hydrogarnet. Without the formation of portlandite, which was predicted in the 1:1 and 3:1 cements but not at 9:1 systems, the C-A-S-H phase composition was influenced by the formation of the hydrogarnet phase. The hydrogarnet phase has a similar solubility to that of C-A-S-H at pH > 11.5 [108,149], so both phases co-exist in the 9:1 cement. The amount of siliceous hydrogarnet remains relatively constant throughout the *SH method* simulations for each BFS-PC ratio as a function of temperature.

The Ca/Si values within C-A-S-H were generally under-predicted in the *NS method* due to the competition with other calcium containing phases. However, the Al/Si was generally over-predicted

due to the lower Gibbs energy of the 5CA and INFCA end-members (end-member model used to describe C-A-S-H phase, Table A8.3 in the Appendix). This was exhibited further by the sudden increase of the Al/Si in the C-A-S-H phase once the decomposition of ettringite occurs. A combination of these two factors led to an increase in availability of calcium for higher portlandite formation observed in the 1:1 and 3:1 cements. Within the 9:1 systems, the Ca/Si was over-predicted consistently due to the lower Ca/Si end-members withdrawing the calcium from solution in place of forming portlandite.

The Ca/Si in the *SH method* was generally over-predicted due to the C-A-S-H phase containing a higher calcium content when compared to siliceous hydrogarnet which was competing for calcium. Similarly, the Al/Si within C-A-S-H was reduced in the *SH method* compared to the NS method due to siliceous hydrogarnet containing a higher Al/Si ratio than the end-members used for the creation of C-A-S-H and was stable throughout the temperature range (60–90 °C), whereas phases such as ettringite were not stable across the temperature range in the *NS method* (30–60 °C).

This impact on the level of change of the Ca/Si and Al/Si at each temperature point was not explicitly observed via the SEM-EDS data, however the general trends of decreasing Ca/Si and increasing Al/Si with the increase of temperature were observed in both modelling methods and in the SEM-EDS data as exhibited in Figure 5.13.

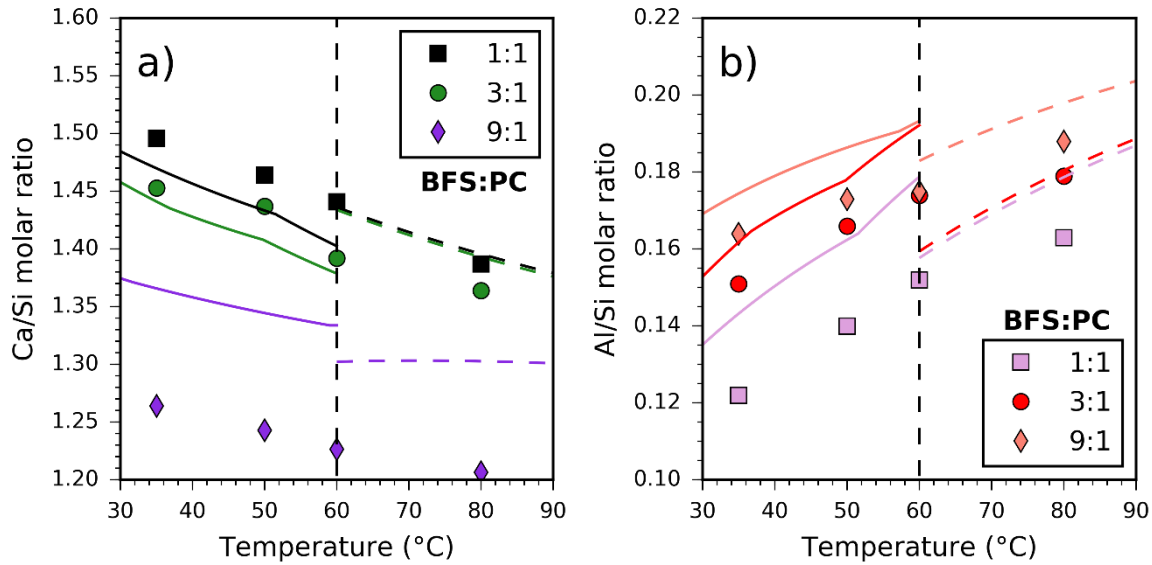


Figure 5.13: Molar ratios of a) Ca/Si and b) Al/Si within C-A-S-H as a function of temperature using the two different modelling approaches (*SH* above, and *NS* below, a cutoff temperature of 60 °C in each case) as a function of the BFS:PC ratios. The symbols correspond to SEM-EDS results, while the lines represent the modelling results. The solid line represents the *NS* method and the dotted line represents the *SH* method.

For both methods, the polymerisation of the aluminosilicate chains was well represented due to the resulting reduction of Ca/Si and increase in Al/Si in the C-A-S-H phase, with increased curing temperature. For the 1:1 and 3:1 samples, the Ca/Si was under-predicted and the Al/Si was over-predicted by up to 2.1 % and 13.8% respectively. Integrating aluminium-containing end-members into C-A-S-H models has been a continual issue. Recreating aluminium end-members with lower (Al/Si = 0.1) or very high (Al/Si = 0.33) Al contents based on the additive method proposed by Kulik [64] and Myers [146], did not provide useful additions to the C-A-S-H model for the cementitious systems simulated in this study. The highly stable nature of the current end-members causes a redundancy in other end-members because they do not form in any meaningful amounts to contribute to the phase assemblage of blended cements or the chemical composition of C-A-S-H in varying environments. This is further highlighted by the results of the 9:1 cement system, which rigidly maintains a Ca/Si ratio between 1.3 and 1.37, accumulating the remaining calcium in the system that cannot reach the higher Ca concentration required to form portlandite. As a result of the C-A-S-H phase restricting the formation of portlandite, its Ca/Si ratio was over-predicted in the 9:1 system by up to 7.4%. The higher Al/Si ratio expected in the 9:1 cement resulted in greater accuracy, whereby the Al/Si was over-estimated by no more than 7.6%.

5.6.2 Chemical composition of the hydrotalcite-like phase (MA-OH-LDH – solid solution model) using thermodynamic modelling as a function of temperature

The chemical composition of the hydrotalcite-like LDH phase (calculated using the MA-OH-LDH) was reliant on the other phases formed, Figure 5.14. The *NS* method produced a lower Mg/Al due to the lower temperatures and the greater diversity of Al containing phases. Increasing the temperature reduced the availability of Al due to the increasing Al/Si within C-A-S-H, however for phase transition areas such as the diminishing levels of the other sulphate and carbonate AFm and AFt phases, more Al became available to form hydrotalcite-like LDH. The decrement of the Mg/Al value from 52 °C and above was a result of the decomposition of ettringite in the 1:1 cement and the decomposition of hemicarbonate in the 3:1 cement. The 9:1 cement maintained an increasing Mg/Al value due to the minimal alteration of changes in the available phases. Corresponding with experimental data, the Mg/Al ratio was larger in cements that had lower BFS content [44,45].

The *SH* method resulted in a greater and more consistent Mg/Al ratio due to the presence of siliceous hydrogarnet dominating the availability of Al, resulting in less freely available Al.

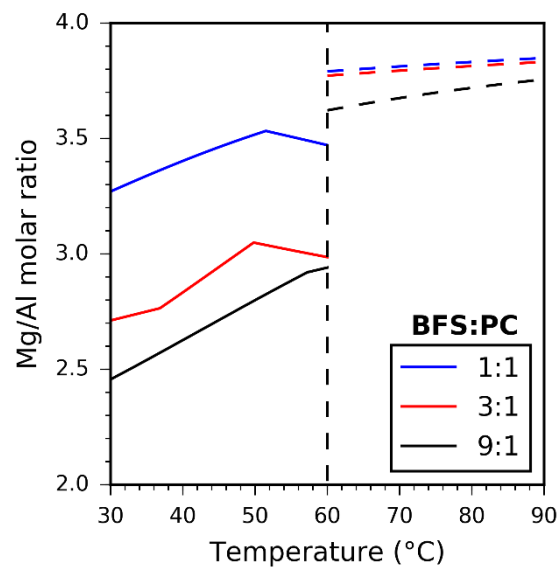


Figure 5.14: Molar ratio of Mg/Al within the magnesium hydrotalcite-like LDH phase of 1:1, 3:1 and 9:1 BFS-PC, using the MA-OH-LDH model developed by Myers et al [123].

5.7 Conclusions

The alteration in phase assemblages in hydrated mature BFS-PC systems which are subjected to step-changes in temperature occurs relatively rapidly and is of importance in the context of emplacement of cemented nuclear waste in a geological disposal facility. Sulphate and carbonate containing AFm and AFt type phases are not greatly affected by the increase of temperature from 35 to 50 °C after 360 days of curing at 35 °C; transferring these samples to an environment of 50 °C did not cause major phase changes. However, the higher water content phases such as ettringite and hemihydrate become destabilised at around 60 °C. When a 360-day cured cement is transferred from 35 to 80 °C environments, a rapid transition occurs: after 3 to 7 days, the sulphate and carbonate AFm and AFt phases have been destabilised and replaced by siliceous hydrogarnet.

Thermodynamic modelling of these systems has been shown to accurately replicate the changes in phase assemblage observed when cements are transferred to higher temperature after 360 days of curing, when held at the elevated temperature for 28 days at a range of temperatures, and up to 360 days in the case of a transfer to an 80 °C environment.

The phase assemblage formed after a subsequent decrease of temperature from 80 °C to 50 °C (after 360 days at 35°C and another 360 days at 80 °C) could be accurately predicted by a model which allowed siliceous hydrogarnet to form, although this phase needed to be suppressed in simulations of the samples which had never been heated above 60°C. This provides further evidence that the absence of siliceous hydrogarnet from cement phase assemblages at near-ambient or slightly elevated temperature is due to kinetic, rather than pure thermodynamic, limitations.

Description of the chemical composition of the C-A-S-H phase followed the trends observed experimentally in BFS-PC cements. The Ca/Si values were very slightly under-predicted for the 1:1 and 3:1 systems, and over-predicted in the 9:1 cement by up to 7.4%. The Al/Si ratio was over-predicted in all cements, by up to 13.8% in the worst cases. Inclusion of additional end-members with low (Al/Si = 0.1) or high Al/Si (Al/Si = 0.33) values based on the additive method did not contribute any meaningful change on the chemical composition of the C-A-S-H phase.

Understanding of how the C-A-S-H phase forms and alters with composition, and the quantity of other phase formation, is important in waste immobilisation applications as it enables prediction of how this key phase interacts with dissolved species including radionuclides. Additional studies are required to determine the effects of alkali, aluminium and groundwater leaching effects on the C-A-S-H phase, but this study has provided essential insight into the temperature effects that may influence PC-BFS blends in this safety-critical application.

6 Using Pitzer parameters in GEMS for predicting blended cements.

6.1 Introduction

Thermodynamic modelling of cement phases has been used extensively in the past to predict the phase assemblages of many varieties of cements. Utilizing geochemical software such as GEMSelektor (GEMS), PHREEQC, MTDATA or Geochemist's workbench (GwB) can provide good results when predicting how the initial chemistries of cements will influence the solids formed, whether considering ordinary Portland cements [113,119–121,126,150,151] or cements containing supplementary cementitious materials (SCMs) [101,102,122,124,125,183,220].

The methodologies for determining stable phase assemblages may be determined from two main approaches: by Gibbs energy minimisation (GEM), or through the law of mass action (LMA). Both techniques include a mass balance approach to ensure all material available in the system which may react is accounted for. The GEM method uses Gibbs energy as the basis for determining whether a solid phase is stable within the system by considering the phase Gibbs energy as a sum of the chemical potentials (μ_i) of the aqueous species that form the solid phase and applying a correction for the activity coefficient (γ_i). The activity coefficient provides description of the non-ideal scenario, which is indicative of the electrolyte solution environment. Activity coefficients are also used in conjunction with the LMA method, however in this case the molar concentrations that combine to form the solubility product (K_{sp}) are effectively modified. Both approaches apply the activity coefficient factor as a means of more accurately portraying the aqueous solution and the effect the solution may have on aqueous ions, therefore leading to impact on the formation of solid phases. How GEM and LMA methods are utilised in cement chemistry are well documented [118,120,128,132,180,221].

Activity coefficient equations are generally derived from a basic Debye-Hückel-type equation as seen in Equation 6.1 and expanded in section 6.2.1 (Activity coefficient models). The Debye-Hückel functional form may be used for dilute electrolytes, however at higher ionic strengths, more detailed methods are used.

$$\log \gamma_i = -Az_i^2\sqrt{I} \quad \mathbf{6.1}$$

Where A is a temperature dependent variable ($A = 1.824928 \times 10^6 \rho_o^{1/2} (\epsilon T)^{-3/2}$, with ρ_o the density of water, ϵ the dielectric constant of water, and T in kelvin) [136], z_i is the charge of aqueous species i , I is the ionic strength of the solution ($I = 0.5 \sum_{i=1}^n c_i z_i^2$, where c_i is the molal concentration of species i), and γ_i is the activity coefficient of species i .

Adaptation of Equation 6.1 by adding additional terms to better describe the electrolyte being simulated, has led to the improvement of aqueous solution modelling and to the creation of other models effective at varying ionic strengths. The Pitzer model utilises ion-specific interaction parameters alongside the ionic strength to provide greater accuracy for the activity coefficients for individual aqueous species. The Pitzer model has been highlighted for its benefits over other activity coefficient models due to the higher level of accuracy in more concentrated solutions [66,100,110,111,143,145]. Portland cements, blended cements and alkali activated material (AAM) generally have ionic strength values of 0.1 to 2.0 mol/L in their pore solutions [104,120].

Improved accuracy for determining the hydration of cement phases may be important, and additionally, cement is currently used as a waste immobilisation or encapsulation method for various waste streams [11,15,147,184,222]. Waste streams may increase the IS of the system, including through corrosion of the waste, and require the use of improved aqueous solution models such as the Pitzer method. Groundwater interaction models that consider the eventuality of a waste package interacting with nearby groundwater may also benefit from the inclusion of a more robust aqueous solution model. Therefore, the applicability and the possible improvements for modelling cement hydration and pore solution chemistry were tested in this chapter.

6.2 Modelling approach

6.2.1 Activity coefficient models

Thermodynamic modelling was performed using GEMS in conjunction with the CEMDATA14 database for cement phases, and data from the literature when considering non-cement oriented systems (phases used are the same as the *NS method*, summarized in Table A8.3). The GEMS software determines the minimum Gibbs energy of the system by precipitating solids out of solution through

equilibrium solvers [132,180]. This method determines molar amounts of phases based on the chemical potential of each phase that may be created:

$$G = \sum_j x_j \mu_j \quad 6.2$$

Where, x_j and μ_j are the mole fraction and chemical potential of solid phase, j , respectively. Solid phases are calculated to have formed if the sum of the chemical potentials of the aqueous species become more negative than the chemical potential of the solid and the ΔG becomes negative ($\Delta G = \Delta G(\text{products}) - \sum_i \Delta G(\text{aqueous reactants})_i$). In an ideal system, the standard chemical potential, μ_i^0 , for aqueous species i would be used, however systems in reality are not ideal. Therefore, an additional term must be applied to the chemical potential which includes an activity coefficient, γ_i , to define a more realistic chemical potential of each species based on the chemical environment of the system:

$$\mu_i = \mu_i^0 + RT \ln \gamma_i c_i \quad 6.3$$

Where R is the ideal gas constant ($8.314 \text{ J mol}^{-1} \text{ K}^{-1}$), T is temperature (K) and c_i is the molal concentration of species i . There are many methods for determining the activity coefficient. Most common methods involve using the Davies (Equation 6.4 [129]), Truesdell-Jones (Equation 6.5 [134]) or Helgeson (Equation 6.6 [137]) equations which are variations of the Debye-Hückel equation (Equation 6.1). Each of the methods utilize the ionic strength ($I = 0.5 \sum_{i=1}^n c_i z_i^2$, where c_i is the molal concentration and z_i is the charge of species i) of the system and provide activity coefficients based on the charge of the species. They provide little variation based on the species and are applicable up to varying ionic strengths. Within GEMS, these activity coefficient models are built into the software and have been used to good effect for predicting a range of cement hydrate systems [101,102,122,124,125,183,220].

$$\log_{10}\gamma_i = -Az_i^2 \left(\frac{\sqrt{I}}{1 + \sqrt{I}} + 0.3I \right) \quad I < 0.1 - 0.7 \quad \mathbf{6.4}$$

$$\log_{10}\gamma_i = \frac{-Az_i^2\sqrt{I}}{1 + aB\sqrt{I}} + bI \quad I < 0.5 - 2 \quad \mathbf{6.5}$$

$$\log_{10}\gamma_i = \frac{-A_\gamma z_i^2\sqrt{I}}{1 + aB_\gamma\sqrt{I}} + b_\gamma I + \log_{10} \frac{X_{jw}}{X_w} \quad I < 0.5 - 2 \quad \mathbf{6.6}$$

Another approach is to use ion specific activity coefficients determined using the Pitzer model [100,135,144], which is a significantly more complex method and requires ion-specific parameters, thus an expansive database, as shown in Equation 6.7 to 6.13. There have been different variations of the Pitzer model, however the one used within GEMS is the Harvie, Moller and Weare (HMW) [100,144] formulation. The equations are presented here to yield the activity coefficients, γ_M , for cationic species, M . In Equation 6.7 and 6.8, m_c is the molality (mol/kg solvent) of cation c , with charge z_c . Subscripts M , c and c' refer to cations. The subscripts can be exchanged for X , a and a' to refer to anions. The summation index, c , denotes the sum over all cations in the system. The double summation index, $c < c'$, relates to the sum over all interactions with dissimilar cations. Equivalent definitions apply to the summation indices for anions. Further explanation of the terms have been well documented in previous publications [100,135,144,145].

$$\begin{aligned} \ln\gamma_M = z_M^2 F + \sum_a m_a (2B_{Ma} + ZC_{Ma}) & \quad I < 0.5 - 6.0 \quad \mathbf{6.7} \\ + \sum_c m_c (2\Phi_{Mc} + \sum_a m_a \Psi_{Mca}) & \\ + \sum_{a < a'} \sum m_a m_{a'} \Psi_{aa'M} + |z_M| \sum_{c < c'} \sum_a m_c m_a C_{ca} & \end{aligned}$$

The Pitzer-HMW approach incorporates the use of a virial coefficient expansion in terms of molality. An initial term which encompasses the system as a whole, in this case the Debye-Hückel type term (F) (Equation 6.8), is followed by interaction coefficients that consider the interaction between pairs of aqueous species (B 's, C 's and Φ 's) and a term that includes ternary species interactions (Ψ).

$$F = -A^\phi \left[\frac{\sqrt{I}}{1 + b\sqrt{I}} + \frac{2}{b} + \ln(1 + b\sqrt{I}) \right] + \sum_c \sum_a m_c m_a B'_{ca} + \sum_{c < c'} \sum_{c'} m_c m_{c'} \Phi'_{cc'} \quad 6.8$$

$$+ \sum_{a < a'} \sum_{a'} m_a m_{a'} \Phi'_{aa}$$

Where A^ϕ equals 0.392 for water and b is a universal empirical parameter equal to 1.2, both at 25 °C [138].

$$B_{MX}^\phi = B_{MX}^{(0)} + B_{MX}^{(1)} e^{-\alpha_{MX}\sqrt{I}} + B_{MX}^{(2)} e^{-\alpha'_{MX}\sqrt{I}} \quad 6.9$$

$$B_{MX} = B_{MX}^{(0)} + B_{MX}^{(1)} g(\alpha_{MX}\sqrt{I}) + B_{MX}^{(2)} g(\alpha'_{MX}\sqrt{I}) \quad 6.10$$

$$B'_{MX} = \frac{\partial B_{MX}}{\partial I} = B_{MX}^{(1)} \frac{g'(\alpha_{MX}\sqrt{I})}{I} + B_{MX}^{(2)} \frac{g'(\alpha'_{MX}\sqrt{I})}{I} \quad 6.11$$

Where the functions $g(x)$ and $g'(x)$ are defined (with $x = \alpha_{MX}\sqrt{I}$) as:

$$g(x) = 2(1 - (1 + x)e^x)/x^2 \quad 6.12$$

$$g'(x) = -2\left(1 + x + \frac{x^2}{2}\right)e^{-x}/x^2 \quad 6.13$$

It is important to note that for electrolyte interactions where the charges are 1-1 or 1-2, only the terms including $B_{MX}^{(0)}$ and $B_{MX}^{(1)}$ are necessary. In this instance $\alpha = 2$, however for 2-2 electrolyte interactions the $B_{MX}^{(2)}$ term is included, with $\alpha = 1.4$ and $\alpha' = 12.0$. The alteration to the B_{MX} equations based on the 2-2 electrolyte takes into account the increased likelihood of higher valence ions to interact within the solution.

Inclusion of only the B_{MX} terms has been credited to be sufficient for many electrolytes up to an ionic strength of 4 mol/L [138,139]. To increase the range of validity of this method, the third virial coefficient for binary interactions, C_{MX} and the mixed electrolyte ψ and Φ coefficients may be used

[140,141]. The third virial coefficient C_{MX} of binary ion interactions is defined to be independent of ionic strength. The Φ term describes the interactions between like-charged ions ($\Phi_{cc} = \theta_{MM} + {}^E\theta_{MM}$). The θ_{MM} parameters account for unsymmetric mixing effects involving 1-2 or 1-3 ion interactions, and ${}^E\theta_{MM}$ can be derived to account for the excess energy of mixing. The ψ term describes ternary ion interactions ψ_{ijk} , of two ions with the same signed charge and one ion with a differently signed charge.

6.2.2 Incorporating Pitzer equations into GEMS

Previous investigations using the Pitzer parameters with thermodynamic models for cement systems have been conducted by Damidot et al. [98,99,148] and Duchesne and Reardon [66]. Within these investigations, PHREEQE was utilised alongside the PHRQPITZ speciation code used at that time; these models are now incorporated into the PHREEQC code [115]. Using the Pitzer parameters within PHREEQC is quite simple as it contains a database within the software and can be easily applied. However, within GEMS, the user has to manually input the Pitzer interaction values based on the ion code assigned to each by the software. This can be a tedious and time consuming task for simple systems, and for complex systems such as cements, it is a greater problem. Therefore, a programme was created here, that can convert the aqueous species listings obtained using GEMS and provides an output file containing the Pitzer parameters in a format that can be used within GEMS.

Utilisation of the Pitzer model requires extensive databases for complex systems such as cement hydration. Other geochemical modelling packages such as PHREEQC and GwB have databases containing Pitzer parameters incorporated into the software. The PHREEQC database has been incorporated into the one used within this study, with additional parameters included where possible, or values updated and replaced where better parameter values have been identified. A simple ion-interaction and database lookup programme has been created using Python to use specifically with the Pitzer model user interface applied in GEMS (Figure 6.1).

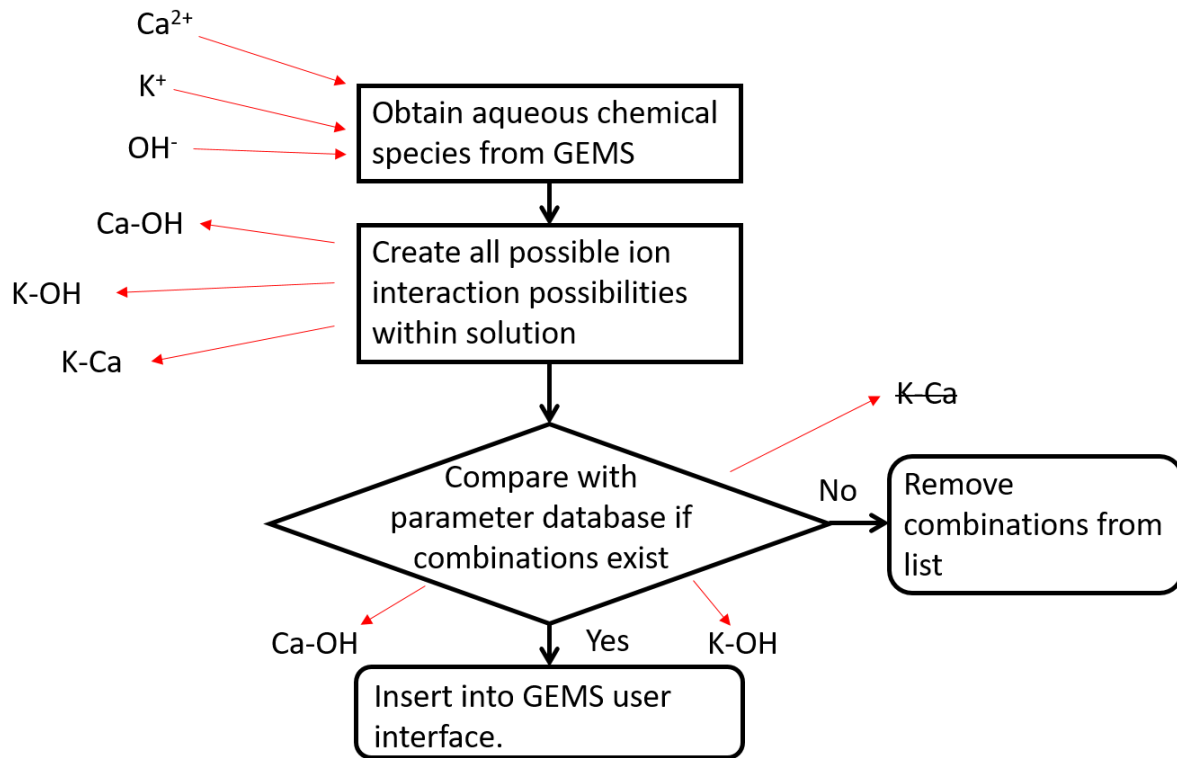


Figure 6.1: Programme structure for Pitzer parameter database lookup.

6.2.3 Estimating Pitzer parameters

Interaction parameters are generally determined through empirical means by using solubility data over a wide range of ionic strengths of binary or ternary systems. Using this method in multi-species systems has been proven to work effectively for systems including up to 11 aqueous species [223,224], proving that these binary electrolyte values can be applied to more complex scenarios. Simulation of a BFS-PC cement may include the use of greater than 70 aqueous species, creating a significantly more complex system. As a result of the large number of aqueous species, there may not be interaction parameters available within the literature to describe some important interactions. For example, to form katoite (C₃AH₆), interaction parameters between Ca²⁺- OH⁻ and Ca²⁺- AlO₂⁻ would be highly desirable to be used, however, within the literature there are not parameters available for Ca²⁺- AlO₂⁻ interactions. Therefore, missing interaction parameters have been estimated using Equation 6.14 and 6.15, from Simoes et al. [225]:

$$B_{MX}^{(0)} = 0.04850z_M^{1.62}z_X^{-1.35}|r_M - 1.5r_X|^{1.2} + 0.03898 \quad \mathbf{6.14}$$

$$B_{MX}^{(1)} = 0.00738z_X^{-0.4}(z_M^2z_X^{0.6}(1 + |r_M - 1.2r_X|^{0.2}))^2 + 0.16800z_M^2z_X^{0.2}(1 + |r_M - 1.2r_X|^{0.2}) - 0.09320z_X^{-0.4} \quad \mathbf{6.15}$$

Where z_M and z_X are the charges of the cation and anion, respectively, and r_M and r_X are the ionic radii of the cation and anion, respectively. This method was proven to be effective across a range of ionic strengths, when only the $B_{MX}^{(0)}$ and $B_{MX}^{(1)}$ values were used in binary solutions [225]. This method was verified using the osmotic coefficient data for binary ion interactions in solution, which is a technique often used to derive Pitzer parameters. A strong correlation of ionic radius and charge with the second virial coefficient parameters ($B_{MX}^{(0)}$ and $B_{MX}^{(1)}$) was determined to create Equation 6.14 and 6.15. Simoes et al. [225] highlighted that this technique was not ideal for producing parameters for ion pairs/complexes for 1-1 electrolytes. The model does not account for the parameters independent of ionic strength such as the C_{MX} values, therefore its results become less accurate above ionic strengths of ~ 4 mol/L. When considering cement systems, this method may be viable due to cement pore solutions generally registering an ionic strength range of 0.5 to 3 mol/L [104,120].

A database of ionic radii was created using the data collected by Marcus [226,227], similar to the approach of Simoes et al. [225]. A similar database lookup tool was created to ensure that the correct interaction parameters were used in the simulations in GEMS.

6.2.4 Testing applicability of the Pitzer model and simulation setup

The solubilities of common cement phases were simulated using the Pitzer model (P), and compared to results obtained using the Truesdell-Jones equation (T). Solubility data from the literature, describing the invariant points for phase transitions based on composition in the system, were used as the main basis for comparison. Trials of the Pitzer model using only parameters created using the Simoes estimation equations (S) and using Pitzer parameters taken from the literature which are supplemented by Simoes-method estimated parameters (SP), were tested. A comparison and lookup tool was created to compile the SP parameters. The tool determined which ionic interactions had Pitzer parameters from the literature, and these were supplemented by filling the missing parameters based on the ionic interactions created for the Simoes (S) method.

Invariant points for multi-component systems such as Ca-Al-SO₄-OH and Ca-Al-CO₃-OH, up to 1440 different precursor compositions, were determined and 2310 in the presence of sodium or potassium. Available amounts of Ca(OH)₂, Al(OH)₃ and CaSO₄ or CaCO₃ were varied to provide a full compositional array. The minimum and maximum concentrations of the precursors used were highlighted in Table 6.1.

Table 6.1: Concentration limits and step sizes for the concentration arrays used to model the Ca-Al-SO₄-OH and Ca-Al-CO₃-OH systems.

Precursor	Concentration limits (mmol/L)	Step size (mmol/L)
Al(OH) ₃	0.005 – 1.6 (5) ^a	0.4 (0.5) ^a
Ca(OH) ₂	0.001 – 40 (2)	4 (0.5)
CaSO ₄	0.005 – 17 (100)	4 (2)
CaCO ₃	0.005 – 17	4

^aThe values in parentheses are the upper limits or step sizes used for the simulations including sodium or potassium.

6.2.5 Assessing the quality of the calculated data

A sum of square errors (SSE) analysis approach was conducted to assess the quality of simulating the variables affected by the various modelling methods:

$$SSE = \sum_i (y_i - y_{m,i})^2 \quad 6.16$$

Where y_i is the experimental value and $y_{m,i}$ is the corresponding modelled value. A lower SSE value implies a better fit of the simulated results.

The Pitzer model and Truesdell-Jones equations use molality as the basis for the calculations. The density of the aqueous phase from the modelling results was used throughout as a means of converting the molality into molarity so that the modelling results may be a direct comparison of the experimental data collected which are represented as mmol/L. This was done as molality is a measure

of millimoles per kilogram of water in the system, as opposed to millimoles per litre of aqueous solution which requires a density correction.

6.3 Pore solution extraction from hydrated samples

Pore solutions of blended BFS-PC cement samples were tested to provide data for direct comparison of the modelling approaches. The steel die method was used to extract the pore solution [118,177–179]. Three formulations of BFS-PC: 1:1, 3:1 and 9:1, were tested at different curing ages. A constant water to solids ratio (w/s) of 0.35 and curing temperature of 35 °C were used. Samples were poured into 500 mL HDPE bottles and sealed with a screw cap with Parafilm wrapped around the top.

Samples had the top and bottom of the cylinders removed to ensure a flat surface when being placed into a cement pore press. The total volume of the sample was thus reduced to 468 mL for all of the samples. The pore press design displayed in Figure 6.2 highlights the dimensions of the press used. A hole in the middle of the base of the press directed the pore fluid through a channel which had a syringe attached at the end. Before squeezing the samples, a hole was drilled into the centre of the sample to create a channel for the pore water to flow without creating a blockage in the hole in the base of the pore press. Samples were placed inside the press and gradually exposed to pressures of up to 550 MPa.

Samples were initially planned to be tested at 28, 56, 90, 180 and 360 days following the curing ages used for characterisation performed throughout this thesis. Recurrent issues leading to the damage of the pore press caused consistent delays and resulted in missing curing ages for some of the samples of each formulation.

Extracted pore fluid was tested using ICP-OES (Spectro Ciros Vision ICP-ES) to obtain the concentrations of major elements such as: Al, Ca, Fe, K, Mg, Na, Si and S. The samples were filtered and diluted by a minimum of 5 times. In the case of the 360 day 9:1 sample, the pore fluid was diluted by 10 times due to the high concentration of sulphur in solution.

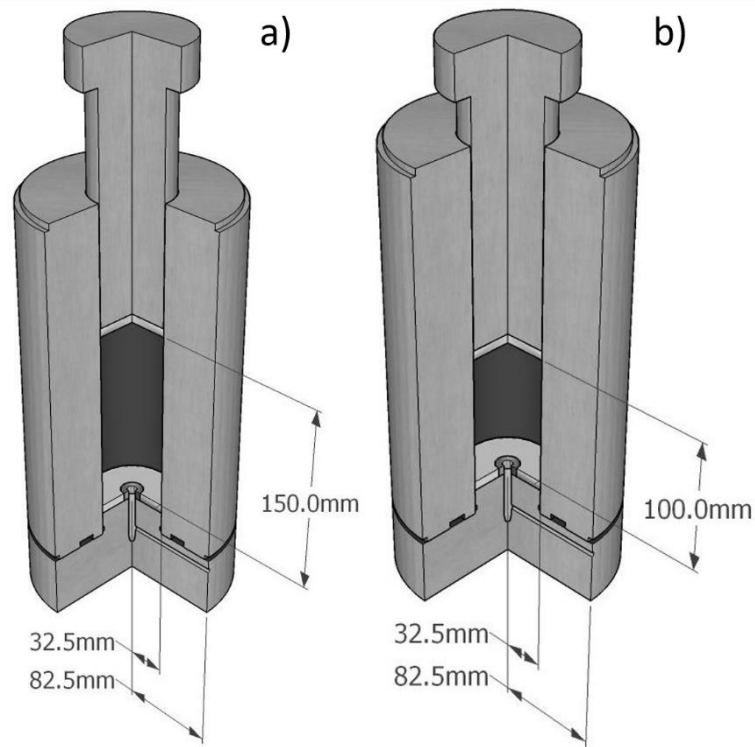


Figure 6.2: Pore press used for acquisition of pore fluid from cured BFS-PC cement samples. The dimensions of the press are represented: a) before the sample has been compressed, and b) at the expected maximum level of compression of a cement sample.

6.4 Modelling results comparing the Pitzer model with the Truesdell-Jones equation

The majority of the thermodynamic data used in the CEMDATA14 database for the cement phases were developed using the extended Debye-Hückel model (Equation 6.4) to provide the activity coefficients to create the Gibbs energy of formation or solubility products [118,149,150]. The phases therefore are optimised for this specific aqueous model. The characterisation of most cement phases is generally in good agreement with solubility data. However, utilisation of the Pitzer model to provide an ion specific activity coefficient may improve the results.

The Truesdell-Jones (T) and the Pitzer (P) model using parameters from the literature, were used to model common cement hydrates in solution to determine whether the Pitzer model provided a greater level of accuracy. The Pitzer model using only Simoes et al. [225] parameters (S) and parameters that were supplemented by Simoes et al. The (SP) were also compared to assess whether

the inclusion of estimated parameters improved the fitting of data. Table A8.6 and Table A8.7 (Appendix.) contain the Pitzer parameters used throughout the study.

6.4.1 Portlandite

Portlandite ($\text{Ca}(\text{OH})_2$) is one of the most common hydrates found within a cement phase assemblage, and Ca^{2+} and OH^- ions form a large portion of the solute in cement pore solutions. Parameters for the interaction of Ca^{2+} and OH^- in various aqueous environments were rigorously tested in previous years, therefore providing a worthwhile basis to compare modelling approaches and parameters [66,100].

6.4.1.1 Portlandite in the presence of NaCl

In multi-electrolyte systems the inclusion and exclusion of different aqueous ions was an important factor to consider. In the studies focused on parameterisation of ions involved in portlandite solubility studies, the CaOH^+ complex ion was not included in the parameterisation. Instead, this species was implicitly accounted for through the inclusion of the $B_{MX}^{(2)}$ and C_{MX} interaction parameters, which are ordinarily utilised for 2-2 ionic charged species and imply ternary ion interactions, respectively [66,139]. In general, ion pairs such as CaOH^+ are not parameterised because of the unsymmetric nature of the ions in solution. This unsymmetric behaviour has created issues in fitting parameters to ion pairs because the nature of fitting the parameters has an underlying relationship to the difference in ionic radii of the interacting ions [138,225]. This is highlighted further through the impact that not accounting for this unsymmetrical behaviour leads to an under-prediction of calcium concentration in solution when using the Simoes-method parameters. This issue was present in all calcium-containing systems.

However, within aqueous solution modelling software, ion pairs are considered in the solution chemistry by default. This is the case within the GEMS software. The inclusion of non-parameterised aqueous species may have large implications or create errors when modelling an aqueous system. Figure 6.3a highlights the impact that a non-specifically-parameterised ion (CaOH^+) and an aqueous species ($\text{NaOH}(\text{aq})$) have on the solubility of portlandite calculated using the Pitzer model within a NaCl electrolyte. The speciation of calcium into Ca^{2+} and CaOH^+ , when the CaOH^+ was permitted to form in solution, caused a significant error in the precipitation of portlandite. Coupled with the consumption of Na^+ ions to form $\text{NaOH}(\text{aq})$, which reduced apparent ionic strength, there was an error

in the calculated calcium concentration by up to 97.9% at a concentration of 3.75 mol/L of NaCl. This level of error is highlighted by Figure 6.3b, where the Pitzer equation with no parameters in this system was compared to the Truesdell-Jones (T) method.

Without the second and third virial coefficients (B_{MX} and C_{MX} , respectively) the Pitzer activity equation is greatly simplified:

$$\ln\gamma_M = z_M^2 F \quad \mathbf{6.17}$$

$$F = -A^\phi \left[\frac{\sqrt{I}}{1 + b\sqrt{I}} + \frac{2}{b} + \ln(1 + b\sqrt{I}) \right] \quad \mathbf{6.18}$$

The version of the Pitzer model displayed in Equation 6.17 becomes inadequate for $IS > 0.1$ as the equation represents long-range interactions of a very dilute electrolyte, whereas this is not the case in the actual system. The example displayed in Figure 6.3b further highlights the need for complete parameterisation of the aqueous species involved in a solution when using the Pitzer model. The Pitzer model solely using the Debye-Hückel term (denoted in Figure 6.3b as PF) provides a significantly worse fit. For further studies of prominent cement phases, the inclusion of neutral aqueous species or ion pairs were removed in the instances that no Pitzer parameters were available.

The Simoes parameters were tested alongside the Pitzer parameters in Figure 6.3a and provide a good agreement with the solubility data, reaching a maximum error of 34.2% at 3.75 mol/L of NaCl. The Simoes parameters follow a similar trend to the solubility data, which makes this method a potentially viable approach to fill vacancies in the Pitzer parameter database, although it is evidently less desirable than the use of parameters specifically fitted to the system of interest.

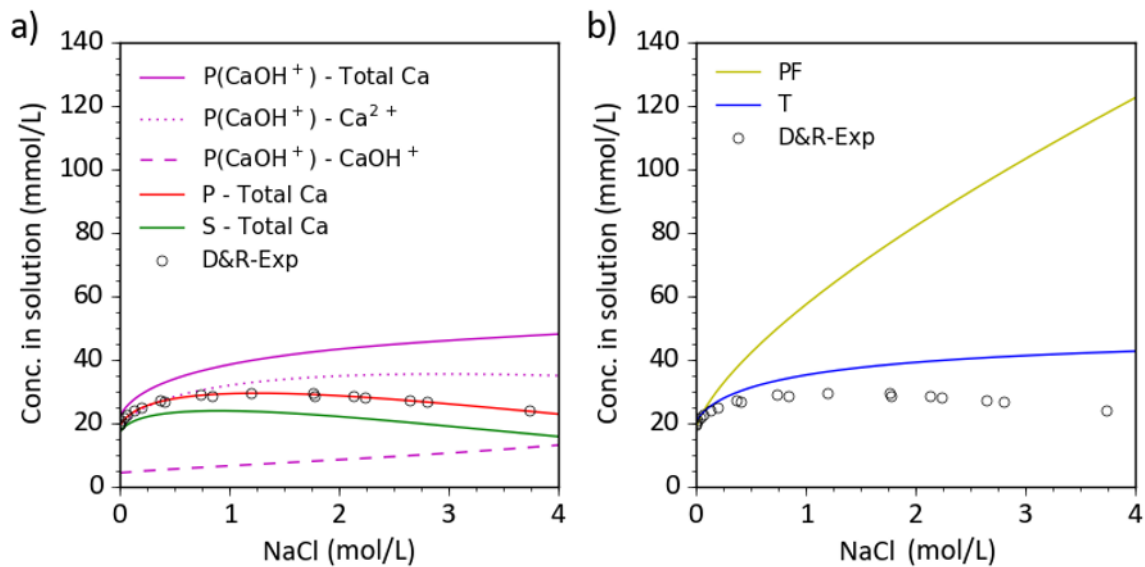


Figure 6.3: The application of different parameterisations of the Pitzer aqueous solution model to the prediction of portlandite solubility in NaCl solutions: a) highlighting the importance of selection and parameterisation of the aqueous species; P(CaOH⁺) denotes the Pitzer model including CaOH⁺ in the calculations, P denotes a fully parameterised Pitzer model without CaOH⁺, and S denotes the Pitzer model using only the parameters generated from the Simoes estimation equations; b) showing the detrimental effect that the Pitzer model with all parameters set to zero (PF – equation 6.17) has on the predictions in comparison with the Truesdell-Jones (T) equation. Both plots show experimental data from Duchesne and Reardon [66].

6.4.1.2 Portlandite in the presence of NaOH and KOH

Cement pore solutions are high in pH due to the dominance of alkaline constituents such as NaOH and KOH [33,104,228]. Portlandite precipitation in water occurs between 18.2 and 22.6 mmol/L of Ca(OH)₂ [66]. The inclusion of additional ions such as Na⁺, K⁺ and OH⁻ ions in solution, as KOH or NaOH are introduced, gradually reduces the activity coefficients of Ca²⁺ and OH⁻ through affecting the IS in the activity coefficient models, up to mid molal values (0.3 < IS < 1.0 mol/L), after which point the activity coefficients begin to increase as a result of the ‘salting out’ effect [116]. Ordinarily for the *T* method, the activity coefficient will begin to increase after 0.7 mol/L to compensate for the increasing abundance of like-signed ions in solution, which increases the effect of the long-range coulombic

forces on the ions [136]. Addition of greater concentrations of OH^- due to the increasing level of NaOH or KOH compensates for the reduction of the activity coefficient.

This simple relationship of portlandite solubility decreasing with the addition of NaOH or KOH was well represented by the *T*, *P* and *S* methods, Figure 6.4. There was marginal difference in the initial solubility of portlandite in water at 20.3, 22.1 and 17.2 mmol/L for the *T*, *P* and *S* methods, respectively. A constant under-prediction of the calcium solubility was observed using the Simoes parameters within the NaOH system, however for the KOH system, the fit was near identical to the Pitzer parameters. This may be affected by the impact of the difference of the ionic radii of the aqueous pairing. The ionic radius of K^+ (1.38 Å) is more similar to the ionic radius of OH^- (1.33 Å) than Na^+ (1.02 Å) is compared to OH^- . This improved level of symmetry of the ions may be the cause of the improved fit of the KOH system.

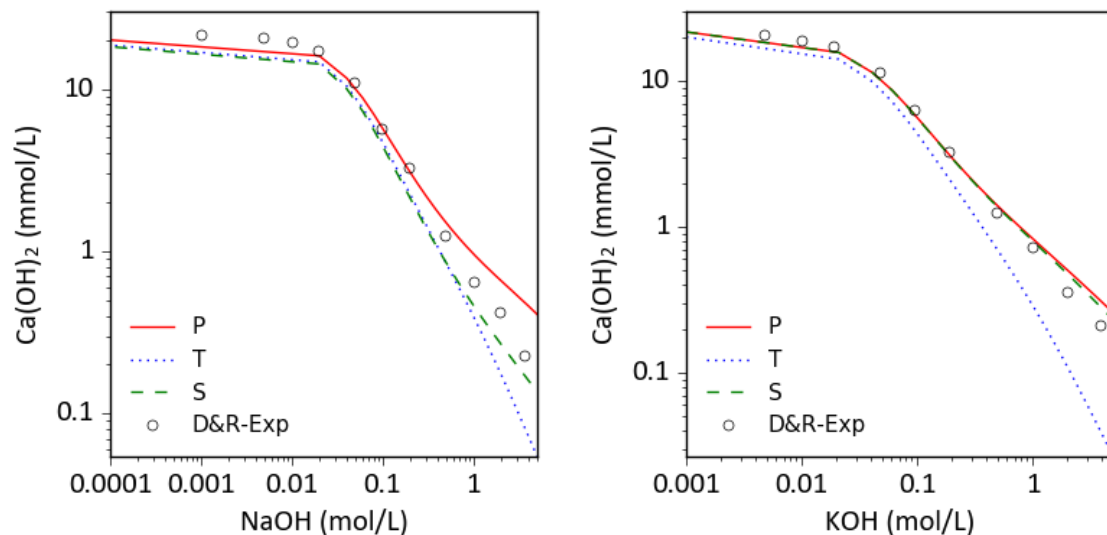


Figure 6.4: Portlandite solubility in a) NaOH and b) KOH, with different aqueous modelling approaches, Pitzer parameter sets, and aqueous species used for calculations. P denotes a fully parameterised Pitzer model, T denotes the Truesdell-Jones equation, and S denotes the Pitzer model including parameters generated only from the Simoes Pitzer estimation equations. Experimental data are from Duchesne and Reardon [66] (D&R-Exp).

6.4.2 Ca-Al-OH

Interactions between calcium and aluminium ions are a key aspect in cement hydration, particularly when considering the aluminium-containing AFm and AFt phases that form due to the $\text{Ca}_2\text{Al}(\text{OH})_6^+$ ions encapsulating SO_4^{2-} or CO_3^{2-} ions, either as columns in the case of AFt phases or as layers for AFm phases [97,229,230]. The generalised structures are $[\text{Ca}_3\text{Al}(\text{OH})_6 \cdot 12\text{H}_2\text{O}]_2 \cdot \text{X}_3 \cdot x\text{H}_2\text{O}$ and $[\text{Ca}_2\text{Al}(\text{OH})_6 \cdot 12\text{H}_2\text{O}]_2 \cdot \text{X} \cdot x\text{H}_2\text{O}$ for AFt and AFm phases, respectively, where X denotes a double negatively charged ion and x denotes the number of moles of water.

Lothenbach et al. produced solubility data over a range of $\text{CaO}/\text{Al}_2\text{O}_3$ molar ratios (0.5 – 1.2) [231]. These results are compared to the outcomes of the different modelling methods in Figure 6.5. Each of the modelling methods provided a prediction of the same phases at each $\text{CaO}/\text{Al}_2\text{O}_3$ ratio, and there were minimal differences in the predicted concentrations of aqueous species remaining in solution. The main aluminium species observed was AlO_2^- (used as a master species in GEMS to represent $\text{Al}(\text{OH})_4^-$), providing over 99.99% of the aluminium in the modelled results. Above a pH of 4.5, AlO_2^- is known to be the dominant aluminium aqueous species [232]. Pitzer parameters exist for Ca^{2+} - OH^- interactions, however, there are no parameters for Ca^{2+} - AlO_2^- interactions, or any other aluminium species interaction parameters within this system. Therefore, incorporation of a Ca^{2+} - AlO_2^- parameter into the Pitzer database using the Simoes parameters was expected to provide a more precise fit of the solubility data (Appendix – Table A8.6).

The comparison of the models displayed that minimal difference was observed predicting the aqueous solution. The Truesdell-Jones equation provides a better fit overall, particularly excelling at predicting the calcium concentration. This is to be expected as the C_3AH_6 Gibbs energy value in the database was fitted using the extended Debye-Hückel equation, in a form similar to the Truesdell-Jones equation [92,150,233]. The introduction of the Ca^{2+} - AlO_2^- interaction parameters provided minimal benefit in terms of improving the quality of prediction of phase formation or solubility.

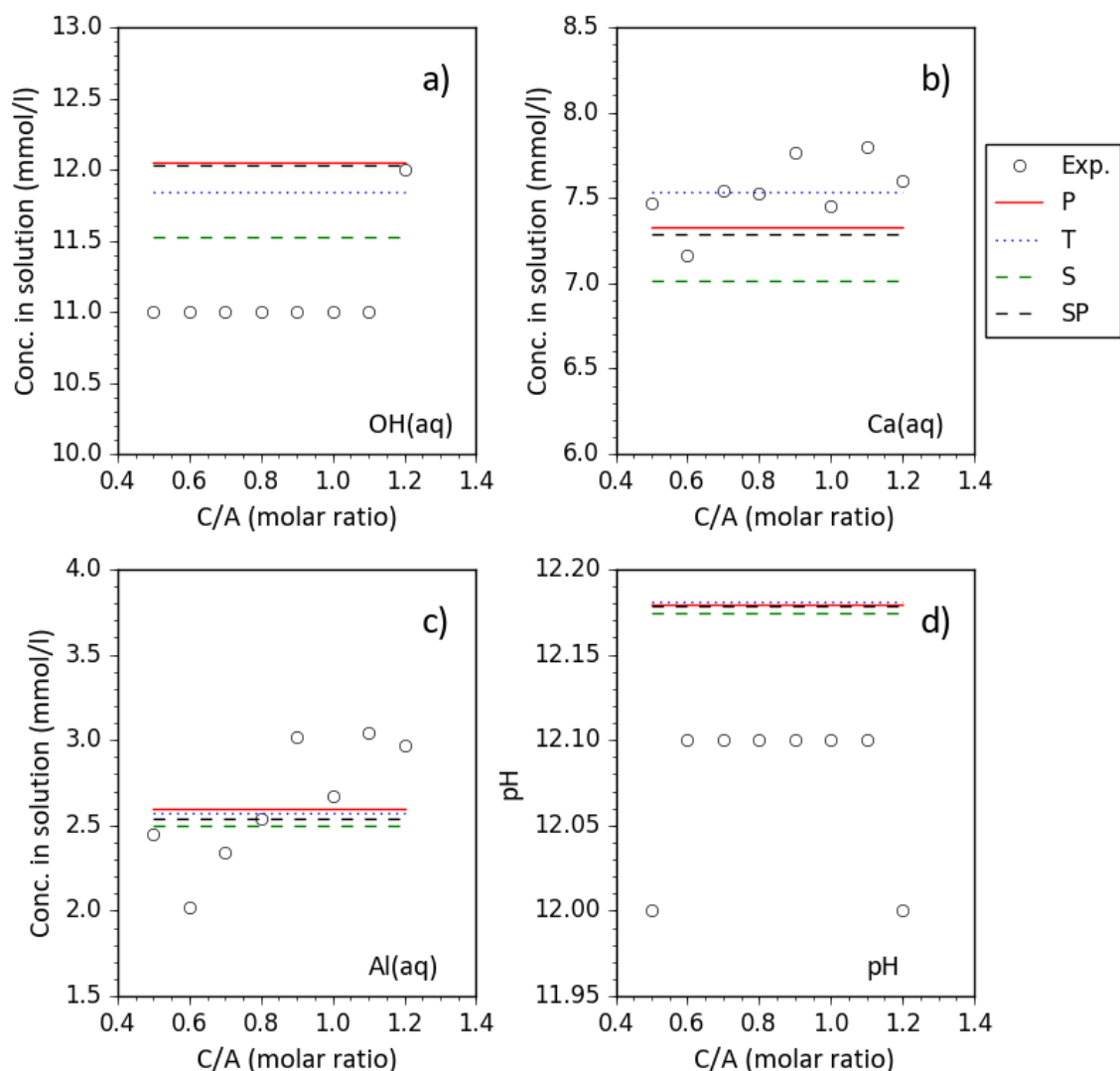


Figure 6.5: Modelling the aqueous solution within the Ca-Al-OH system based on the solubility data of Lothenbach et al. [233]. The Pitzer aqueous solution model using parameters from the literature, P, was compared with parameters obtained from estimating interaction parameters using the equations created by Simoes et al. [225], S; with the literature data being supplemented by estimated parameters, SP; and with the Truesdell-Jones aqueous solution model, T. The variables affected were a) OH⁻ concentration, b) Ca concentration, c) Al concentration and d) pH.

For further examination of the quality of the fit to data, the models were compared with the invariant points determined by Matschei et al. [150] for Ca-Al-OH systems. The stable phase invariant points $C_3AH_6 + Al(OH)_3$ and $C_3AH_6 + CH$ were considered. In the presence of NaOH and KOH, only the $C_3AH_6 + CH$ invariant points determined by Jones et al. [234,235] were considered, due to the low saturation concentration of calcium in the presence of aluminium and in a highly alkaline environment.

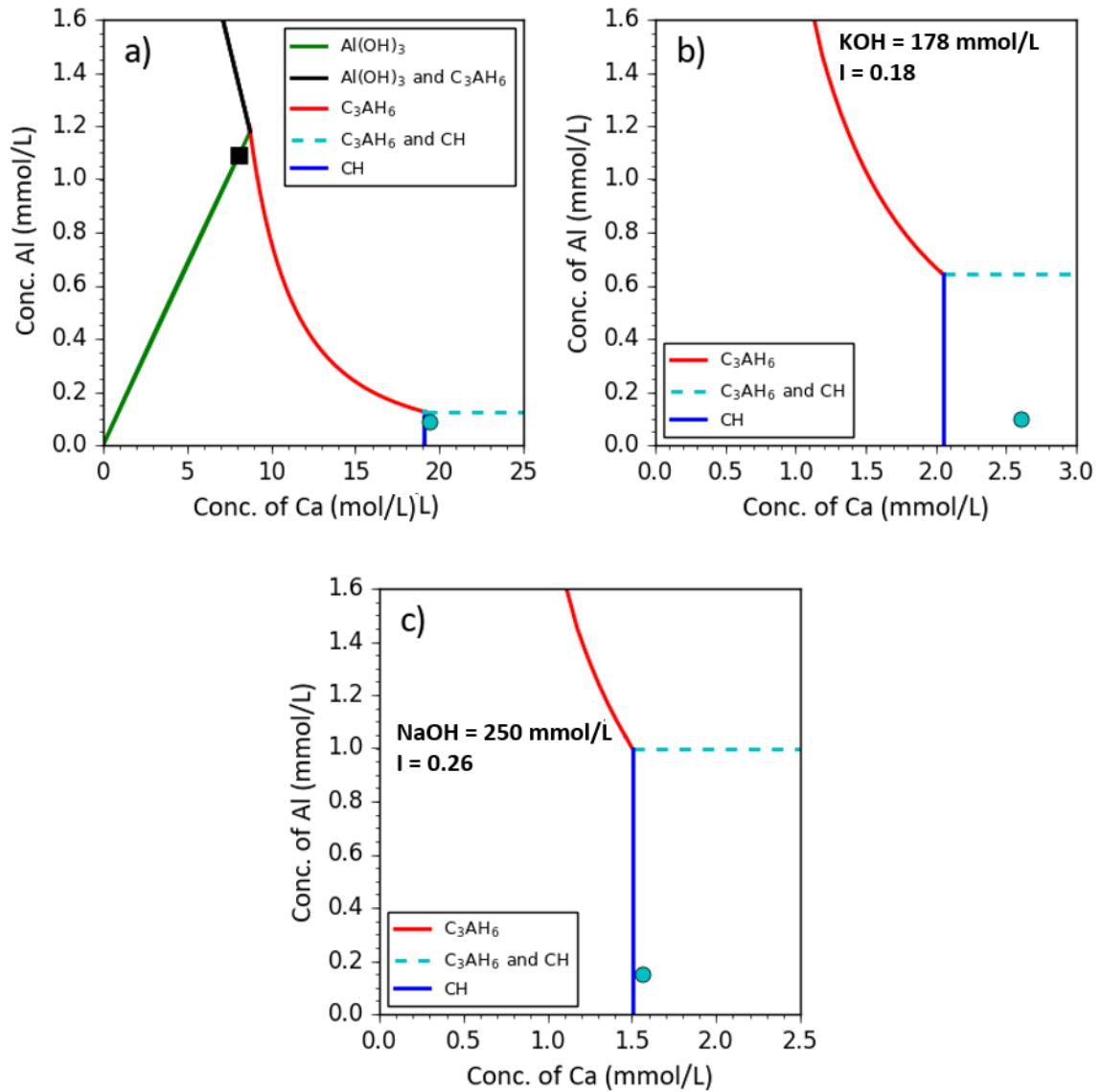


Figure 6.6: Invariant points using the Pitzer model for the a) Ca-Al-OH, b) Ca-Al-K-OH and c) Ca-Al - Na-OH systems. The coloured lines represent the phases present in the modelling at given concentrations. The square represents the invariant point of $\text{Al(OH)}_3 + \text{C}_3\text{AH}_6$ [150] and the circle represents invariant point of $\text{C}_3\text{AH}_6 + \text{CH}$ (a) - [150], b) - [234] and c) - [235].

Table 6.2: Invariant points determined using the P, T, S and SP methods in the Ca-Al-OH system. The term nm denotes a value that was not measured.

Phases at invariant point	Concentration (mmol/L)		pH	Model
	Ca	Al		
No added alkali				
C ₃ AH ₆ + Al(OH) ₃	8.03	1.09	12.10	Experimental [150]
	8.75	1.18	12.14	P
	9.19	1.21	12.10	T
	8.33	1.16	12.13	S
	8.75	1.19	12.14	SP
C ₃ AH ₆ + CH	19.37	0.09	12.52	Experimental [150]
	19.15	0.12	12.47	P
	20.30	0.13	12.48	T
	17.22	0.12	12.46	S
	19.15	0.13	12.47	SP
Alkali = NaOH (250 mmol/L)				
C ₃ AH ₆ + CH	1.56	0.15	13.23	Experimental [235]
	1.50	1.00	13.26	P
	1.63	0.84	13.24	T
	0.77	0.81	13.25	S
	1.56	1.02	13.23	SP
Alkali = KOH (178 mmol/L)				
C ₃ AH ₆ + CH	2.61	0.10	nm	Experimental [234]
	2.05	0.64	13.13	P
	2.31	0.63	13.13	T
	1.22	0.61	13.12	S
	2.10	0.65	13.12	SP

Determination of the invariant points for each model provided good agreement with the experimental data (Table 6.2). Without additional alkalis, the Pitzer parameters were marginally more effective at predicting the solubility of the calcium and aluminium in solution. Inclusion of NaOH and KOH into the system, led to a slight increase in accuracy for determining the $C_3AH_6 + CH$ invariance point for the *T* method as the saturation concentration of aluminium was larger in the other methods. The prediction of calcium saturation was lower in the *P*, *S* and *SP* methods as was the case for the portlandite solubility studies, however the difference between these methods and the *T* method was minimal. The additional $Ca^{2+}-AlO_2^-$ interaction parameters made no improvement due to the low concentration of aqueous species.

6.4.3 Ca-Al-SO₄-OH

Gypsum ($CaSO_4$) acts as a precursor for ettringite ($Ca_6Al_2(SO_4)_3(OH)_{12} \cdot 26H_2O$) and calcium monosulphoaluminate (monosulphate (Ms), $(3CaO \cdot Al_2O_3 \cdot CaSO_4 \cdot 12H_2O)$) formation and is commonly present in PC. The impact on the prediction of the precipitation of gypsum in a Ca-SO₄-OH environment using the various aqueous solution models may be observed in Figure 6.7 and Table 6.3. The invariant point taken from Matschei et al. [150] was similar to the work summarised by Duchesne and Reardon [66] whereby, once portlandite formed, up to 13 mmol/L of $CaSO_4$ was required to form gypsum. There was minimal difference between the different modelling approaches, and the Pitzer model provided a slightly more accurate fit especially when considering the invariant point. The decreased solubility of calcium and sulphate species resulted in precipitation at lower calcium and sulphur levels. The exclusion of the $CaOH^+$ ion and $CaSO_4(aq)$ species from the Pitzer simulations assisted in reducing the content of calcium and sulphur in aqueous form, to create the portlandite-gypsum invariant point.

Removing additional aqueous species from the calculations in the Truesdell-Jones method (e.g. the $CaOH^+$ complex ion, and the $CaSO_4(aq)$ neutral complex) led to decreased solubility of portlandite and gypsum, however when the thermodynamic data were created for the CEMDATA databases, these aqueous species were available to form. Therefore, the aqueous species were included in the formation of common cement hydrates [118,150,151].

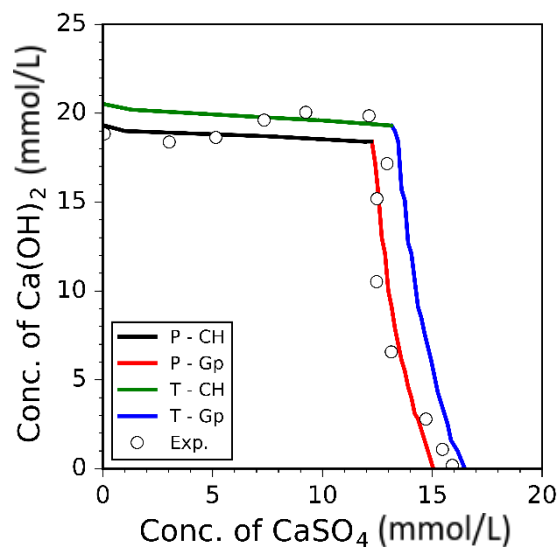


Figure 6.7: Simulated portlandite and gypsum precipitation using the P and T methods. The coloured lines denote when portlandite (CH) or gypsum (Gp) were predicted to precipitate from solution using the different activity coefficient models. Data obtained from Duchesne and Reardon [66].

Inclusion of aluminium into the system greatly reduces the amount of SO_4^{2-} required to form sulphur-containing phases, as Table 6.4 shows. Low solubility of aluminium in solution coupled with the low sulphate content of monosulphate (12.9 wt.%) in comparison with gypsum (46.5 wt.%), meant that only low levels of aluminium and sulphate were required to form invariant points of the multi-phase system. As a result of such low concentrations in solution, there was little variation in the invariant points for the different modelling methods, as the ionic strength was low.

The key instance where a notably large difference occurred was for the $\text{C}_3\text{AH}_6 + \text{CH} + \text{Ms}$ invariant point, whereby the S method was unable to form this point. The S method had predicted much lower calcium saturation concentrations due to the estimated Pitzer parameters created, which reduces the activity coefficient of Ca^{2+} ions when compared to the other methods. The SO_4^{2-} activity coefficient was affected in a similar manner which reduced the SO_4^{2-} saturation concentration. A consequence was that the lower aluminium and sulphate concentration phases were not formed. The first instance of aluminium and sulphur containing phases was at the $\text{Ett} + \text{Ms} + \text{CH}$ invariant point which was four and ten times as much aluminium and sulphur, respectively, compared to the $\text{C}_3\text{AH}_6 + \text{CH} + \text{Ms}$ invariant point.

Table 6.3: Invariant points determined using the *P*, *T*, and *S* methods in the Ca-SO₄-OH system.

Phases at invariant point	Concentration (mmol/L)		pH	Model
	Ca	S		
CH + Gypsum	30.69	12.47	12.43	Experimental [150]
	30.95	12.25	12.43	P
	32.90	13.30	12.43	T
	28.60	8.80	12.43	S

Minimal solubility data exist for Ca-Al-SO₄-OH-K or Ca-Al-SO₄-OH-Na systems, and the data available were recorded before phases such as monosulphate were widely considered in such measurements [234–236]. In the sodium and potassium containing systems the Gyp + CH + Ett and Gyp + CH were considered. The Ca-Al-SO₄-OH system was exposed to 89 and 125 mmol/L of K₂O and Na₂O, respectively.

All of the models accurately predicted the calcium, sulphate and pH concentrations. However, aluminium prediction was 10⁴ times lower in the simulated results when compared to the experimental data. This may be because no ICP analysis was performed by Jones [234,235] and the stable invariance point was determined through undersaturation studies using a fixed mass of aluminium and variable calcium and sulphur masses. Therefore, the calcium and sulphur concentrations at the point of precipitation were more rigorously tested than that for the aluminium content. Comparing the Matschei et al. [150] solubility data in the Ca-Al-SO₄-OH system with those determined by Jones et al. [236], the aluminium concentration was much lower in the more modern results determined by Maschei et al. The calcium and sulphur concentrations were different by up to 5 mmol/L, which provides some credence to the data collected by Jones et al. in the studies used in Table 6.5. Therefore, definitively deciding which model performed better may not be possible based on the presented data. However, an understanding of how the phases behave in the presence of sodium and potassium, and increasing pH, may still be predicted using the data.

Table 6.4: Invariant points determined using the *P*, *T*, *S* and *SP* methods in the Ca-Al-SO₄-OH system.

Phases at invariant point	Concentration (mmol/L)			pH	Model
	Ca	Al	S		
C ₃ AH ₆ + CH + Ms	19.35	0.09	0.001	12.48	Experimental [150]
	19.15	0.12	0.001	12.47	P
	20.40	0.09	0.002	12.47	T
	-	-	-	-	S
	19.22	0.12	0.001	12.47	SP
Ett + Ms + CH	19.35	0.038	0.01	12.48	Experimental [150]
	19.12	0.040	0.01	12.47	P
	20.81	0.040	0.01	12.47	T
	17.19	0.038	0.01	12.47	S
	19.11	0.042	0.01	12.47	SP
Gyp + CH + Ett	30.69	5.70x10 ⁻⁷	12.47	12.43	Experimental [150]
	30.78	5.48x10 ⁻⁷	12.25	12.43	P
	32.59	5.70x10 ⁻⁷	13.23	12.43	T
	24.33	5.39x10 ⁻⁷	8.05	12.39	S
	30.70	6.21x10 ⁻⁷	12.24	12.43	SP
Gyp + CH	30.69	-	12.47	12.43	Experimental [150]
	30.95	-	12.25	12.43	P
	32.90	-	13.30	12.43	T
	28.60	-	8.80	12.43	S
	31.32	-	12.40	12.43	SP

In the presence of additional alkalis, the formation of sulphur-containing phases requires greater levels of sulphate in solution at a higher pH (Table 6.5). Feng et al. [113] and Damidot and Glasser [112,148] modelled the effect of alkalis on the phase formation in the Ca-Al-SO₄-OH system in the presence of NaOH and KOH. Each of the studies concluded that the greater reduction of the Ca²⁺ activity coefficient in the system led to greater levels of predicted precipitation of portlandite, following the trend observed in Figure 6.4. The decreased predicted solubility of portlandite at higher pH consumed calcium from the solution and thus required greater levels of sulphate in solution to form the sulphur-containing phases, when compared to systems without added alkalis.

The IS of the potassium and sodium-containing systems reached a maximum of 0.25 and 0.35 molal, respectively, in the simulations. Both simulations are within the effective IS range of the Truesdell-Jones model, which resulted in minimal difference of the sets of results across the different models. Only the additional inclusion of Ca²⁺-AlO₂⁻ parameters were used in the *SP* method due to the highly parameterised species used, and this additional parameter had minimal impact on the effectiveness of the Pitzer method.

Table 6.5: Invariant points determined using the *P*, *T*, *S* and *SP* methods in the Ca-Al-SO₄-OH systems with the inclusion of KOH or NaOH.

Phases at invariant point	Concentration (mmol/L)			pH	Model
	Ca	Al	S		
KOH (178 mmol/L)					
Gyp + CH + Ett	16.50	4.00x10 ⁻²	66.00	-	Experimental [234]
	17.16	1.29x10 ⁻⁶	69.19	12.44	P
	17.21	1.26x10 ⁻⁶	68.13	12.44	T
	11.09	1.19x10 ⁻⁶	65.40	12.43	S
	16.95	1.32x10 ⁻⁶	69.04	12.44	SP
Gyp + CH	16.65	-	66.90		Experimental [234]
	17.18	-	68.27	12.70	P
	17.26	-	68.11	12.72	T
	11.36	-	65.10	12.69	S
	16.97	-	68.11	12.70	SP
NaOH (250 mmol/L)					
Gyp + CH + Ett	15.39	2.50x10 ⁻²	93.90	12.77	Experimental [235]
	16.24	1.61x10 ⁻⁶	97.86	12.75	P
	15.70	1.47x10 ⁻⁶	95.44	12.44	T
	10.29	1.38x10 ⁻⁶	95.76	12.45	S
	15.70	1.74x10 ⁻⁶	97.47	12.47	SP
Gyp + CH	15.39	-	93.90	12.77	Experimental [235]
	16.18	-	95.20	12.75	P
	15.60	-	95.18	12.78	T
	10.29	-	93.17	12.75	S
	15.73	-	94.99	12.75	SP

6.4.4 Ca-Al-CO₃-OH

Finely ground calcite or limestone (CaCO₃) are used as supplementary cementitious materials in PC and blended cements [95,96], which leads to the formation of calcium monocarboaluminate (monocarbonate (Mc), (3CaO·Al₂O₃·(CaCO₃)·11H₂O)) and calcium hemicarboaluminate (hemicarbonate (Hc), (3CaO·Al₂O₃·(CaCO₃)_{0.5}·11.5H₂O)) phases in the presence of aluminium. The aqueous species for the Ca-Al-CO₃-OH system are generally well parameterised for the Pitzer model although, similar to the Ca-Al-SO₄-OH system, the Ca²⁺-AlO₂⁻ interaction parameters are not available in the literature.

The low content of CO₃²⁻ required to form hemicarbonate (3.9 wt.%) means that there is a lower minimum carbonate concentration required to form a Ca-Al-CO₃-OH phase compared to the case of Ca-Al-SO₄-OH system. The C₃AH₆ + CH + Hc invariant point requires similar calcium and aluminium content, however 1000 times less CO₃²⁻, compared to the amount of SO₄²⁻ required to form C₃AH₆ + CH + Ms. Less CO₃²⁻ was required for each of the stable invariant points, only up to 0.0065 mmol/L of CO₃²⁻ was required at the maximum concentration of this ion (forming calcite + CH predicted using the *T* method).

The Truesdell-Jones equation provided more accurate fitting of the CO₃²⁻ species, however the Pitzer methods were no more than 0.0052 mmol/L different from the experimental results. The Pitzer model provided a more accurate representation of calcium concentrations in solution and the calculated aluminium concentration was similar for both methods.

Similar to the Ca-Al-SO₄-OH system, the main impact on the quality of predictions was from the different selection of aqueous species. The CaOH⁺ and CaCO₃(aq) complexes were not used with the Pitzer model, as the rest of the parameters had been fitted without them. The result of not having these aqueous species available was a reduced calcium and carbonate content required in solution before the phases precipitated. Additional Simoes-method parameters added to the Pitzer database had minimal effect on the saturation concentrations of aqueous species.

Table 6.6: Invariant points determined using the *P*, *T*, *S* and *SP* methods in the Ca-Al-CO₃-OH systems.

Phases at invariant point	Concentration (mmol/L)			pH	Model
	Ca	Al	C		
C ₃ AH ₆ + CH + Hc	19.37	0.09	8.30x10 ⁻⁶	12.48	Experimental [150]
	19.16	0.13	3.26x10 ⁻⁷	12.47	P
	20.38	0.13	1.74x10 ⁻⁶	12.46	T
	17.22	0.12	2.82x10 ⁻⁷	12.47	S
	19.15	0.13	2.99x10 ⁻⁷	12.47	SP
Mc + Hc + CH	19.36	0.04	3.00x10 ⁻⁴	12.48	Experimental [150]
	19.12	0.04	4.83x10 ⁻⁵	12.44	P
	20.38	0.04	2.60x10 ⁻⁴	12.45	T
	17.19	0.03	4.23x10 ⁻⁵	12.45	S
	19.12	0.04	4.54x10 ⁻⁵	12.43	SP
Mc + Calcite + CH	19.35	0.007	0.0065	12.48	Experimental [150]
	19.10	0.008	0.0012	12.43	P
	20.38	0.007	0.0065	12.43	T
	17.18	0.007	0.0011	12.41	S
	19.10	0.007	0.0011	12.43	SP
Calcite + CH	19.34	-	0.0065	12.48	Experimental [150]
	19.10	-	0.0013	12.46	P
	20.38	-	0.0065	12.44	T
	17.17	-	0.0011	12.45	S
	19.10	-	0.0011	12.45	SP

6.4.5 Mg-Al-OH

Magnesium inclusion in BFS and partial amounts in PC cause the precipitation of a hydrotalcite-group layered double hydroxide (LDH) type phase (Mg_(1-x)Al_x(OH)_(2+x)·mH₂O, 0.2 ≤ x ≤ 0.33) [103]. Pitzer parameters for Mg²⁺, and in certain instances MgOH⁺, species are well defined in the literature in the

presence of anions other than OH⁻ [135,143,237,238]. Neither species was parameterised with the AlO₂⁻ species, which in pH environments common to cement acts as a precursor to the formation of hydrotalcite-LDH. The Simoes method is available to provide interaction parameters for the Mg²⁺-AlO₂⁻ interactions, however no ionic radius data were available for MgOH⁺, for similar reasons to why no CaOH⁺ ionic radius data may be found. Only mixed electrolyte terms for H⁺-Mg²⁺ (θ_{cc}) and OH⁻-AlO₂⁻ (θ_{aa}) were obtained for the Pitzer model using terms from the literature [237,239].

A magnesium aluminium hydrotalcite-LDH solid solution model (MA-OH-LDH) was used to test the various aqueous solution models. The MA-OH-LDH model represents a solid solution of hydrotalcite-LDH with a varying Mg/Al of 2 to 4 [124,146]. An aqueous environment containing Mg-Al-OH would expect to yield up to three solid phases, such as brucite, gibbsite and hydrotalcite-LDH. The invariant points of these phases have been studied extensively and are summarised in Table 6.7 [194,195,240,241].

Table 6.7: Invariant points within the Mg-Al-OH system determined from XRD analysis of the crystal structure compared to the invariant points determined from the MA-OH-LDH solid solution model [146].

Invariant Points (Al/Al+Mg, molar ratios)			
Brucite + HT	HT	HT + Gibbsite	Reference
-	0.23	0.33	[241]
-	0.25	0.44	[195] ¹
0.004	0.17	0.33	[194]
0.002	0.25	0.33	This study

¹The samples tested in this study contained hydroxycarbonates.

Simulation of the Mg-Al-OH system was conducted through applying a range of Al/Al+Mg molar ratios, where the total Al+Mg content was set to 1 mol/L in 1 L of water. From Al/Al+Mg = 0.002 – 0.23, the model predicts a region of hydrotalcite-LDH and brucite formation. A pure hydrotalcite-LDH phase forms in the region Al/Al+Mg = 0.25 – 0.33 (Figure 6.8) which is within the range determined experimentally (0.23 – 0.44 [195,241]). A mixed hydrotalcite-LDH and gibbsite region was observed at Al/Al+Mg > 0.33. This phase assemblage was observed for all aqueous solution models.

The low level of solubility of the phases in this system resulted in no difference in the invariant points between the different modelling approaches. The inclusion of the six $B_{MX}^{(0)}$ and six $B_{MX}^{(1)}$ parameters obtained using the Simoes estimations had no effect in this system compared to the under-parameterised Pitzer method and the Truesdell-Jones method.

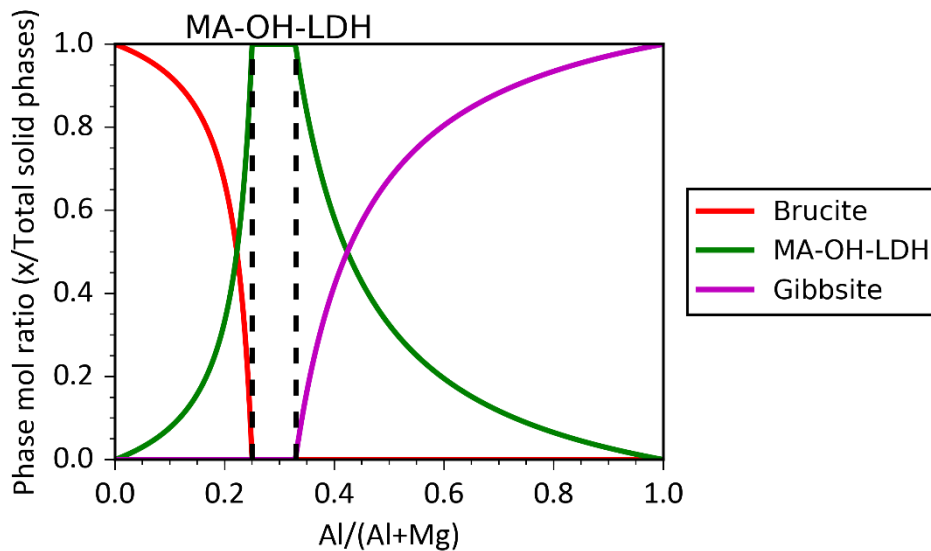


Figure 6.8: Phase diagram of the Mg-Al-OH system constructed through thermodynamic modelling. The MA-OH-LDH phase consists of a solid-solution model fitted by Myers et al. [146].

The Pitzer model for the Mg-Cl-Na-Al-OH system was well parameterised and provided a more thorough basis to assess the precipitation of hydrotalcite-like LDH phases using the various aqueous solution models. The data used were created by Gao and Li [242] to assess the solubility of $\text{Mg}_4\text{Al}_2(\text{OH})_{14}\cdot 3\text{H}_2\text{O}$, which is an end-member in the MA-OH-LDH model. The MA-OH-LDH model was used in this study as opposed to restricting the solid composition to the single phase $\text{Mg}_4\text{Al}_2(\text{OH})_{14}\cdot 3\text{H}_2\text{O}$, due to the flexibility of the MA-OH-LDH model at predicting the chemical structure of hydrotalcite, and because the MA-OH-LDH model has been used in previous BFS cement hydration modelling studies [122,124].

The simulation consisted of $\text{Al}(\text{OH})_3$ and $\text{Mg}(\text{OH})_2$ at concentrations of 62.5 and 125 mmol/L, respectively in 1 L of water. A varying concentration of NaCl from 0 – 2.5 mol/L was added to the system. The comparison of the results of the different modelling methods in comparison to the solubility data [242] can be seen in Figure 6.9.

Pitzer parameters for the Mg-Cl-Na-Al-OH system required minimal additions due to the work that has been conducted in the past modelling magnesium oxychloride solubility [100,110].

Considering the sum of squared errors (SSE) across the eight NaCl concentrations, Table 6.8, the Pitzer parameters and SP method performed better than the S and T methods when considering the pH, magnesium concentration and aluminium concentration. The pH was most accurately portrayed by the SP method, which had an incremental improvement on the Pitzer parameters (Figure 6.9a). The Simoes parameters performed similarly to the Pitzer parameters up until 0.5 mol/L of NaCl, however the S method became steadily less effective, as did the Truesdell-Jones equation.

Table 6.8: The sum of squared errors (SSE) for the pH, OH⁻, Mg and Al concentrations in solution, comparing the thermodynamic modelling results in GEMS to the experimental data for the Mg-Al-Na-Cl-OH system. The four aqueous solution model methods compared were the Pitzer model with literature parameters (P), Pitzer model using estimated Simoes parameters (S), Pitzer parameters from the literature supplemented by Simoes parameters (SP) and the Truesdell-Jones equation (T).

pH (SSE)	Concentration (SSE – x10 ⁻⁸ mmol/L)			Model
	OH ⁻	Mg	Al	
0.13	14.50	0.97	2.89	P
0.22	16.00	2.66	3.15	T
0.15	8.95	1.25	3.55	S
0.12	9.87	1.05	2.92	SP

Across the four modelling approaches the AlO₂⁻ and Mg²⁺ were the dominant species of their respective elements in solution (both above 95%). Therefore, AlO₂⁻-Mg²⁺ interactions were added to the SP parameters. Additionally, Mg²⁺-OH⁻ parameters were also available. The effect of the Pitzer parameters on the activity coefficients of the OH⁻, AlO₂⁻ and Mg²⁺ ions (Figure 6.9d, e and f, respectively) can highlight the impact of the modelling method and the parameters used on the system. All of the models were within a factor of 10 of each other when predicting the AlO₂⁻ concentration, however the difference between the activity coefficients was as high as 72.3 % (S, 0.96 cf. P, 0.45). For the Mg²⁺ species, the difference was more significant as the highest difference was

105.9 % (SP, 0.39 cf. T, 0.12). The OH^- activity coefficient was least affected as the greatest difference was 30.2 % (S, 0.8 cf. P, 0.59). The maximum differences were observed at an NaCl concentration of 2.5 mol/L.

The much greater increase of γ_{OH^-} , $\gamma_{\text{AlO}_2^-}$ and $\gamma_{\text{Mg}^{2+}}$ at high ionic strength using the parameters determined by the *S* method led to decreasing levels of ions required to form MA-OH-LDH. Using the *P* and *SP* parameters, the decrease in Mg^{2+} activity coefficients at $0 < \text{NaCl} < 0.75$ mol/L, followed by an increase at $\text{NaCl} > 0.75$ mol/L, caused the concentration of magnesium required to form MA-OH-LDH to increase and then decrease as NaCl was added. Simultaneously, the levelling and lower $\gamma_{\text{AlO}_2^-}$ causes more aluminium to be required to form MA-OH-LDH as the NaCl concentration increased. The activity of AlO_2^- was greatly influenced by the $\text{Na}^+\text{-AlO}_2^-$ parameters in the *SP* method, taken from Park and Englezos [239], as there was infinitesimal variation in the AlO_2^- activity coefficient between the *P* and *SP* method. The Park and Englezos $\text{Na}^+\text{-AlO}_2^-$ parameters are up to two orders of magnitude smaller than the Simoes parameters for the same species, which is the cause of the large difference in the AlO_2^- activity coefficient between the *P* and *S* methods.

The inclusion of $\text{Mg}^{2+}\text{-OH}^-$ parameters had an impact on $\gamma_{\text{Mg}^{2+}}$ in the *SP* method compared to the *P* method, as $\gamma_{\text{Mg}^{2+}}$ was 0.1 units higher at $[\text{NaCl}] = 2.5$ mol/L in the *SP* method. The $\text{Mg}^{2+}\text{-OH}^-$ parameters included with the *SP* method were of a similar magnitude to the $\text{Mg}^{2+}\text{-Cl}^-$ parameters. The comparable difference between the parameters allowed the Simoes parameters to affect $\gamma_{\text{Mg}^{2+}}$. Further evidence of this can be observed in the difference in γ_{OH^-} , which varies between the *P* and *SP* methods due to the inclusion of $\text{Mg}^{2+}\text{-OH}^-$ parameters in the *SP* method. The lack of change in $\gamma_{\text{AlO}_2^-}$ with the inclusion of the $\text{Mg}^{2+}\text{-AlO}_2^-$ parameters indicates that it had minimal effect on the system and did not affect $\gamma_{\text{Mg}^{2+}}$. Overall, the inclusion of the additional Simoes-method parameters to the Pitzer database had a minimal effect on the solubility of MA-OH-LDH.

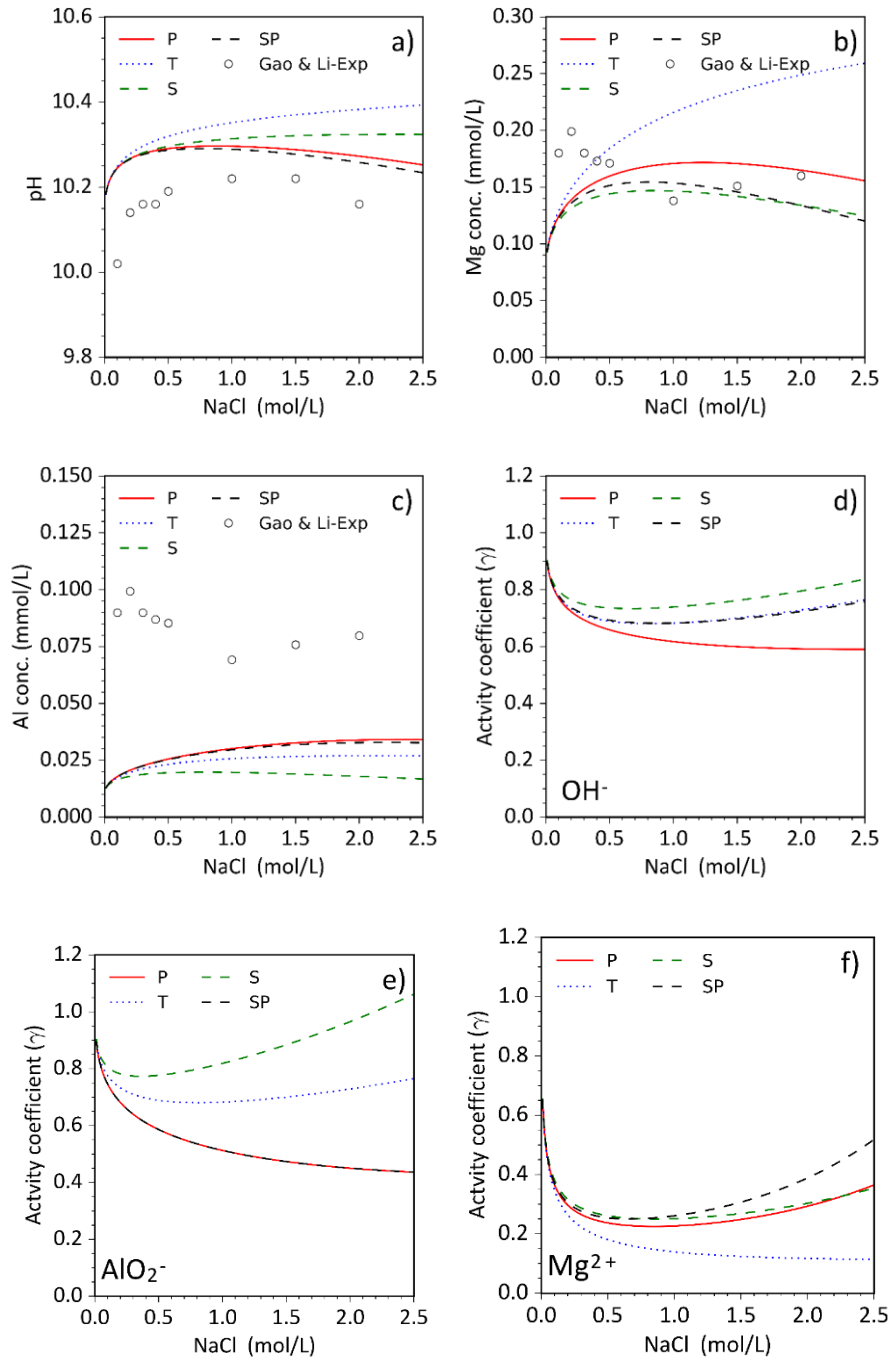


Figure 6.9: Aqueous solution properties in the Mg-Cl-Na-Al-OH system ($\text{MgOH}_2 = 0.125 \text{ mol/L}$, $\text{Al}(\text{OH})_3 = 0.0625 \text{ mol/L}$, and $0 < \text{NaCl} < 2.5 \text{ mol/L}$), considering the effect of increasing concentration of NaCl on: a) pH, b) magnesium solubility, c) aluminium solubility, d) γ_{OH^-} , e) $\gamma_{\text{AlO}_2^-}$ and f) $\gamma_{\text{Mg}^{2+}}$, using different aqueous solution methods. P denotes a fully parameterised Pitzer model, T denotes the Truesdell-Jones equation, S denotes the Pitzer model including parameters generated only from the Simoes Pitzer estimation equations and SP denotes the Pitzer parameters supplemented with Simoes parameters. Solubility data were taken from Gao and Li [242].

6.4.6 Ca-Si-Al-OH

The main hydrate phase in blended cement C-A-S-H is comprised of aluminosilicate chains which encompass a calcium oxide layer (Figure 6.10a). The composition of this phase is highly dependent on the chemical environment of the system which causes variation in the Ca/Si and Al/Si molar ratios within the phase [57,58,63,85].

A water-filled interlayer space between two silicate or aluminosilicate chains allows for the sorption of cations which act as charge balancers. In the presence of high concentrations of calcium and additional alkalis (e.g. Na⁺ and K⁺), the increased OH⁻ ions reduce the content of bridging sites in the silicate chains and increase the Ca/Si ratio of the C-S-H/C-A-S-H phases (Figure 6.10b) [59].

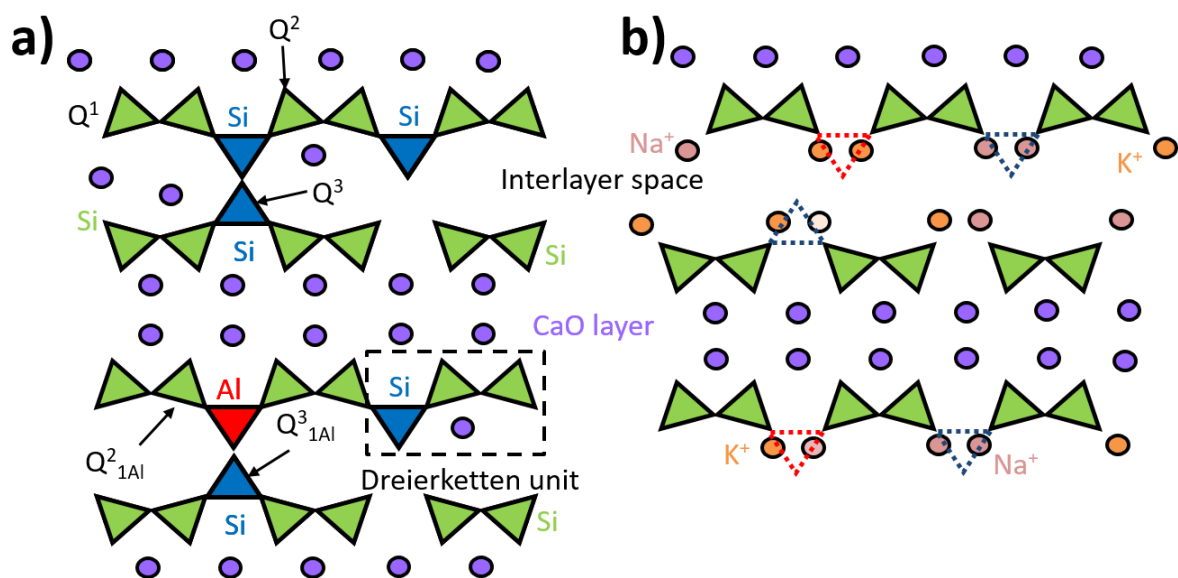


Figure 6.10: The C-S-H/C-A-S-H structure using a) dreierketten units and b) in high Na⁺ and K⁺ concentrations. The green triangles represent paired silicate dimers, blue triangles are bridging silicon tetrahedra, the red triangles represent silicon replacement with aluminium, the purple, orange and pink circles represent Ca²⁺, K⁺ and Na⁺ ions respectively.

6.4.6.1 Ca-Si-OH

Walker et al. [65] conducted a thorough review of the solubility of C-S-H and the value of the studies created in the literature. Based on rigorous selection criteria, Walker et al. were able to reduce an identified 777 data entries from the literature to 207 reliable points, and included an additional 26 at

low Ca/Si (0.19 – 0.83) [53,54,65,69–83]. This data-set was used in this study to compare the different aqueous modelling methods with the CSHQ model developed by Kulik [64].

Pitzer parameters with calcium and silicon interactions do not exist in the literature. The disordered nature of C-S-H, low solubility and low ionic strength of the solutions used in determining the solubility data are likely to be the main cause. Various aqueous models using different software packages exist and the current model used as default in the CEMDATA14 database, the CSHQ model, consistently over-predicts silicon concentrations in solution [64]. The model is limited to a minimum Ca/Si of 0.67 and maximum Ca/Si of 1.67 as a result of reaching the solubility points of amorphous silica and portlandite, respectively. The CSHQ model developed by Kulik [64] was used to simulate the Ca-Si-OH systems in sections 6.4.6.1 and 6.4.6.2 of this study.

Further consideration was given to the aqueous species available in the system because a number of aqueous species interactions were not parameterised. Figure 6.11a and b depict the effect of the Ca/Si ratio on the aqueous speciation for calcium and silicon, respectively. The modelled work shown in Figure 6.11 was performed using the Truesdell-Jones equation. Silicon was split between the HSiO_3^- , $\text{CaSiO}_3(\text{aq})$ and $\text{SiO}_2(\text{aq})$ species in solution. Increasing calcium content caused the $\text{SiO}_2(\text{aq})$ species to no longer appear at $\text{Ca/Si} > 1.0$, by which point the $\text{CaSiO}_3(\text{aq})$ species became dominant in solution as the Ca/Si ratio exceeded the Ca/Si molar ratio of the $\text{CaSiO}_3(\text{aq})$ species ($\text{Ca/Si} = 1.0$). A declining content of silicon in solution caused the silicon concentration in solution to be heavily dependent on the $\text{CaSiO}_3(\text{aq})$ species. However, as a mole fraction of all of the calcium in solution, the $\text{CaSiO}_3(\text{aq})$ declined as the calcium content increased, due to the increasing pH rising to 12.5. At a pH of 11.7 and Ca/Si of 1.04, the concentration of CaOH^+ becomes more prominent than the $\text{CaSiO}_3(\text{aq})$. Miron et al. [109] determined that there are no solubility studies that provide adequate thermodynamic data for the $\text{CaSiO}_3(\text{aq})$ species, however it has provided a useful addition to modelling databases to improve calcium and silicon solubility studies up to temperatures of 500 °C.

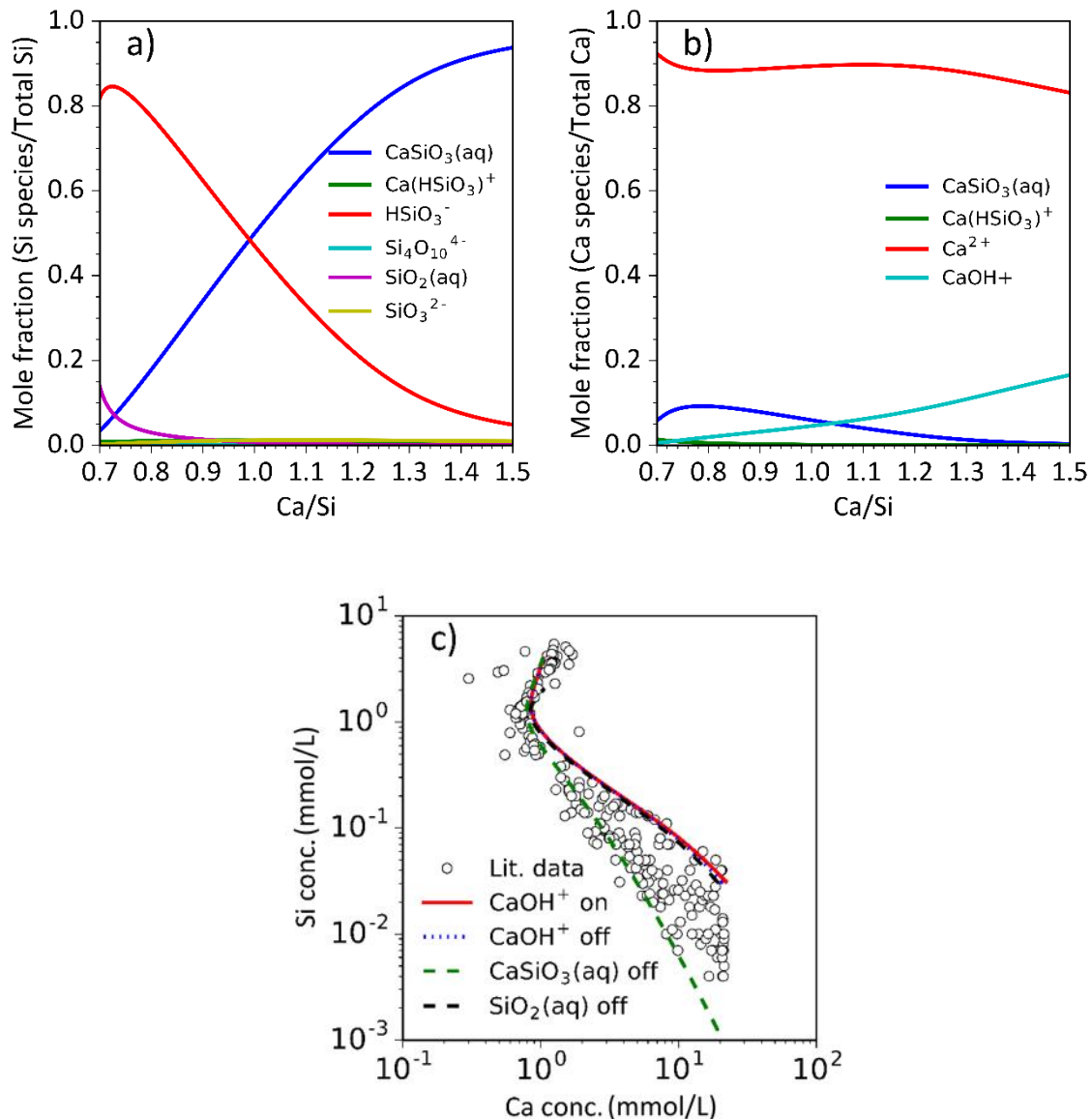


Figure 6.11: Considering the aqueous speciation of a) calcium and b) silicon in the Ca-Si-OH system, and c) how removing different aqueous species impacts the solubility of calcium and silicon using the Truesdell-Jones equation. Experimental data collected from the literature: [53,54,65,69–83].

Altering the chemical species available in the system caused observable effects on calcium and silicon solubility (Figure 6.11c). Removing CaOH^+ (from Figure 6.11c: the blue dotted line – ‘ CaOH^+ off’) or $\text{SiO}_2(\text{aq})$ (from Figure 6.11c: the black dotted line – ‘ $\text{SiO}_2(\text{aq})$ off’) species had minimal impact on the predicted solubility of C-S-H, however due to the high dependence of silicon species on formation of $\text{CaSiO}_3(\text{aq})$ at $\text{Ca/Si} > 1.0$, the silicon concentration was significantly affected; when the $\text{CaSiO}_3(\text{aq})$ species was removed (from Figure 6.11c: the green dotted line – ‘ $\text{CaSiO}_3(\text{aq})$ off’), the silicate concentration was reduced by up to 1000 times in solution. When the $\text{CaSiO}_3(\text{aq})$ species was removed

from the system, the CaOH^+ concentration increased up until portlandite began to form. This effect occurred for each of the modelling approaches (*P*, *T*, *S* and *SP* methods)

In the systems studied in the previous sections ($\text{Ca-Al-SO}_4\text{-OH}$, $\text{Ca-Al-CO}_3\text{-OH}$ and Mg-Al-OH), the aqueous neutral complexes were removed, however in the Ca-Si-OH system, due to the large detrimental impact of the removal of $\text{CaSiO}_3(\text{aq})$ (from Figure 6.11c: the green dotted line – ‘ $\text{CaSiO}_3(\text{aq})$ off’) on the silicon concentration, it was maintained for the Pitzer models.

The Pitzer methods had CaOH^+ and $\text{SiO}_2(\text{aq})$ species removed from among the possible aqueous species. Removal of these species with the use of the different aqueous models proved to have little effect on the pH, calcium and silicon in the aqueous solution, Figure 6.12a and b, respectively. Figure 6.11a and b shows that the CaOH^+ and $\text{SiO}_2(\text{aq})$ species were ever more than 20% of the Ca or Si present, respectively, and that was at extreme compositions, hence these species had minimal impact on the system. The different modelling methods did provide a variation on the Ca/Si at different calcium and silicon concentrations, Figure 6.12c and d, respectively.

Using the known ionic radii of SiO_3^{2-} and HSiO_3^- from the literature [226,227], it was possible to estimate interaction parameters with calcium for these species. The $\text{Ca}^{2+}\text{-SiO}_3^{2-}$ interaction parameters had no effect on the system due to the low concentration of SiO_3^{2-} in solution as shown in Figure 6.11a. Inclusion of $\text{Ca}^{2+}\text{-HSiO}_3^-$ parameters had minimal impact on the system overall but reduced the saturation concentrations of silicon in the *S* and *SP* methods. The observable deviation of the solubility of silicon of the *S* and *SP* methods from the *P* method occurs at 0.7 mmol/L of silicon in solution. The HSiO_3^- species becomes less prevalent in solution as the calcium content increases, however due to the low concentration of silicon overall, it decreases the saturation concentration of silicon within the Ca/Si range of 0.72 to 1.5.

The $\text{Ca}^{2+}\text{-HSiO}_3^-$ parameters increased the saturation concentration of calcium in the *SP* method compared to the *P* method, creating a maximum difference of 0.03 mmol/L (at Ca/Si = 1.63) between the predictions obtained using the two sets of parameters. This alteration affected the aqueous phase composition at which portlandite began to precipitate once the CSHQ model reached its maximum Ca/Si ratio of 1.63. The calcium concentration required to form portlandite in each model is

summarised in Table 6.9. The concentrations are the same for portlandite solubility from section 6.4.1: *Portlandite*. In the previous section, the *SP* method was not tested as the Simoes method provided no additional parameters.

Table 6.9: Concentration of calcium required in the Ca-Si-OH system for portlandite to precipitate.

Calcium concentration (mmol/L)	Model
19.10	P
20.40	T
17.20	S
19.13	SP

The Pitzer models predicted that less calcium was required to reach the portlandite phase boundary than the Truesdell-Jones equation. This effect is mainly attributed to the removal of the CaOH^+ species from the Pitzer methods. A definitive point defining at what concentrations does portlandite precipitate in the presence of C-S-H has not been determined experimentally, due to the gel-like nature of the phase and the varying solubility data [54,65,243].

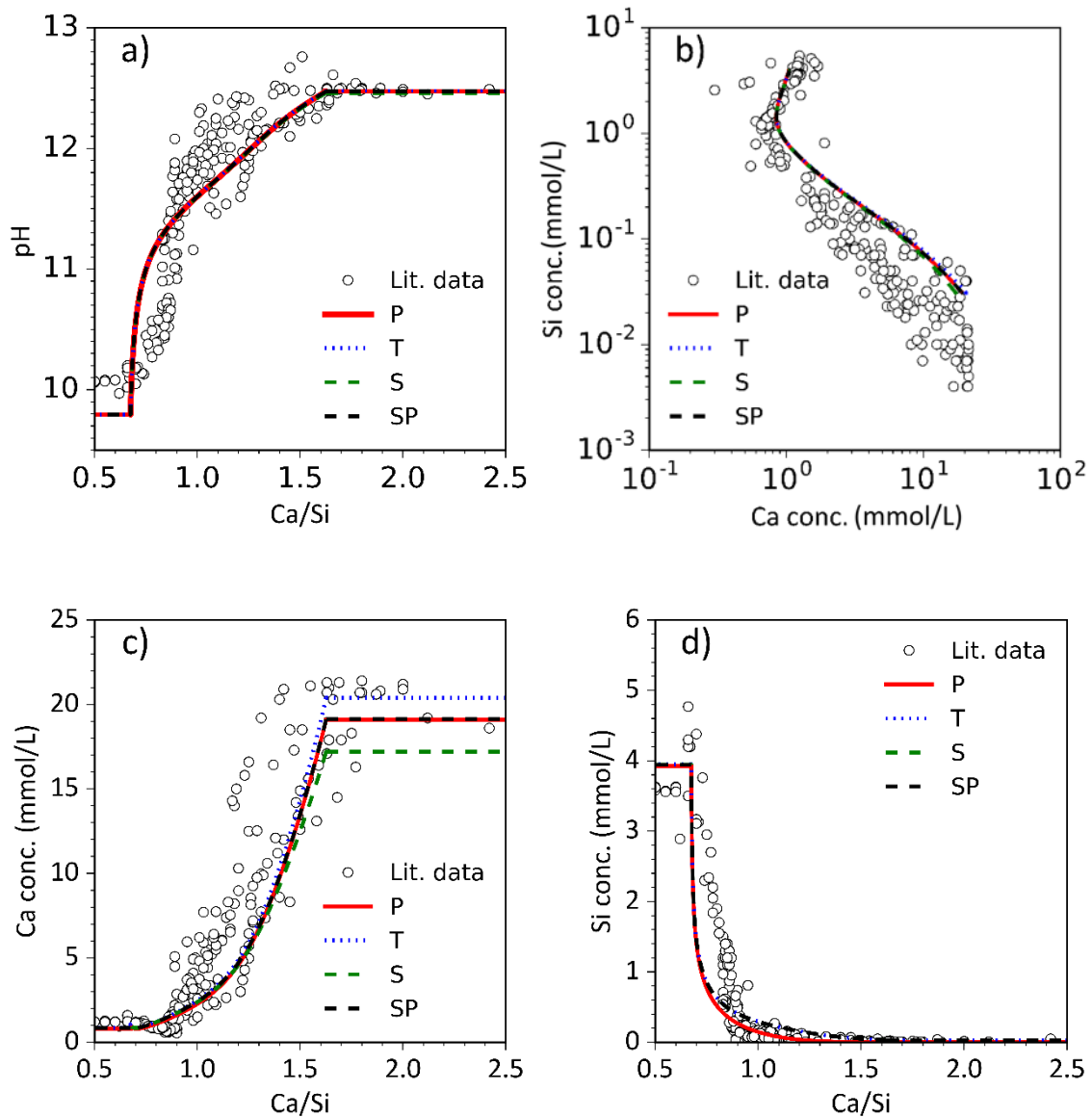


Figure 6.12: Comparison of a) pH, b) calcium vs. silicon concentration, c) calcium concentration vs. Ca/Si of the C-S-H, and d) silicon concentration vs. Ca/Si of the C-S-H, in the Ca-Si-OH system. Literature data are from [53,54,65,69–83], compared to predictions from different aqueous solution models, with the CaOH^+ and $\text{SiO}_2(\text{aq})$ species removed from the Pitzer models. The Pitzer aqueous solution model using parameters from the literature is denoted P; with parameters obtained from estimating interaction parameters using method of Simoes et al. [225] is shown as S; the literature data supplemented by estimated parameters is SP; and the Truesdell-Jones aqueous solution model, T.

6.4.6.2 Impact of Na₂O and K₂O

The alkali sorption experiments conducted by Hong and Glasser [59] were used as a point of comparison for the different modelling approaches in sodium and potassium environments. Varying molar ratios of Ca(OH)₂ and SiO₂ were used, at a liquid/solid mass ratio of 15 (0.6 g solids in 9 g of water). The Ca/Si molar ratios studied were 0.85, 1.2, 1.5 and 1.8, at alkali concentrations of 1, 5, 15, 50, 100 and 300 mmol/L. For ease of visualisation, only the data for 1, 50 and 300 mmol/L of Na₂O and K₂O are presented in Figure 6.13. Calcium saturation concentration and pH were the available comparative values from that study. The NaOH (aq) and KOH (aq) complex species were removed from the Pitzer models as Pitzer parameters for these species are not parameterised, and all other species that were used to model the Ca-Si-OH system remained the same as for section 6.4.6.

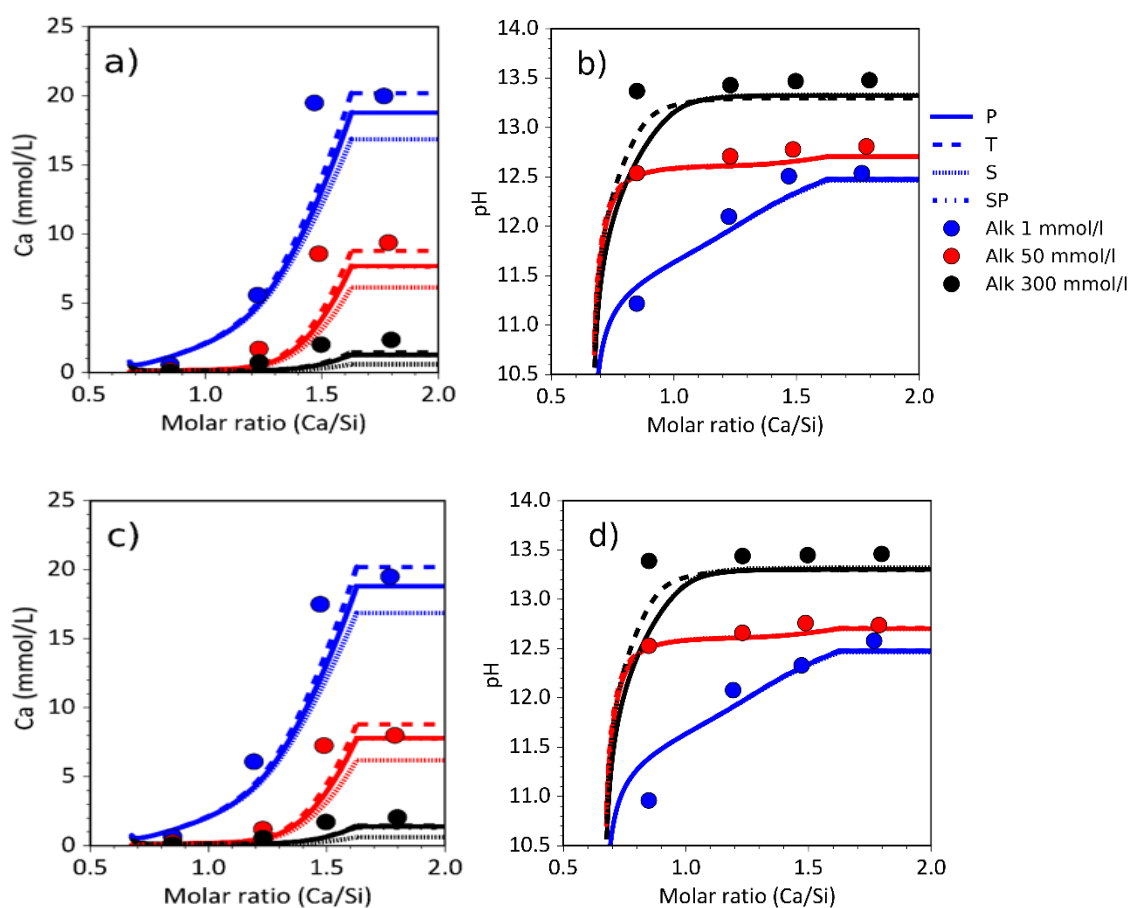


Figure 6.13: Modelling the impact of K₂O concentration on the a) calcium concentration and b) pH, and the impact of Na₂O concentration on the c) calcium concentration and d) pH. The concentrations of K₂O and Na₂O modelled were 1, 50 and 300 mmol/L, for models *P*, *S*, *SP*, and *T*. Solubility data taken from Hong and Glasser (filled circles) [59].

Pitzer parameters were developed for the interactions of $\text{Na}^+\text{-HSiO}_3^-$ and $\text{K}^+\text{-HSiO}_3^-$ by Provis et al. [244] through modelling silicon speciation in highly alkaline environments and compared with ^{29}Si NMR results. The Q^0 species with a charge of -1 was used from the Provis et al. [244] study as this was representative of the aqueous HSiO_3^- species.

The different modelling methods had little impact on the calculated pH in relation to Ca/Si for the different alkali concentrations, in the range $\text{Ca/Si} > 1.0$ (Figure 6.13b and d). As was the case in the Ca-Si-OH system, the variation in calcium solubility was minimal between the different methods until the point of portlandite precipitation, where the calcium concentration required to form portlandite followed the order: $\text{T} > \text{P/SP} > \text{S}$. The CSHQ model was effective at modelling the inclusion of sodium and potassium in solution, as the solubility of portlandite reduced at higher concentrations of alkalis, as was observed experimentally [59].

Table 6.10: The logarithm of the sum of square errors (SSE) for calcium and pH concentration calculated across the 1, 5, 15, 50, 100 and 300 mmol/L concentrations of Na_2O or K_2O , using the different modelling methods. Solubility data taken from Hong and Glasser [59]. The Pitzer aqueous solution model, P, was compared with parameters obtained from estimating interaction parameters using the equations created by Simoes et al. [225], S; with the literature data being supplemented by estimated parameters, SP; and with the Truesdell-Jones aqueous solution model, T.

Alkali	$\log \text{SSE}([\text{Ca}^{2+}]/[\text{mmol/L}])$	$\log \text{SSE}(\text{pH})$	Model
K_2O	2.25	-0.44	P
	2.18	-0.46	T
	2.40	-0.44	S
	2.25	-0.44	SP
Na_2O	1.98	-0.14	P
	1.97	-0.15	T
	2.10	-0.13	S
	1.98	-0.14	SP

The logarithm of the sum of squared errors (SSE) was calculated across the 1, 5, 15, 50, 100 and 300 mmol/L concentrations of Na_2O or K_2O for each method, Table 6.10. The IS did not exceed 0.3 for

these systems, therefore the inclusion of the Pitzer models had little effect on the outcome, as was shown in the minimal difference in the log SSE values.

6.4.6.3 Ca-Al-Si-OH

The C-A-S-H model used to describe the solid phase formation in the Ca-Al-Si-OH system was updated from the C(-N)-A-S-H solid solution model developed by Myers et al. [146]. The sodium end-members were removed and the JenD end-member from the CSHQ model [64] was included in the updated model (Table 6.11). The solid-solution model used six end-members which had a chemical composition range of $0.66 < \text{Ca/Si} < 2.24$ and $0 < \text{Al/Si} < 0.26$. Each of the six end-members contained calcium and silicon, however, only two end-members contained aluminium. The applicability of this ideal solid solution model and the effect of the different aqueous models were tested using the solubility data collected by L'Hopital et al. [63] for the Ca-Al-Si-OH system. The modelling was conducted by replicating the various molar ratios used in the study, with the mass of the precursor solids (CaO, SiO₂ and CaO·Al₂O₃) set to 2 g and the water/solids mass ratio held constant at 45.

Table 6.11: Thermodynamic properties of C-S-H and C-A-S-H end-members in the model used for simulation of C-A-S-H formation. Standard thermodynamic properties at 25 °C and 1 bar

Phases	ΔH_f° (kJ mol ⁻¹)	ΔG_f° (kJ mol ⁻¹)	Ca/Si (molar ratio)	Al/Si (molar ratio)	Reference
5CA, C _{1.25} A _{0.125} S ₁ H _{1.625}	-2491	-2293	1.25	0.25	[146]
INFCA, C ₁ A _{0.15625} S _{1.1875} H _{1.65625}	-2551	-2343	0.84	0.26	[146]
JenD, C _{1.5} S _{0.67} H _{2.5}	-2401	-2169	2.24	-	[64]
T2C, C _{1.5} S ₁ H _{2.5}	-2721	-2298	1.50	-	[122]
T5C, C _{1.25} S _{1.25} H _{2.5}	-2780	-2517	1.00	-	[146]
TobH, C ₁ S _{1.5} H _{2.5}	-2831	-2560	0.66	-	[146]

The results obtained using the C-A-S-H model for each modelling approach were similar for each model, as shown by the log SSE values summarised in Table 6.12, therefore only the results obtained for the Pitzer model are displayed in Figure 6.14 and Figure 6.15.

Table 6.12: Log SSE values, comparing the calculated results using the C-A-S-H end-member model with measured solubilities in the Ca-Al-Si-OH system [63].

Log SSE(Molar ratios)		Log SSE(Concentration/[mmol/L])				Log SSE(pH)	Model
Ca/Si	Al/Si	Ca	Si	Al	OH ⁻		
-0.88	-1.22	2.03	1.94	-0.93	2.49	-0.22	P
-0.89	-1.22	2.00	1.65	-0.92	2.40	-0.23	T
-0.86	-1.22	2.15	1.94	-0.94	2.36	-0.21	S
-0.88	-1.22	2.03	1.94	-0.93	2.49	-0.22	SP

A greater range of calcium containing end-members provides an improved description of the Ca/Si ratio compared to the Al/Si ratio in the C-A-S-H phase (Figure 6.14a and Figure 6.14b, respectively). The C-A-S-H model was most accurate for compositions of Ca/Si > 0.8 and Al/Si < 0.33. The Ca/Si was inaccurate by more than 0.1 for three instances: Ca/Si = 0.6 and Al/Si = 0.33, Ca/Si = 0.8 and Al/Si = 0.33 and, Ca/Si = 1.4 and Al/Si = 0.1. The Ca/Si was over-predicted in the Ca/Si = 0.6 and 0.8 systems due to the increased pH following the replacement of SiO₂ by CaO·Al₂O₃ (CA). The higher pH shown in Figure 6.14c caused the higher Ca/Si end-members to become more stable, thus increasing the Ca/Si ratio.

The model prediction of Al/Si ratio was less accurate due to the limited number of aluminium-containing end-members within the model. Additional end-members were introduced with chemical compositions Ca/Si = 1.4 and Al/Si 0.05; and Ca/Si 1.0 and Al/Si = 0.1; to provide greater diversity of the Al/Si values. However, due to the stability of the current end-members, the additional end-members did not have any impact on the system when included. There was generally good agreement at low and mid-range Al/Si values, but Al/Si was generally over-predicted at Ca/Si > 1.0 and Al/Si > 0.1 as the bulk composition of the system approached the chemical composition of the 5CA and INFCA end-members.

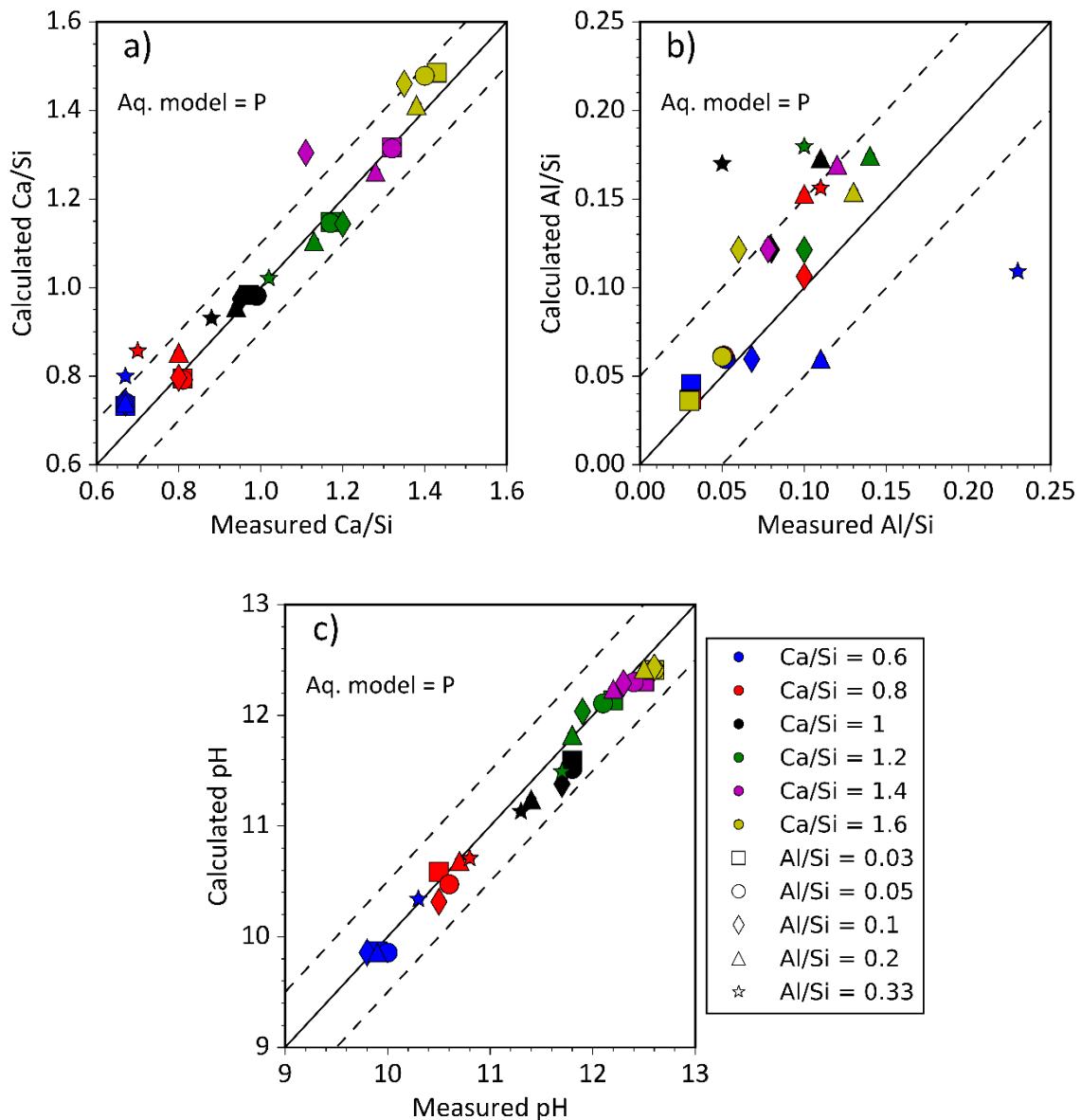


Figure 6.14: Comparison of the measured values (from L'Hopital et al. [63]) for a) Ca/Si, b) Al/Si and c) pH versus the values calculated using the C-A-S-H end-member model. The Pitzer model (P) was used to compare the datasets in the above graphs. The different colours represent the Ca/Si ratios in the bulk solution, ranging from 0.6 to 1.6, and the different shapes represent a range of Al/Si ratios from 0.03 to 0.33. The dotted lines indicate the estimated experimental error for the data acquisition, represented as difference from the solid line $y = x$.

The predicted concentration of the hydroxyl ion, silicon and calcium aqueous species, were within an order of magnitude of the measured values, Figure 6.15. Under-prediction of aluminium in solution occurred for the low Al/Si systems (0.03 and 0.05) as the available aluminium was withdrawn into the C-A-S-H model (Figure 6.15a). It must be noted that the aluminium concentration in the experimental

data used here was recorded as <0.0037 mmol/L for the Al/Si = 0.03 and 0.05 systems (denoted by the red dotted line in Figure 6.15a), as the aluminium concentration was below the detectable limit [63], therefore the much lower aluminium concentration determined using the end-member model may be more accurate than the plotted results indicate. The lowest silicon concentration using the end-member model was 0.03 mmol/L, which was similar to that determined in the C-S-H system due to the inclusion of the TobH end-member for both systems.

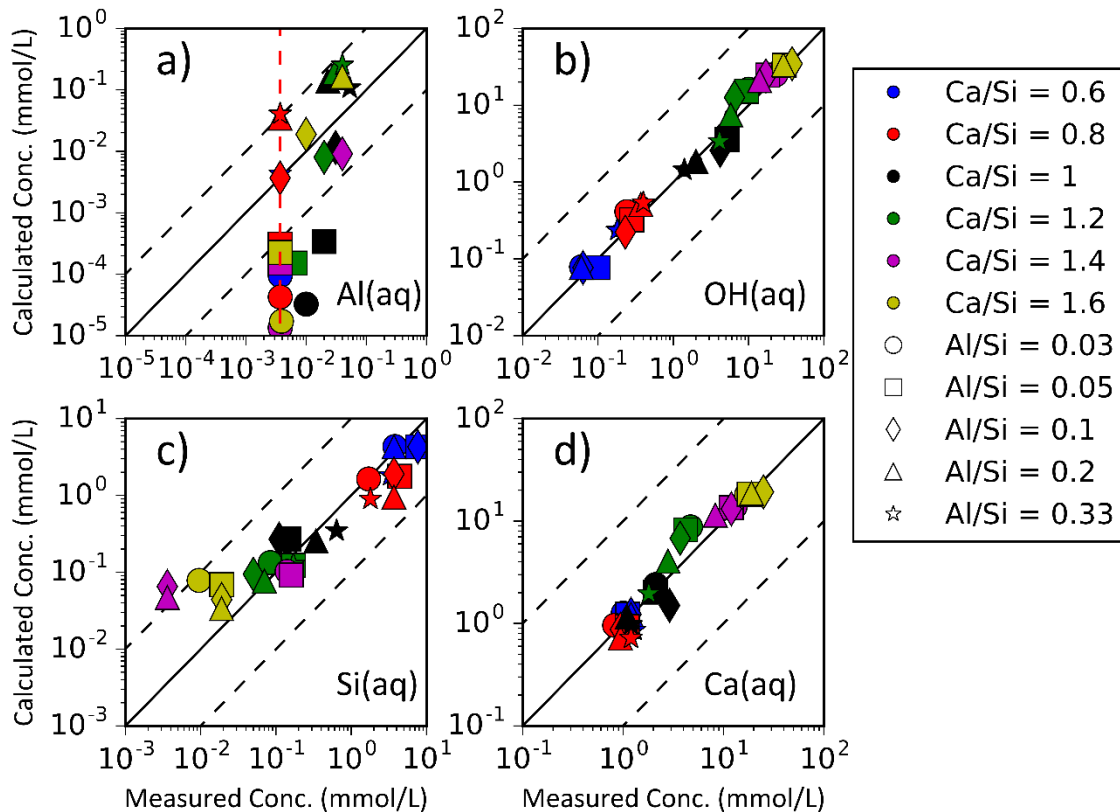


Figure 6.15: Comparison of the calculated and measured concentration of aqueous species a) aluminium, b) OH⁻, c) silicon and d) calcium, using the C-A-S-H end-member model to compare to solubility data from L'Hopital et al. [63]. The different colours represent the Ca/Si ratios in the bulk solution, ranging from 0.6 to 1.6, and the different shapes represent a range of Al/Si ratios from 0.03 to 0.33. The dotted lines indicate a ± 1 order of magnitude difference from the solid line $y = x$. The red dotted line in a) denotes the experimental detection limit.

For the Pitzer models the CaOH⁺ and AlOOH (aq) species were restricted from forming. The different aqueous solution models performed similarly as shown in Table 6.12. The low ionic strength of the system, reaching a maximum of 0.047 mol/L, was low enough to not gain benefit from the inclusion

of Pitzer parameters. The log SSE values show that the Truesdell-Jones model was the most accurate when considering the aqueous concentrations and molar ratios of the C-A-S-H phase.

Additional parameters were included in the *SP* model compared to the Pitzer database, these were the $\text{Ca}^{2+}\text{-HSiO}_3^-$, $\text{Ca}^{2+}\text{-SiO}_3^{2-}$ and $\text{Ca}^{2+}\text{-AlO}_2^-$ interactions. However, no discernible difference was noted with the inclusion of these parameters.

6.4.6.4 Impact of KOH and NaOH

The applicability of the solid solution model and the effect of the different aqueous models in the presence of sodium and potassium were tested using the solubility data collected by L'Hopital et al. [108]. The modelling was conducted by simulating the various molar ratios used in the study, ensuring the mass of the precursor solids (CaO , SiO_2 and $\text{CaO}\cdot\text{Al}_2\text{O}_3$) was 2 g and the water to solids mass ratio was constant at 45. In the solubility study, the majority of the tests were performed with an Al/Si of 0.05 and a range of Ca/Si ratios from 0.6 to 1.6 [108]. The samples with various Ca/Si and Al/Si ratios were mixed with potassium hydroxide and sodium hydroxide concentrations ranging from 0.01 mol/L to 0.5 mol/L. Commonly, BFS-PC cements with a minimum BFS replacement level of 50% produce a C-A-S-H composition with $\text{Al/Si} > 0.1$ [44,45,122]. Therefore, the synthetic Al/Si used in the study was not ideal for testing the solid and aqueous solution models in increased alkaline conditions, but the data appear to be the best available in the literature so were used as far as possible.

The ideal solid solution model and the different aqueous models performed similarly for the KOH and NaOH systems. The KOH studies contained a larger range of concentrations and were therefore selected to be presented in Figure 6.16 and Figure 6.17.

The ideal solid solution model performed well across the range of Ca/Si ratios examined (Figure 6.16a). The modelling of the lower Ca/Si ratio of 0.6 was greatly influenced by the addition of KOH, as at low concentrations (0.01 mol/L) the model prediction of Ca/Si in the solid phase was increased by up to 0.08 compared to the system without added alkalis. However, the experimental data did not exhibit any increase in Ca/Si at such low KOH concentrations [108]. The INFCA and T5C end-members were increasingly dominant as the KOH content increased, which caused Ca/Si and Al/Si to increase (Figure 6.16a and b). Above Ca/Si = 0.6, the model performed well, and the Al/Si ratio was similar to 0.05 for

all other Ca/Si ratios. The calculated pH for each chemical composition fell within the margin of error from the experimental results, Figure 6.16c.

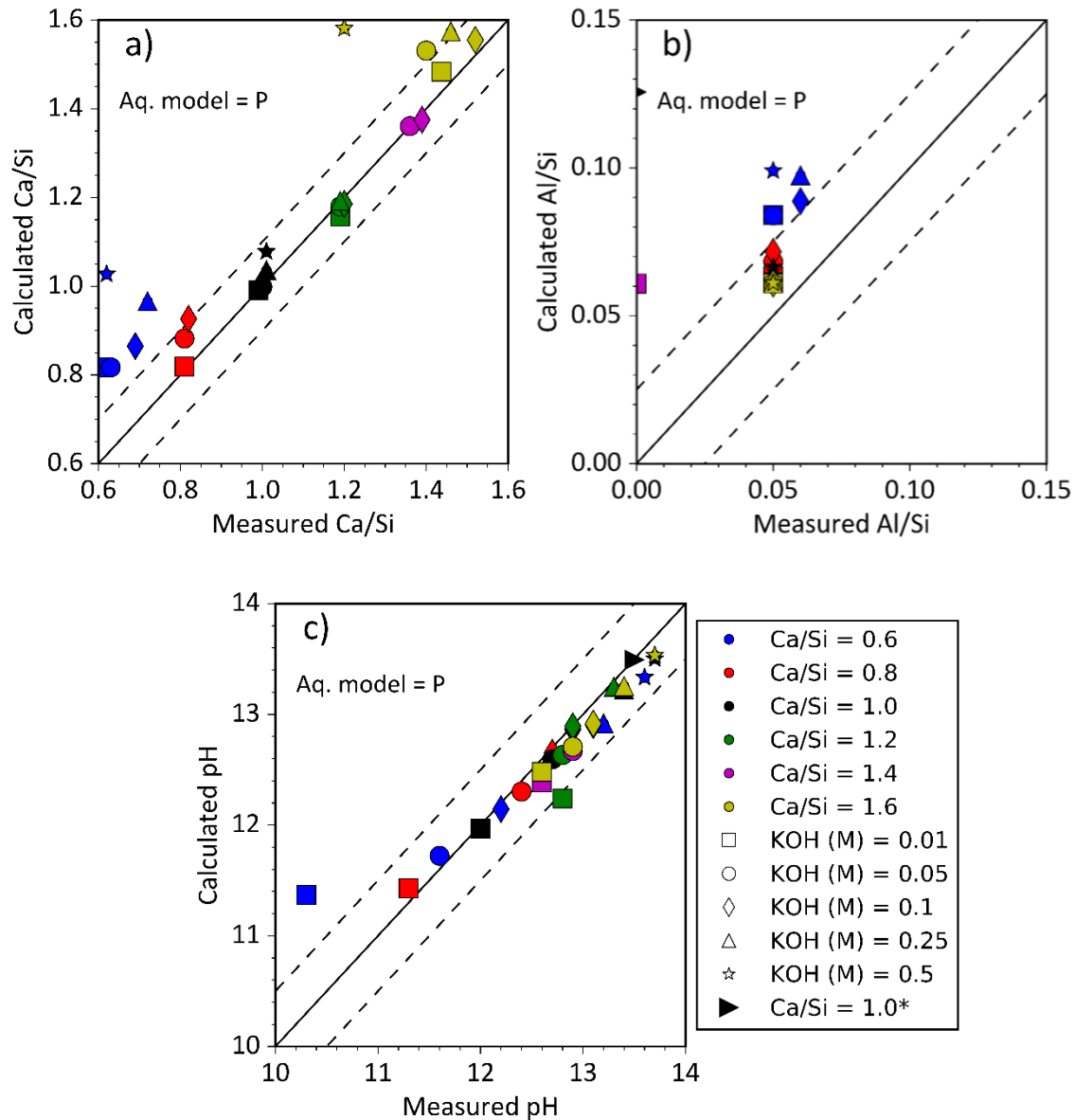


Figure 6.16: Comparison of the calculated and measured values for a) Ca/Si, b) Al/Si and c) pH, using data collected by L'Hopital et al. [63]. The Pitzer model (P) was used in all model calculations shown. The different colours represent a range of Ca/Si in the bulk solution from 0.6 to 1.6 and the different shapes represent a range of KOH concentration from 0.01 to 0.5 mol/L. The dotted lines indicate the maximum possibility of error for the data acquisition from the experimental study, as difference from the solid line $y = x$. The black triangle represents Ca/Si = 1.0, Al/Si = 0.1 and a KOH concentration of 0.5 mol/L.

The aqueous solution species were effectively modelled, as the hydroxyl ion, silicon and calcium concentrations were predicted to within an order of magnitude of the experimental results. The aluminium concentration was under-predicted again because of the low detection level of aluminium. This was an issue in systems where the added alkali concentration was less than 0.1 mol/L. However, the aluminium prediction was most accurate for the Ca/Si = 0.6 tests, contrary to the prediction of Al/Si. The prominence of the aluminium end-members at higher Ca/Si, whereby the Ca/Si began to equal that used in the end-members, caused the withdrawal of additional aluminium from solution. The ratios Al/Si of 0.25 and 0.26 within the 5CA and INFCA end-members, respectively, caused this reduction of aluminium in solution. However, the correct trend of increasing aluminium in solution as greater levels of KOH and NaOH were introduced into solution was observed in the simulations

Silicon concentration increased and calcium decreased in solution with increasing KOH and NaOH content in the simulations, as was expected based on the literature [59,108,245]. This was the result of shifting the equilibrium of the system in favour of higher Ca/Si in the C-A-S-H phase. Increasing the alkalinity significantly reduced the calcium concentration in solution, by an order of magnitude comparing Figure 6.15d and Figure 6.17d. The minimum calcium concentration limit of the end-members in the solid solution model was reached at approximately 0.1 mmol/L in the Ca/Si = 0.6, 0.8 and 1.0 systems, which caused the plateau in Figure 6.17d. In contrast, the silicon concentration increased by up to two orders of magnitude when comparing the same Ca/Si values in the Ca-Al-Si-OH system, highlighting the reduction of the silicon content in the C-A-S-H phase due to the impact of additional alkalis.

The Pitzer models applied here had the CaOH^+ , $\text{AlO}_2\text{H}(\text{aq})$, $\text{KOH}(\text{aq})$ and $\text{NaOH}(\text{aq})$ species restricted from forming. The ionic strength of the alkaline systems reached a maximum of 0.5 mol/L which was within the effective limit for the Truesdell-Jones equation; this meant that in the KOH and NaOH systems, minimal difference between the modelling approaches were observed. The log SSE values for the NaOH systems were lower than for the KOH systems due to the larger number of data points analysed in the KOH systems (Table 6.13).

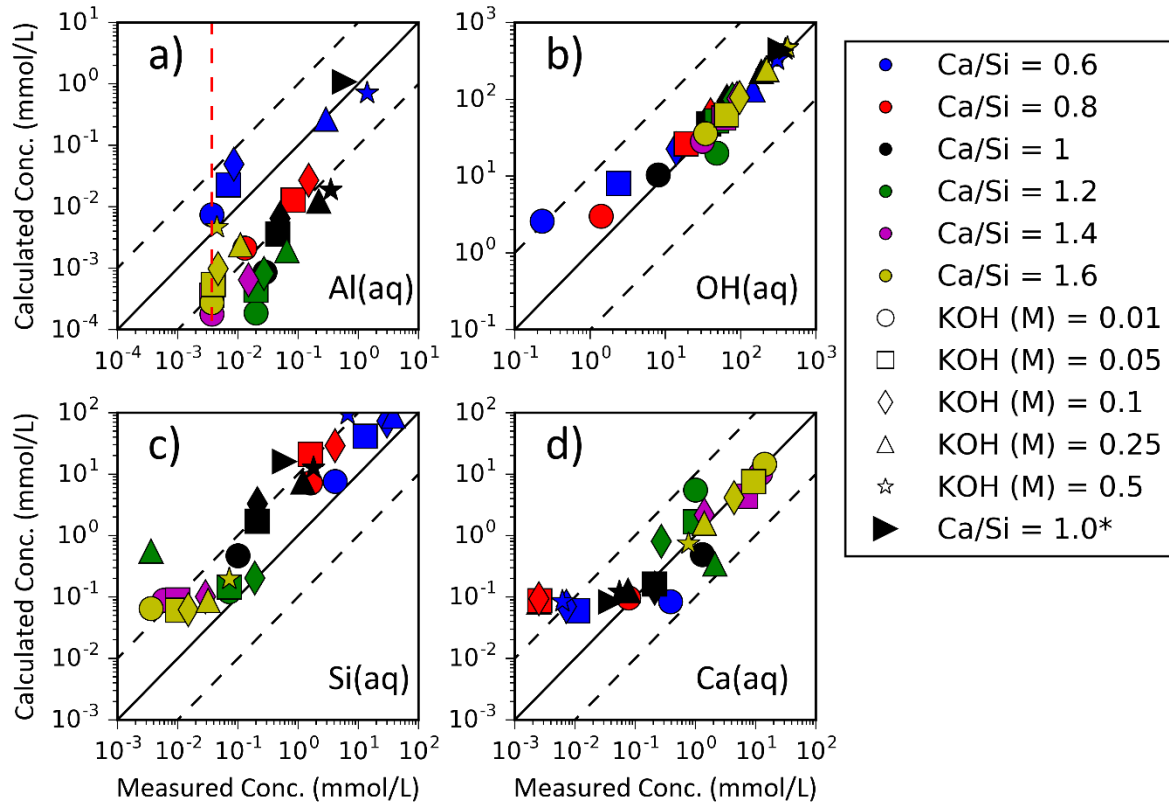


Figure 6.17: Comparison of the calculated and measured concentration of aqueous species a) aluminium, b) OH^- , c) silicon and d) calcium, using solubility data from L'Hopital et al. [63]. The different colours represent a range of Ca/Si ratios in the bulk solution from 0.6 to 1.6, and the different shapes represent a range of KOH concentration from 0.01 to 0.5 mol/L. The dotted lines indicate a ± 1 order of magnitude difference from the solid line $y = x$. The black triangle represents Ca/Si = 1.0, Al/Si = 0.1 and a potassium hydroxide concentration of 0.5 mol/L. The red dotted line in a) denotes the experimental detection limit.

The largest difference between the modelling methods was observed in the concentration of aluminium. The Truesdell-Jones model was more effective than the Pitzer models, despite the inclusion of interaction parameters for Na^+ and K^+ ions with the AlO_2^- species. At higher ionic strengths ($IS > 2.5$ mol/L) the Pitzer model has been observed to model the interactions of sodium and aluminium with greater accuracy than the Truesdell-Jones equation, Figure 6.18, by comparing the solubility of gibbsite in the presence of NaOH. Consistently, the Truesdell-Jones equation calculated that less aluminium was required to form gibbsite, compared to the Pitzer model. Therefore, the fact that these systems had $IS < 0.5$ mol/L resulted in minimal differences in the results, however the C-A-S-H phase precipitated at lower aluminium concentrations using the Truesdell-Jones equation, which

was the cause of the greater level of accuracy. Including the NaOH (aq) or KOH (aq) dissolved complexes led to an improved fit of the Pitzer models (not presented in Table 6.13) due to the reduction of Na⁺ and K⁺ ions in solution; however, the Truesdell-Jones method was still more effective at modelling the aluminium concentration.

Table 6.13: The log SSE values highlighting the difference of the modelled results compared to the calculated results using the C-A-S-H end-member model, compared to the solubility study of the Ca-Al-Si-OH system in NaOH or KOH [108].

Alkali	Log SSE(Molar ratios)		Log SSE(Concentration/[mmol/L])mol/L				Log SSE(pH)	Model
	Ca/Si	Al/Si	Ca	Si	Al	OH ⁻		
KOH	0.37	-1.86	1.64	4.20	0.22	4.60	0.30	P
	0.36	-1.87	1.58	4.15	-0.04	4.34	0.30	T
	0.37	-1.86	1.80	4.20	0.30	4.62	0.30	S
	0.36	-1.86	1.63	4.19	0.24	4.32	0.31	SP
NaOH	-1.12	-2.42	0.53	3.56	0.13	4.12	-0.49	P
	-1.15	-2.43	0.58	3.51	-0.59	3.70	-0.41	T
	-1.11	-2.42	0.96	3.56	0.25	4.12	-0.50	S
	-1.12	-2.42	0.53	3.55	0.30	4.14	-0.49	SP

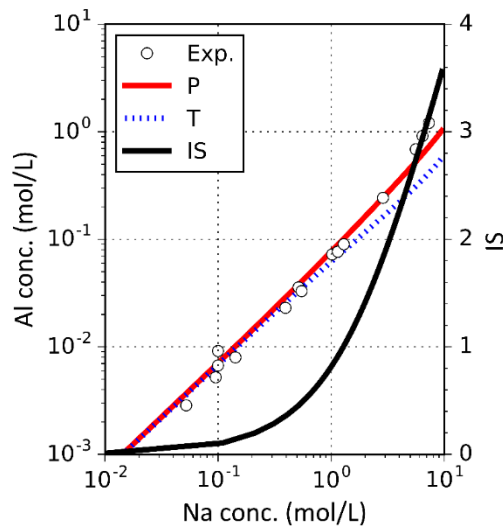


Figure 6.18: Comparison of the Pitzer model (P) and Truesdell-Jones (T) equation for prediction of gibbsite precipitation in the presence NaOH across a range of ionic strengths (IS). The experimental data was taken from Wesolowski [111].

6.5 Pore solution of blended cements

Improving the pore solution modelling of cements was the key objective of this study when considering the application of the Pitzer model to the description of aqueous solutions. To this end, thermodynamic models of the pore solution of 1:1, 3:1 and 9:1 BFS:PC cements cured at 35 °C with a constant w/s of 0.35, for up to 360 days of curing, were compared against experimental results. The precursor materials used were the same as those used in Chapter 4.

The pore solution modelling results were obtained simultaneously alongside the modelling performed in Chapter 4. Experimentally, pore solution was acquired using the steel die method as explained in section 0.

6.5.1 Experimental results

Pore solution was intended to be collected at 14, 28, 56, 90, 180 and 360 days for the three BFS-PC formulations (1:1, 3:1 and 9:1 - Table 6.14). However, due to repeated damage to the hydraulic press used to apply the load to the pore press, and recurring internal damage to the pore press itself, pore solution was not able to be collected for each of the planned curing ages for each formulation.

Table 6.14: Pore solution chemistry determined for the 1:1, 3:1 and 9:1 BFS-PC cements at curing ages ranging from 14 to 360 days. nm denotes a value which was not measured. Curing ages for the samples were different due to malfunctions of the pore press at different dates of pore solution acquisition.

BFS-PC	Curing age (days)	Concentration (mmol/L)							pH
		Al	Ca	K	Mg	Na	S	Si	
1:1	14	0.32	0.64	345	0.001	165	32.1	1.65	nm
	28	0.47	1.28	368	0.007	196	70.2	4.20	13.28
	56	0.15	0.55	279	0.004	165	54.6	2.37	nm
	90	1.65	1.24	252	0.815	150	38.1	6.20	13.30
3:1	56	0.35	0.97	161	0.000	124	81.1	1.66	13.18
	90	0.20	0.79	142	0.013	108	6.74 ¹	0.74	13.23
	180	0.35	1.80	127	0.197	104	14.0 ¹	1.64	13.17
	360	0.54	1.60	123	0.168	97.9	43.7 ¹	3.20	13.15
9:1	28	0.52	0.54	79.8	0.022	66.1	49.9 ¹	1.83	13.06
	56	0.72	2.74	103	0.416	83.1	287	1.55	13.10
	90	0.57	1.11	96.7	0.002	77.4	359	0.40	13.11
	180	0.31	1.15	88.2	0.042	78.3	471	0.51	13.05
	360	0.59	2.25	77.8	0.264	70.9	477	0.97	13.06

¹Sulphur concentration may have been under-recorded. Suspected to have been under-recorded by the analytical instrumentation due to the precipitation of sulphide species during ICP analysis, which may have led to reduced vaporisation in the ICP equipment, leading to a reduced measurement of sulphur.

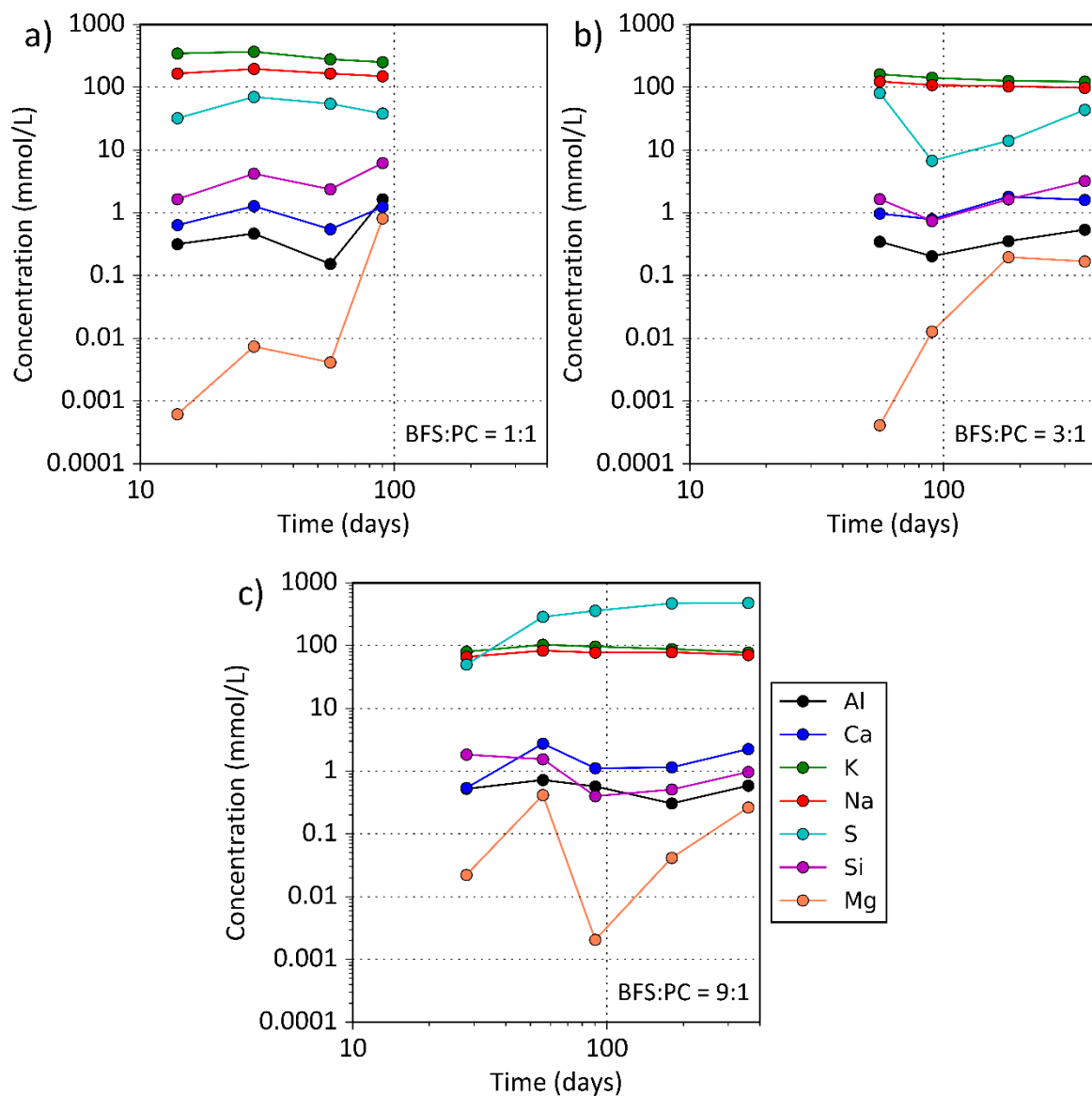


Figure 6.19: Pore solution compositions of the a) 1:1, b) 3:1 and c) 9:1 BFS-PC cements at different curing ages.

The concentration of sodium and potassium was larger in the pore solutions of the higher PC content formulations, as PC was the major source of alkalis in these cements and proceeded to decrease with time. There was up to 175 mmol/L more potassium in the 1:1 system than the 3:1 or 9:1 (Figure 6.19a, b and c, respectively) systems at the curing ages of 56 and 90 days (up to 91.7% > 3:1 or 9:1), whereas the difference in sodium concentration was up to 80 mmol/L (up to 66.1%) greater in the 1:1 cement. The potassium concentration was higher than sodium in each formulation due to the higher alkali distribution ratio (R_d) of sodium in the C-A-S-H phase [59,85,108] and that there was greater mass of

potassium in the starting materials (Table 3.1 in Chapter 3). The decreasing concentration of potassium and sodium was due to the increasing content of C-A-S-H as the degree of hydration (DoH) of slag increased [122].

Calcium concentration did not drop below 3 mmol/L in solution due to the high alkalinity of the systems, with pH values greater than 13.0 at each curing age. Concentrations of sodium and potassium greater than 70 mmol/L, as observed in each of the pore solution results, have been shown to reduce the solubility of any of the calcium containing phases [59,66,108,234]. The reduction of the potassium and sodium concentrations in the 9:1 system was linked to the marginally higher concentration of calcium in solution compared to the 1:1 and 3:1 cements.

Silicon concentration in solution was lower with increasing BFS content in the system. The decreased pH and calcium concentration allowed the extension of the aluminosilicate chains within the C-A-S-H phase, withdrawing greater levels of silicon from solution [122]. Higher alkalinity also reduces the mean chain length (MCL) of aluminosilicate chains. An example of this may be seen in the analysis of 20 year old BFS-PC cement [45] and 18 year old alkali activated slag (AAS) [218]. The 75 and 90% BFS replacement of the PC produced MCLs of 16.1 and 14.3, respectively compared to the AAS MCL of 9.7. The BFS-PC systems contained less aluminium and silicon than the AAS system, however the lower pH of the BFS-PC cement promotes the polymerisation of silica tetrahedra as less silanol groups are deprotonated [59,62]. This reduction of deprotonation due to the presence of less OH^- ions in solution causes greater levels of silicon to precipitate into the aluminosilicate chain.

Aluminium concentration was twice as high in the 1:1 cement compared to the 3:1 and 9:1 cements after 90 days (0.21 and 0.10 mmol/L, respectively). Inclusion of greater levels of magnesium to form hydrotalcite-like LDH, and elongated aluminosilicate chains in the C-A-S-H phase, cause the reduction of dissolved aluminium in solution. The reduced pH contributes to the reduction of solubility of aluminium phases, as was shown with gibbsite precipitation in the presence of NaOH [111], and aluminium uptake in the C-A-S-H phase [108].

Total sulphur concentration in PC decreases with time as the sulphate species precipitates into ettringite or monosulphate, whereby the concentration plateaus after 10 to 100 days [104,118]; this

was observed in the 1:1 formulation by 90 days. The main sulphur species present in BFS is sulphide which does not form the sulphur-containing AFm or AFt phases as readily as sulphate can. Consequently, the reduced sulphur species remains in solution and are expected to be the cause of the higher sulphur concentration in the 9:1 system, which increased with time as the DoH of the slag increased. The sulphur content was more similar to AAS systems than PC systems [114,246]. This may also have occurred in the 1:1 system but no pore solution was able to be collected after 90 days.

The sulphur content in the 28 day 9:1 and 3:1 samples after 56 days, was suspected to have been under-recorded by the analytical instrumentation due to the precipitation of sulphide species during ICP analysis, which may have led to reduced vaporisation in the ICP equipment, leading to a reduced measurement of sulphur. Therefore, the majority of the 3:1 sulphur analysis may be inaccurate. However, a trend of increasing sulphur concentration was observed for the 3:1 and 9:1 systems after 56 days of hydration. This potential under-recording of sulphur was noted in Table 6.14 as these samples were not diluted up to 10 times.

The concentrations of magnesium recorded using ICP-OES were generally less than 1 ppm due to the low solubility of the hydrotalcite-like LDH phase [109]. The detection limit for the equipment was also around 1 ppm, therefore the magnesium concentrations determined may be subject to some error.

6.5.2 Thermodynamic modelling of pore solutions

The Pitzer and Truesdell-Jones modelling results are visualised in Figure 6.20a – f. The different modelling approaches highlight the applicability of each method to modelling the pore solution of BFS-PC cements. Figure 6.20a, c and e represent the modelling performed using the Pitzer model for the 1:1, 3:1 and 9:1 formulations, respectively, and Figure 6.20b, d and f represent the modelling performed using the Truesdell-Jones equation for the 1:1, 3:1 and 9:1 formulations, respectively.

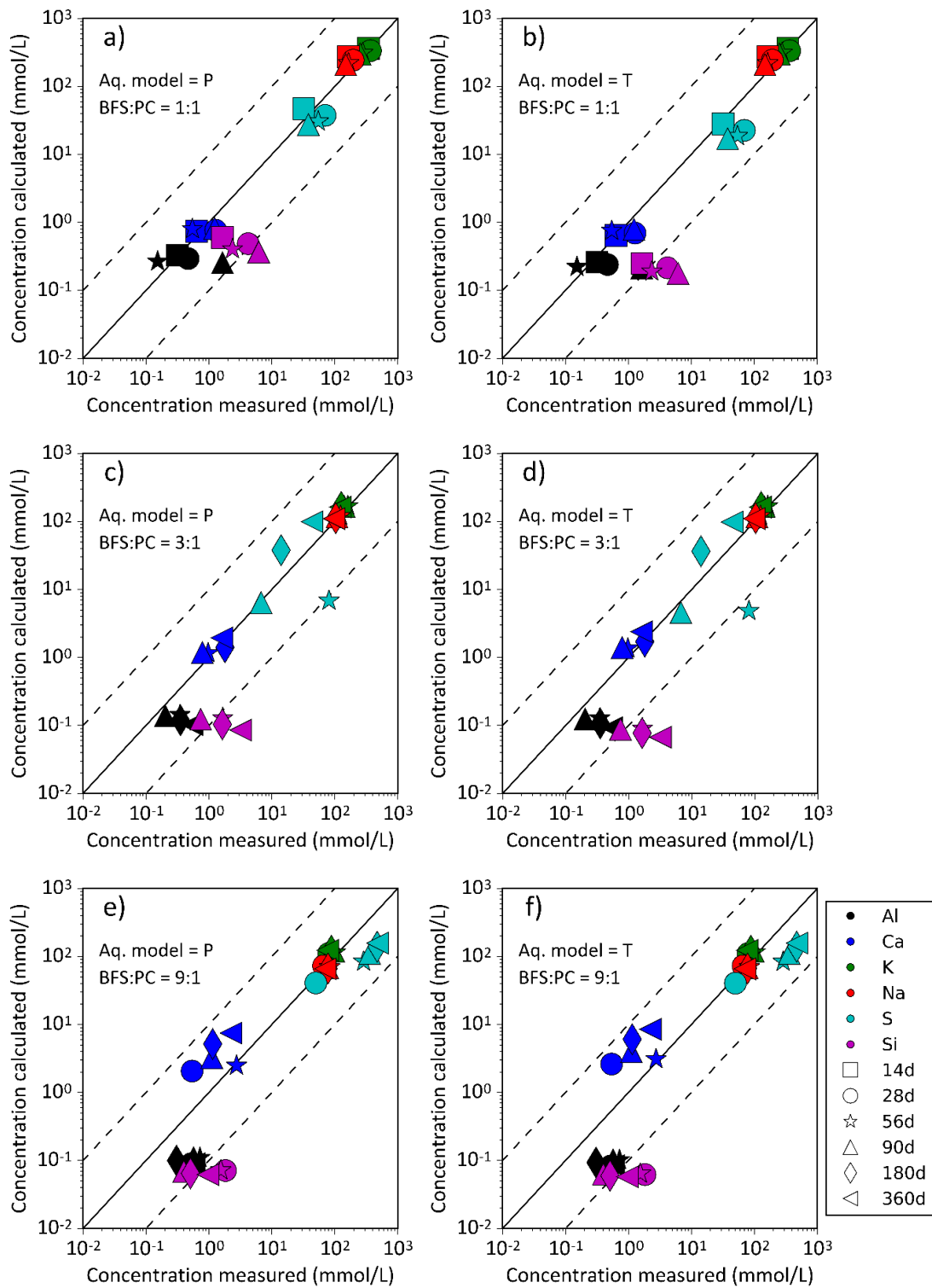


Figure 6.20: Simulation of the pore solution of BFS-PC with varying ratios, a) and b) 1:1, c) and d) 3:1 and e) and f) 9:1. The different aqueous solution models used were Pitzer – a), c) and e), and Truesdell-Jones equation – b), d) and f). Colours indicate the different aqueous elements, and the different curing ages are shown as different shapes.

Alkali distribution ratios (R_d) were used to simulate alkali uptake in the C-A-S-H phase for sodium and potassium, as in chapters 4 and 5. Alkali distribution ratios for Na_2O and K_2O of 2 and 1.2, respectively, were used for the C-A-S-H phase in each of the modelling approaches. These values were chosen as they are similar to the values determined by Hong and Glasser [59,85] for C-S-H and C-A-S-H phases with Ca/Si values between 1.2 and 1.6.

The alkali retention factors chosen were effective at simulating the effect of alkali binding with C-A-S-H for sodium and potassium species in solution. The experimental data show a rise in sodium and potassium concentrations after 28 days in the 1:1 formulation (Figure 6.20a and b), however once the C-A-S-H phase became dominant, the sodium and potassium concentrations declined in the pore solution. The 3:1 and 9:1 systems displayed the highest sodium and potassium concentrations after 56 days, thereafter the concentrations decreased until 360 days following the experimental results, Figure 6.20c and d and Figure 6.20e and f, respectively.

Modelling of the sulphur species was accurate for each formulation, as only a single data point was incorrect by more than an order of magnitude (56 days – 3:1, Figure 6.20c and d), despite the experimental error. The correct trends for each system were observed using the modelling approach, whereby as the degree of hydration of the slag increased, more sulphur was observed in the pore solution in the 3:1 and 9:1 systems. The main sulphur species in the simulation results was HS^- in the 3:1 and 9:1 systems, particularly at later ages when the sulphate from the PC had been consumed. The dominance of the HS^- species based on the modelling work occurs when the clinker phases reduce their rate of hydration and stop contributing high levels of calcium to the system. In the 3:1 system, this occurs at 136 days in the simulation (HS^- consists of 99.99% of aqueous sulphur species in solution), whereby a sudden increase of HS^- occurs as the level of monosulphate remains constant, as no more sulphate or calcium ions are introduced into the system. Excessive oxidation of the sulphur species in the initial hydration of BFS-PC in the 9:1 modelling results, and the subsequent inclusion as sulphate into the monosulphate phase was the cause of the under-prediction of sulphur concentrations in this system. Monosulphate reached 94.2% of the maximum phase volume after 3 days which was the point where HS^- exceeded 90% of the sulphur species in solution as any available SO_4^{2-} was withdrawn into the monosulphate.

Calcium prediction was accurate across the formulations. Calcium concentrations in the 1:1 and 3:1 simulations were below 1.8 mmol/L, which corresponds to what was observed in the experimental results. The higher concentrations of potassium and sodium decreased the saturation concentration of the calcium in solution, causing calcium to precipitate at lower concentrations. However, comparing the 3:1 and 9:1 formulations, the combined sodium and potassium concentration was 90 mmol/L greater in the 3:1 system. The decreased solubility of calcium being affected by potassium concentration was displayed in Figure 6.4b; this led to an increase in calcium concentration in the 9:1 pore solution, which was effectively simulated in Figure 6.20e and f.

Silicon concentration was under-predicted for each of the systems using the C-A-S-H model, however the correct trend of greater levels of silicon remaining in solution with increasing PC content was observed. Simulation of silicon concentration was least effective in the 1:1 system, simulating up to 17 times less Si being present in solution compared to the recorded value. However, that difference was only 5.83 mmol/L on an absolute scale. Compared to the acceptable difference between potassium concentrations in the modelled and experimental results (e.g. concentration of potassium for 3:1 at 90 days of curing: experimental 141.7 mmol/L and simulated 163.50 mmol/L), the precision of the silicon concentration was within 6 mmol/L, which was significantly lower than that of the potassium example. The formation of CaSiO_3 (aq) was the limiting factor for the silicon in solution, as any excess silicon was withdrawn into this aqueous complex species, which was the cause of the lack of variability in silicon concentration for all simulations. When simulations were run without the CaSiO_3 (aq) species in solution, greater levels of silicon were drawn into the C-A-S-H phase, which caused worse agreement with the experimental results.

The same effect observed for aluminium concentration for C-A-S-H and gibbsite when using the different modelling methods, was observed in the pore solution simulations. Aluminium solubility increased using the Pitzer model as it was recorded up to 100 times as much aluminium in the pore solution in the 3:1 and 9:1 systems when compared to the Truesdell-Jones. Over-prediction of aluminium using the Pitzer model and under-prediction using the Truesdell-Jones model resulted in both the modelling methods recording values in the accepted range.

The consistently good agreement of calcium and aluminium concentration in solution using both modelling methods, indicates that the C-A-S-H model adequately interacts with the other hydration

phases within the CEMDATA14 database and accurately portrays the pore solution. The limited accuracy of the silicon concentration is a point requiring improvement for the C-A-S-H model. However, the limitation on the capability to model silicon concentrations is derived from the CSHQ model where the formation of the CaSiO_3 (aq) species acts a limiting factor. Perhaps redevelopment or reparameterisation of the CaSiO_3 (aq) species may improve silicon simulation as was suggested by Miron et al.[109].

Simulation of the magnesium concentration was challenging across the formulations and curing ages. The simulated values in the pore solution were 10^3 mmol/L lower than those determined from ICP. However, the values determined from ICP were below the lowest detectable limit for aqueous species (< 1 ppm). Therefore, magnesium was expressed with low solubility in the modelled results, and this can be considered broadly indicative of what was observed in the experimental results.

6.5.3 Influence of the different modelling methods

The aqueous species which were restricted from forming while testing the Pitzer models in previous systems, were also restricted while simulating the BFS-PC pore solution: CaOH^+ , AlO_2H (aq), SiO_2 (aq), CaCO_3 (aq), CaSO_4 (aq), KOH (aq) and NaOH (aq). Many more aqueous species which did not have Pitzer parameters or which were aqueous complexes remained active (e.g. HS^- and MgSO_4 (aq)), however, for many of the unparameterised species, the influence they imposed on the system was presumed minimal. For instance, many iron species were not parameterised, however the dissolved iron content in the BFS-PC systems was very low. The log SSE of each of the aluminium, calcium, potassium, sodium, sulphur and silicon concentrations using the different aqueous models can be seen in Table 6.15.

Using the ionic radius database to produce the *S* parameters, 300 interaction parameters were created due to the inclusion of 69 aqueous species (Table A8.4 found in the Appendix). Inputting such a large number of parameters into the GEMS software was not possible as the programme could not process that amount. The software could not converge on an equilibrium point when inputting more than 280 interaction parameters. Therefore, the cation selection was restricted to Ca^{2+} , K^+ , Mg^{2+} and Na^+ as these are the dominant cation species in BFS-PC cement. All anionic species that may form with these ions using the ionic radius database were included in the Pitzer parameters for the *S* method. The number of parameters was reduced to 128 which GEMS was capable of using. This same approach was used to apply the additional species to the *SP* method. except for the $\text{Mg}^{2+}\text{-OH}^-$ interactions as

these parameters created a worse fit for the MA-LDH-OH model (Figure 6.9). A total of 48 interaction parameters were added to the Pitzer parameters from the literature. The majority of the additional parameters were cationic interactions with $S_2O_3^{2-}$, HSO_3^- , SO_3^{2-} and S^{2-} . However, these sulphur species were significantly lower in concentration compared to the HS^- species. Additional SO_4^{2-} parameters were not necessary as each of the cationic species chosen had corresponding Pitzer parameters with SO_4^{2-} . The calcium interactions with the AlO_2^- and $HSiO_3^-$ were also included.

Table 6.15: Log SSE values of the various aqueous species simulated in the pore solution of the 1:1, 3:1 and 9:1 BFS-PC using the different aqueous solution models, with HS^- Pitzer parameters [247].

BFS:PC	Al	Ca	K	Na	S	Si	Model
1:1	0.30	-0.29	3.70	4.32	3.30	1.72	P
	0.32	-0.24	3.70	4.32	3.60	1.77	T
	0.32	0.32	3.70	4.31	3.27	1.74	S
	0.10	-0.19	3.68	4.31	3.57	1.74	SP
3:1	-0.54	-0.34	3.55	2.47	3.96	1.17	P
	-0.50	0.06	3.55	2.47	3.97	1.18	T
	-0.51	0.22	3.55	2.47	3.96	1.17	S
	-0.21	-0.37	3.51	2.44	3.88	1.18	SP
9:1	0.03	1.70	3.69	2.68	5.50	0.81	P
	0.04	1.88	3.69	2.68	5.50	0.81	T
	0.04	1.40	3.69	2.68	5.50	0.81	S
	0.04	1.45	3.69	2.68	5.50	0.81	SP

The Pitzer models, compared to the Truesdell-Jones equation, provided minimal improvement across the different formulations, when comparing the simulated aqueous concentrations to the experimental results. The *P* method generally performs as well as the *T* method, or slightly better as can be seen for calcium simulation in the 3:1 system (*P* = -0.34 and *T* = 0.06, Table 6.15). The ionic strengths of these systems range from 0.3 – 0.5 mol/L, which was not high enough to cause a significant effect on the different models.

Part of the reason for the minimal improvement is also likely to be due to the method of creation of the thermodynamic data of the hydration products, as they were all optimised for use with the

Truesdell-Jones or extended Helgeson equations [64,118,146,150]. The greatest impact on these systems was whether the ion interactions were parameterised, as can be most effectively observed in the difference between including, or not, the HS^- parameters (Table 6.15 and Table 6.16) [247]. The higher slag content in the 3:1 and 9:1 systems produced greater levels of HS^- after 90 and 56 days, respectively, according to the simulation results. This increased concentration in the pore solution caused the Ca^{2+} - HS^- parameters to have a greater effect on the calculated saturation concentrations of calcium.

The inclusion of the Simoes parameters combined with the Pitzer parameters from the literature reduced the saturation concentrations of all species, which provided an improved fit for calcium which was generally over-predicted using the Pitzer model.

Table 6.16: Log SSE values of the various aqueous species simulated in the pore solution of the 1:1, 3:1 and 9:1 BFS-PC using the different aqueous solution models, without HS^- Pitzer parameters.

BFS:PC	Al	Ca	K	Na	S	Si	Model
1:1	0.32	-0.19	3.70	4.32	3.60	1.78	P
	0.32	-0.24	3.70	4.32	3.60	1.77	T
	0.32	0.32	3.70	4.31	3.27	1.74	S
	0.27	-0.24	3.70	4.32	3.34	1.74	SP
3:1	-0.44	0.69	3.48	2.37	3.88	1.18	P
	-0.50	0.06	3.55	2.47	3.97	1.18	T
	-0.51	0.22	3.55	2.47	3.96	1.17	S
	-0.57	-0.40	3.55	2.47	3.96	1.17	SP
9:1	0.40	2.06	3.59	2.82	5.60	0.83	P
	0.04	1.88	3.69	2.68	5.50	0.83	T
	0.04	1.40	3.69	2.68	5.50	0.81	S
	0.02	1.61	3.69	2.68	5.50	0.81	SP

6.5.4 Computing time

The main drawback of the Pitzer model was the significant increase in computing time. The simulation setup for 360 days' hydration of BFS-PC used 360 steps. Table 6.17 highlights the difference in simulation run-time between the two techniques. The Pitzer method required significantly longer to run the one year simulation compared to the Truesdell-Jones equation, with minimal improvement in the predictions.

Table 6.17: Time taken to run the simulations for the 1:1, 3:1 and 9:1 BFS-PC systems to simulate one year of hydration using the Pitzer model and the Truesdell-Jones equation.

Formulation (BFS:PC)	Time to complete simulation (s)		
	Pitzer	Truesdell-Jones	Δt (P-T)
1:1	466	41	425
3:1	863	50	813
9:1	166	32	244

* Computer specifications – Intel(R) Core™ i7-4500 CPU, installed RAM 16.00 GB, and 64-bit operating system.

Perhaps in simulations which consider the interaction of cement systems with highly concentrated groundwaters or other aqueous systems, the Pitzer model may prove more effective and produce different results to the Truesdell-Jones equation as was the case in the Mg-Al-Cl-OH and Na-Al-OH systems (Figure 6.9 and Figure 6.18, respectively). However, simulating BFS-PC hydration was effective using the Truesdell-Jones equation which requires less time to run.

6.6 Conclusions

Cement phases generally have very low solubility which causes them to form stable phase assemblages. This low solubility leads to ionic strength values of less than 0.5 mol/L in their pore solutions. Low ionic strength means that it is possible to describe pore solution chemistry using less complicated aqueous solution models such as the extended Debye-Hückel or Truesdell-Jones equations, as opposed to more complicated and parameter intensive models such as the Pitzer model which are needed at higher ionic strengths. Thermodynamic modelling of cement systems using the Pitzer model requires a vast database of aqueous species interactions, where the majority of the species do not yet have full parameter sets available for the Pitzer model.

Considering aqueous systems that contain common cement phases such as: Ca-Al-SO₄-OH, Ca-Al-CO₃-OH, Mg-Al-OH and Ca-Al-Si-OH, the use of the Pitzer model provided little to no improvement in prediction of the solubility of the cementitious phases. When including extra species such as Na, K or Cl into these systems to increase the ionic strength, minimal difference was still observed as most of the experimental data from the literature did not exceed an IS of 0.5 mol/L. Although the solubility data have been used effectively to produce thermodynamic data of common cement phases, these datasets did not highlight the improvement that the Pitzer model may bring at very high ionic strengths. In general the difference between the Pitzer model and the commonly used Truesdell-Jones equation was minimal, ranging from 0.001 to 10 mmol/L in ionic concentrations.

Updating the Pitzer parameters obtained from the literature with parameters estimated using the method of Simoes et al. did not significantly improve the quality of the fit for aqueous species. Overall, the inclusion of the estimated Pitzer parameters led to minimal improvement for simulating the pore solution of BFS-PC, but may still be a useful tool for completing a Pitzer parameter cement database. It is critical to carefully consider which species (or complexes) are included in the aqueous phase model, as the inclusion of extra complexes which were not used in parameterising the solid phase chemistry can cause errors. The GEMS lookup tool was vital for improving the efficiency for compiling Pitzer parameters into a useful format to be used with the GEMS software.

In conclusion, the Pitzer model provides little improvement compared to the Truesdell-Jones equation when considering the aqueous chemistry in equilibrium with cement phases. The added computing time and complications of using the model are not necessary for simulating BFS-PC hydration, therefore will not be recommended for simple BFS-PC systems. Perhaps when other cements or wastes are introduced, or when simulating interactions between cement and high ionic strength solutions, then it may prove beneficial, but currently it is unnecessary for hydration of standard blended cements.

7 Conclusions and future work

7.1 Conclusions

The work presented in this thesis has shown the efficacy of using thermodynamic modelling to simulate cement hydration of BFS-PC systems of variable BFS-PC ratios. The use of GEMS was shown to provide reliable results when simulating cement hydration in conditions which ILW encapsulated waste packages are stored or expected to be stored. Degree of hydration data of the precursor materials, characterisation of the cement phase assemblage, chemical analysis of the C(-A)-S-H phase and pore solution data were obtained to create a complete dataset required to effectively assess the quality of thermodynamic modelling. Assessment of the Truesdell-Jones and Pitzer activity coefficient models was performed to improve the quality of results created through thermodynamic modelling.

The two techniques used to determine DoH of the slag phase in Chapter 4, EDTA selective dissolution and ^{29}Si MAS NMR were in good agreement. Deconvolution of the ^{29}Si spectra were used to determine the DoH of alite and belite. The input data obtained from the techniques provided useful input parameters for simulating cement hydration up to 360 days in the 1:1, 3:1 and 9:1 BFS-PC formulations. Portlandite, monosulphate, hemicarbonates, magnesium hydrotalcite-like and C(-A)-S-H were present in each formulation from 28 to 360 days of curing. Ettringite formed in the 1:1 formulation due to the higher level of sulphate, provided by gypsum within the system. Qualitatively the simulation results were in good agreement with the experimental work as they displayed the same phases as determined through XRD, ^{29}Si and ^{27}Al NMR analysis. ^{29}Si NMR provided useful data concerning the chemical structure of C(-A)-S-H in BFS-PC. The Ca/Si determined from ^{29}Si NMR was much lower than expected compared to literature data, whereby the maximum Ca/Si in the 1:1 formulation was 1.13, in the case where values of Ca/Si > 1.4 were expected. However, the ^{29}Si NMR results were useful for identifying the trend of decreasing Ca/Si as BFS replacement increased. The overlapping of the PC and BFS ^{29}Si environments near the Q¹ sites were the cause for the lower values. The Al/Si values determined were largest in the 9:1 and lowest in the 1:1 formulations. The 1:1, 3:1 and 9:1 formulations had Al/Si values which averaged 0.12, 0.14 and 0.15 between 28 and 360 days of curing at 35 °C. The Al/Si calculated through thermodynamic modelling was over-predicted in the 1:1 system and was more accurate when simulating the 3:1 and 9:1 formulations. At lower temperatures using DoH data, thermodynamic modelling was effective at simulating BFS-PC hydration.

Changing the curing temperatures in Chapter 5, simulated the possible conditions expected in a future GDF site for storing ILW. Samples cured for 360 days at 35 °C, followed by curing at temperatures of 50 °C, 60 °C and 80 °C, showed minimal signs of additional hydration of the slag after 28 days under these new conditions. The alteration in curing temperature resulted in the destabilisation of ettringite and hemicarbonates at temperatures above 60 °C. After 28 days of curing at 80 °C the sulphur and carbon containing AFm and AFt phases destabilised and siliceous hydrogarnet formed. The silicon replacement of OH⁻ in the siliceous hydrogarnet increased as the level of BFS replacement increased. The silicon content in the siliceous hydrogarnet phase was 0.92 mol in the 1:1, and 1.05 mol in the 3:1 and 9:1 cements. The silicon content in these phases was most similar to the C₃AS_{0.84}H_{4.30} phase found in the CEMDATA14 database, which was used in the higher temperature simulations. Two modelling approaches were used to simulate the increasing temperature in the GDF: the *NS* method was used for the temperature range 30 to 60 °C and did not contain C₃AS_{0.84}H_{4.30} as a possible hydrate phase and the *SH* method was used for the temperature range 60 to 80 °C and contained C₃AS_{0.84}H_{4.30} as a possible phase. Siliceous hydrogarnet was not formed in the formulations cured at temperatures of 60 °C and below, however siliceous hydrogarnet was a major hydrate phase at 80 °C. Between 60 and 80 °C, siliceous hydrogarnet began to form, therefore it is included within that temperature range. The same phases were observed in the modelling results as were observed in the experimental work. The Ca/Si and Al/Si in C(-A)-S-H were determined through SEM-EDS. The Ca/Si decreased in each formulation as the temperature increased as the Al/Si increased. The condensation reaction of the monomer and dimer silicates lead to the removal of calcium ions from the C(-A)-S-H phase. This reaction causes an abundance of silicate chain sites which allows the possibility of further aluminium incorporation in the aluminosilicate chain. The Ca/Si values were very slightly under-predicted for the 1:1 and 3:1 systems for the *NS* method but slightly over-predictive in the *SH* method. In the 9:1 formulation both, methods over-predicted 7.4%. The Al/Si ratio was over-predicted in all cements and for each method, by up to 13.8%. Thermodynamic modelling was capable of determining the phase assemblage BFS-PC over a range of temperatures using two modelling approaches.

Improving the aqueous solution modelling in Chapter 6 indicated that the Pitzer model provided minimal benefit when simulating the precipitation of cement hydrates. A GEMS Pitzer parameter lookup tool was created to produce a set of Pitzer parameters in a format which may be used in GEMS. This tool greatly reduced the length of time required to acquire all necessary Pitzer parameters. The Pitzer model required a large database of interaction parameters for the cement systems which may

contain up to 69 species. It was shown that the absence of interaction parameters may cause errors. Inclusion of estimated Pitzer parameters using the Simoes et al. methodology were used to fill any vacancies in the database. The additional parameters produced minor improvements, or caused larger deviations from solubility data, as was the case in the Mg-Al-Na-Cl-OH system. Pore solution data was calculated using the *P*, *T*, *S* and *SP* methods. The log SSE values were similar for each modelling method, however the calculation of calcium in the *P* method showed the greatest level of improvement. The required time to run a simulation using the Pitzer parameters to calculate 360 days of cement hydration required up to 10 minutes, however the Truesdell-Jones equation required less than 1 minute to complete the same simulation. Simulating cement hydration does not require the Pitzer model to acquire reliable results, however for future applications when modelling of cement interactions with the corroded waste form or the cement comes into contact with groundwater, the Pitzer model may provide more accurate results.

The work presented here demonstrates the reliability to simulate BFS-PC hydration under conditions expected of the encapsulated ILW.

7.2 Future work

Although the work presented here identifies the applicability of thermodynamic modelling of cement systems used by the nuclear industry, additional work can be done to improve the quality of the modelling work or provide greater predictive abilities:

- Continue to create complete experimental datasets of hydrated cement systems which include degree of hydration data, chemical compositions of solid-solutions, characterisation of the phases assemblage, quantification of the phase assemblage and pore solution.
- Continue producing solubility data of cement phases. Solubility of C-A-S-H in the presence of alkalis at various Ca/Si and Al/Si and additional alkalis to improve solid solution models of this phase. Produce more solubility studies of the common hydrate phases in varying alkaline concentrations.
- Include radionuclides in the precursor materials to test the applicability of thermodynamic modelling for ILW encapsulation.
- Couple predictive hydration models of BFS-PC. The predictive model results may be used as precursor input values.

- Extend the length of time the samples are exposed to elevated temperatures. Raise samples to 80 °C and lower them for longer than 28 days to assess whether siliceous hydrogarnet alters in structure or destabilises at lower temperatures in BFS-PC.
- Collect pore water data of BFS-PC hydration at different temperatures.
- Maintain and update the Pitzer parameter database.
- Potentially use the solubility studies for fitting Pitzer interaction parameters.
- Use thermodynamic modelling as a tool to simulate groundwater interactions with cement in the case of exposure to the groundwater in the GDF.

8 Appendix

8.1 Analysis of siliceous hydrogarnet phase

The cubic structure of siliceous hydrogarnet indicates the silicon content within this phase as governed by the lattice parameter a . The data collected to create Figure 5.5 from section 5.4.3 are reported in Table A8.1.

Table A8.1: Silicon hydrogarnet phases silicon content linked to the lattice parameter a .

Lattice parameter a (Å)	Si content (mol per formula unit)	Chemical Structure ($\text{Ca}_3\text{Al}_2(\text{SiO}_4)_{3-\gamma}(\text{OH})_{4\gamma}$)	Reference
11.850	3.00	$\text{Ca}_3\text{Al}_2(\text{SiO}_4)_{3.00}$	PDF 33–0260
12.000	2.00	$\text{Ca}_3\text{Al}_2(\text{SiO}_4)_{2.00}(\text{OH})_{4.00}$	PDF 31–0250
12.093	2.00	$\text{Ca}_3\text{Al}_2(\text{SiO}_4)_{2.00}(\text{OH})_{4.00}$	[211]
12.215	1.50	$\text{Ca}_3\text{Al}_2(\text{SiO}_4)_{1.50}(\text{OH})_{6.00}$	[211]
12.288	1.20	$\text{Ca}_3\text{Al}_2(\text{SiO}_4)_{1.20}(\text{OH})_{7.20}$	[210]
12.290	1.00	$\text{Ca}_3\text{Al}_2(\text{SiO}_4)_{1.00}(\text{OH})_{8.00}$	PDF 32–0151
12.312	1.10	$\text{Ca}_3\text{Al}_2(\text{SiO}_4)_{1.10}(\text{OH})_{7.60}$	[210]
12.324	1.05	$\text{Ca}_3\text{Al}_2(\text{SiO}_4)_{1.05}(\text{OH})_{7.79}$	(3:1/9:1 – this study)
12.337	1.00	$\text{Ca}_3\text{Al}_2(\text{SiO}_4)_{1.00}(\text{OH})_{8.00}$	[211]
12.355	0.92	$\text{Ca}_3\text{Al}_2(\text{SiO}_4)_{0.92}(\text{OH})_{8.30}$	(1:1 – this study)
12.376	0.84	$\text{Ca}_3\text{Al}_2(\text{SiO}_4)_{0.84}(\text{OH})_{8.64}$	[149]
12.410	0.70	$\text{Ca}_3\text{Al}_2(\text{SiO}_4)_{0.7}(\text{OH})_{9.20}$	[210]
12.480	0.41	$\text{Ca}_3\text{Al}_2(\text{SiO}_4)_{0.41}(\text{OH})_{10.36}$	[149]
12.495	0.33	$\text{Ca}_3\text{Al}_2(\text{SiO}_4)_{0.33}(\text{OH})_{10.68}$	[217]
12.507	0.30	$\text{Ca}_3\text{Al}_2(\text{SiO}_4)_{0.30}(\text{OH})_{10.80}$	[210]
12.528	0.18	$\text{Ca}_3\text{Al}_2(\text{SiO}_4)_{0.18}(\text{OH})_{11.28}$	[217]
12.529	0.18	$\text{Ca}_3\text{Al}_2(\text{SiO}_4)_{0.18}(\text{OH})_{11.28}$	[217]
12.547	0.10	$\text{Ca}_3\text{Al}_2(\text{SiO}_4)_{0.1}(\text{OH})_{11.60}$	[217]
12.563	0.04	$\text{Ca}_3\text{Al}_2(\text{SiO}_4)_{0.04}(\text{OH})_{11.84}$	[217]
12.575	0.00	$\text{Ca}_3\text{Al}_2(\text{OH})_{12.00}$	[217]
12.580	0.00	$\text{Ca}_3\text{Al}_2(\text{OH})_{12.00}$	PDF 24-0217

The higher silicon content phase ($\text{C}_3\text{AS}_{0.84}\text{H}_{4.30}$) best represents the siliceous hydrogarnet forming in the tD curing conditions evaluated in this study, considering the XRD results reported in Figure A8.1 and Figure A8.2. Figure A8.1 a-c) highlights the formation of siliceous hydrogarnet in 1:1, 3:1 and 9:1 BFS-PC cements when cured up to curing condition 28D. The silicon content in the BFS-PC cements did not varied after 360 days at 80 °C, indicating that at longer ages, the $\text{C}_3\text{AS}_{0.84}\text{H}_{4.30}$ phase was stable.

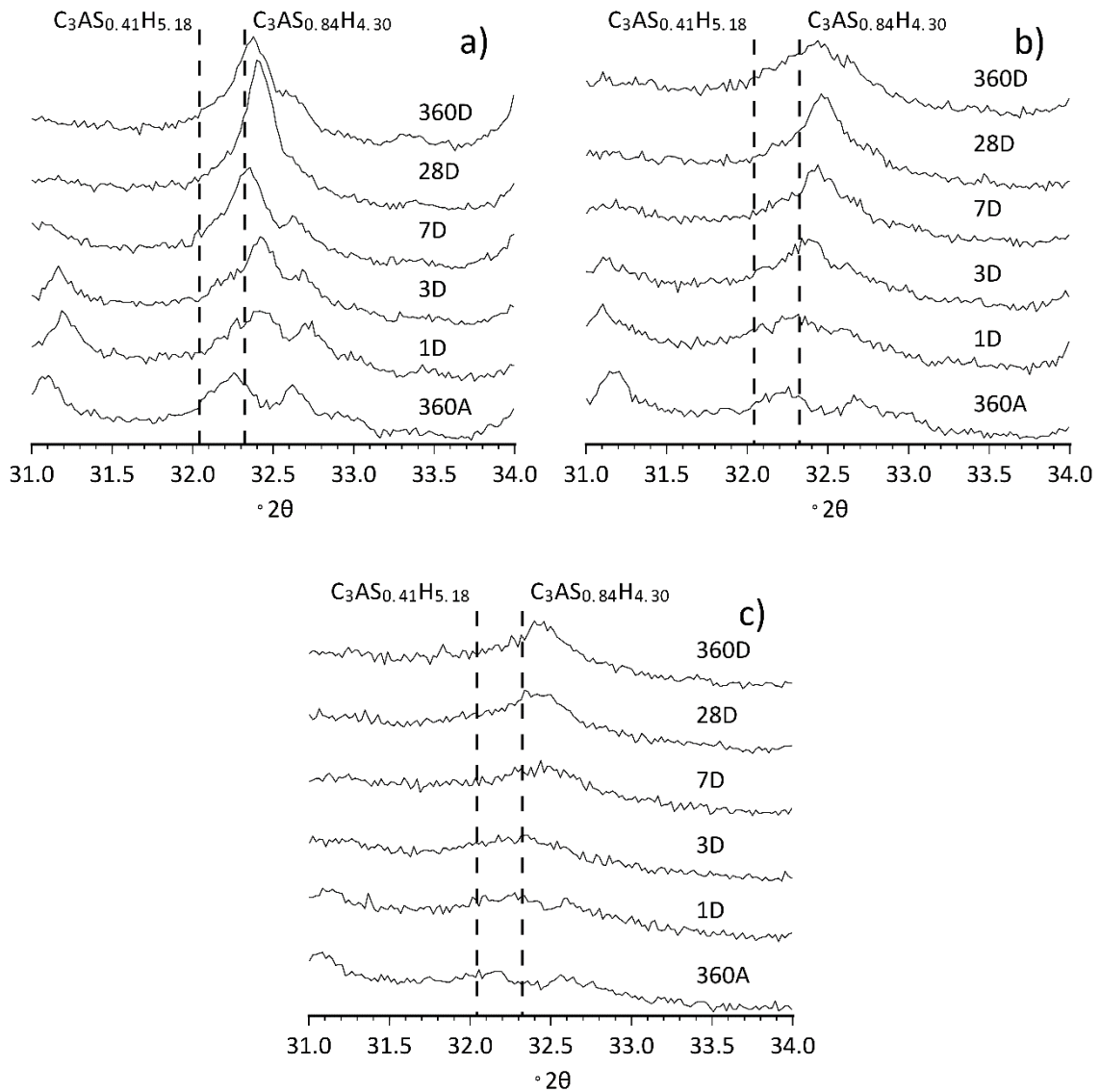


Figure A8.1: XRD patterns for cements with BFS:PC ratios a) 1:1, b) 3:1 and c) 9:1 after curing at 35 °C for one year and being transferred to 80 °C for up to 360 days (temperature profile D). The $C_3AS_{0.41}H_{5.18}$ and $C_3AS_{0.84}H_{4.30}$ chemical formulae depict the siliceous hydrogarnet phases available in the CEMDATA14 database.

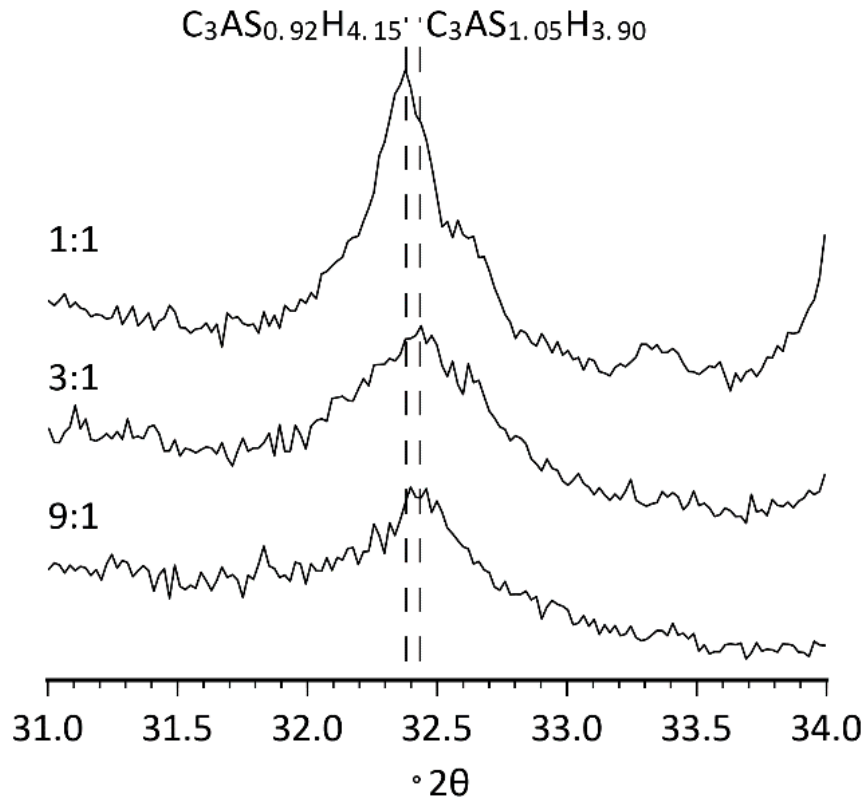


Figure A8.2: XRD patterns of cements with BFS:PC ratios 1:1, 3:1 and 9:1 after curing at 35 °C for 360 days and being transferred to 80 °C for 360 days (temperature profile D). Silicon content of the siliceous hydrogarnet determined from unit cell analysis, Figure 5.5 from section 5.4.3 of the main article.

8.2 Summary of SEM-EDS results

The SEM-EDS data collected to determine the chemical composition of the C-A-S-H phase, as a function of various temperature regimes are reported in Table A8.2. These results are represented in Figures 5.7 and 5.8 from the main manuscript.

Table A8.2: Results of calibrated SEM-EDS analysis of the Ca/Si and Al/Si ratios of the C-A-S-H phase, for different BFS:PC ratios and temperature regimes.

Temperature regime	BFS:PC blend	Ca/Si	Al/Si	Mean Si/Ca	Std. dev. Si/Ca	Mean Al/Ca	Std. dev. Al/Ca
360A	1:1	1.49	0.12	0.44	0.67	0.08	0.14
360A	3:1	1.45	0.15	0.46	0.69	0.10	0.18
360A	9:1	1.27	0.17	0.56	0.79	0.13	0.21
720A	1:1	1.49	0.12	0.43	0.67	0.08	0.15
720A	3:1	1.45	0.16	0.51	0.69	0.11	0.20
720A	9:1	1.27	0.17	0.57	0.79	0.13	0.26
28B	1:1	1.47	0.15	0.49	0.68	0.10	0.18
28B	3:1	1.43	0.17	0.51	0.70	0.12	0.20
28B	9:1	1.24	0.17	0.59	0.81	0.14	0.22
28C	1:1	1.45	0.16	0.40	0.69	0.11	0.35
28C	3:1	1.39	0.17	0.52	0.72	0.12	0.23
28C	9:1	1.22	0.17	0.61	0.82	0.14	0.23
28D	1:1	1.39	0.17	0.56	0.72	0.12	0.18
28D	3:1	1.37	0.18	0.55	0.73	0.13	0.24
28D	9:1	1.21	0.19	0.64	0.83	0.16	0.26
360D	1:1	1.37	0.16	0.50	0.73	0.12	0.23
360D	3:1	1.35	0.18	0.51	0.74	0.13	0.25
360D	9:1	1.19	0.19	0.61	0.84	0.16	0.28
28E	1:1	1.39	0.17	0.56	0.72	0.12	0.24
28E	3:1	1.37	0.18	0.54	0.73	0.13	0.23
28E	9:1	1.22	0.18	0.54	0.82	0.15	0.28

8.3 Thermodynamic data for phases used in simulations

This study uses an adapted solid-solution model for C-A-S-H adapted from the work of Myers et al. [146] and Kulik [64], Table A8.3. This adaptation was used to provide a greater Ca/Si ratio within the modelled C-A-S-H gel to describe BFS:PC cements, as opposed to the alkali-activated slags for which the Myers model was originally developed. A similar approach was also adopted by Elakneswaran et al. [125] using PHREEQC [115,129]. A hydrotalcite-like solid solution model (MA-OH-LDH [146]) replaced the OH-hydrotalcite phase found within CEMDATA14 to better represent the magnesium aluminate hydrate (M-A-H) phase. A summary of the solid phases and in which modelling method they were utilised are summarised in Table A8.3. The *NS* method phases were used in Chapters 4, 5 and 6 whereas, the *SH* method was used in Chapter 5. Aqueous and gaseous phases included within this study are summarised in Table A8.4 and Table A8.5, respectively. The same aqueous and gaseous species were used throughout each modelling method.

Table A8.3: Thermodynamic properties of the solid phases forming in each of the modelling approaches. The 'x' marked in the 'Presence in simulation' column, denotes whether the phase was allowed to form in the two different modelling options. Standard thermodynamic properties at 25 °C and 1 bar.

Phases	V° ($\text{cm}^3 \text{ mol}^{-1}$)	ΔH_f° (kJ mol^{-1})	ΔG_f° (kJ mol^{-1})	ΔS_f° ($\text{J mol}^{-1} \text{ K}^{-1}$)	C_p° ($\text{J mol}^{-1} \text{ K}^{-1}$)	Reference	Presence in simulation	
							30 °C - 60 °C (NS)	60 °C - 90 °C (SH)
Clinkers								
C ₃ S	73.2	-2931	-2794	169	172	[151]	x	x
C ₂ S	51.8	-2308	-2193	128	129	[151]	x	x
C ₃ A	89.2	-3561	-3382	205	209	[151]	x	x
C ₄ AF	130	-5080	-4786	326	396	[151]	x	x
AH ₃ (microcrystalline)	32.0	-1265	-1148	140	93.1	[233]	x	x
Portlandite, CH	33.1	-985	-897	83.4	87.5	[248]	x	x
SiO ₂ (amorphous)	29.0	-903	-849	41.3	44.5	[152,249]	x	x
C ₂ AH ₈	90.1	-5278	-4696	450	521	[233]	x	x
Katoite, C ₃ AH ₆	150	-5537	-5008	422	446	[233]	x	x
C ₄ AH ₁₉	382	-1002	-8750	1120	1382	[233]	x	x

Table A8.3 continued

CAH ₁₀	194	-5288	-4623	610	668	[233]	x	x
Strätlingite, C ₂ ASH ₈	216	-6360	-5705	546	603	[150]	x	x
Lime, C	16.8	-635	-604	39.7	42.8	[249]	x	x
Brucite, MH	24.6	-923	-832	63.1	77.3	[249–251]	x	x
Sulphates								
Ettringite, C ₆ A ₃ H ₃₂	707	-17535	-15206	1900	2174	[151]	x	x
Gypsum, C ₂ H ₂	74.7	-2023	-1798	194	186	[250,251]	x	x
Anhydrite, C ₂	45.9	-1435	-1322	107	99.6	[250,251]	x	x
<i>Calcium monosulfoaluminate–hydroxoaluminate hydrate non-ideal solid solution [150]</i>								
Calcium monosulfoaluminate hydrate, C ₄ A ₅ H ₁₂	309	-8750	-7779	821	942	[150]	x	x
C ₄ AH ₁₃	274	-8300	-7324	700	930	[233]	x	x
<i>C–A–S–H gel ideal solid solution end-members, 'C–A–S–H_{ss-hi}' [122]</i>								
5CA, C _{1.25} A _{0.125} S ₁ H _{1.625}	57.3	-2491	-2293	163	177	[146]	x	x
INFCA, C ₁ A _{0.15625} S _{1.1875} H _{1.65625}	59.3	-2551	-2343	154	181	[146]	x	x

Table A8.3 continued

JenD*, C _{1.5} S _{0.67} H _{2.5} ^a	80.6	-2401	-2169	173	209	[146]	x	x
T2C*, C _{1.5} S ₁ H _{2.5} ^b	80.6	-2721	-2298	167	237	[122]	x	x
T5C, C _{1.25} S _{1.25} H _{2.5}	79.3	-2780	-2517	160	234	[146]	x	x
TobH, C ₁ S _{1.5} H _{2.5}	85.0	-2831	-2560	153	231	[146]	x	x
Hydrogarnet solid solution model, C ₃ (A,F)S _{0.84} H _{4.32}								
C ₃ AS _{0.84} H _{4.32_0.5}	71.2	-2924	-2682	187	206	[149]	-	x
C ₃ FS _{0.84} H _{4.32_0.5}	74.3	-2411	-2240	420	216	[149]	-	x
<i>MA-OH-LDH ideal solid solution end-members, 'MA-OH-LDH_ss' [123]</i>								
M ₄ AH ₁₀	219	-7160	-6358	549	648	[103,252]	x	x
M ₆ AH ₁₂	305	-9007	-8023	675	803	[123]	x	x
M ₈ AH ₁₄	392	-10853	-9687	801	958	[123]	x	x
Carbonates								
Aragonite, C _c	34.2	-1207	-1128	90.2	81.3	[250,251]	x	x
Calcite, C _c	36.9	-1207	-1129	92.7	81.9	[250,251]	x	x

Table A8.3 continued

Magnesite, $M\bar{c}$	28.0	-1113	-1029	65.7	75.8	[250,251]	x	x
MA- \bar{c} -LDH, $M_4A\bar{c}H_9$	220	-7374	-6580	551	647	[151]	x	x
Calcium monocarboaluminate hydrate, $C_4A\bar{c}H_{11}$	262	-8250	-7337	657	881	[150]	x	x
Calcium hemicarboaluminate hydrate, $C_4A\bar{c}_{0.5}H_{12}$	285	-8270	-7336	713	906	[150]	x	x
Calcium tricarboaluminate hydrate, $C_6A\bar{c}_3H_{32}$	650	-16792	-14566	1858	2121	[150]	x	x

^aThe asterisk for the T2C* end-member depicts a slight change of the Gibbs free energy determined by Myers et al [146] to better incorporate the higher Ca/Si end-member, JenD, from the CSHQ model developed by Kulik [64].

x - denotes when a phase was available to form within the two different modelling approaches.

Table A8.4: Aqueous species used during the modelling. Standard thermodynamic properties at 25 °C and 1 bar.

Species/complex ^a	V° (cm ³ mol ⁻¹)	ΔH_f° (kJ mol ⁻¹)	ΔG_f° (kJ mol ⁻¹)	ΔS_f° (J mol ⁻¹ K ⁻¹)	C_p° (J mol ⁻¹ K ⁻¹)	Reference
Al ³⁺	-45.2	-530.6	-483.7	-325.1	-128.7	[253]
AlO ⁺ (+ H ₂ O = Al(OH) ₂ ⁺)	0.3	-713.6	-660.4	-113	-125.1	[253]
AlO ₂ ⁻ (+ 2H ₂ O = Al(OH) ₄ ⁻)	9.5	-925.6	-827.5	-30.2	-49	[253]
AlOOH ^o (+ 2H ₂ O = Al(OH) ₃ ^o)	13	-947.1	-864.3	20.9	-209.2	[253]
AlOH ²⁺	-2.7	-767.3	-692.6	-184.9	56	[253]
AlHSiO ₃ ²⁺ (+ H ₂ O = AlSiO(OH) ₃ ²⁺)	-40.7	-1718	-1541	-304.2	-215.9	[150]
AlSiO ₅ ³⁻ (+ 2H ₂ O = AlSiO ₃ (OH) ₄ ³⁻)	-43.6	-2014.2	-1769	-66.3	-292.2	[250,251]
AlSO ₄ ⁺	-6.0	-1423	-1250	-172.4	-204.0	[150]
Al(SO ₄) ₂ ⁻	31.1	-2338	-2006	-135.5	-268.4	[150]
Ca ²⁺	-18.4	-543.1	-552.8	-56.5	-30.9	[253]
CaOH ⁺	5.8	-751.6	-717	28	6	[253]
CaHSiO ₃ ⁺ (+ H ₂ O = CaSiO(OH) ₃ ⁺)	-6.7	-1687	-1574	-8.3	137.8	[137]
CaSiO ₃ ^o (+ H ₂ O = CaSiO ₂ (OH) ₂ ^o)	15.7	-1668	-1518	-136.7	88.9	[150]

Table A8.4 continued

CaSO ₄ ⁰	4.7	-1448	-1310	20.9	-104.6	[137]
CaCO ₃ ⁰	-1.6	-1202	-1099	10.5	-123.9	[137]
CaHCO ₃ ⁺	13.3	-1232	-1146	66.9	233.7	[250,251]
Na ⁺	-1.2	-240.3	-261.9	58.4	38.1	[253]
NaOH ⁰	3.5	-470.1	-418.1	44.8	-13.4	[253]
NaSO ₄ ⁻	18.6	-1147	-1010	101.8	-30.1	[150]
NaCO ₃ ⁻	-0.4	-938.6	-797.1	-44.3	-51.3	[250,251]
NaHCO ₃ ⁰	32.3	-929.5	-847.4	154.7	200.3	[250,251]
HSiO ₃ ⁻ (+ H ₂ O = SiO(OH) ₃ ⁻)	4.5	-1145	-1014	20.9	-87.2	[137]
SiO ₂ ⁰ (+ 2H ₂ O = Si(OH) ₄ ⁰)	16.1	-887.9	-833.4	41.3	44.5	[152,254]
SiO ₃ ²⁻ (+ H ₂ O = SiO ₂ (OH) ₂ ²⁻)	34.1	-1099	-938.5	-80.2	119.8	[150]
S ₂ O ₃ ²⁻	27.6	-649.9	-520.0	66.9	-238.5	[253]
HSO ₃ ⁻	33.0	-627.7	-529.1	139.7	-5.4	[253]
SO ₃ ²⁻	-4.1	-636.9	-487.9	-29.3	-281.0	[253]
HSO ₄ ⁻	34.8	-889.2	-755.8	125.5	22.7	[253]

Table A8.4 continued

SO_4^{2-}	12.9	-909.7	-744.5	18.8	-266.1	[253]
H_2S°	35.0	-39.0	-27.9	125.5	179.2	[253]
HS^-	20.2	-16.2	12.0	68.2	-93.9	[253]
S^{2-}	20.2	92.2	120.4	68.2	-93.9	[253]
Mg^{2+}	-22.0	-465.9	-454.0	-138.1	-21.7	[253]
MgOH^+	1.6	-690.0	-625.9	-79.9	129.2	[253]
$\text{MgHSiO}_3^+ (+ \text{H}_2\text{O} = \text{MgSiO}(\text{OH})_3^+)$	-10.9	-1614	-1477	-99.5	158.6	[253]
MgSO_4°	1.8	-1369	-1212	-50.9	-90.3	[250,251,253]
$\text{MgSiO}_3^\circ (+ \text{H}_2\text{O} = \text{MgSiO}_2(\text{OH})_2^\circ)$	12.1	-1597	-1425	-218.3	98.2	[250,251]
MgCO_3°	-16.7	-1132	-999.0	-100.4	-116.5	[137,250,251]
MgHCO_3^+	9.3	-1154.0	-1047	-12.6	254.4	[250,251]
CO_2°	32.8	-413.8	-386.0	117.6	243.1	[250,251,254]
CO_3^{2-}	-6.1	-675.3	-528.0	-50.0	-289.3	[253]
HCO_3^-	24.2	-690.0	-586.9	98.5	-34.8	[253]
CH_4°	37.4	-87.8	-34.4	87.8	277.3	[250,251,255]

Table A8.4 continued

OH ⁻	-4.7	-230	-157.3	-10.7	-136.3	[253]
H ⁺	0	0	0	0	0	[253]
H ₂ O [°]	18.1	-285.9	-237.2	69.9	75.4	[256]
H ₂ [°]	25.3	-4.0	17.7	57.7	166.9	[250,251,254]
N ₂ [°]	33.4	-10.4	18.2	95.8	234.2	[254]
O ₂ [°]	30.5	-12.2	16.4	109	234.1	[254]

[°] denotes neutral species within aqueous solution.

Table A8.5: Gaseous species used for thermodynamic modelling. Standard thermodynamic properties at 25 °C and 1 bar.

Gases*	ΔH_f° (kJ mol ⁻¹)	ΔG_f° (kJ mol ⁻¹)	ΔS_f° (J mol ⁻¹ K ⁻¹)	C_p° (J mol ⁻¹ K ⁻¹)	Reference
N ₂	0	0	191.6	29.1	[257]
O ₂	0	0	205.1	29.3	[257]
H ₂	0	0	130.7	28.8	[257]
CO ₂	-393.5	-394.4	213.7	37.1	[257]
CH ₄	-74.8	-50.7	186.2	35.7	[257]
H ₂ S	-20.6	-33.8	205.8	34.2	[257]

8.4 Pitzer parameter database

The Pitzer parameters used in Chapter 6 are summarised in Tables A8.6 and A8.7.

Table A8.6: Binary species Pitzer parameters.

Cation (M)	Anion (X)	Binary Pitzer Parameter				Binary Pitzer Parameter Reference			
		B ⁽⁰⁾	B ⁽¹⁾	B ⁽²⁾	C ⁽⁰⁾	B ⁽⁰⁾	B ⁽¹⁾	B ⁽²⁾	C ⁽⁰⁾
Al ³⁺	HSO ₄ ⁻	1.025	5.426		-0.0486	[135]	[135]		[258]
Al ³⁺	SO ₄ ²⁻	0.822	21.22	-4813	-0.0799	[143]	[143]	[143]	[143]
Ca ²⁺	CO ₃ ²⁻	0.16	2.1	-46		[259]	[259]		
Ca ²⁺	HCO ₃ ⁻	0.39975	2.977			[135]	[237]		
Ca ²⁺	HS ⁻	0.069	2.264			[247]	[247]		
Ca ²⁺	HSO ₄ ⁻	0.2145	2.5275			[135]	[135]		
Ca ²⁺	NO ₃ ⁻	0.1683	1.65		-0.00687	[143]	[143]		
Ca ²⁺	OH ⁻	-0.1421	-0.3727	-11.052	-0.0092	[66]	[66]	[66]	[66]
Ca ²⁺	SO ₄ ²⁻	0.2	3.546	-54.24	0.114	[135]	[237]	[135]	[237]
Ca ²⁺	Cl ⁻	0.31	1.7085	-1.13	0.00215	[143]		[66]	[66]
Ca ²⁺	ClO ₄ ⁻	0.438	1.76			[259]	[259]		
Fe ²⁺	HSO ₄ ⁻	0.4273	3.48			[260]	[135]		
Fe ²⁺	NO ₃ ⁻	0.367078	1.584761			[261]	[261]		
Fe ²⁺	SO ₄ ²⁻	0.2568	3.063	-42	0.0209	[260]	[260]	[260]	[260]
H ⁺	HSO ₄ ⁻	0.2709	0.0299			[262]	[262]		
H ⁺	NO ₃ ⁻	0.111	0.3805		-0.00424	[143]	[143]		[143]
H ⁺	SO ₄ ²⁻	-0.0216	0.1194		0.0317	[262]	[262]		[262]
H ⁺	Cl ⁻	0.1775	0.2945			[66]		[66]	

Table A8.6 continued

H ⁺	ClO ₄ ⁻	0.1813	0.276		0.0008	[143]	[143]	[66]
K ⁺	AlO ₂ ⁻	0.094	0.32		-0.0012	[111]	[111]	[111]
K ⁺	CO ₃ ²⁻	0.1305	1.43		0.00024	[143]	[260]	[143]
K ⁺	HCO ₃ ⁻	-0.01558	0.25		0.00469	[143]	[237]	[143]
K ⁺	HS ⁻	-0.337	0.884			[247]	[247]	
K ⁺	HSiO ₃ ⁻	0.208	0.34			[244]	[244]	
K ⁺	HSO ₄ ⁻	-0.0003	0.1735			[260]	[135]	
K ⁺	OH ⁻	0.1298	0.32		0.0041	[66]	[66]	[135]
K ⁺	SCN ⁻	0.04159	0.1048		-0.00254	[143]	[143]	
K ⁺	SO ₃ ²⁻	0.065	1			[135]	[135]	
K ⁺	SO ₄ ²⁻	0.0317	0.756		0.00818	[237]	[237]	[237]
Mg ²⁺	CO ₃ ²⁻	0.18	1.804	-46		[259]	[259]	
Mg ²⁺	HCO ₃ ⁻	0.033	0.84975			[135]	[135]	
Mg ²⁺	HS ⁻	0.466	2.264			[247]	[247]	
Mg ²⁺	HSO ₄ ⁻	0.4746	1.729			[260]	[260]	
Mg ²⁺	NO ₃ ⁻	0.3405	12.9	-46		[143]	[263]	[135]
Mg ²⁺	SO ₄ ²⁻	0.2135	3.367	-40.15	0.02875	[237]	[237]	[143] [237]
Mg ²⁺	Cl ⁻	0.3553	1.65		0.00651	[143]	[237]	[237]
Mg ²⁺	ClO ₄ ⁻	0.4956	2.097			[143]	[143]	
MgOH ⁺	Cl ⁻	-0.1	1.658			[260]	[260]	
Na ⁺	AlO ₂ ⁻	-0.0083	0.071		0.00977	[239]	[239]	[239]
Na ⁺	CO ₃ ²⁻	0.04625	1.389		0.0044	[143]	[260]	[260]
Na ⁺	HCO ₃ ⁻	-0.05876	0.5535	8.22		[143]	[143]	[237]

Table A8.6 continued

Na ⁺	HS ⁻	-0.103	0.884			[247]	[247]		
Na ⁺	HSiO3 ⁻	0.162	0.34			[244]	[244]		
Na ⁺	HSO ₄ ⁻	0.0454	0.398			[260]	[260]		
Na ⁺	OH ⁻	0.0864	0.253	0.0044		[239]	[239]	[239]	
Na ⁺	S ₂ O ₃ ²⁻	0.06306	1.254	0.004673		[143]	[143]	[143]	
Na ⁺	SCN ⁻	0.1048	0.3242			[143]	[143]		
Na ⁺	SO ₃ ²⁻	0.08015				[264,265]			
Na ⁺	SO ₄ ²⁻	0.01959	1.049	0.005416	0.005416	[143]	[143]		
Na ⁺	Cl ⁻	0.07831	0.2769	0.006718		[143]	[143]	[237]	[143]
Na ⁺	ClO ₄ ⁻	0.05422	0.2861	0.00148		[143]	[143]	[143]	[237]
NH ₄ ⁺	SO ₄ ²⁻	-0.05094	0.2068	-0.00285		[143]	[143]	[143]	

Table A8.7: Mixed electrolyte Pitzer parameters.

Aq. Species	Aq. Species	Aq. Species	Parameter Type	Parameter value	Reference
CO ₂	Ca ²⁺	-	λ_{nc}	0.183	[260]
CO ₂	K ⁺	-	λ_{nc}	0.051	[260]
CO ₂	Mg ²⁺	-	λ_{nc}	0.183	[260]
CO ₂	Na ⁺	-	λ_{nc}	0.085	[260]
SiO ₂	Ca ²⁺	-	λ_{nc}	0.2925	[266]
SiO ₂	K ⁺	-	λ_{nc}	0.03224	[266]
SiO ₂	Mg ²⁺	-	λ_{nc}	0.2925	[266]
SiO ₂	Na ⁺	-	λ_{nc}	0.0925	[266]
CO ₂	HSO ₄ ⁻	-	λ_{na}	-0.003	[260]

Table A8.7 continued

CO ₂	SO ₄ ²⁻	-		0.075	[237]
			λ_{na}		
SiO ₂	NO ₃ ⁻	-		-0.0094	[266]
			λ_{na}		
SiO ₂	SO ₄ ²⁻	-		-0.13963	[266]
			λ_{na}		
Ca ²⁺	H ⁺	-		0.092	[135]
			θ_{cc}		
Ca ²⁺	K ⁺	-		0.032	[135]
			θ_{cc}		
Ca ²⁺	Na ⁺	-		0.07	[135]
			θ_{cc}		
K ⁺	H ⁺	-		0.005	[135]
			θ_{cc}		
K ⁺	Na ⁺	-		-0.012	[135]
			θ_{cc}		
Mg ²⁺	Ca ²⁺	-		0.007	[135]
			θ_{cc}		
Mg ²⁺	H ⁺	-		0.1	[260]
			θ_{cc}		
Mg ²⁺	Na ⁺	-		0.07	[135]
			θ_{cc}		
Na ⁺	H ⁺	-		0.0368	[264,265]
			θ_{cc}		
NH ₄ ⁺	H ⁺	-		-0.019	[135]
			θ_{cc}		
AlO ₂ ⁻	OH ⁻	-		-0.2255	[239]
			θ_{aa}		
ClO ₄ ⁻	Cl ⁻	-		0.0341	[267]
			θ_{aa}		
CO ₃ ²⁻	OH ⁻	-		0.1	[135]
			θ_{aa}		
CO ₃ ²⁻	SO ₄ ²⁻	-		0.02	[135]
			θ_{aa}		
HCO ₃ ⁻	CO ₃ ²⁻	-		-0.04	[135]
			θ_{aa}		
HCO ₃ ⁻	SO ₄ ²⁻	-		0.01	[135]
			θ_{aa}		
OH ⁻	Cl ⁻	-		-0.05	[135]
			θ_{aa}		
OH ⁻	SO ₄ ²⁻	-		-0.013	[135]
			θ_{aa}		
Ca ²⁺	K ⁺	SO ₄ ²⁻		-0.0365	[237]
			ψ_{cca}		
Cl ⁻	H ⁺	Ca ²⁺		-0.015	[135]
			ψ_{cca}		

Table A8.7 continued

Cl ⁻	H ⁺	Mg ²⁺		-0.011	[135]
			Ψ_{cca}		
Cl ⁻	H ⁺	Na ⁺		-0.004	[135]
			Ψ_{cca}		
Cl ⁻	Mg ²⁺	MgOH ⁺		0.028	[260]
			Ψ_{cca}		
Cl ⁻	Na ⁺	Ca ²⁺		-0.007	[135]
			Ψ_{cca}		
Cl ⁻	Na ⁺	Mg ²⁺		-0.012	[135]
			Ψ_{cca}		
ClO ₄ ⁻	H ⁺	Na ⁺		-0.016	[135]
			Ψ_{cca}		
CO ₃ ²⁻	Na ⁺	K ⁺		0.003	[135]
			Ψ_{cca}		
H ⁺	K ⁺	SO ₄ ²⁻		0.197	[260]
			Ψ_{cca}		
HCO ₃ ⁻	Na ⁺	K ⁺		-0.003	[135]
			Ψ_{cca}		
HSO ₄ ⁻	H ⁺	K ⁺		-0.0265	[135]
			Ψ_{cca}		
HSO ₄ ⁻	H ⁺	Mg ²⁺		-0.0178	[135]
			Ψ_{cca}		
HSO ₄ ⁻	H ⁺	Na ⁺		-0.0129	[135]
			Ψ_{cca}		
NO ₃ ⁻	H ⁺	Na ⁺		-0.0274	[268]
			Ψ_{cca}		
NO ₃ ⁻	Na ⁺	K ⁺		-0.001	[135]
			Ψ_{cca}		
SO ₄ ²⁻	Ca ²⁺	Mg ²⁺		0.024	[135]
			Ψ_{cca}		
SO ₄ ²⁻	K ⁺	Mg ²⁺		-0.048	[135]
			Ψ_{cca}		
SO ₄ ²⁻	Na ⁺	Ca ²⁺		-0.055	[135]
			Ψ_{cca}		
SO ₄ ²⁻	Na ⁺	K ⁺		-0.01	[135]
			Ψ_{cca}		
SO ₄ ²⁻	Na ⁺	Mg ²⁺		-0.015	[135]
			Ψ_{cca}		
SO ₄ ²⁻	Na ⁺	NH ₄ ⁺		-0.0013	[135]
			Ψ_{cca}		
Ca ²⁺	Cl ⁻	OH ⁻		-0.025	[135]
			Ψ_{aac}		
K ⁺	CO ₃ ²⁻	HCO ₃ ⁻		0.012	[135]
			Ψ_{aac}		
K ⁺	OH ⁻	AlO ₂ ⁻		-0.0388	[239]
			Ψ_{aac}		

Table A8.7 continued

K ⁺	OH ⁻	CO ₃ ²⁻		-0.01	[135]
			Ψ_{aac}		
K ⁺	SO ₄ ²⁻	CO ₃ ²⁻		-0.009	[135]
			Ψ_{aac}		
K ⁺	SO ₄ ²⁻	HSO ₄ ⁻		-0.0677	[135]
			Ψ_{aac}		
K ⁺	SO ₄ ²⁻	OH ⁻		-0.05	[135]
			Ψ_{aac}		
Mg ²⁺	SO ₄ ²⁻	HCO ₃ ⁻		-0.161	[135]
			Ψ_{aac}		
Mg ²⁺	SO ₄ ²⁻	HSO ₄ ⁻		-0.0425	[135]
			Ψ_{aac}		
Na ⁺	Cl ⁻	ClO ₄ ⁻		-0.0057	[267]
			Ψ_{aac}		
Na ⁺	Cl ⁻	OH ⁻		-0.006	[135]
			Ψ_{aac}		
Na ⁺	CO ₃ ²⁻	HCO ₃ ⁻		0.002	[135]
			Ψ_{aac}		
Na ⁺	OH ⁻	AlO ₂ ⁻		-0.0048	[111]
			Ψ_{aac}		
Na ⁺	OH ⁻	CO ₃ ²⁻		-0.017	[135]
			Ψ_{aac}		
Na ⁺	SO ₄ ²⁻	CO ₃ ²⁻		-0.005	[135]
			Ψ_{aac}		
Na ⁺	SO ₄ ²⁻	HCO ₃ ⁻		-0.005	[135]
			Ψ_{aac}		
Na ⁺	SO ₄ ²⁻	HSO ₄ ⁻		-0.0094	[135]
			Ψ_{aac}		
Na ⁺	SO ₄ ²⁻	OH ⁻		-0.009	[135]
			Ψ_{aac}		

References

- [1] L. Arnold, *Windscale 1957: Anatomy of a Nuclear Accident*, 3rd ed., Palgrave Macmillan, New York, 1995. doi:10.1007/978-1-349-24008-1.
- [2] J. Mahaffey, *Atomic Accidents: A History of Nuclear Meltdowns and Disasters: From the Ozark Mountains to Fukushima*, 1st ed., Pegasus Books, New York, 2014.
- [3] BEIS, *Digest of UK energy statistics 2017*, (2017) 260 pp. doi:10.1016/0301-4215(88)90136-X.
- [4] NDA, *Radioactive Wastes in the UK: Summary of Data for International Reporting 2016, 2017*.
- [5] M.I. Ojovan, W.E. Lee, *An introduction to nuclear waste immobilisation*, Elsevier, Amsterdam, 2006. doi:10.1016/S1369-7021(06)71394-3.
- [6] NDA, *Radioactive Wastes in the UK: UK Radioactive Waste Inventory Report, 2017*. <https://ukinventory.nda.gov.uk/wp-content/uploads/sites/18/2014/01/2016UKRWMI-UK-Radioactive-waste-inventory-report.pdf>.
- [7] G.V. Hutson, *Waste Treatment*, in: Wilson, P.D. (Ed.), *The Nuclear Fuel Cycle: from Ore to Wastes*, 1st ed., Oxford University Press, 1996.
- [8] H. Godfrey, G. Cann, *Effect of chloride on magnox corrosion with respect to carbon-14 release post closure*, NNL, Risley. (2015).
- [9] NDA, *Radioactive Wastes in the UK: A Summary of the 2013 Inventory*, Cumbria, UK, 2013. www.nda.gov.uk/ukinventory.
- [10] NDA, *Geological Disposal: Guidance on the application of the Waste Package Specifications for unshielded waste packages*, Oxford, UK, 2014. www.nda.gov.uk.
- [11] M. Atkins, F.P. Glasser, *Application of Portland cement-based materials to radioactive waste immobilization*, *Waste Manag.* 12 (1992) 105–131. doi:10.1016/0956-053X(92)90044-J.
- [12] M. Moranville-Regourd, *Cements made from blastfurnace slag*, in: Hewlett, P.C. (Ed.), *Lea's Chemistry of Cement and Concrete*, 4th ed., 2003. doi:10.1016/B978-075066256-7/50023-0.
- [13] F.P. Glasser, *Progress in the immobilization of radioactive wastes in cement*, *Cem. Concr. Res.* 22 (1992) 201–216. doi:10.1016/0008-8846(92)90058-4.
- [14] J.H. Sharp, J. Hill, N.B. Milestone, E.W. Miller, *Cementitious Systems for Encapsulation of Intermediate Level Waste*, in: *Proc. ICEM 2003 9th Int. Conf. Radioact. Waste Manag. Environ. Remediat.*, 2003: pp. 1–10. doi:10.1115/ICEM2003-4554.

- [15] N.C. Collier, N.B. Milestone, The encapsulation of Mg(OH)₂ sludge in composite cement, *Cem. Concr. Res.* 40 (2010) 452–459. doi:10.1016/j.cemconres.2009.10.007.
- [16] J. Hill, J.H. Sharp, The mineralogy and microstructure of three composite cements with high replacement levels, *Cem. Concr. Compos.* 24 (2002) 191–199. doi:10.1016/S0958-9465(01)00041-5.
- [17] C.A. Utton, M. Hayes, J. Hill, N.B. Milestone, J.H. Sharp, Effect of temperatures up to 90 °C on the early hydration of Portland-blastfurnace slag cements, *J. Am. Ceram. Soc.* 91 (2008) 948–954. doi:10.1111/j.1551-2916.2007.02124.x.
- [18] C.H. Bland, J.H. Sharp, A conduction calorimetric study of gasifier slag-portland cement blends, *Cem. Concr. Res.* 21 (1991) 359–367. doi:10.1016/0008-8846(91)90017-C.
- [19] M.J. Angus, I.H. Godfrey, M. Hayes, S. Foster, Managing change in the supply of cement powders for radioactive waste encapsulation – Twenty years of operational experience, in: WM2010 Conf. Phoenix, U.S.A, 2010.
- [20] NDA, Geological Disposal: An introduction to the generic Disposal System Safety Case, 2010. doi:978-1-84029-445-3.
- [21] NDA, The 2013 UK Radioactive Waste Inventory, 2013.
- [22] S.J. Benbow, M.O. Rivett, N. Chittenden, A.W. Herbert, S. Watson, S.J. Williams, S. Norris, Potential migration of buoyant LNAPL from Intermediate Level Waste (ILW) emplaced in a Geological Disposal Facility (GDF) for UK radioactive waste, *J. Contam. Hydrol.* 167 (2014) 1–22. doi:10.1016/j.jconhyd.2014.07.011.
- [23] DECC, Implementing Geological Disposal: A Framework for the long-term management of higher activity radioactive waste, 2014.
- [24] A.J. Francis, R. Cather, I.G. Crossland, Science Report Nirex Safety Assessment Research Programme: Development of the Nirex Reference Vault Backfill; Report on Current Status in 1994, (1997).
- [25] R.G.W. Vasconcelos, N. Beaudoin, A. Hamilton, N.C. Hyatt, J.L. Provis, C.L. Corkhill, Characterisation of a high pH cement backfill for the geological disposal of nuclear waste: The Nirex Reference Vault Backfill, *Appl. Geochem.* 89 (2017) 180–189. doi:10.1016/j.apgeochem.2017.11.007.
- [26] NDA, A Review of the Development of Bentonite Barriers in the KBS-3V Disposal Concept,

- Harwell Oxford, UK, 2014. doi:10.1007/978-1-61779-821-4.
- [27] F.M. McEvoy, D.I. Schofield, R.P. Shaw, S. Norris, Tectonic and climatic considerations for deep geological disposal of radioactive waste: A UK perspective, *Sci. Total Environ.* 571 (2016) 507–521. doi:10.1016/j.scitotenv.2016.07.018.
- [28] NDA, Geological Disposal: Near-field evolution status report, 2010.
- [29] BEIS, Implementing Geological Disposal – Working With Communities, 2018.
- [30] F.M.I. Hunter, B.T. Swift, An assessment of the generation of GDF-derived gas using the 2007 Derived Inventory, AMEC. (2013).
- [31] S.C. Boden, Nirex Vault Environment Feasibility Study: Summary Report, NNC Ltd. (2002).
- [32] W. Kurdowski, Cement manufacture, in: Bensted, J. Barnes, P. (Eds.), *Structure and Performance of Cements*, 2nd ed., Spon Press, 2002.
- [33] H.F.W. Taylor, *Cement Chemistry*, 2nd ed., Thomas Telford Services Ltd, London, 1990. doi:10.1016/S0958-9465(98)00023-7.
- [34] J.W. Bullard, H.M. Jennings, R.A. Livingston, A. Nonat, G.W. Scherer, J.S. Schweitzer, K.L. Scrivener, J.J. Thomas, Mechanisms of cement hydration, *Cem. Concr. Res.* 41 (2011) 1208–1223. doi:10.1016/j.cemconres.2010.09.011.
- [35] C.D. Lawrence, The Production of Low-Energy Cements, in: Hewlett, P.C. (Ed.), *Lea's Chemistry of Cement and Concrete*, 4th ed., 2003. doi:10.1016/B978-075066256-7/50021-7.
- [36] F. Massazza, Pozzolana and Pozzolanic Cements, in: Hewlett, P.C. (Ed.), *Lea's Chemistry of Cement and Concrete*, 4th ed., 2004.
- [37] B. Lothenbach, K.L. Scrivener, R.D. Hooton, Supplementary cementitious materials, *Cem. Concr. Res.* 41 (2011) 1244–1256. doi:10.1016/j.cemconres.2010.12.001.
- [38] P.W. Scott, The Chemistry and Mineralogy of Some Granulated and Pelletized Blastfurnace Slags, *Mineral. Mag.* 50 (1986) 141–147. doi:10.1180/minmag.1986.050.355.19.
- [39] E. Lang, Blastfurnace cements, in: Bensted, J., Barnes, P. (Eds.), *Structure and Performance of Cements*, 2nd ed., Spon Press, 2002.
- [40] J.I. Escalante, L.Y.Y. Gómez, K.K. Johal, G. Mendoza, H. Mancha, J. Méndez, Reactivity of blast-furnace slag in Portland cement blends hydrated under different conditions, *Cem. Concr. Res.* 31 (2001) 1403–1409. doi:10.1016/S0008-8846(01)00587-7.

- [41] J.S. Lumley, R.S. Gollop, G.K. Moir, H.F.W. Taylor, Degrees of reaction of the slag in some blends with Portland cements, *Cem. Concr. Res.* 26 (1996) 139–151. doi:10.1016/0008-8846(95)00190-5.
- [42] Y. Kawabata, K. Yamada, Evaluation of Alkalinity of Pore Solution Based on the Phase Composition of Cement Hydrates with Supplementary Cementitious Materials and its Relation to Suppressing ASR Expansion, *J. Adv. Concr. Technol.* 13 (2015) 538–553. doi:10.3151/jact.13.538.
- [43] K.L. Scrivener, P. Juilland, P.J.M. Monteiro, *Advances in understanding hydration of Portland cement*, Elsevier Ltd, 2015. doi:10.1016/j.cemconres.2015.05.025.
- [44] I.G. Richardson, G.W. Groves, Microstructure and microanalysis of hardened cement pastes involving ground granulated blast-furnace slag, *J. Mater. Sci.* 27 (1992) 6204–6212. doi:10.1007/BF01133772.
- [45] R. Taylor, I.G. Richardson, R.M.D. Brydson, Composition and microstructure of 20-year-old ordinary Portland cement–ground granulated blast-furnace slag blends containing 0 to 100% slag, *Cem. Concr. Res.* 40 (2010) 971–983. doi:10.1016/j.cemconres.2010.02.012.
- [46] R. Snellings, A. Salze, K.L. Scrivener, Use of X-ray diffraction to quantify amorphous supplementary cementitious materials in anhydrous and hydrated blended cements, *Cem. Concr. Res.* 64 (2014) 89–98. doi:10.1016/j.cemconres.2014.06.011.
- [47] I. Odler, Hydration, Setting and Hardening of Portland Cement, in: Hewlett, P.C. (Ed.), *Lea's Chemistry of Cement and Concrete*, 4th ed., 2003. doi:10.1016/B978-075066256-7/50018-7.
- [48] B. Lothenbach, A. Nonat, Calcium silicate hydrates: Solid and liquid phase composition, *Cem. Concr. Res.* 78 (2015) 57–70. doi:10.1016/j.cemconres.2015.03.019.
- [49] I.G. Richardson, The calcium silicate hydrates, *Cem. Concr. Res.* 38 (2008) 137–158. doi:10.1016/j.cemconres.2007.11.005.
- [50] G.K. Sun, J.F. Young, R.J. Kirkpatrick, The role of Al in C-S-H: NMR, XRD, and compositional results for precipitated samples, *Cem. Concr. Res.* 36 (2006) 18–29. doi:10.1016/j.cemconres.2005.03.002.
- [51] M.D. Andersen, H.J. Jakobsen, J. Skibsted, Incorporation of aluminum in the calcium silicate hydrate (C-S-H) of hydrated Portland cements: A high-field ^{27}Al and ^{29}Si MAS NMR investigation, *Inorg. Chem.* 42 (2003) 2280–2287. doi:10.1021/ic020607b.

- [52] J. Skibsted, H.J. Jakobsen, C. Hall, Quantification of calcium silicate phases in Portland cements by ^{29}Si MAS NMR spectroscopy, *J. Chem. Soc. Faraday Trans.* 91 (1995) 4423–4430. doi:10.1039/FT9959104423.
- [53] A. Atkinson, J.A. Hearne, C.F. Knights, Aqueous Chemistry and Thermodynamic Modelling of $\text{CaO-SiO}_2\text{-H}_2\text{O}$ gels, *J. Chem. Soc.* 0 (1989) 2371–2379. doi:10.1039/DT9890002371.
- [54] J.J. Chen, J.J. Thomas, H.F.W. Taylor, H.M. Jennings, Solubility and structure of calcium silicate hydrate, *Cem. Concr. Res.* 34 (2004) 1499–1519. doi:10.1016/j.cemconres.2004.04.034.
- [55] I.G. Richardson, J.G. Cabrera, The nature of C-S-H in model slag-cements, *Cem. Concr. Compos.* 22 (2000) 259–266. doi:10.1016/S0958-9465(00)00022-6.
- [56] A. Nonat, The structure and stoichiometry of C-S-H, *Cem. Concr. Res.* 34 (2004) 1521–1528. doi:10.1016/j.cemconres.2004.04.035.
- [57] F. Puertas, M. Palacios, H. Manzano, J.S. Dolado, A. Rico, J. Rodríguez, A model for the C-A-S-H gel formed in alkali-activated slag cements, *J. Eur. Ceram. Soc.* 31 (2011) 2043–2056. doi:10.1016/j.jeurceramsoc.2011.04.036.
- [58] I.G. Richardson, Model Structures for C-(A)-S-H(I), *Acta Crystallogr. Sect. B Struct. Crystallogr. Cryst. Chem.* B70 (2014) 903–923. doi:10.1107/S2052520614021982.
- [59] S.Y. Hong, F.P. Glasser, Alkali binding in cement pastes. Part I: the C-S-H phase, *Cem. Concr. Res.* 29 (1999) 1893–1903. doi:10.1016/S0008-8846(99)00187-8.
- [60] S.A. Bernal, R. San Nicolas, R.J. Myers, R. Mejía De Gutiérrez, F. Puertas, J.S.J. Van Deventer, J.L. Provis, MgO content of slag controls phase evolution and structural changes induced by accelerated carbonation in alkali-activated binders, *Cem. Concr. Res.* 57 (2014) 33–43. doi:10.1016/j.cemconres.2013.12.003.
- [61] T.T.H. Bach, E. Chabas, I. Pochard, C. Cau Dit Coumes, J. Haas, F. Frizon, A. Nonat, Retention of alkali ions by hydrated low-pH cements: Mechanism and Na^+/K^+ selectivity, *Cem. Concr. Res.* 51 (2013) 14–21. doi:10.1016/j.cemconres.2013.04.010.
- [62] H. Stade, On the reaction of C-S-H(di, poly) with alkali hydroxides, *Cem. Concr. Res.* 19 (1989) 802–810. doi:10.1016/0008-8846(89)90051-3.
- [63] E. L'Hôpital, B. Lothenbach, D.A. Kulik, K. Scrivener, Influence of calcium to silica ratio on aluminium uptake in calcium silicate hydrate, *Cem. Concr. Res.* 85 (2016) 111–121. doi:10.1016/j.cemconres.2016.01.014.

- [64] D.A. Kulik, Improving the structural consistency of C-S-H solid solution thermodynamic models, *Cem. Concr. Res.* 41 (2011) 477–495. doi:10.1016/j.cemconres.2011.01.012.
- [65] C.S. Walker, S. Sutou, C. Oda, M. Mihara, A. Honda, Calcium silicate hydrate (C-S-H) gel solubility data and a discrete solid phase model at 25 °C based on two binary non-ideal solid solutions, *Cem. Concr. Res.* 79 (2016) 1–30. doi:10.1016/j.cemconres.2015.07.006.
- [66] J. Duchesne, E.J. Reardon, Measurement and prediction of portlandite solubility in alkali solutions, *Cem. Concr. Res.* 25 (1995) 1043–1053. doi:10.1016/0008-8846(95)00099-X.
- [67] K.L. Scrivener, A. Nonat, Hydration of cementitious materials, present and future, *Cem. Concr. Res.* 41 (2011) 651–665. doi:10.1016/j.cemconres.2011.03.026.
- [68] C.-T.A. Chen, W.L. Marshall, Amorphous silica solubilities IV. Behavior in pure water and aqueous sodium chloride, sodium sulfate, magnesium chloride, and magnesium sulfate solutions up to 350°C, *Geochim. Cosmochim. Acta.* 46 (1982) 279–287. doi:10.1016/0016-7037(82)90255-1.
- [69] M. Grutzeck, A. Benesi, B. Fanning, Silicon-29 Magic Angle Spinning Nuclear Magnetic Resonance Study of Calcium Silicate Hydrates, *J. Am. Ceram. Soc.* 72 (1989) 665–668. doi:10.1111/j.1151-2916.1989.tb06192.x.
- [70] J. Haas, Etude expérimentale et modélisation thermodynamique du système CaO-SiO₂-(Al₂O₃)-H₂O, Université de Bourgogne, Français, 2012.
- [71] A.W. Harris, M.C. Manning, W.M. Tearle, C.J. Tweed, Testing of models of the dissolution of cements - Leaching of synthetic CSH gels, *Cem. Concr. Res.* 32 (2002) 731–746. doi:10.1016/S0008-8846(01)00748-7.
- [72] P. Henocq, Modélisation des interactions ioniques à la surface des Silicates de Calcium Hydratés, L'Université Laval, Quebec, Canada, 2005.
- [73] I. Pointeau, Etude Mécanistique et modelisation de la retention de radionucleides par les silicates de calcium hydrates (CSH) des ciments, Chimie, L'Université de Reims Champagne-Ardenne, Reims, France, 2000.
- [74] D. Sugiyama, Chemical alteration of calcium silicate hydrate (C-S-H) in sodium chloride solution, *Cem. Concr. Res.* 38 (2008) 1270–1275. doi:10.1016/j.cemconres.2008.06.002.
- [75] S.W. Swanton, H.J. Fairbrother, N.A. Turner, The effect of sodium chloride on the dissolution of calcium silicate hydrate gels. II., 2006. doi:10.1016/j.wasman.2006.01.022.

- [76] C.S. Walker, D. Savage, M. Tyrer, K.V. Ragnarsdottir, Non-ideal solid solution aqueous solution modeling of synthetic calcium silicate hydrate, *Cem. Concr. Res.* 37 (2007) 502–511. doi:10.1016/j.cemconres.2006.12.002.
- [77] M. Atkins, F.P. Glasser, A. Kindness, Cement hydrate phase: Solubility at 25°C, *Cem. Concr. Res.* 22 (1992) 241–246. doi:10.1016/0008-8846(92)90062-Z.
- [78] A. V. Chambers, T.G. Heath, F.M.I. Hunter, M.C. Manning, S.J. Williams, The effect of sodium chloride on the dissolution of calcium silicate hydrate gels, 2005. doi:10.1016/j.wasman.2006.01.022.
- [79] A.-C. Courault, Simulation expérimentale des C-S-H dans les bétons modernes: Etude de la composition et des propriétés à l'équilibre dans des milieux complexes, Laboratoire de Recherches sur la Réactivité des Solides, Université de Bourgogne, 2000.
- [80] E.P. Flint, L.S. Wells, Study of the system CaO-SiO₂-H₂O at 30 °C and of the reaction of water on the anhydrous calcium silicates, *Bur. Stand. J. Res.* 12 (1934) 751–783. doi:10.6028/jres.012.060.
- [81] B.K. Fujii, W. Kondo, Heterogeneous Equilibrium of Calcium Silicate Hydrate in water at 30 °C, *J. Chem. Soc. Dalt. Trans.* (1981) 645–651.
- [82] F. Glasser, M. Tyrer, K. Quillin, The chemistry of blended cements and backfills intended for use in radioactive waste disposal, Bristol (United Kingdom), 1999.
- [83] S.A. Greenberg, T.N. Chang, Investigation of the Colloidal Hydrated Calcium Silicates. II. Solubility Relationships in the Calcium Oxide-Silica-Water System at 25°, *J. Phys. Chem.* 69 (1965) 182–188. doi:10.1021/j100885a027.
- [84] I.G. Richardson, G.W. Groves, Microstructure and microanalysis of hardened ordinary Portland cement pastes, *J. Mater. Sci.* 28 (1993) 265–277. doi:10.1007/BF00349061.
- [85] S.Y. Hong, F.P. Glasser, Alkali sorption by C-S-H and C-A-S-H gels: Part II. Role of alumina, *Cem. Concr. Res.* 32 (2002) 1101–1111. doi:10.1016/S0008-8846(02)00753-6.
- [86] I.G. Richardson, A.R. Brough, R. Brydson, G.W. Groves, C.M. Dobsont, Location of aluminum in substituted calcium silicate hydrate (C-S-H) gels as determined by ²⁹Si and ²⁷Al NMR and EELS, *J. Am. Ceram. Soc.* 76 (1993) 2285–2288. doi:10.1111/j.1151-2916.1993.tb07765.x.
- [87] L. Pegado, C. Labbez, S. V. Churakov, Mechanism of aluminium incorporation into C-S-H from ab initio calculations, *J. Mater. Chem. A.* 2 (2014) 3477. doi:10.1039/c3ta14597b.

- [88] W. Loewenstein, The distribution of aluminum in the tetrahedra of silicates and aluminates., *Am. Mineral.* 39 (1954) 92–96.
- [89] V. Kocaba, Development and evaluation of methods to follow microstructural development of cementitious systems including slags, 2009. doi:10.5075/epfl-thesis-4523.
- [90] K. Luke, E. Lachowski, Internal composition of 20-year-old fly ash and slag-blended ordinary portland cement pastes, *J. Am. Ceram. Soc.* 91 (2008) 4084–4092. doi:10.1111/j.1551-2916.2008.02783.x.
- [91] E.M. Gartner, J.F. Young, D.A. Damidot, I. Jawed, Hydration of Portland Cement, in: Bensted, J., Barnes, P. (Eds.), *Structure and Performance of Cements*, 2nd ed., Spos Press, 2002.
- [92] T. Matschei, *Thermodynamics of Cement Hydration*, University of Aberdeen, 2007.
- [93] A. Quennoz, K.L. Scrivener, Interactions between alite and C₃A-gypsum hydrations in model cements, *Cem. Concr. Res.* 44 (2013) 46–54. doi:10.1016/j.cemconres.2012.10.018.
- [94] B. Lothenbach, G. Le Saout, E. Gallucci, K. Scrivener, Influence of limestone and anhydrite on the hydration of Portland cements, *Cem. Concr. Res.* 38 (2008) 848–860. doi:10.1016/j.cemconcomp.2013.11.007.
- [95] T. Matschei, B. Lothenbach, F.P. Glasser, The role of calcium carbonate in cement hydration, *Cem. Concr. Res.* 37 (2007) 551–558. doi:10.1016/j.cemconres.2006.10.013.
- [96] S. Adu-Amankwah, M. Zajac, C. Stabler, B. Lothenbach, L. Black, Influence of limestone on the hydration of ternary slag cements, *Cem. Concr. Compos.* 100 (2017) 96–109. doi:10.1016/j.cemconcomp.2013.11.007.
- [97] T. Matschei, B. Lothenbach, F.P. Glasser, The AFm phase in Portland cement, *Cem. Concr. Res.* 37 (2007) 118–130. doi:10.1016/j.cemconres.2006.10.010.
- [98] D. Damidot, F.P. Glasser, Thermodynamic investigation of the CaO-Al₂O₃-CaSO₄-H₂O system at 25°C and the influence of Na₂O, *Cem. Concr. Res.* 23 (1993) 221–238. doi:10.1016/0008-8846(93)90153-Z.
- [99] D. Damidot, S. Stronach, A. Kindness, M. Atkins, F.P. Glasser, Thermodynamic investigation of the CaO-Al₂O₃-CaCO₃-H₂O closed system at 25°C and the influence of Na₂O, *Cem. Concr. Res.* 24 (1994) 563–572. doi:10.1016/0008-8846(94)90145-7.
- [100] C.E. Harvie, N. Møller, J.H. Weare, The prediction of mineral solubilities in natural waters: The Na-K-Mg-Ca-H-Cl-SO₄-OH-HCO₃-CO₃-CO₂-H₂O system to high ionic strengths at 25 °C,

- Geochim. Cosmochim. Acta. 48 (1984) 723–751. doi:10.1016/0016-7037(84)90098-X.
- [101] M. Ben Haha, B. Lothenbach, G. Le Saout, F. Winnefeld, Influence of slag chemistry on the hydration of alkali-activated blast-furnace slag — Part I: Effect of MgO, *Cem. Concr. Res.* 41 (2011) 955–963. doi:10.1016/j.cemconres.2011.05.002.
- [102] M. Ben Haha, B. Lothenbach, G. Le Saout, F. Winnefeld, Influence of slag chemistry on the hydration of alkali-activated blast-furnace slag — Part II: Effect of Al₂O₃, *Cem. Concr. Res.* 42 (2012) 74–83. doi:10.1016/j.cemconres.2011.08.005.
- [103] I.G. Richardson, Clarification of possible ordered distributions of trivalent cations in layered double hydroxides and an explanation for the observed variation in the lower solid-solution limit, *Acta Crystallogr. Sect. B Struct. Sci. Cryst. Eng. Mater.* 69 (2013) 629–633. doi:10.1107/S2052519213027905.
- [104] A. Vollpracht, B. Lothenbach, R. Snellings, J. Haufe, The pore solution of blended cements: a review, *Mater. Struct.* 49 (2015) 3341–3367. doi:10.1617/s11527-015-0724-1.
- [105] Z. Tan, *Experimental Study and Numerical Simulation of Tube Hydroforming*, Ghent University, 2015.
- [106] E. Schäfer, *Einfluss der Reaktionen verschiedener Zementhauptbestandteile auf den Alkalihaushalt der Porenlösung des Zementsteins*, Technischen Universität Clausthal, 2004.
- [107] Z. Tan, G. De Schutter, G. Ye, Y. Gao, L. Machiels, Influence of particle size on the early hydration of slag particle activated by Ca(OH)₂ solution, *Constr. Build. Mater.* 52 (2014) 488–493. doi:10.1016/j.conbuildmat.2013.11.073.
- [108] E. L'Hôpital, B. Lothenbach, K. Scrivener, D.A. Kulik, Alkali uptake in calcium alumina silicate hydrate (C-A-S-H), *Cem. Concr. Res.* 85 (2016) 122–136. doi:10.1016/j.cemconres.2016.03.009.
- [109] G.D. Miron, T. Wagner, D.A. Kulik, B. Lothenbach, An internally consistent thermodynamic dataset for aqueous species in the system Ca-Mg-Na-K-Al-Si-O-H-C-Cl to 800 °C and 5 KBAR, *Am. J. Sci.* 317 (2017) 755–806. doi:10.2475/07.2017.01.
- [110] M. Altmaier, V. Metz, V. Neck, R. Müller, T. Fanghänel, Solid-liquid equilibria of Mg(OH)₂(cr) and Mg₂(OH)₃Cl·4H₂O(cr) in the system Mg-Na-H-OH-Cl-H₂O at 25°C, *Geochim. Cosmochim. Acta.* 67 (2003) 3595–3601. doi:10.1016/S0016-7037(03)00165-0.
- [111] D.J. Wesolowski, Aluminum Speciation and Equilibria in Aqueous-Solution: I. The Solubility of Gibbsite in the system Na-K-Cl-OH-Al(OH)₄ from 0 to 100 °C, *Geochim. Cosmochim. Acta.* 56

- (1992) 1065–1091. doi:Doi 10.1016/0016-7037(92)90048-N.
- [112] D. Damidot, F.P. Glasser, Thermodynamic investigation of the CaO-Al₂O₃-CaSO₄-K₂O-H₂O system at 25°C, *Cem. Concr. Res.* 23 (1993) 1195–1204. doi:10.1016/0008-8846(93)90180-H.
- [113] P. Feng, C. Miao, J.W. Bullard, Factors Influencing the Stability of AFm and Aft in the Ca-Al-S-O-H System at 25°C, *J. Am. Ceram. Soc.* 99 (2016) 1031–1041. doi:10.1111/jace.13971.
- [114] A. Gruskovnjak, B. Lothenbach, L. Holzer, R. Figi, F. Winnefeld, Hydration of alkali-activated slag: comparison with ordinary Portland cement, *Adv. Cem. Res.* 18 (2006) 119–128. doi:10.1680/adcr.2006.18.3.119.
- [115] D.L. Parkhurst, C.A.J. Appelo, Description of Input and Examples for PHREEQC Version 3 — A Computer Program for Speciation, Batch-Reaction, One-Dimensional Transport, and Inverse Geochemical Calculations., U.S. Geol. Surv. Tech. Methods, B. 6, Chapter A43. (2013) 6–43A. doi:10.1016/0029-6554(94)90020-5.
- [116] C.M. Bethke, Activity coefficients, in: *Geochemical and Biogeochemical Reaction Modelling*, 2nd ed., Cambridge University Press, 2007. doi:10.1017/CBO9780511619670.011.
- [117] J. Bruno, D. Bosbach, D.A. Kulik, A. Navrotsky, Chemical thermodynamics of solid solutions of interest in radioactive waste management: a state-of-the-art report, OECD, 2007. doi:978-92-64-02655-1.
- [118] B. Lothenbach, F. Winnefeld, Thermodynamic modelling of the hydration of Portland cement, *Cem. Concr. Res.* 36 (2006) 209–226. doi:10.1016/j.cemconres.2005.03.001.
- [119] B.Z. Dilnesa, E. Wieland, B. Lothenbach, R. Dähn, K.L. Scrivener, Fe-containing phases in hydrated cements, *Cem. Concr. Res.* 58 (2014) 45–55. doi:10.1016/j.cemconres.2013.12.012.
- [120] D. Damidot, B. Lothenbach, D. Herfort, F.P. Glasser, Thermodynamics and cement science, *Cem. Concr. Res.* 41 (2011) 679–695. doi:10.1016/j.cemconres.2011.03.018.
- [121] B. Lothenbach, Thermodynamic equilibrium calculations in cementitious systems, *Mater. Struct.* 43 (2010) 1413–1433. doi:10.1617/s11527-010-9592-x.
- [122] D.P. Prentice, S.A. Bernal, M. Bankhead, M. Hayes, J.L. Provis, Phase evolution of slag-rich cementitious grouts for immobilisation of nuclear wastes, *Adv. Cem. Res.* 30 (2018) 345–360. doi:10.1680/jadcr.17.00198.
- [123] R.J. Myers, B. Lothenbach, S.A. Bernal, J.L. Provis, Thermodynamic modelling of alkali-activated slag cements, *Appl. Geochemistry.* 61 (2015) 233–247. doi:10.1016/j.apgeochem.2015.06.006.

- [124] R.J. Myers, S.A. Bernal, J.L. Provis, Phase diagrams for alkali-activated slag binders, *Cem. Concr. Res.* 95 (2017) 30–38. doi:10.1016/j.cemconres.2017.02.006.
- [125] Y. Elakneswaran, E. Owaki, S. Miyahara, M. Ogino, T. Maruya, T. Nawa, Hydration study of slag-blended cement based on thermodynamic considerations, *Constr. Build. Mater.* 124 (2016) 615–625. doi:10.1016/j.conbuildmat.2016.07.138.
- [126] R.H. Davies, J.A. Gisby, A. Dinsdale, M. Tyrer, C.S. Walker, F.P. Glasser, Thermodynamic modelling of phase equilibria in cement systems: multiple sublattice model for solids in equilibrium with non-ideal aqueous phase, *Adv. Appl. Ceram.* 113 (2014) 509–516. doi:10.1179/1743676114Y.0000000205.
- [127] F. Winnefeld, B. Lothenbach, Hydration of calcium sulfoaluminate cements — Experimental findings and thermodynamic modelling, *Cem. Concr. Res.* 40 (2010) 1239–1247. doi:10.1016/j.cemconres.2009.08.014.
- [128] D.A. Kulik, Geochemical thermodynamic modelling of ion partitioning, *EMU Notes Mineral.* 10 (2010) 65–138. doi:10.1180/EMU-notes.10.3.
- [129] C.A.J. Appelo, D. Postma, *Geochemistry, Groundwater and Pollution*, 2nd ed., 2005.
- [130] K.A. Stroud, D.J. Booth, *Advanced Engineering Mathematics*, 5th ed., Palgrave Macmillan, 2011.
- [131] G.M. Anderson, D.A. Crerar, *Thermodynamics in Geochemistry: The Equilibrium Model*, 1993.
- [132] D.A. Kulik, T. Wagner, S. V. Dmytrieva, G. Kosakowski, F.F. Hingerl, K. V. Chudnenko, U.R. Berner, GEM-Selektor geochemical modeling package: revised algorithm and GEMS3K numerical kernel for coupled simulation codes, *Comput. Geosci.* 17 (2013) 1–24. doi:10.1007/s10596-012-9310-6.
- [133] G.M. Anderson, *Thermodynamics of Natural Systems*, Cambridge University Press, Cambridge, 2005. doi:10.1017/CBO9780511840258.
- [134] H.C. Helgeson, D.H. Kirkham, G.C. Flowers, Theoretical prediction of the thermodynamic behavior of aqueous electrolytes by high pressures and temperatures IV; calculation of activity coefficients, osmotic coefficients and apparent molal & standard relative partial molal properties to 600°C & 5 kBar, *Am. J. Sci.* 281 (1981) 1249–1516. doi:10.2475/ajs.281.10.1249.
- [135] K.S. Pitzer, Ion interaction approach: theory and data correlation, in: Pitzer, K. S. (Ed.), *Activity Coefficients in Electrolyte Solutions*, 2nd ed., 1991.

- [136] D. Langmuir, Activity Coefficients of Dissolved Species in: Aqueous Environmental Geochemistry, 1997. doi:10.1029/97EO00355.
- [137] D.A. Sverjensky, E.L. Shock, H.C. Helgeson, Prediction of the thermodynamic properties of aqueous metal complexes to 1000°C and 5 kb, *Geochim. Cosmochim. Acta.* 61 (1997) 1359–1412.
- [138] K.S. Pitzer, Thermodynamics of electrolytes. I. Theoretical basis and general equations, *J. Phys. Chem.* 77 (1973) 268–277. doi:10.1021/j100621a026.
- [139] K.S. Pitzer, G. Mayorga, Thermodynamics of electrolytes. II. Activity and osmotic coefficients for strong electrolytes with one or both ions univalent, *J. Phys. Chem.* 77 (1973) 2300–2308. doi:10.1021/j100638a009.
- [140] K.S. Pitzer, G. Mayorga, Thermodynamics of electrolytes. III. Activity and osmotic coefficients for 2-2 electrolytes, *J. Solution Chem.* 3 (1974) 539–546. doi:10.1007/BF00648138.
- [141] K.S. Pitzer, J.J. Kim, Thermodynamics of Electrolytes. IV. Activity and Osmotic Coefficients for Mixed Electrolytes, *J. Am. Chem. Soc.* 96 (1974) 5701–5707. doi:10.1021/ja00825a004.
- [142] P.M. May, D. Rowland, Thermodynamic Modeling of Aqueous Electrolyte Systems: Current Status, *J. Chem. Eng. Data.* (2017) acs.jced.6b01055. doi:10.1021/acs.jced.6b01055.
- [143] P.M. May, D. Rowland, G. Hefter, E. Königsberger, A generic and updatable pitzer characterization of aqueous binary electrolyte solutions at 1 bar and 25 °C, *J. Chem. Eng. Data.* 56 (2011) 5066–5077. doi:10.1021/je2009329.
- [144] C.E. Harvie, J.H. Weare, The prediction of mineral solubilities in natural waters: The Na-K-M-Ca-Cl-SO₂-H₂O system from zero to high concentration at 25°C, *Geochim. Cosmochim. Acta.* 44 (1980) 981–997. doi:10.1016/0016-7037(80)90287-2.
- [145] D. Rowland, E. Königsberger, G. Hefter, P.M. May, Aqueous electrolyte solution modelling: Some limitations of the Pitzer equations, *Appl. Geochemistry.* 55 (2015) 170–183. doi:10.1016/j.apgeochem.2014.09.021.
- [146] R.J. Myers, S.A. Bernal, J.L. Provis, A thermodynamic model for C-(N-)A-S-H gel: CNASH_{ss}. Derivation and validation, *Cem. Concr. Res.* 66 (2014) 27–47. doi:10.1016/j.cemconres.2014.07.005.
- [147] M.U. Okoronkwo, M. Balonis, L. Katz, M.C.G. Juenger, G. Sant, A thermodynamics-based approach for examining the suitability of cementitious formulations for solidifying and

- stabilizing coal-combustion wastes, *J. Environ. Manage.* 217 (2018) 278–287. doi:10.1016/j.jenvman.2018.02.095.
- [148] D. Damidot, F.P. Glasser, Investigation of the CaO-Al₂O₃-SiO₂-H₂O system at 25 °C by thermodynamic calculations, *Cem. Concr. Res.* 25 (1995) 22–28. doi:10.1016/0008-8846(94)00108-B.
- [149] B.Z. Dilnesa, B. Lothenbach, G. Renaudin, A. Wichser, D.A. Kulik, Synthesis and characterization of hydrogarnet Ca₃(Al_xFe_{1-x})₂(SiO₄)_y(OH)_{4(3-y)}, *Cem. Concr. Res.* 59 (2014) 96–111. doi:10.1016/j.cemconres.2014.02.001.
- [150] T. Matschei, B. Lothenbach, F.P. Glasser, Thermodynamic properties of Portland cement hydrates in the system CaO-Al₂O₃-SiO₂-CaSO₄-CaCO₃-H₂O, *Cem. Concr. Res.* 37 (2007) 1379–1410. doi:10.1016/j.cemconres.2007.06.002.
- [151] B. Lothenbach, T. Matschei, G. Möschner, F.P. Glasser, Thermodynamic modelling of the effect of temperature on the hydration and porosity of Portland cement, *Cem. Concr. Res.* 38 (2008) 1–18. doi:10.1016/j.cemconres.2007.08.017.
- [152] D.A. Kulik, M. Kersten, Aqueous solubility diagrams for cementitious waste stabilization systems. 4. A carbonation model for Zn-Doped calcium silicate hydrate by Gibbs energy minimization, *Environ. Sci. Technol.* 36 (2002) 2926–2931. doi:10.1021/es010250v.
- [153] R. Snellings, X-ray powder diffraction applied to cement, in: Scrivener, K., Snellings, R., Lothenbach, B. (Eds.), *A Practical Guide to Microstructural Analysis of Cementitious Materials*, 1st ed., 2015. doi:10.1201/b19074-5.
- [154] K. Luke, F.P. Glasser, Selective dissolution of hydrated blast furnace slag cements, *Cem. Concr. Res.* 17 (1987) 273–282. doi:10.1016/0008-8846(87)90110-4.
- [155] V. Kocaba, E. Gallucci, K.L. Scrivener, Methods for determination of degree of reaction of slag in blended cement pastes, *Cem. Concr. Res.* 42 (2012) 511–525. doi:10.1016/j.cemconres.2011.11.010.
- [156] P.T. Durdziński, M. Ben Haha, S.A. Bernal, N. De Belie, E. Gruyaert, B. Lothenbach, E. Menéndez Méndez, J.L. Provis, A. Schöler, C. Stabler, Z. Tan, Y. Villagrán Zaccardi, A. Vollpracht, F. Winnefeld, M. Zajac, K.L. Scrivener, Outcomes of the RILEM round robin on degree of reaction of slag and fly ash in blended cements, *Mater. Struct.* 50 (2017) 135. doi:10.1617/s11527-017-1002-1.
- [157] J.I. Escalante-García, A.F. Fuentes, A. Gorokhovskiy, P.E. Fraire-Luna, G. Mendoza-Suarez,

- Hydration Products and Reactivity of Blast-Furnace Slag Activated by Various Alkalis, *J. Am. Ceram. Soc.* 86 (2003) 2148–2153. doi:10.1111/j.1151-2916.2003.tb03623.x.
- [158] H.M. Dyson, I.G. Richardson, A.R. Brough, A combined ^{29}Si MAS NMR and selective dissolution technique for the quantitative evaluation of hydrated blast furnace slag cement blends, *J. Am. Ceram. Soc.* 90 (2007) 598–602. doi:10.1111/j.1551-2916.2006.01431.x.
- [159] K. Scrivener, R. Snellings, B. Lothenbach, *A Practical Guide to Microstructural Analysis of Cementitious Materials*, (2016) 1–509.
- [160] I. Ismail, S.A. Bernal, J.L. Provis, S. Hamdan, J.S.J. Van Deventer, Drying-induced changes in the structure of alkali-activated pastes, *J. Mater. Sci.* 48 (2013) 3566–3577. doi:10.1007/s10853-013-7152-9.
- [161] I.G. Richardson, L. Black, J. Skibsted, R.J. Kirkpatrick, Characterisation of cement hydrate phases by TEM, NMR and Raman spectroscopy, *Adv. Cem. Res.* 22 (2010) 233–248. doi:10.1680/adcr.2010.22.4.233.
- [162] S.L. Poulsen, V. Kocaba, G. Le Saoût, H.J. Jakobsen, K.L. Scrivener, J. Skibsted, Improved quantification of alite and belite in anhydrous Portland cements by ^{29}Si MAS NMR: effects of paramagnetic ions., *Solid State Nucl. Magn. Reson.* 36 (2009) 32–44. doi:10.1016/j.ssnmr.2009.05.001.
- [163] J. Skibsted, Nuclear magnetic resonance spectroscopy of proteins, in: Scrivener, K., Snellings, R., Lothenbach, B. (Eds.), *A Practical Guide to Microstructural Analysis of Cementitious Materials*, 1st ed., 2016.
- [164] R.J. Myers, S.A. Bernal, R. San Nicolas, J.L. Provis, Generalized structural description of calcium-sodium aluminosilicate hydrate gels: the cross-linked substituted tobermorite model., *Langmuir.* 29 (2013) 5294–306. doi:10.1021/la4000473.
- [165] E. L'Hôpital, B. Lothenbach, G. Le Saout, D.A. Kulik, K. Scrivener, Incorporation of aluminium in calcium-silicate-hydrates, *Cem. Concr. Res.* 75 (2015) 91–103. doi:10.1016/j.cemconres.2015.04.007.
- [166] C.L. Edwards, L.B. Alemany, A.R. Barron, Solid-state ^{29}Si NMR analysis of cements: Comparing different methods of relaxation analysis for determining spin-lattice relaxation times to enable determination of the $\text{C}_3\text{S}/\text{C}_2\text{S}$ ratio, *Ind. Eng. Chem. Res.* 46 (2007) 5122–5130. doi:10.1021/ie070220m.
- [167] R.J. Myers, S.A. Bernal, J.D. Gehman, J.S.J. Van Deventer, J.L. Provis, The role of Al in cross-

- linking of alkali-activated slag cements, *J. Am. Ceram. Soc.* 98 (2015) 996–1004. doi:10.1111/jace.13360.
- [168] S.A. Bernal, J.L. Provis, B. Walkley, R. San Nicolas, J.D. Gehman, D.G. Brice, A.R. Kilcullen, P. Duxson, J.S.J. Van Deventer, Gel nanostructure in alkali-activated binders based on slag and fly ash, and effects of accelerated carbonation, *Cem. Concr. Res.* 53 (2013) 127–144. doi:10.1016/j.cemconres.2013.06.007.
- [169] H.F.W. Taylor, Modification of the Bogue calculation, *Adv. Cem. Res.* 2 (1989) 73–77. doi:10.1680/adcr.1989.2.6.73.
- [170] I.G. Richardson, G.W. Groves, The incorporation of minor and trace elements into calcium silicate hydrate (C-S-H) gel in hardened cement pastes, *Cem. Concr. Res.* 23 (1993) 131–138. doi:10.1016/0008-8846(93)90143-W.
- [171] J. Skibsted, M.D. Andersen, The effect of alkali ions on the incorporation of aluminum in the calcium silicate hydrate (C-S-H) phase resulting from portland cement hydration studied by ^{29}Si MAS NMR, *J. Am. Ceram. Soc.* 96 (2013) 651–656. doi:10.1111/jace.12024.
- [172] Z. Dai, T.T. Tran, J. Skibsted, Aluminum incorporation in the C-S-H phase of white portland cement-metakaolin blends studied by ^{27}Al and ^{29}Si MAS NMR spectroscopy, *J. Am. Ceram. Soc.* 97 (2014) 2662–2671. doi:10.1111/jace.13006.
- [173] M.D. Andersen, H.J. Jakobsen, J. Skibsted, A new aluminium-hydrate species in hydrated Portland cements characterized by ^{27}Al and ^{29}Si MAS NMR spectroscopy, *Cem. Concr. Res.* 36 (2006) 3–17. doi:10.1016/j.cemconres.2005.04.010.
- [174] P. Faucon, A. Delagrave, J.C. Petit, C. Richet, J.M. Marchand, H. Zanni, Aluminum incorporation in calcium silicate hydrates (C-S-H) depending on their Ca/Si ratio, *J. Phys. Chem. B.* 103 (1999) 7796–7802. doi:10.1021/jp990609q.
- [175] X. Pardal, F. Brunet, T. Charpentier, I. Pochard, A. Nonat, ^{27}Al and ^{29}Si solid-state NMR characterization of calcium-aluminosilicate-hydrate, *Inorg. Chem.* 51 (2012) 1827–1836. doi:10.1021/ic202124x.
- [176] I.G. Richardson, A.R. Brough, G.W. Groves, C.M. Dobson, The characterization of hardened alkali-activated blast-furnace slag pastes and the nature of the calcium silicate hydrate (C-S-H) phase, *Cem. Concr. Res.* 24 (1994) 813–829. doi:10.1016/0008-8846(94)90002-7.
- [177] R.S. Barneyback, S. Diamond, Expression and analysis of pore fluids from hardened cement pastes and mortars, *Cem. Concr. Res.* 11 (1981) 279–285. doi:10.1016/0008-8846(81)90069-7.

- [178] J. Duchesne, M.A. Bérubé, Evaluation of the validity of the pore solution expression method from hardened cement pastes and mortars, *Cem. Concr. Res.* 24 (1994) 456–462. doi:10.1017/CBO9781107415324.004.
- [179] V. Räsänen, V. Penttala, The pH measurement of concrete and smoothing mortar using a concrete powder suspension, *Cem. Concr. Res.* 34 (2004) 813–820. doi:10.1016/j.cemconres.2003.09.017.
- [180] T. Wagner, D.A. Kulik, F.F. Hingerl, S. V. Dmytrievava, Gem-selector geochemical modeling package: TSolMod library and data interface for multicomponent phase models, *Can. Mineral.* 50 (2012) 1173–1195. doi:10.3749/canmin.50.5.1173.
- [181] I.G. Richardson, G.W. Groves, The structure of the calcium silicate hydrate phases present in hardened pastes of white Portland cement/blast-furnace slag blends, *J. Mater. Sci.* 32 (1997) 4793–4802. doi:10.1023/A:1018639232570.
- [182] M.L.D. Gougar, B.E. Scheetz, D.M. Roy, Ettringite and C-S-H portland cement phases for waste ion immobilization: A review, *Waste Manag.* 16 (1996) 295–303. doi:10.1016/S0956-053X(96)00072-4.
- [183] P.T. Durdziński, M. Ben Haha, M. Zajac, K.L. Scrivener, Phase assemblage of composite cements, *Cem. Concr. Res.* 99 (2017) 172–182. doi:10.1016/j.cemconres.2017.05.009.
- [184] N. Mobasher, H. Kinoshita, S.A. Bernal, C.A. Sharrard, Ba(OH)₂ - Blast furnace slag composite binders for encapsulation of sulphate bearing nuclear waste, *Adv. Appl. Ceram.* 113 (2014) 460–465. doi:10.1179/1743676114Y.0000000148.
- [185] C. Cau Dit Coumes, S. Courtois, S. Peysson, J. Ambroise, J. Pera, Calcium sulfoaluminate cement blended with OPC: A potential binder to encapsulate low-level radioactive slurries of complex chemistry, *Cem. Concr. Res.* 39 (2009) 740–747. doi:10.1016/j.cemconres.2009.05.016.
- [186] X. Ke, S.A. Bernal, J.L. Provis, Controlling the reaction kinetics of sodium carbonate-activated slag cements using calcined layered double hydroxides, *Cem. Concr. Res.* 81 (2016) 24–37. doi:10.1016/j.cemconres.2015.11.012.
- [187] X. Ke, S.A. Bernal, J.L. Provis, Uptake of chloride and carbonate by Mg-Al and Ca-Al layered double hydroxides in simulated pore solutions of alkali-activated slag cement, *Cem. Concr. Res.* 100 (2017) 1–13. doi:10.1016/j.cemconres.2017.05.015.
- [188] F. Deschner, B. Lothenbach, F. Winnefeld, J. Neubauer, Effect of temperature on the hydration of Portland cement blended with siliceous fly ash, *Cem. Concr. Res.* 52 (2013) 169–181.

- doi:10.1016/j.cemconres.2013.07.006.
- [189] R.J. Myers, E. L'Hôpital, J.L. Provis, B. Lothenbach, Effect of temperature and aluminium on calcium (alumino)silicate hydrate chemistry under equilibrium conditions, *Cem. Concr. Res.* 68 (2015) 83–93. doi:10.1016/j.cemconres.2014.10.015.
- [190] J.I. Escalante-García, J.H. Sharp, Effect of temperature on the hydration of the main clinker phases in Portland cements: part II, blended cements, *Cem. Concr. Res.* 28 (1998) 1245–1257. doi:10.1016/S0008-8846(98)00115-X.
- [191] J.I. Escalante-García, J.H. Sharp, The chemical composition and microstructure of hydration products in blended cements, *Cem. Concr. Compos.* 26 (2004) 967–976. doi:10.1016/j.cemconcomp.2004.02.036.
- [192] B.A. Clark, P.W. Brown, The formation of calcium sulfoaluminate hydrate compounds: Part I, *Cem. Concr. Res.* 29 (1999) 1943–1948. doi:10.1016/S0008-8846(99)00200-8.
- [193] A. Schöler, B. Lothenbach, F. Winnefeld, M. Zajac, Hydration of quaternary Portland cement blends containing blast-furnace slag, siliceous fly ash and limestone powder, *Cem. Concr. Compos.* 55 (2015) 374–382. doi:10.1016/j.cemconcomp.2014.10.001.
- [194] M.C. Gastuche, G. Brown, M.M. Mortland, Mixed Magnesium-Aluminium Hydroxides, *Clay Miner.* 7 (1967) 193–201. doi:10.1180/claymin.1967.007.2.06.
- [195] I. Pausch, H.H. Lohse, K. Schürmann, R. Allmann, Syntheses of disordered and Al-rich hydrotalcite-like compounds, *Clays Clay Miner.* 34 (1986) 507–510. doi:10.1346/CCMN.1986.0340502.
- [196] I.G. Richardson, The importance of proper crystal-chemical and geometrical reasoning demonstrated using layered single and double hydroxides, *Acta Crystallogr. B.* 69 (2013) 150–162. doi:10.1107/S205251921300376X.
- [197] J.L. Provis, S.A. Bernal, Geopolymers and Related Alkali-Activated Materials, *Annu. Rev. Mater. Res.* 44 (2014) 299–327. doi:10.1146/annurev-matsci-070813-113515.
- [198] F. Brunet, T. Charpentier, C.N. Chao, H. Peycelon, A. Nonat, Characterization by solid-state NMR and selective dissolution techniques of anhydrous and hydrated CEM V cement pastes, *Cem. Concr. Res.* 40 (2010) 208–219. doi:10.1016/j.cemconres.2009.10.005.
- [199] H.F.W. Taylor, K. Mohan, G.K. Moir, Analytical study of pure and extended portland cement pastes: I, Pure Portland cement pastes, *J. Am. Ceram. Soc.* 68 (1985) 685–690.

doi:10.1111/j.1151-2916.1985.tb10124.x.

- [200] J. Skocek, M. Zajac, C. Stabler, M. Ben Haha, Predictive modelling of hydration and mechanical performance of low Ca composite cements: Possibilities and limitations from industrial perspective, *Cem. Concr. Res.* 100 (2017) 68–83. doi:10.1016/j.cemconres.2017.05.020.
- [201] L. Nedyalkova, B. Lothenbach, J. Tits, E. Wieland, U. Mäder, Effect of redox conditions on sulfur and selenium binding in AFm phases, *Goldschmidt Abstr.* (2017).
- [202] J.J. Thomas, D. Rothstein, H.M. Jennings, B.J. Christensen, Effect of hydration temperature on the solubility behavior of Ca-, S-, Al-, and Si-bearing solid phases in Portland cement pastes, *Cem. Concr. Res.* 33 (2003) 2037–2047. doi:10.1016/S0008-8846(03)00224-2.
- [203] T. Matschei, F.P. Glasser, Temperature dependence, 0 to 40 °C, of the mineralogy of Portland cement paste in the presence of calcium carbonate, *Cem. Concr. Res.* 40 (2010) 763–777. doi:10.1016/j.cemconres.2009.11.010.
- [204] S. Martínez-Ramírez, M. Frías, The effect of curing temperature on white cement hydration, *Constr. Build. Mater.* 23 (2009) 1344–1348. doi:10.1016/j.conbuildmat.2008.07.012.
- [205] S. Bahafid, S. Ghabezloo, M. Duc, P. Faure, J. Sulem, Effect of the hydration temperature on the microstructure of Class G cement: C-S-H composition and density, *Cem. Concr. Res.* 95 (2017) 270–281. doi:10.1016/j.cemconres.2017.02.008.
- [206] C.C. Castellano, V.L. Bonavetti, H.A. Donza, E.F. Irassar, The effect of w/b and temperature on the hydration and strength of blastfurnace slag cements, *Constr. Build. Mater.* 111 (2016) 679–688. doi:10.1016/j.conbuildmat.2015.11.001.
- [207] T.T.H. Bach, C. Cau Dit Coumes, I. Pochard, C. Mercier, B. Revel, A. Nonat, Influence of temperature on the hydration products of low pH cements, *Cem. Concr. Res.* 42 (2012) 805–817. doi:10.1016/j.cemconres.2012.03.009.
- [208] J.I. Escalante-García, J.H. Sharp, Effect of temperature on the hydration of the main clinker phases in Portland cements: Part I, neat cements, *Cem. Concr. Res.* 28 (1998) 1245–1257. doi:10.1016/S0008-8846(98)00115-X.
- [209] B.A. Clark, P.W. Brown, The formation of calcium sulfoaluminate hydrate compounds: Part II, *Cem. Concr. Res.* 30 (2000) 233–240. doi:10.1016/S0008-8846(99)00234-3.
- [210] M.U. Okoronkwo, F.P. Glasser, Compatibility of hydrogarnet, $\text{Ca}_3\text{Al}_2(\text{SiO}_4)_x(\text{OH})_{4(3-x)}$, with sulfate and carbonate-bearing cement phases: 5–85 °C, *Cem. Concr. Res.* 83 (2016) 86–96.

- doi:10.1016/j.cemconres.2016.01.013.
- [211] K. Kyritsis, N. Meller, C. Hall, Chemistry and morphology of hydrogarnets formed in cement-based CASH hydroceramics cured at 200° to 350°C, *J. Am. Ceram. Soc.* 92 (2009) 1105–1111. doi:10.1111/j.1551-2916.2009.02958.x.
- [212] K.L. Scrivener, A. Bazzoni, B. Mota, J.E. Rossen, Electron Microscopy, in: Scrivener, K. L., Snellings, R., Lothenbach, B. (Eds), *A Practical Guide to Microstructural Analysis of Cementitious Materials*, 1st ed., CRC Press, 2016. doi:10.1007/978-1-62703-776-1.
- [213] J.E. Rossen, K.L. Scrivener, Optimization of SEM-EDS to determine the C–A–S–H composition in matured cement paste samples, *Mater. Charact.* 123 (2017) 294–306. doi:10.1016/j.matchar.2016.11.041.
- [214] M. Regourd, Structure and behaviour of slag Portland cement hydrates, *Proc. 7th Int. Congr. Chem. Cem. Paris, Fr. I* (1980) III-2/10-26.
- [215] J.J. Thomas, H.M. Jennings, A colloidal interpretation of chemical aging of the C-S-H gel and its effects on the properties of cement paste, *Cem. Concr. Res.* 36 (2006) 30–38. doi:10.1016/j.cemconres.2004.10.022.
- [216] X. Cong, R.J. Kirkpatrick, Effects of the temperature and relative humidity on the structure of CSH gel, *Cem. Concr. Res.* 25 (1995) 1237–1245. doi:10.1016/0008-8846(95)00116-T.
- [217] J.M. Rivas Mercury, P. Pena, A.H. De Aza, X. Turrillas, I. Sobrados, J. Sanz, Solid-state ²⁷Al and ²⁹Si NMR investigations on Si-substituted hydrogarnets, *Acta Mater.* 55 (2007) 1183–1191. doi:10.1016/j.actamat.2006.09.032.
- [218] I.G. Richardson, S. Li, Composition and structure of an 18-year-old 5M KOH-activated ground granulated blast-furnace slag paste, *Constr. Build. Mater.* 168 (2018) 404–411. doi:10.1016/j.conbuildmat.2018.02.034.
- [219] O. Burciaga-Díaz, L.Y. Gómez-Zamorano, J.I. Escalante-García, Influence of the long term curing temperature on the hydration of alkaline binders of blast furnace slag-metakaolin, *Constr. Build. Mater.* 113 (2016) 917–926. doi:10.1016/j.conbuildmat.2016.03.111.
- [220] F. Deschner, F. Winnefeld, B. Lothenbach, S. Seufert, P. Schwesig, S. Dittrich, F. Goetz-Neunhoeffer, J. Neubauer, Hydration of Portland cement with high replacement by siliceous fly ash, *Cem. Concr. Res.* 42 (2012) 1389–1400. doi:10.1016/j.cemconres.2012.06.009.
- [221] D.A. Kulik, Dual-thermodynamic estimation of stoichiometry and stability of solid solution end

- members in aqueous-solid solution systems, *Chem. Geol.* 225 (2006) 189–212. doi:10.1016/j.chemgeo.2005.08.014.
- [222] S.A. Walling, H. Kinoshita, S.A. Bernal, N.C. Collier, J.L. Provis, Structure and properties of binder gels formed in the system $\text{Mg}(\text{OH})_2\text{-SiO}_2\text{-H}_2\text{O}$ for immobilisation of Magnox sludge, *Dalt. Trans.* 44 (2015) 8126–8137. doi:10.1039/C5DT00877H.
- [223] E. Königsberger, G. Eriksson, P.M. May, G. Hefter, Comprehensive model of synthetic Bayer liquors. Part 1. Overview, *Ind. Eng. Chem. Res.* 44 (2005) 5805–5814. doi:10.1021/ie050024k.
- [224] E. Königsberger, S. Bochmann, P.M. May, G. Hefter, Thermodynamics of impurities in hydrometallurgical processes, *Pure Appl. Chem.* 83 (2011) 1075–1084. doi:10.1351/PAC-CON-11-02-07.
- [225] M.C. Simoes, K.J. Hughes, D.B. Ingham, L. Ma, M. Pourkashanian, Estimation of the Pitzer Parameters for 1–1, 2–1, 3–1, 4–1, and 2–2 Single Electrolytes at 25 °C, *J. Chem. Eng. Data.* 61 (2016) 2536–2554. doi:10.1021/acs.jced.6b00236.
- [226] Y. Marcus, Thermodynamics of Solvation of Ions Part 5. Gibbs Free Energy of Hydration at 298.15 K, *J. Chem. Soc., Faraday Trans.* 87 (1991) 2995–2999. doi:10.1017/CBO9781107415324.004.
- [227] Y. Marcus, A simple empirical model describing the thermodynamics of hydration of ions of widely varying charges, sizes, and shapes, *Biophys. Chem.* 51 (1994) 111–127. doi:10.1016/0301-4622(94)00051-4.
- [228] G. Plusquellec, M.R. Geiker, J. Lindgård, J. Duchesne, B. Fournier, K. De Weerd, Determination of the pH and the free alkali metal content in the pore solution of concrete: Review and experimental comparison, *Cem. Concr. Res.* 96 (2017) 13–26. doi:10.1016/j.cemconres.2017.03.002.
- [229] E.E. Lachowski, S.J. Barnett, D.E. Macphee, Transmission electron optical study of ettringite and thaumasite, *Cem. Concr. Compos.* 25 (2003) 819–822. doi:10.1016/S0958-9465(03)00107-0.
- [230] I. Baur, P. Keller, D. Mavrocordatos, B. Wehrli, C.A. Johnson, Dissolution-precipitation behaviour of ettringite, monosulfate, and calcium silicate hydrate, *Cem. Concr. Res.* 34 (2004) 341–348. doi:10.1016/j.cemconres.2003.08.016.
- [231] B. Lothenbach, L. Pelletier-Chaignat, F. Winnefeld, Stability in the system $\text{CaO-Al}_2\text{O}_3\text{-H}_2\text{O}$, *Cem. Concr. Res.* 42 (2012) 1621–1634. doi:10.1016/j.cemconres.2012.09.002.

- [232] G.D. Miron, T. Wagner, D.A. Kulik, C.A. Heinrich, Internally consistent thermodynamic data for aqueous species in the system Na-K-Al-Si-O-H-Cl, *Geochim. Cosmochim. Acta.* 187 (2016) 41–78. doi:10.1016/j.gca.2016.04.026.
- [233] B. Lothenbach, L. Pelletier-Chaignat, F. Winnefeld, Stability in the system CaO-Al₂O₃-H₂O, *Cem. Concr. Res.* 42 (2012) 1621–1634. doi:10.1016/j.cemconres.2012.09.002.
- [234] F.E. Jones, The Quinary System CaO–Al₂O₃–CaSO₄–K₂O–H₂O (1 per cent KOH) at 25°C, *J. Phys. Chem.* 48 (1944) 356–378. doi:10.1021/j150438a002.
- [235] F.E. Jones, The quinary system CaO-Al₂O₃-CaSO₄-Na₂O-H₂O (1 per cent NaOH) at 25°C, *J. Phys. Chem.* 48 (1944) 379–394. doi:10.1021/j150438a003.
- [236] F.E. Jones, The Quaternary System CaO–Al₂O₃–CaSO₄–H₂O at 25°C. Equilibria with Crystalline Al₂O₃–3H₂O, Alumina Gel, and Solid Solution, *J. Phys. Chem.* 48 (1944) 311–356. doi:10.1021/j150438a001.
- [237] C.A.J. Appelo, Principles, caveats and improvements in databases for calculating hydrogeochemical reactions in saline waters from 0 to 200 °C and 1 to 1000 atm, *Appl. Geochemistry.* 55 (2015) 62–71. doi:10.1016/j.apgeochem.2014.11.007.
- [238] E. Konigsberger, P. Schmidt, H. Gamsj, Solid-Solute Phase Equilibria in Aqueous Solution. VI . Solubilities , Complex Formation, and Ion-Interaction Parameters for the System Na⁺ - Mg²⁺ - ClO₄⁻ - CO₂ - H₂O at 25 °C, 21 (1992) 1195–1216.
- [239] H. Park, P. Englezos, Osmotic coefficient data for NaOH-NaCl-NaAl(OH)₄-H₂O system measured by an isopiestic method and modeled using Pitzer’s model at 298.15 K, *Fluid Phase Equilib.* 155 (1999) 251–259. doi:10.1016/S0378-3812(98)00460-9.
- [240] F. Cavani, F. Trifirò, A. Vaccari, Hydrotalcite-type anionic clays: Preparation, properties and applications., *Catal. Today.* 11 (1991) 173–301. doi:10.1016/0920-5861(91)80068-K.
- [241] G. Mascolo, O. Marino, A new synthesis and characterization of magnesium-aluminium hydroxides, *Miner. Mag.* 43 (1980) 619.
- [242] W. Gao, Z. Li, Solubility and K_{SP} of Mg₄Al₂(OH)₁₄·3H₂O at the various ionic strengths, *Hydrometallurgy.* 117–118 (2012) 36–46. doi:10.1016/j.hydromet.2012.02.003.
- [243] A. Kumar, B.J. Walder, A. Kunhi Mohamed, A. Hofstetter, B. Srinivasan, A.J. Rossini, K. Scrivener, L. Emsley, P. Bowen, The Atomic-Level Structure of Cementitious Calcium Silicate Hydrate, *J. Phys. Chem. C.* (2017) acs.jpcc.7b02439. doi:10.1021/acs.jpcc.7b02439.

- [244] J.L. Provis, P. Duxson, G.C. Lukey, F. Separovic, W.M. Kriven, J.S.J. Van Deventer, Modeling speciation in highly concentrated alkaline silicate solutions, *Ind. Eng. Chem. Res.* 44 (2005) 8899–8908. doi:10.1021/ie050700i.
- [245] D.E. Machphee, K. Luke, F.P. Glasser, E.E. Lachowski, Solubility and aging of calcium silicate hydrates in alkaline solutions at 25 °C, *J. Am. Ceram. Soc.* 72 (1989) 646–654. doi:10.1111/j.1151-2916.1989.tb06189.x.
- [246] S. Song, H.M. Jennings, Pore solution chemistry of alkali-activated ground granulated blast-furnace slag, *Cem. Concr. Res.* 29 (1999) 159–170. doi:10.1016/S0008-8846(98)00212-9.
- [247] F.J. Millero, The thermodynamics and kinetics of the hydrogen sulfide system in natural waters, *Mar. Chem.* 18 (1986) 121–147. doi:10.1016/0304-4203(86)90003-4.
- [248] R.A. Robie, B.S. Hemingway, Thermodynamic properties of minerals and related substances at 298.15 K and 1 bar (10^5 Pascals) pressure and at higher temperatures, 1995.
- [249] H.C. Helgeson, J.M. Delany, H.W. Nesbitt, Summary and critique of the thermodynamic properties of rock-forming minerals, *Am. J. Sci.* 278 (1978) 1–229.
- [250] W. Hummel, U. Berner, E. Curti, F.J. Pearson, T. Thoenen, Nagra/PSI Chemical Thermodynamic Data Base 01/01, Parkland, Florida, 2002.
- [251] T. Thoenen, W. Hummel, U. Berner, E. Curti, The PSI/Nagra Chemical Thermodynamic Database 12/07, Villigen PSI, Switzerland, 2014.
- [252] R.K. Allada, A. Navrotsky, J. Boerio-Goates, Thermochemistry of hydrotalcite-like phases in the MgO-Al₂O₃-CO₂-H₂O system: A determination of enthalpy, entropy, and free energy, *Am. Mineral.* 90 (2005) 329–335. doi:10.2138/am.2005.1737.
- [253] E.L. Shock, D.C. Sassani, M. Willis, D.A. Sverjensky, Inorganic species in geologic fluids: Correlations among standard molal thermodynamic properties of aqueous ions and hydroxide complexes, *Geochim. Cosmochim. Acta.* 61 (1997) 907–950. doi:10.1016/S0016-7037(96)00339-0.
- [254] E.L. Shock, H.C. Helgeson, D.A. Sverjensky, Calculation of the thermodynamic and transport properties of aqueous species at high pressures and temperatures: Standard partial molal properties of inorganic neutral species, *Geochim. Cosmochim. Acta.* 53 (1989) 2157–2183. doi:10.1016/0016-7037(89)90341-4.
- [255] E.L. Shock, H.C. Helgeson, Calculation of the thermodynamic and transport properties of

- aqueous species at high pressures and temperatures: Standard partial molal properties of organic species, *Geochim. Cosmochim. Acta.* 54 (1990) 915–945. doi:10.1016/0016-7037(90)90429-O.
- [256] J.W. Johnson, E.H. Oelkers, H.C. Helgeson, SUPCRT92: A software package for calculating the standard molal thermodynamic properties of minerals, gases, aqueous species, and reactions from 1 to 5000 bar and 0 to 1000 °C, 1992. doi:10.1016/0098-3004(92)90029-Q.
- [257] D.D. Wagman, W.H. Evans, V.B. Parker, R.H. Schumm, I. Halow, The NBS tables of chemical thermodynamic properties. Selected values for inorganic and C1 and C2 organic substances in SI units, *J. Phys. Chem. Ref. Data.* 18 (1982) 1807–1812. doi:10.1063/1.555845.
- [258] G.M. Marion, J.K. Crowley, B.J. Thomson, J.S. Kargel, N.T. Bridges, S.J. Hook, A. Baldrige, A.J. Brown, B. Ribeiro da Luz, C.R. de Souza Filho, Modeling aluminum-silicon chemistries and application to Australian acidic playa lakes as analogues for Mars, *Geochim. Cosmochim. Acta.* 73 (2009) 3493–3511. doi:10.1016/j.gca.2009.03.013.
- [259] G.M. Rosenblatt, Estimation of activity coefficients in concentrated sulfite-sulfate solutions, *AIChE J.* 27 (1981) 619–626. doi:10.1002/aic.690270413.
- [260] C.A.J. Appelo, D.L. Parkhurst, V.E.A. Post, Equations for calculating hydrogeochemical reactions of minerals and gases such as CO₂ at high pressures and temperatures, *Geochim. Cosmochim. Acta.* 125 (2014) 49–67. doi:10.1016/j.gca.2013.10.003.
- [261] G.M. Marion, D.C. Catling, J.S. Kargel, Modeling aqueous ferrous iron chemistry at low temperatures with application to Mars, *Geochim. Cosmochim. Acta.* 67 (2003) 4251–4266. doi:10.1016/S0016-7037(03)00372-7.
- [262] S.L. Clegg, J.A. Rard, K.S. Pitzer, Thermodynamic Properties of 0-6 mol kg⁻¹: Aqueous Sulfuric Acid from 273.15 to 328.15 K, *J. Chem. Soc. Faraday Trans.* 90 (1994) 1875–1894. doi:10.1039/FT9949001875.
- [263] R.N. Roy, J. Zhang, M.A. Sibbles, F.J. Millero, The pK₂* for the Dissociation of H₂SO₃ in NaCl Solutions with Added Ni²⁺, Co²⁺, Mn²⁺, and Cd²⁺ at 25 °C, *Ocean Sci.* 20 (1991) 467–478. doi:10.1007/BF00650803.
- [264] H. Kim, W.J. Frederick, Evaluation of Pitzer Ion Interaction Parameters of Aqueous Electrolytes at 25°C. 2. Ternary Mixing Parameters, *J. Chem. Eng. Data.* 33 (1988) 177–184. doi:10.1021/je00052a035.
- [265] H.-T. Kim, W.J. Frederick, Evaluation of Pitzer Ion Interaction Parameters of Aqueous

- Electrolytes at 25°C. 1. Single Salt Parameters, *J. Chem. Eng. Data.* 33 (1988) 177–184. doi:10.1021/je00052a035.
- [266] M. Azaroual, C. Fouillac, J.M. Matray, Solubility of silica polymorphs in electrolyte solutions, I. Activity coefficient of aqueous silica from 25° to 250°C, Pitzer's parameterisation, *Chem. Geol.* 140 (1997) 155–165. doi:10.1016/S0009-2541(97)00046-6.
- [267] C.Y. Chan, K.H. Khoo, Calculation of activities and solubilities of alkali metal perchlorates at high ionic strengths in multicomponent aqueous systems, *J. Solution Chem.* 17 (1988) 547–567. doi:10.1007/BF00651462.
- [268] C.F. Weber, Calculation of Pitzer Parameters at High Ionic Strengths, *Ind. Eng. Chem. Res.* 39 (2000) 4422–4426. doi:10.1021/ie000411o.

Publications from thesis

Journal Publications

D. P. Prentice, S. A. Bernal, M. Bankhead, M. Hayes and J. L. Provis. *“Phase evolution of slag-rich cementitious grouts for immobilisation of nuclear wastes”*, *Advances in Cement Research*. 2017, 30(8), pp. 345-360.

D. P. Prentice, B. Walkley, S. A. Bernal, M. Bankhead, M. Hayes and J. L. Provis. *“Thermodynamic modelling of BFS-PC cements under temperature conditions relevant to the geological disposal of nuclear wastes”*, Manuscript submitted to *Cement and Concrete Research*. (Accepted 12/1/2019)

Conference Publications

D. P. Prentice, S. A. Bernal, M. Bankhead, M. Hayes and J. L. Provis. *“Thermodynamic modelling of Portland/slag nuclear wasteforms”*, in: 35th Cement and Concrete Science Conference, Aberdeen, 2015.

D. P. Prentice, S. A. Bernal, M. Bankhead, M. Hayes and J. L. Provis. *“Phase evolution of slag-rich cementitious grouts for immobilisation of nuclear wastes: an experimental and modelling approach”*, in: 36th Cement and Concrete Science Conference, Cardiff, 2016.

Prentice, D., Bernal, S., Bankhead, M., Hayes, M. and Provis, J. *“Using the Pitzer model to predict aqueous solution compositions of Portland cements blended with supplementary materials”*, 71st RILEM week and ICACMS 2017, Chennai, 2017.

Other conference presentations

D. P. Prentice, S. A. Bernal, M. Bankhead, M. Hayes and J. L. Provis. *“Using Pitzer parameters to predict aqueous solutions of synthetic C-A-S-H gels”*, in 1st International Conference on Construction Materials for Sustainable Future, Zadar, 2017 (Poster presentation)

D. P. Prentice, S. A. Bernal, M. Bankhead, M. Hayes and J. L. Provis. "*Phase assemblage within Portland/slag blended cements: A thermodynamic modelling and experimental approach*", in: 4th Mechanisms and Modelling of Waste/Cement Interactions, Murten, 2016 (Oral presentation).

D. P. Prentice, S. A. Bernal, M. Bankhead, M. Hayes and J. L. Provis. "*Thermodynamic modelling of cementitious materials*", in The NNL Waste Management, Decommissioning and Disposal (WMD&D) Signature Research Programme (SRP) Seminar, Warrington, 2015 (Oral and poster presentation).